Durham E-Theses

Variable-temperature photoluminescence emission instrumentation and measurements on low yield metals

ARMSTRONG, HELEN

Variable-temperature photoluminescence emission instrumentation and measurements on low yield metals

Helen Armstrong

A thesis submitted in partial fulfilment of the requirements

for the degree of Doctor of Philosophy

Department of Physics, University of Durham

2010

Abstract

Measurements of the photoluminescence emission spectra of 99.999 % purity gold, 99.9999 % purity copper, polycrystalline $PbMo_6S_8$ and single crystal YBCO were made for λ_{ex} = 488 nm as a function of temperature (72 K $\leq$ T $\leq$ 300 K), time (t $\leq$ 12 hours), excitation power (P $\leq$ 120 mW) and position on the sample using a high sensitivity instrument which was designed, commissioned and calibrated for this study.

We present the first measurements of the photoluminescence emission spectra of gold and copper as a function of temperature which show peak photoluminescence emission intensity increasing by approximately a factor of two for gold and a factor of five for copper between 300 K and 79 K. Full width half maximum (FWHM) and peak photoluminescence emission wavelength showed no dependence upon temperature. The spectra compare well to published data and data modelled using theories presented in the literature.

Variable temperature measurements on the superconductors $PbMo_6S_8$ and YBCO in their normal state show peak photoluminescence intensity increasing by a factor of 1.5 between 300 K and 80 K for $PbMo_6S_8$ and a factor of 2 between 300 K and 131 K for YBCO. A decrease in FWHM of 20 - 30 nm is observed with no change in peak photoluminescence wavelength. Measurements for 99.99 % purity single crystal niobium, polycrystalline $SnMo_6S_8$ and single crystal DyBCO superconductors are also presented, however, these samples exhibited problems with oxidation, impurities or damage to the sample surface.

Two interesting features which remain unexplained from this work include a variation in photoluminescence emission intensity over < 12 hours with a period of ~400 minutes for gold and copper and a continuous decrease in intensity for niobium, $SnMo_6S_8$ and YBCO and an increase in photoluminescence emission intensity by a factor of 4 at low temperatures in $PbMo_6S_8$, $SnMo_6S_8$ and YBCO.

Table of contents

Declaration

I hereby declare that the work contained within this thesis is my own original work and nothing that is the result of collaboration unless otherwise stated. No part of this thesis has been submitted for a degree or other qualification at this or any other university.

The copyright of this thesis rests with the author. No quotation from it should be published without prior written consent and information derived from it should be acknowledged

Helen Armstrong

March 2010

Acknowledgements

There are many people who deserve thanks for the help and support they have shown me throughout my PhD. Firstly, I express my appreciation to my supervisors: Professor Damian Hampshire and Dr Douglas Halliday who have given me guidance and support over the last four and a half years. I would also like to thank Dr Stewart Clark for his calculations of the density of states and band structures for all the samples presented in this thesis.

My thanks also go to the many technicians in the Physics Department at Durham University who have supported me during my time here. I am truly thankful to Norman Thompson, David Pattison and Duncan McCallum for their tireless efforts in mending broken equipment at a moments notice and helping with the installation and removal of several lasers. To the staff in the electronics workshop I pass on my thanks for their help in fixing switches, power supplies and for their continued advice on all things electrical. I would also like to thank the mechanical workshop for the many sample holders, mounts, magnets and furnace equipment which they have built for me over the last four years. Their patience and understanding as I learnt CAD has been exceptional. To Wayne Dobby I add my thanks for the years of equipment loans and enjoyable afternoons spent teaching in the 3rd year undergraduate labs.

I would like to express my gratitude to my friends and family for their support and love over what has been an interesting four and a half years. To Helen Vaughan and Margaret Harris who were on hand 24 hours a day when it all became too much and who dragged me out of the dark of the lab or joined me down there on more than one occasion. I would also like to thank Chris Saunter for his ideas, support and loan of some very expensive equipment! Without his help I would still be aligning optics the wrong

way! My special thanks go to the many members of the Superconductivity group that I have known over the last four years, without whom, I would not have made it through the rollercoaster of results collection. To David Taylor, Matthew King, George Carty, Jian-Yong Xiang, Xifeng Lu, Elizabetta Pusccuddu, Joshua Higgins, Mark Raine and Steven Pragnell I say thank you for so many years of support, confidence and ideas. Thanks must also go to the Nanoscale Science and Technology Group; Del Atkinson, Lara Bogart, David Eastwood, Rachael Houchin, Jenny King and Miriana Vadala who have provided much needed support and friendship through the long and winding process of thesis writing.

Finally, to my parents and brother, I cannot express how much their love and support have meant to me for all these years. They have always encouraged me to follow whichever career I chose and have always had an understanding ear when times have been hard. Last but by no means least, I thank Andy for being my rock and for having dinner and a welcoming smile for me to come home to every night.

Chapter 1. Introduction

The phenomenon of luminescence was first documented in China nearly 2000 years ago as bioluminescence from plants and animals [1]. The discovery of the "Bolognian Stone" in Italy in 1602 was the first recorded evidence of luminescence from an inorganic material [2]. The stone excited great interest in the scientific community as it was observed to emit light at decreasing intensities over a period of hours after it had been exposed to sunlight. The material is now known to be barite, which emits light by phosphorescence (delayed luminescence emission). Thanks to the work of scientists over the last 400 years, phosphorescence is now used in applications throughout households and workplaces and is utilised in everyday objects such as watches, children's toys and emergency signage.

Luminescence is the general term applied to the emission of light through the recombination of pairs of electrons and holes which have been promoted into excited states though the application of an additional source of energy. Common excitation sources (and the term for their associated luminescence emission processes) include; heat (thermoluminescence), chemical reactions (chemoluminescence), biological processes (bioluminescence) and electron irradiation (cathodoluminescence). Photoluminescence, which will be the main process investigated in this thesis, relates to radiative recombination of electron – hole pairs which have been excited by light.

Photoluminescence spectroscopy is an extremely useful, non destructive method of probing the electronic structure of a sample of within a few hundred nanometres of its surface and is the standard analytical technique in the semiconductor industry to determine sample quality [3-5]. The technique is also being pioneered in the field of

medical imaging for tracking biological cells as they move around the body using a fluorescent marker to tag the cells [6]. Research into the fabrication of more efficient solar cells and organic light emitting diodes for use in flat panel televisions and lighting also use photoluminescence as an analysis technique during manufacturing and development as it is a fast and robust technique for identifying the sample characteristics [7, 8].

Despite the range of applications of photoluminescence to a multitude of organic and inorganic materials, there has been little research dedicated to the photoluminescence emission from metals. The study of photoluminescence emission from metals has been limited mainly by the experimental complications of trying to measure the low emission yields exhibited by these materials [9-11]. By their nature, metals have a high density of free electrons leading to large electrical conductivities. These free electrons limit the photoluminescence emission yield since they increase the probability of non-radiative recombination which directly competes with the radiative recombination processes of photoluminescence emission.

Little work has been carried out on the photoluminescence emission from superconducting materials again due to their low emission yields. A superconductor is a remarkable material which exhibits zero electrical resistivity and expels all magnetic flux below its critical temperature. Superconductors are commonly discussed as being one of two types; conventional low temperature superconductors and high temperature superconductors. The mechanism of superconductivity in conventional low temperature superconductors was proposed in BCS theory (Bardeen, Cooper and Schreiffer) published in 1957 [12]. However, the mechanism behind superconductivity in high temperature (unconventional) superconductors has not been satisfactorily explained by any theories to date. Additional experimental evidence from new experimental

techniques is required to help formulate new theories for the mechanism of superconductivity in these materials. It is hoped that photoluminescence spectroscopy can fill this role by probing the optical and electronic properties close to the Fermi energies for a range of materials as they enter the superconducting state.

The aim of this work is to present a systematic study of photoluminescence emission as a function of temperature for metallic non-superconducting samples (gold and copper), metallic superconducting samples (niobium) and a selection of low temperature (Chevrel phase) and high temperature (DyBCO and YBCO) superconductors in their non-superconducting (normal) state. Using a systematic study across a range of samples, changes in the electronic and optical properties specific to certain materials will be identified as a function of temperature to give new insights into the mechanisms operating in the different classes of materials.

The thesis is structured as follows: Chapter 2 considers the processes occurring in photoluminescence emission in terms of absorption, relaxation and recombination processes. Work from the literature on the photoluminescence emission from metals and superconductors is discussed including detail of the electronic structure and optical and transport measurements of these materials. A brief summary of experimental geometries for the measurement of photoluminescence emission is given along with a discussion of the advantages and disadvantages of a range of optical components and cryostats.

Chapter 3 focuses on the use of commercial equipment for the characterisation of the optical and electronic properties of metallic and superconducting samples. The chapter is split into three sections. The first section considers the use of commercial apparatus for the measurement of photoluminescence emission from samples with low emission yields. The advantages and disadvantages of the equipment are discussed with the aid of preliminary measurements on Chevrel phase superconductor samples. The

second section presents spectra for the refractive index, extinction coefficient and reflectivity for all samples studied in this thesis using measurements made on a commercial variable angle ellipsometer. Where available, the measured spectra are also compared with data from the literature. Finally, electrical transport and AC susceptibility measurements from a Quantum Design Physical Properties Measurement System (PPMS) are presented and the critical temperatures (T_C) identified for all superconducting samples under investigation.

Chapter 4 details the design, commissioning and calibration of an instrument to measure low yield photoluminescence emission from metals and superconductors as a function of temperature. The optical, thermal and electrical requirements of such a system are discussed including a thorough investigation of sample temperature under laser illumination.

Chapter 5 presents experimental data for high purity gold and copper samples with chapter 6 presenting data for superconducting samples (niobium, $PbMo_6S_8$, $SnMo_6S_8$, $Sn_{1-x}Eu_xMo_6S_8$ x = 0.35, $Pb_{1-x}Gd_xMo_6S_8$ x = 0.35, DyBCO and YBCO). Spatially resolved photoluminescence emission spectra are shown from across the sample surfaces along with the dependence of the photoluminescence emission on excitation power, temperature and time. Calculated photoluminescence emission spectra for each of the samples are compared with experimentally measured spectra using refractive index, extinction coefficient and reflectivity data measured in chapter 3. A thorough discussion of the data is presented at the end of each chapter.

Finally, chapter 7 presents the conclusions of the study and discusses possible directions for future work in the field of photoluminescence emission spectroscopy of metals and superconductors.

Chapter 2. Review of the literature

2.1. Introduction

Photoluminescence emission spectroscopy probes the electronic structure within a few hundred nanometres of a sample's surface. It is capable of determining the band gap in semiconductors and gives information about impurity states and dopants [3-5]. The technique has been applied to many different materials including polymers, glasses and semiconductors but the study of photoluminescence emission from metals and superconductors has been limited mainly due to the extremely low emission yields exhibited by these materials [9-11]. Indeed, measurements reported for photoluminescence emission from superconducting alloys and ceramics as a function of temperature are not consistent with each other [13-20]. The following chapter reviews the studies on metals and superconductors in the literature and tries to determine the limitations of current understanding of photoluminescence emission from these materials.

Chapter 2 is divided into the following sections – which sequentially increase in complexity. Section 2.2. gives an overview of the processes of absorption, reflection and transmission of light using classical optics following from Maxwell's equations. Section 2.3. includes the ideas of the interaction of light with simple metals containing a Fermi surface. Section 2.4. considers the photoluminescence processes occurring in semiconductors with section 2.5. looking at the theory of photoluminescence in metals. Experimental results for the photoluminescence emission from metals are presented in

section 2.5.6. including a discussion of the dependence of photoluminescence emission on sample purity, polarisation of the excitation light, temperature, surface roughness and oxidation. Section 2.6. then looks at the work carried out to date observing photoluminescence emission from superconducting materials including measurements made as a function of temperature across the superconducting transition temperature. A brief overview of the theory of superconductivity is also given in this section along with a discussion of optical and electrical transport properties of these materials. Finally, section 2.7. looks at the requirements for successful experimental design for the measurement of low yield photoluminescence emission.

2.2. Classical Optics

The following section follows the structure commonly found in optics textbooks and considers the absorption, reflection and transmission of light though matter [21]. The results derived below follow from considering a continuum model in conjunction with the introduction of energy dissipation in the framework of Maxwell's equations. The terms for absorption and reflectivity are defined using the optical constants of refractive index and extinction coefficient (n and κ, respectively).

2.2.1. Absorption, reflection and transmission

The intensity, $I(z)$, of an electromagnetic wave travelling through a medium decreases over a distance, z, due to absorption, α, within the medium [22]

$$I(z) = I_0 \exp(-\alpha z), \qquad (2.1)$$

where, I_0 is the optical intensity at $z = 0$.

The absorption coefficient is defined as the fraction of power absorbed per unit length of a medium. It can be expressed in terms of the extinction coefficient of the sample, κ, and the frequency of light incident on the sample, ω, [23, 24]

$$\alpha = \frac{2\kappa\omega}{c} = \frac{4\pi\kappa}{\lambda}, \tag{2.2}$$

where λ is the wavelength of the electromagnetic wave and c is the velocity of an electromagnetic wave in free space. The extinction coefficient is the damping constant of the electromagnetic wave in the medium and is related to the refractive index, n, of a medium via the complex refractive index, $\tilde{n}$ [25-27] where

$$\tilde{n} = n + i\kappa. \tag{2.3}$$

The real part of the complex refractive index is defined as the ratio of the velocity of an electromagnetic wave in free space with the phase velocity of light in a medium, v_p, [28, 29]

$$n = \frac{c}{v_p}, \tag{2.4}$$

The velocity of light in a medium is expressed in terms of the electrical conductivity of the medium, σ, the relative permittivity, ε_r, relative permeability, μ_r, and the permittivity and permeability of free space (ε_0 and μ_0 respectively) [30],

$$\frac{1}{v^2} = \varepsilon_0\varepsilon_r\mu_0\mu_r - i\mu_0\mu_r\frac{\sigma}{2\pi v}. \tag{2.5}$$

Rearranging equations (2.3), (2.4) and (2.5) allows the complex refractive index to be written in terms of the electrical conductivity and dielectric constant [31, 32]

$$\tilde{n}^2 = \mu_r\varepsilon_r + i\frac{\mu_r\sigma}{\varepsilon_0\omega}, \tag{2.6}$$

or equally in terms of real and imaginary parts [31]:

$$\varepsilon_r\mu_r = n^2 - \kappa^2, \tag{2.7}$$

$$\sigma\mu_r = n\kappa\nu. \tag{2.8}$$

For all materials, the sum of the reflection, $\Re$, absorption, α, and transmission, D, of light through a medium is equal to unity, [33]

$$\Re + \alpha + D = 1, \tag{2.9}$$

For a metal, the proportion of transmitted light is negligible and equation (2.9) can be simplified to $\Re = 1 - \alpha$. Figure 2.1 shows the criteria for the reflection and transmission of light at a boundary in a metal [34].

Reflectivity is defined as the ratio of reflected intensity to incident intensity. Solving the equations for the reflected, transmitted and absorbed electromagnetic waves (Figure 2.1) using the criteria that the components of the electric and magnetic fields (E_y and H_z, respectively) must be continuous across the boundary, gives an expression for reflectivity, [34]

$$\Re = \frac{|\beta|^2}{|\alpha|^2} = \frac{\beta\beta^*}{\alpha\alpha^*} = \frac{(\tilde{n} - \mu_0\mu_r)(\tilde{n}^* - \mu_0\mu_r)}{(\tilde{n} + \mu_0\mu_r)(\tilde{n}^* + \mu_0\mu_r)}, \tag{2.10}$$

$$E_{y(abs)} = H_{y(abs)} = \alpha\exp i(\omega t - \omega x/c)$$

$$E_{y(ref)} = -H_{y(ref)} = \beta\exp i(\omega t + \omega x/c)$$

Vacuum
$n = 1$

$x = 0$

Metal
$\tilde{n} = n + i\kappa$

$$E_{y(trans)} = \xi\exp i(\omega t + \omega\tilde{n}x/c)$$
$$H_{z(trans)} = \xi(\tilde{n}/\mu_0\mu_r)\exp i(\omega t + \omega\tilde{n}x/c)$$
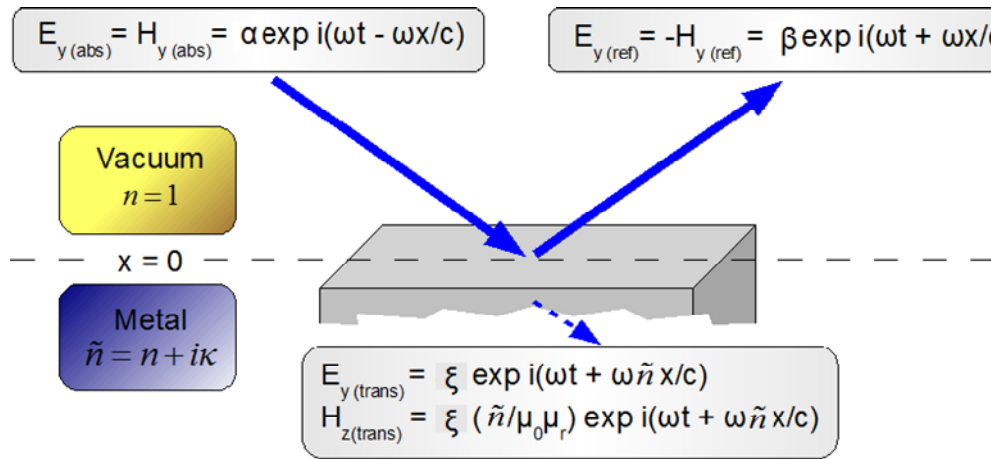
Figure 2.1 Absorption, reflection and transmission of an electromagnetic plane wave of frequency ω which is incident on a metallic surface with components of electric and magnetic field, E_y and H_y, respectively. Adapted from the works of Fox and Sokolov [32, 35]. Where α, β and ξ are the constants for absorption, reflection and transmission, respectively.

with substitution of $\tilde{n} = n - i\kappa$ leading to [34, 36, 37]

$$\Re = \frac{\left(n - \mu_0 \mu_r\right)^2 + \kappa^2}{\left(n + \mu_0 \mu_r\right)^2 + \kappa^2} .$$ (2.11)

2.3. Light in simple metals with a Fermi surface

The Drude-Lorentz model can be used to describe the interaction of light with a simple metal. The light sets up an oscillating AC electric field, E, in the metal which causes a displacement of the electrons, x, for which the equation of motion can be written as [38]

$$m\frac{d^2 x}{dt^2} + m\gamma \frac{dx}{dt} = -eEe^{-i\omega t} ,$$ (2.12)

where e is the charge of an electron, m is its mass, γ is the damping parameter, ω is the frequency of the oscillation and t is time. The first term represents the acceleration of the electrons, the second term is the frictional damping force acting on the electrons and the third term is the driving force exerted by the light. Solving the equation using the substitution of $x = x_0 e^{-i\omega t}$ gives an equation for the displacement of the electrons of

$$x(t) = \frac{eE}{m(\omega^2 + i\gamma\omega)} .$$ (2.13)

The definition of the electric displacement, D, in terms of electric field, E, and polarisation, P, is

$$D = \varepsilon_0 E + P ,$$ (2.14)

where the polarisation of the free electron gas is equal to

$$P = -Nex ,$$ (2.15)

and N is the density of free electrons. Substitution of equations (2.13) into (2.15) then equation (2.14) gives

$$D = \varepsilon_0 E - Nex$$
$$= \varepsilon_0 E - \frac{Ne^2 E}{m(\omega^2 + i\gamma\omega)} \qquad (2.16)$$

Rearrangement of equation (2.16) leads to the equation for the plasma frequency, ω_p, where [39-42]

$$\omega_p^2 = \left(\frac{Ne^2}{\varepsilon_0 m} \right)^{\frac{1}{2}}. \qquad (2.17)$$

Equations (2.16) and (2.17) can be used to find the equation for the dielectric constant of a lightly damped system ($\gamma = 0$), where it can be seen that ε_r is equal to zero at the plasma frequency,

$$\varepsilon_r = 1 - \frac{\omega_p^2}{\omega^2}. \qquad (2.18)$$

Using this relationship for ε_r, the optical spectrum of a simple metal can be split into three main regions depending upon the sign of the dielectric constant. In its most simplistic form, when $\varepsilon_r < 0$ total reflection occurs from the metal surface and when $\varepsilon_r > 0$ the metal is transparent. An absorption edge is present in the absorption spectrum of metals caused by the oscillation of the electrons and ions under the application of an AC electric field e.g. light.

In metals, the density of free electrons (N) is large, which leads to a plasma frequency in the ultraviolet region of the spectrum and therefore a high reflectivity in the visible region. A sharp transition from reflecting to transparent is only observed at the plasma frequency if no other absorption processes take place at this frequency.

Figure 2.2 shows the calculated refractive index and extinction coefficient for aluminium.
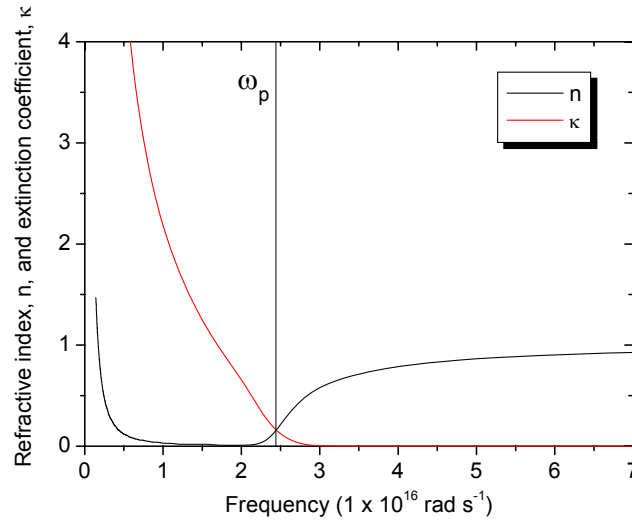
Figure 2.2 Refractive index, n, and extinction coefficient, κ, as a function of frequency for aluminium calculated using the free electron model.

Table 2.1 shows the calculated wavelengths for the boundaries for the absorbing, reflecting and transparent regions of gold, copper and aluminium using equations (2.17) and (2.18) from the free electron model. The optical constants for each region are summarised below.

Absorbing region ($\omega << \gamma$) and ($0 < \omega\tau < 1$) [43, 44]

When the frequency is much less than γ, the region is absorbing and n is equal to κ [43]

$$n^2 = \kappa^2 \simeq \frac{Ne^2}{2\varepsilon_0 m\gamma\omega} .$$
(2.19)

Reflecting region ($\gamma << \omega << \omega_p$) [43, 44]

In this region, n is smaller than κ, which is greater than unity, and is approximated by [44]

$$n \approx \frac{\omega_p \gamma}{2\omega^2}, \tag{2.20}$$

$$\kappa \approx \sqrt{\left(\frac{\omega_p}{\omega}\right)^2 - 1} \approx \frac{\omega_p}{\omega}. \tag{2.21}$$

There is almost total reflection (little absorption) as the real part of ε_r is negative. This can be quantified as

$$\alpha = \frac{2\gamma}{\omega_p} \tag{2.22}$$

Theory and experiment do not compare well using the free electron model in the reflecting region.

Transparent region $\omega > \omega_p$

In this region, ω is greater than γ by a factor of 100 and the reflectivity is very low. The real part of ε_r is greater than zero and the imaginary part is much smaller than 1. n and κ approximate to [44]

$$n \approx \sqrt{1 - \left(\frac{\omega_p}{\omega}\right)^2} \approx 1, \tag{2.23}$$

$$\kappa \approx \frac{\omega_p \gamma}{2\omega^2} \approx 0. \tag{2.24}$$

Metal	Boundary of absorbing region $\gamma \gg \omega$	Reflecting region $\omega_p \gg \omega \gg \gamma$	Transparent region $\omega > \omega_p$
Gold	$\gg$ 51 μm	51 μm – 137 nm	< 137 nm
Copper	$\gg$ 47 μm	47 μm – 115 nm	< 115 nm
Aluminium	$\gg$ 115 μm	115 μm – 79 nm	< 79 nm

Table 2.1 Boundaries of the main spectral regions for Cu, Au and Al predicted by the free electron model (equations (2.16) and (2.17)).

2.4. Photoluminescence in semiconductors

2.4.1. Basic photoluminescence processes

The text-book description of photoluminescence emission in semiconductors is a three stage process. Firstly, a photon of energy E_{ex} is absorbed by the sample, promoting the electron to a higher state and leaving a hole in the lower state. The electron and hole then relax into the excited state with the lowest available energy. Finally, the electron and hole pair recombine, releasing a photon with an energy, $E_{em,}$ which is lower than the original excitation energy (Figure 2.3).

In solid state materials, the strongest photoluminescence (PL) emission is generally found in semiconductors due to the fundamental band gap at the Fermi energy. The band gap has an energy which is comparable to the energy of the incident excitation light, leading to strong absorption and emission.
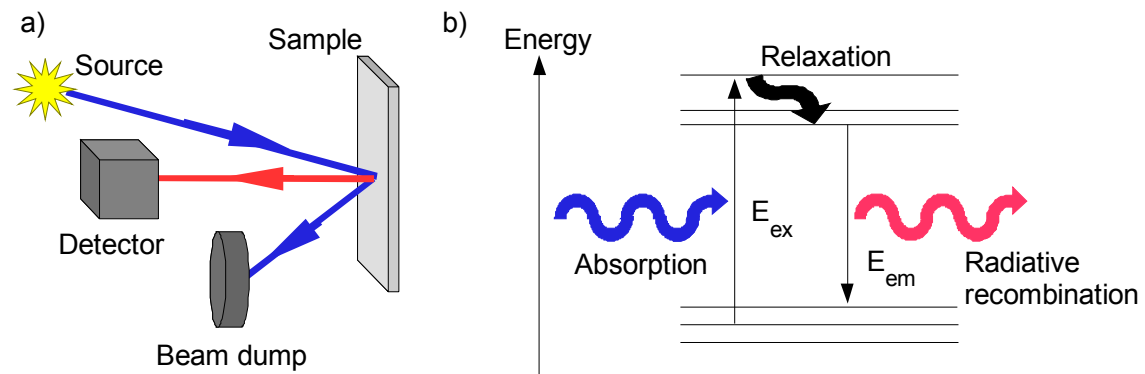
Figure 2.3a) Schematic representation of a basic photoluminescence emission spectroscopy setup and b) the electronic processes taking place during photoluminescence emission. E_{ex} is energy of the excitation photon and E_{em} the energy of the emitted photon.

2.4.2. Absorption: Direct and indirect transitions

The first stage in the photoluminescence emission process is the absorption of light to promote electron - hole pairs into an excited state. The principal absorption processes in solid state matter occur as inter-band transitions (band to band), intra-band transitions (within a band) or between impurity states and the conduction or valence bands. Transitions involving impurities are most common in doped semiconductors [45]. Inter-band transitions can take place by direct and indirect transitions whereas intra-band transitions only occur via indirect transitions [46].

For both direct transitions (Figure 2.4a) and indirect transitions (Figure 2.4b) an electron is excited vertically on an E-k diagram with no change in momentum followed by an oblique transition with associated change in momentum caused by either the absorption or emission of a phonon. For direct transitions the change in momentum of the excited electrons is typically of the order of 100 times less than the size of the Brillouin zone and is therefore approximated to a single vertical transition with no change in momentum. Indirect transitions are more dependent upon wavelength and temperature than direct transitions [47].

Inter-band transitions

The absorption probability of an inter-band transition as a function of frequency, $\alpha(\omega)$, can be expressed as [45, 48]

$$\alpha(\omega) \approx \frac{\left(\hbar\omega - E_g\right)^{\frac{1}{2}}}{\left(\hbar\omega\right)}, \tag{2.25}$$
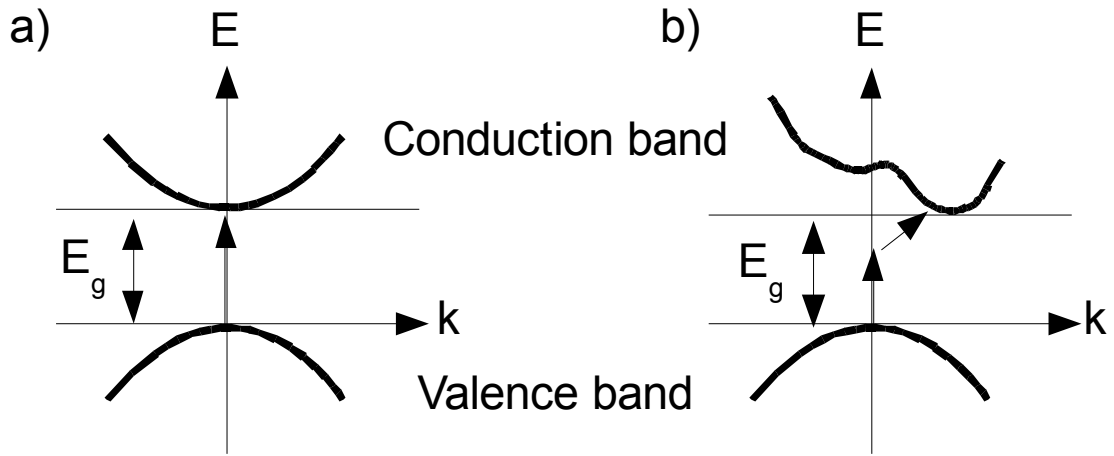
Figure 2.4. Schematic representations of a) Direct and b) indirect transitions (E-k diagram)

where E_g is the energy of the band gap at the Fermi energy with a minimum threshold energy at $\hbar\omega = E_g$ (Figure 2.4). The threshold energy is observed as a fundamental absorption edge in semiconductors and insulators, where the Fermi energy lies within a band gap [49-52].

Quantum mechanical selection rules state that a transition can only occur if the parity of the initial and final states is conserved (Table 2.2). In reality, if the rules forbid the transition at $k = 0$, it is still possible for the transition to occur in the region close by with $k \sim 0$ but the absorption probability is much reduced. In this case, the threshold energy is still at $\hbar\omega = E_g$ and can be written as [47]

$$\alpha(\omega) \approx \frac{\left(\hbar\omega - E_g\right)^{\frac{3}{2}}}{(\hbar\omega)}.$$

(2.26)

Intra-band transitions

Two types of intra-band transition occur in metals and semiconductors. The first type occurs within the sub bands of the conduction or valence bands which are separated due to a spin – orbit interaction. The energy of the incident photon is much less than the energy of the band gap ($\hbar\omega \ll E_g$). Absorption from this type of process is weak [47].

Parity of the initial and final states must be different
$\Delta m_l = -1, 0, 1$
$\Delta l = \pm 1$
$\Delta m_s = 0$
(m_l is the magnetic quantum number, l is the angular momentum quantum number and m_s is the electron spin quantum number)

Table 2.2. Quantum mechanical selection rules [53]

The second type of intra-band transition occurs for free electrons in states close to the Fermi level and is especially characteristic of the alkali metals [11]. The free carriers absorb the incident photons and are promoted to a higher energy within the same band. There is no threshold energy for free carrier absorption and additional scattering mechanisms are required to conserve momentum. For these transitions, the coefficient of absorption is dependent upon the magnitude of free carriers, N [47].

Additional absorption processes can also occur due to transitions between non parabolic bands at the high symmetry points on the Brillouin zone and between regions with parallel band structures [54].

2.4.3. Relaxation

Relaxation (thermalisation) processes occur after optical excitation of an electron into a higher energy state. This is the process by which the electron temperature equilibrates with the lattice temperature. The electron in the excited state and associated hole in the ground state relax their energy by scattering into different momentum states through a series of processes. These processes include; interactions with the lattice

(phonons), grain boundaries, surface defects or through interactions with other electrons in non radiative processes e.g. Auger process [11, 55].

Relaxation occurs on a timescale of approximately 100 fs in most solids. This is much faster than the timescale required for radiative recombination which is on the nanosecond timescale. As such, the majority of electrons will have relaxed into a thermal distribution of lower energy states before recombining [56].

If relaxation does not occur, the term "hot" luminescence is applied to the emission from the sample [11]. Both "hot" and relaxed transitions can occur for inter-band transitions.

2.4.4. Recombination

Recombination is often considered to be the time reversed process of absorption, however, the processes are not identical [57]. Absorption can take place into any excited state above the Fermi energy, whereas, recombination can only occur from a small range of relaxed states above the Fermi energy. As with absorption, recombination processes can occur as inter-band, intra-band, direct and indirect transitions.

The rate of recombination, R, is dependent upon the density of carriers in the upper state, n_u, the density of holes in the lower state, n_l, and the probability of radiative recombination P_{ul} [57],

$$R = n_u n_l P_{ul} .$$
(2.27)

It is possible for radiative recombination to take place via intermediate states. These can take the form of impurity states or other electronic bands. Not all of the intermediate transitions are necessarily radiative as non radiative recombination processes compete directly with the radiative recombination pathways. These non

radiative processes include Auger processes, phonon emission and surface recombination [55].

The transition probability for radiative recombination per unit time ($\Gamma_{i\rightarrow f}$) depends upon the wavefunction of the initial state (Ψ_i) and final state (Ψ_f) of the Hamiltonian, $\hat{H}'$, and is calculated using Fermi's golden rule [58]

$$\Gamma_{i\rightarrow f} = \frac{2\pi}{\hbar} \left| \left\langle \Psi_f \middle| \hat{H}' \middle| \Psi_i \right\rangle \right|^2 \rho\left(E_f\right).$$ (2.28)

The rule states that the transition probability is proportional to the square of the matrix element of the initial and final states $\left| \left\langle \Psi_f \middle| \hat{H}' \middle| \Psi_i \right\rangle \right|$, multiplied by the density of the final states, $\rho\left(E_f\right)$ [59, 60]. As in the case of absorption, quantum mechanical selection rules (Table 2.2) are applied to determine exact transition probabilities [53].

2.5. Photoluminescence in gold and copper – theoretical considerations

2.5.1. Introduction

Photoluminescence emission from metals is much weaker than the emission from semiconductors due to the absence of a fundamental band gap at the Fermi energy. In addition, the high density of free electrons in metals increases the probability of scattering of the excited electrons and holes which directly competes with the radiative recombination pathway, reducing the probability of photoluminescence emission.

Since the Fermi energy of metals lies within a band, transitions occur across a continuous range of energies [61]. The difficulty in measuring the low emission yields has meant that little work has been carried out on the measurement of photoluminescence emission from metals. Measurements in the literature are limited to the metals; gold, copper and silver. In this section the current theory for understanding photoluminescence emission from metals is outlined.

2.5.2. Band structure of gold and copper

As discussed in section 2.4.2. the band structure of a material is of great importance when considering its photoluminescence properties. Metals, by their nature do not contain a band gap at the Fermi energy and, as such, have a considerably more complicated relationship between band structure and photoluminescence emission. The following section will review the band structure of gold and copper.

Gold and copper have a band structure similar to a free electron like metal (parabolic bands) but with the addition of a series of tightly packed d-bands below the Fermi level. The d-bands are relatively flat with energies which remain constant as a function of momentum (Figure 2.6 and Figure 2.5) [62, 63]. Near the L point the conduction band is p-type in nature. An s-like conduction band only is present 4 to 5 eV above the Fermi level. The minimum energy for direct inter-band absorption in copper is 2.1 eV and 2.3 eV in gold [11].
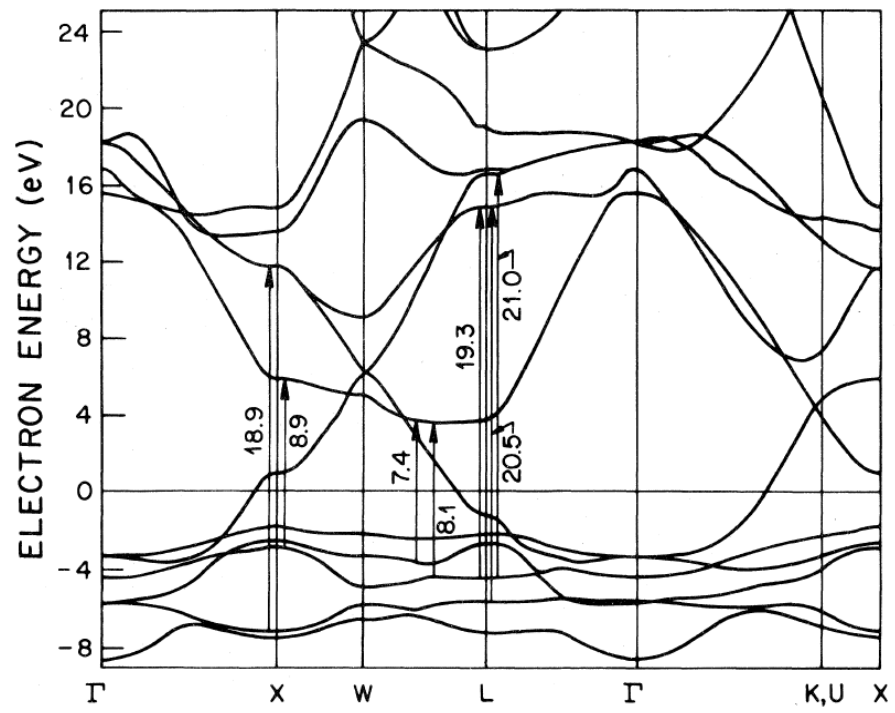
Figure 2.5. Band structure of gold [62]
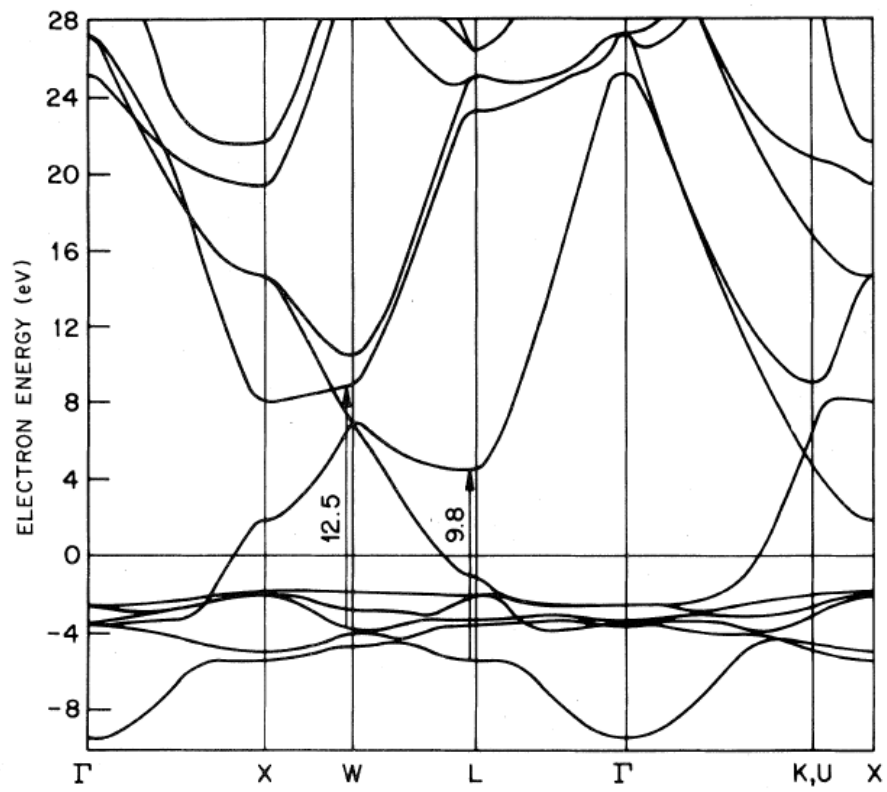
Figure 2.6. Band structure of copper [62]

2.5.3. Model for photoluminescence in gold and copper

The process of photoluminescence emission in gold and copper has been theorised by Mooradian, Whittle, Apell and Boyd [9, 10, 64, 65]. All four works propose that photoluminescence excitation at energies below 3 eV occurs between the filled d-bands below the Fermi energy in to the empty states of the sp-band crossing the Fermi energy. Recombination then occurs between the conduction band electrons just below the Fermi energy and the first d-band state giving an emission peak at 2.15 eV for copper and 2.3 eV for gold (Figure 2.7) [10, 64]. For excitation energies at 3.50 eV, radiative recombination with the second d-band has been observed at 2.90 eV for copper and 2.95 eV for gold [10]. The total single photon excited luminescence has been measured to have a very low quantum efficiency of 10^{-10} [9, 10].

The lowest energy for direct transitions occurs at the L and X symmetry points in the band structure of copper and gold (Figure 2.6 and Figure 2.5) [65]. Transitions at the L point dominate over those at the X point as the density of states is much higher at L
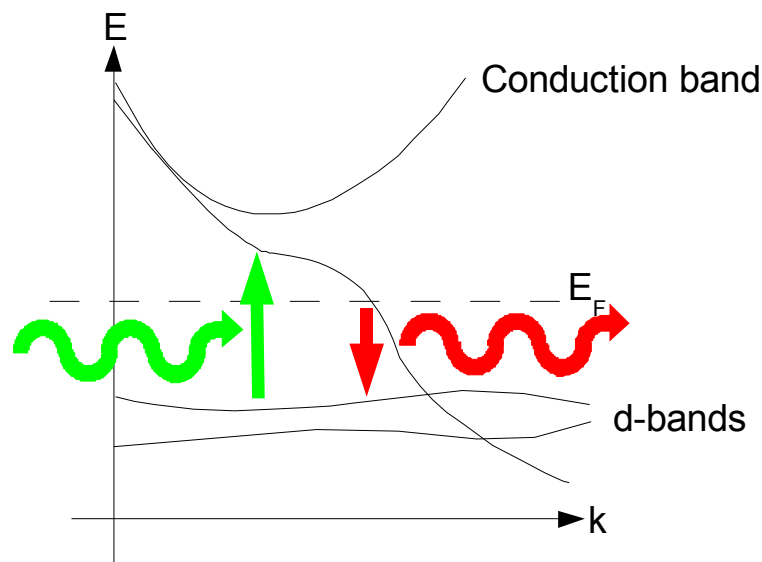
Figure 2.7. Photoluminescence emission process in gold and copper as described by Mooradian, Boyd and Whittle [9, 10, 66].

than at X for both copper and gold and the final states at X lie below the Fermi level and so are already occupied [11, 65].

Whittle discusses photoluminescence emission in metals in general stating that recombination takes place by direct transitions in the bulk volume of metals which is observed as an onset energy for luminescence emission close to the excitation energy [9]. Indirect transitions occur only in the surface region of the metal, where oscillations in the electric field or momentum contributions from the surface of the sample aid in oblique transitions [67].

2.5.4. The role of plasmons in photoluminescence measurements

Enhancement of photoluminescence emission has been widely observed from roughened gold and copper thin film samples [10, 66, 68]. The process of enhancement is attributed to surface plasmons (quasiparticles formed by the oscillation of the free electron gas) which locally enhance the electromagnetic field creating a macroscopic local field correction to which the incident light couples, improving the efficiency of the absorption and emission processes [10]. The formation of plasmons are discussed in detail below.

In a metal, the free (conduction) electron gas can be described as a plasma since it is a medium with an equal concentration of positive and negative charges where at least one of the charges is mobile (conduction electrons) and the other fixed (positive ion cores) [69, 70]. Oscillations in the plasma can occur if the electron gas is longitudinally displaced by an electric field (e.g. from an incident light wave). The displaced electrons oscillate in direction by +/- u (Figure 2.8) and an electric field is created by the displacement of the electrons which sustains the oscillations by acting as a restoring force of magnitude [70]

$$E = \frac{Neu}{\varepsilon_0}.$$ (2.29)

The equation of motion of the oscillation of electron gas is therefore represented by [70]

$$Mm\frac{d^2u}{dt^2} = -NeE = -\left(\frac{N^2e^2}{\varepsilon_0}\right)u,$$ (2.30)

which simplifies to

$$\frac{d^2u}{dt^2} + \omega_p^2 u = 0$$ (2.31)

in the case where the plasma oscillation has a small wavevector and the frequency is approximately equal to ω_p (equation (2.17)). Quantised oscillations in the plasma are termed plasmons.

Interactions between electromagnetic waves and the surface region of a metal are known as surface plasmon polaritons or surface plasmons. The plasma oscillations occur at frequencies ranging from zero, asymptotically towards $\omega_s = \omega_p / \sqrt{2}$ [71]. The interaction decays exponentially on either side of the interface and is thus confined to the surface region [71]. Coupling between light and the longitudinal plasma oscillations is possible if there is a longitudinal component of the electromagnetic wave [72, 73].

Plasmons will not radiate if the metal surface upon which the light is incident is flat (for a surface boundary with air or vacuum). This is due to the phase velocity of the
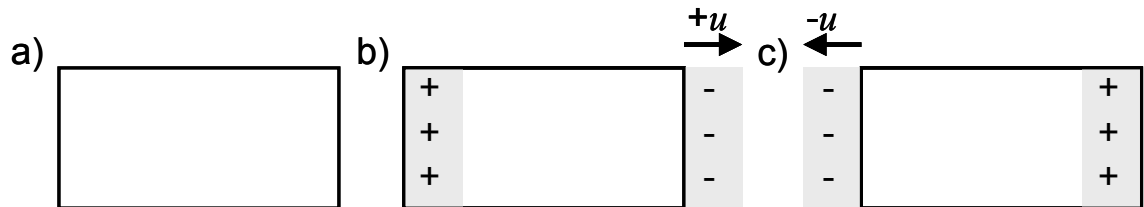
Figure 2.8 Longitudinal plasma oscillations within the bulk (volume) region of a metal. Diagram modified from references [69] and [70].

surface plasmon being less than the velocity of light. In this case, the plasmons do not radiate and instead dissipate their energy as heat [71, 72].

If the metal surface is roughened (with a roughness approximately equal to the wavelength of the incident light), then coupling between light and plasmons can occur. The plasmons are able to radiate due to an increase in plasmon momentum from the local enhancement of the electromagnetic energy density in regions where the sample surface is uneven [71]. The enhancement in electromagnetic energy density occurs due to the electric field attempting to remain perpendicular to the metal surface and is strongest at the tips of protrusions [74].

Optical transitions from the coupling of photons and plasmons can only occur in the volume region of a metal if its thickness is approximately the same as the wavelength of the light [72]. Thus, no interaction of plasmons with light is observed in the volume region of bulk metals with simple geometries and cubic structures [72].

A simplistic, but effective method of modelling the enhancement in luminescence intensity from rough surfaces uses a model of non interacting hemispheroids perpendicular to an infinite conducting plane with dielectric constant ε_m (Figure 2.9) [10]. A full mathematical derivation of the roughness enhancement of photoluminescence emission from gold and copper surfaces is given in the works by Boyd and Whittle [10, 66]. The enhancement is found to be dependent upon the dimensions of the hemispheroids, their volume and quantity, the dielectric constant and the wavelength of the driving field.

The use of rough gold and copper films to enhance photoluminescence emission is often exploited to increase luminescence yields from semiconductors and molecules [75] [76]. Also created by the same effect is the continuum emission observed during Surface Enhanced Raman Scattering (SERS) measurements [77].
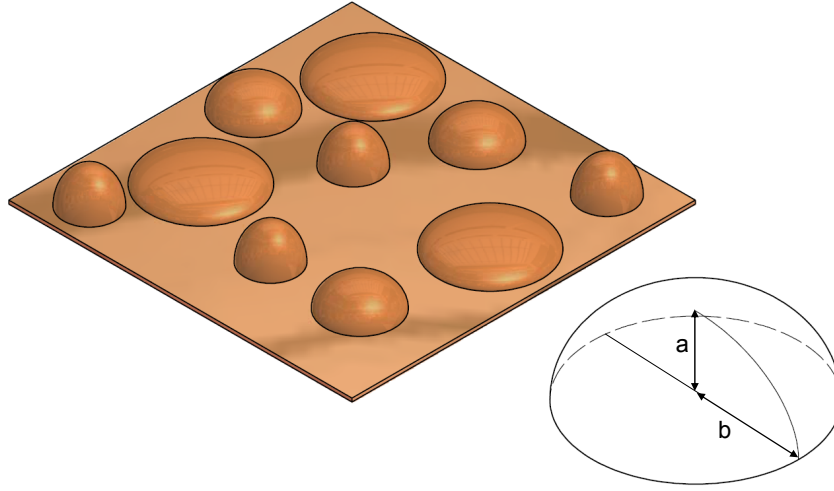
Figure 2.9 Schematic diagram of a hypothetical rough surface formed of hemispheroids on an infinite plane. Roughness enhancement η, is calculated for N number of spheroids per unit volume with dimensions, a and b and volume, V.

An excellent review of surface plasmons has been written by Pitarke [71]. A detailed account of experimental observations of surfaced enhanced photoluminescence on roughened gold and copper surfaces will be discussed in section 2.5.10.

2.5.5. Calculation of photoluminescence emission spectra

Numerical calculation

This section focuses on the work presented in the literature on the calculation of the photoluminescence emission spectra of gold and copper. A numerical comparison between measured and calculated photoluminescence emission spectra is presented in the work by Boyd where the authors represent single photon induced luminescence as [10]

$$I_L(\omega_2)dz = I(\omega_1, z)Y_{1abs}Y_R Y_{em}dz,\qquad(2.32)$$

where z is the depth at which luminescence is excited from a slab of metal of thickness dz, ω_2 is the frequency of emitted luminescence and ω_1 the frequency of the excitation light at a intensity $I(\omega_1,z)$, Y_{1abs} is the probability of single photon absorption, Y_R is the probability of relaxation of electrons and holes from the excited states to emitting states and Y_{em} is the probability of radiative recombination at a frequency ω_2. The excitation intensity is given as

$$I(\omega_1,z) = I_0(\omega_1)|L(\omega_1)|^2 \exp[-\alpha(\omega_1)z],\qquad(2.33)$$

where $I_0(\omega_1)$ is the source intensity and $|L(\omega_1)|^2$ is the Fresnel transmission coefficient.

Simplifications are made by Boyd in evaluating equation (2.32) by assuming that relaxation results in an exponential energy distribution of the electrons and holes (due to thermalisation of the electrons and holes with the lattice) and that the emission probability is equal to the total radiative recombination rate between electrons and holes with an energy separation $\hbar\omega_2$. The assumption is also made that transitions are concentrated close to the symmetry points on the Brillouin zone boundary (at local extrema in the energy bands) where the largest joint density of states exist and where the energy separation is less than the excitation energy. For gold and copper this restricts the transitions to the X and L symmetry points. Regions where the electron and hole pairs would scatter in different **k** directions are also ignored.

To calculate the emission spectra of gold and copper, equation (2.32) is evaluated using the Fresnel coefficients which consider the dielectric constant (ε_m) of the metal and the angles of incidence (θ) and refraction (θ_m) leading to [10]

$$I_L(\omega_2) = .\omega_2 \left[\frac{2\cos\theta_m}{\varepsilon_m^{\frac{1}{2}}(\omega_1)\cos\theta + \cos\theta_m} \right]^2 \left[\frac{2\cos\theta_m}{\varepsilon_m^{\frac{1}{2}}(\omega_2)\cos\theta + \cos\theta_m} \right]^2 \frac{1}{\alpha(\omega_1) + \alpha(\omega_2)} \cdot$$

$$\int_{L,X} \left((E - E_1(\hbar\omega_2))^{\frac{1}{2}} \left\{ \frac{1}{1 + \exp\left(\frac{E}{kT}\right)} + \Theta(E - E_0)\exp\left(\frac{E - E_0}{\delta_e}\right) \right\} \cdot \right.$$ (2.34)

$$\left. \left\{ 1 - \frac{1}{1 + \exp\left(\frac{E - \hbar\omega_2}{kT}\right)} + \Theta(E_0 - \hbar\omega_1 - E - \hbar\omega_2)\exp\left(\frac{E_0 - \hbar\omega_1 - E - \hbar\omega_2}{\delta_h}\right) \right\} \right) dE$$

where E is the energy into which the electrons relax, E_0 is the energy of the initial excited state energy of the electrons, α is the absorption coefficient, T is temperature and δ_e and δ_h are adjustable parameters representing the width of the exponential for the electron and hole distributions respectively. $\Theta(x)$ is the unit step function of the Fermi Dirac distribution and is zero for $x < 0$ and 1 for $x > 0$. The energy, E_1, from inside the integration is expressed as

$$E_1(\hbar\omega) = \Delta_U + m_{2L}\frac{(\Delta_U - \Delta_L - \hbar\omega)}{(m_{2U} - m_{2L})},$$ (2.35)

where Δ_U is the energy of the upper electron band and Δ_L the energy of the lower hole band at the symmetry point and m_{2U} and m_{2L} are the band masses. The term outside the integration in equation (2.34) is a combination of the Fresnell transmission coefficients at ω_1 and ω_2 and a depth z_0. Inside the integration, the first bowed bracket represents the electron population distribution and the second bracket the hole population distribution. Non radiative processes are not included in the calculation by Boyd as the author makes several approximations in equation (2.34) which neglect regions where scattering occurs. A fully worked derivation can be found in reference [10].

A second method of calculating photoluminescence emission from gold and copper is presented by Apell [64]. The probability of a photoluminescence transition, w, is given as

$$w = \left[\sum_f |M_e|^2 \, \delta\left(\varepsilon_f - \varepsilon_j + \omega_2\right) \frac{1}{2\gamma} \right] \left[\frac{|U_{f0}|^2}{2\gamma} \delta\left(\varepsilon_j - \varepsilon_i + \Omega\right) \right] \left[|M_a|^2 \, \delta\left(\varepsilon_i - \varepsilon_\delta + \omega_1\right) \right] (2.36)$$

where ω_1 is the frequency of the photon incident on the sample surface, ω_2 is the frequency of the emitted photon and Ω is energy of the phonons responsible for the scattering of holes during relaxation.

The first term in equation (2.36) is a branching ratio for hole filling by radiative emission versus all other processes, the second term is a branching ratio for hole scattering via phonons versus all other processes and the final term relates to the absorption of incoming photons. In the case of hole filling, the branching ratio incorporates the Auger processes which explains the very low luminescence efficiency of metals. Therefore, the transition probability for luminescence in gold and copper is a self convolution of the joint density of states for the absorption and the emission processes [64].

Several assumptions and simplifications are made by Apell et al. during the evaluation of equation (2.36) including constant matrix elements of the expectation value of the absorption and emission transitions (which are found not to be completely satisfactory as an approximation), the phonon frequency, Ω, being approximately equal to zero (since the uncertainty in the density of states of the d-states is larger than the typical phonon energy of ~ 20 meV) and the density of states of electrons in the s-states being constant over the region of interest. The restrictions $\omega_1 - \omega_2 \leq 1 eV$ and $\omega_1 - \omega_2 \gg \Omega$ are applied leading to an equation for the luminescence intensity of [64]

$$I_{lum} \approx \frac{\omega_2}{\alpha(\omega_2) + \alpha(\omega_1)} \cdot \frac{4}{(1+n_2)^2 + \kappa_2^2} \cdot \frac{1}{(n_2^2 + \kappa_2^2)} \cdot \int_{E_f - \omega_1}^{E_f - \omega_2} \left[\rho_d^<(\varepsilon) \right]^2 d\varepsilon . \quad (2.37)$$

where $\alpha(\omega_2)$ is the absorption coefficient at the emission energy, ω_2, $\alpha(\omega_1)$ is the absorption coefficient at the excitation energy, ω_1, n is the refractive index of the material at ω_2, κ is the extinction coefficient at ω_2 and $\rho_d^<(\varepsilon)$ is the density of states of the electrons in the d-band (i.e. density of states below the Fermi energy, E_f). The calculation does not hold close to the elastic region (close to ω_1) as this region requires special consideration of relaxation processes and is strongly temperature dependent [64].

Analysis of calculated spectra

Equation (2.37) predicts that the peak in the photoluminescence emission spectrum occurs at the energy at which the electron and hole distributions overlap. Since the Fermi level is within the sp-bands for gold and copper, this also coincides with the onset energy for inter-band transitions between the sp- and d-bands. A finite electron density above the Fermi level due to thermal and optical excitation smears out the sharp edge on the high energy side of the photoluminescence emission spectrum. A thermal distribution of relaxed holes in the d-band also contributes to the broadening of the emission spectrum. It should be noted that recombination is not limited to the specific electron and hole created as a pair during excitation but can occur between any electron and hole in sp- and d-bands. The detailed shape of the luminescence spectrum is therefore, dependent upon the density of states below the Fermi energy.

We shall see in our work (Chapter 5) as well as in the literature, that the agreement between the 2.0 eV peak photoluminescence emission energy in the calculated spectra and experimentally measured spectra of copper when excited at 2.34 eV by Boyd is extremely good, with the calculated peak falling within 0.1 eV of the measured peaks

[10]. However, the corresponding peak for gold only shows part of the 2.4 eV peak due to the excitation energy being too low at 2.34 eV. Comparison by Boyd between the spectra of gold at higher excitation energies (3.50 eV) show agreement between calculation and experiment of 0.1 eV and 0.3 eV for the 2.4 eV and 3.1 eV peaks, respectively [10].

Equation (2.34) and (2.37) both describe the photoluminescence emission spectra of gold and copper well. However, equation (2.34) contains parameters which are difficult to obtain experimentally and is also computationally more complex than equation (2.37). Evaluation of equation (2.37) requires knowledge of only three optical parameters and the density of states as a function of energy. The refractive index, extinction coefficient and absorption coefficient are all obtainable using ellipsometry measurements and the density of states from state of the art computational calculations performed by Dr Stewart Clark for the purposes of this work. Equation (2.37) also considers the density of states and non radiative processes in more detail than the work by Boyd. It was for these reasons that it was decided to use equation (2.37) from the work by Apell to calculate the photoluminescence emission spectra measured in this study [64].

2.5.6. Photoluminescence studies of gold and copper – experimental results

The following section presents a review of experimental measurements of photoluminescence emission from gold and copper. The dependence of spectra on

sample form and preparation, polarisation, temperature, roughness and oxidation will be discussed.

2.5.7. Sample form and preparation

Studies have shown that the photoluminescence emission spectra of gold and copper are unaffected by sample form (e.g. ingots, single crystal slices and evaporated films) [9].

There is no consensus in the literature about the procedure for the preparation of gold and copper samples for photoluminescence measurements. Boyd asserts that measurement under high vacuum is an important condition which must be implemented in order to achieve reliable results. However, the studies by Mooradian and Whittle carry out measurements without the sample under vacuum without any apparent problems [9, 10, 66]. This issue became very important in the work presented in this thesis and is returned to in Chapter 5.

2.5.8. Polarisation dependence

The s-direction (also commonly termed the o-direction) and p-direction (e-direction) of polarisation are defined in terms of the oscillation of the electric field of a light wave relative to the optical axis of the sample [78]. The electric field oscillates perpendicular to the optical axis in the case of s-polarised light and parallel to the axis for p-polarised light.

Polarisation dependence of photoluminescence emission from gold and copper is only observed from roughened thin film surfaces [66]. The samples display an increase in photoluminescence emission on the low energy side of the emission maximum when

illuminated by a p-polarised excitation source and an increase on both sides of the peak when excited by s-polarised light. The process of enhancement of photoluminescence from roughened surfaces was discussed in section 2.5.4. above. Measurements on bulk ingots and smooth evaporated films of copper have been shown to have no polarisation dependence which is consistent with its FCC crystal structure [9].

2.5.9. Temperature dependence

Several mechanisms are attributed to the temperature dependence of the optical properties of gold and copper including; volume thermal expansion of the metal with increasing temperature, increased phonon population, Fermi distribution broadening and a shift in the Fermi level and a change in electron – phonon coupling [79]. The change in the optical constants leads to a change in the absorption spectrum of the samples and is of great interest in this study as the values are experimentally measurable and directly relate to the changes in the photoluminescence emission spectra as a function of temperature. Figure 2.10 shows the changes to the optical constants (refractive index and extinction coefficient) of copper at 78 K and 293 K as measured by Johnson [79].

Trends in the experimental data and theoretical predictions for the absorption spectra of copper and gold as a function of temperature qualitatively agree well with one another [79, 80]. Measurements on copper show a constant central energy of the 2.2 eV absorption edge combined with a broadening of the edge with temperature. In gold, the central energy of the 2.5 eV absorption edge also remains constant, but there is no broadening observed as a function of temperature [80]. The Debye Waller theory describes the temperature dependence of the optical properties of gold and copper and predicts a 10 % decrease in the 5 eV absorption peak in copper which is consistent with experimental observations between 423 K and 78 K [79].
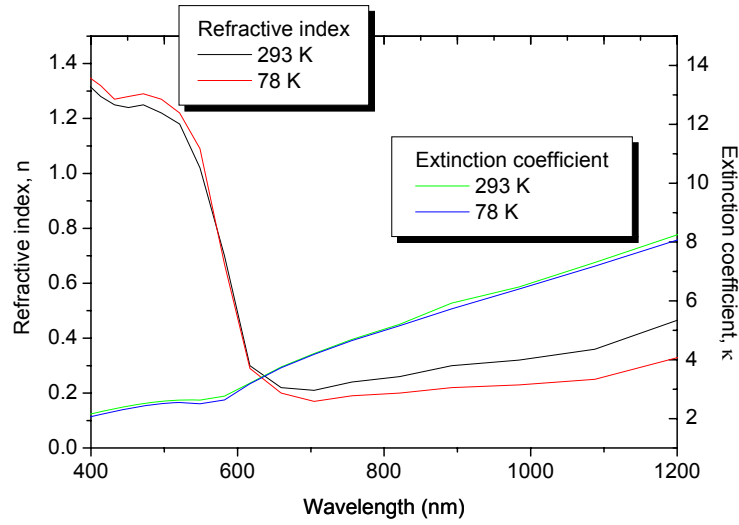
Figure 2.10. Refractive index and extinction coefficient measured for copper by the inversion of normal incidence reflection and transmission measurements of thin copper films at 78 K and 293 K [79].

Discrepancies in the magnitude of the experimentally measured dielectric constant as a function of temperature are observed between several studies and are attributed to surface contamination, oxides, condensation at low temperatures and the effect of cryostat windows [79, 80].

2.5.10. Roughness dependence

Photoluminescence enhancement from roughened gold and copper samples has been observed for corrugated films, films with an island overlayer and samples deposited onto roughened glass surfaces [10, 66, 68]. The typical roughness of all these surfaces is between 100 - 2000 Å [10, 46, 68]. The process of photoluminescence enhancement via the formation plasmons was discussed in detail in section 2.5.4.

Enhancement of photoluminescence emission is most commonly observed in locations where there is a large change in dielectric constant. This can either be between

two materials, one with a strong negative dielectric constant and the other a strong positive dielectric constant or between a surface and vacuum. Very large enhancement in photoluminescence emission is observed when the surface contains sharp protrusions between 100 – 1000's Å in size. This is due to the electric field being concentrated at the sharp protrusion as the field aligns perpendicularly to the sample surface [74]. This effect is known as the "lightning rod" effect.

The enhancement of photoluminescence from roughened gold and copper surfaces varies as a function of emission energy and the polarisation of incident light [10, 11, 66]. When excited by 2.4 eV p-polarised light, little or no enhancement is observed at emission energies above 2.2 eV (inter-band absorption edge) due to the damping of localised plasmon resonances [10, 66]. However, when excited by 2.4 eV s-polarised light, the enhancement occurs across the complete emission range. Figure 2.11 shows the enhancement for p- and s-polarised light in copper [66].
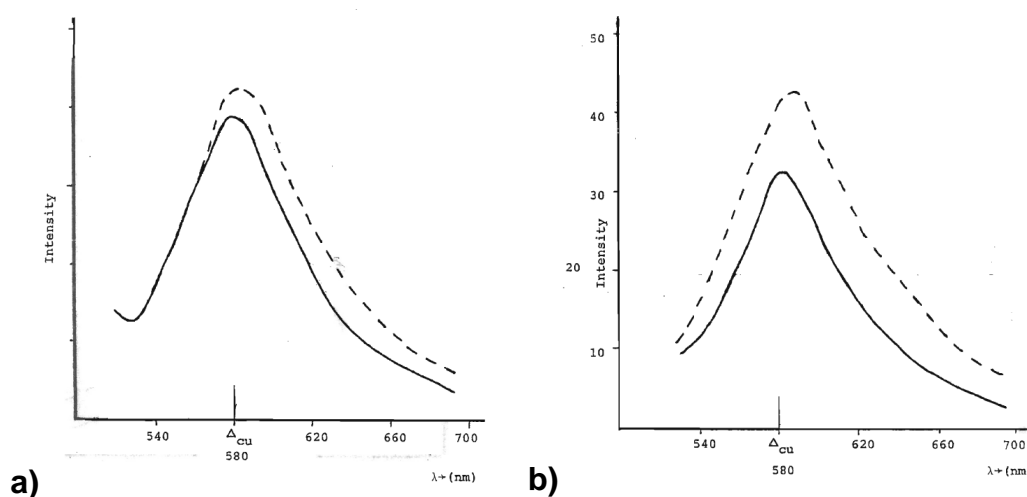
Figure 2.11 Roughness enhancement of the photoluminescence emission spectrum of copper as measured by Whittle [66]. The data represents a smooth sample (solid line) and a sample with a 40 Å island film overlayer (dashed line) excited by a) p-polarised light and b) s-polarised light. The excitation wavelength was 514 nm. No scale is given by Whittle for the data in part a.

For unpolarised light incident on samples deposited on substrates roughened by chemical etching, an enhancement of approximately 8 times that of a smooth surface is observed at an emission energy of 2 eV in copper and a 2.2 times enhancement at approximately 2.2 eV in gold. A shift in the peak photoluminescence emission energy is also observed for these samples (Figure 2.12) [10].

2.5.11. Oxidation

Oxidation in copper involves the diffusion of copper ions rather than the process more common in other metals of the diffusion of oxygen into the metal [81]. The transfer of metal ions occurs through the formation of vacant cationic sites. The contact potential
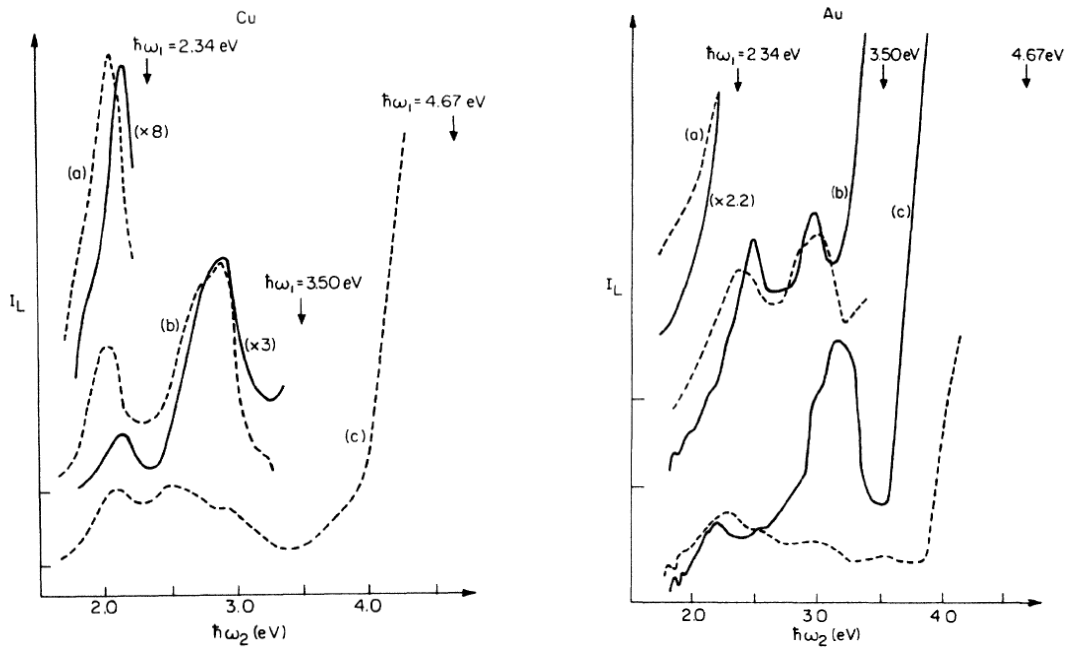
Figure 2.12 Photoluminescence emission spectra for copper and gold as measured by Boyd for smooth (solid line) and rough (dashed line) regions of a 1000 Å thick film on a glass substrate half of which had been roughened by chemical etching. [10]. Measurements were made for 3 excitation energies a) 2.34 eV, b) 3.50 eV and c) 4.67 eV. The scale of the spectra from the smooth surfaces are enhanced by the value shown in the brackets.

difference between the metal and adsorbed oxygen leads to a strong field in the oxide film enabling the metal ions to move within the film without the need for elevated temperatures.

Oxidation in copper occurs rapidly over a short period of time (minutes) before slowing to a rate at which the oxide film becomes stable and increases in thickness at a slower rate. The rate of oxidation in copper can be expressed as [81, 82]

$$
\begin{aligned}
\frac{dX}{dt} &= a\exp(-bX) \\
X &= \left(\frac{1}{b}\right)\ln(abt)
\end{aligned}
\tag{2.38}
$$

where

$$
\begin{aligned}
a &= \Omega N v \exp\left(\frac{W}{kT}\right)\exp\left(\frac{zea'\sigma_0}{\varepsilon kT}\right) \\
b &= \frac{-\rho zea'}{\varepsilon kT}
\end{aligned}
\tag{2.39}
$$

X is the oxide thickness at time t, Ω is the volume of oxide per cuprous ion, N is the number of copper ions per unit area in the oxide at the gas-oxide interface, v is the vibrational frequency, W is the activation energy for the formation of a vacancy, a' is the distance to the top of the barrier, E is the electric field strength and ze is the charge of the copper ion. The temperature dependence of the rate of film formation increases non linearly with temperature from 0.10 Å/hr at 78 K to 0.25 Å/hr at 323 K [81]. The oxide layer can grow to be 15 Å thick at 298 K in only 5 hours [82].

Gold is one of the least reactive elements in the periodic table. Its inert nature is due to the repulsion between the orbitals of the adsorbate and the filled d-states of the metal [83]. The strength of the adsorbate-metal interaction and the energy of the barrier to dissociation is determined by the orbital overlap and the filling of the antibonding states during adsorption [84]. Gold has a higher barrier for dissociation than its

neighbours in the periodic table as well as the least stable chemisorption state. A combination of these factors hampers adsorbate binding and reactivity of gold and prevents the formation of an oxide layer [84].

2.6. Photoluminescence studies of superconductors

2.6.1. Introduction to superconducting materials

The transition of a superconducting material from the normal to superconducting state occurs at a temperature known as the critical temperature, T_C. The phenomenon was first discovered in Hg in 1911 by Heike Kamerlingh Onnes [85]. Two key properties are observable below the critical temperature; zero electrical resistivity and expulsion of magnetic flux (Meissner effect). In their normal (non-superconducting) state, superconductors basically show the usual properties of metals, dependent upon their electronic structure.

One of the aims of this thesis is to measure the photoluminescence emission spectra of a range of superconductors. However, the nature of their electronic structure poses the same difficulty as for the measurement of the photoluminescence emission spectra of metals, in that their emission yields are extremely low. A second complexity with their measurement is the difficulty in achieving sample temperatures below the superconducting transition temperature whilst under laser illumination. This second complexity will be discussed in detail in chapter 4.

With a view to the measurement of photoluminescence emission from a range of superconducting materials, we review the classification of superconductors and give a brief summary of the theory of superconductivity. The band structure and optical and

electronic properties of superconductors are studied to increase the understanding of the photoluminescence emission processes in these materials. Finally, measurements of photoluminescence emission from superconductors as a function of temperature from the literature are reviewed.

2.6.2. Introduction to superconducting materials

Types of superconductors

Superconductors are commonly divided into two classes; conventional and unconventional. Conventional superconductors follow the predictions of the Bardeen, Cooper, Schreiffer (BCS) theory whilst the behaviour of unconventional superconductors cannot be explained by this theory. In the late 1980s, high temperature superconductors (HTS) were synonymous with unconventional superconductors and low temperature superconductors (LTS) with conventional behaviour. However, there have since been discovered a number of superconductors whose behaviour cannot be explained by the BCS theory but which have transition temperatures in the low temperature regime, such as oxygen deficient YBCO.

Classification by composition shows that metallic or elemental superconductors typically have low critical temperatures below 10 K and include Al, Pb, Sn and Nb. Conventional alloys and compounds including materials such as NbTi, Nb_3Sn, the Chevrel phase superconductors and MgB_2 and have transition temperatures below 40 K. The cuprate superconductors are ceramics with a perovskite structure and have transition temperatures ranging from tens of Kelvin to more than 130 K depending upon their structure. Other superconducting materials, which will not be discussed in this work, include heavy fermion superconductors (HFS), the Fullerene (C_{60}), and the recently discovered iron arsenic compounds (pnictides) [86].

Another common method of classifying superconducting materials considers the method of penetration of magnetic fields into the sample. The field above which magnetic flux penetrates into the sample is known as the critical field of the superconductor, H_C. In a type I superconductor, the superconducting state collapses completely at a single magnetic field. However, in a type II superconductor, a mixed state exists between a lower critical field and upper critical field. At the lower critical field, H_{C1}, magnetic flux penetrates the superconductor as quantised flux lines. As magnetic field is increased further, the density of flux lines increases until complete penetration of magnetic flux occurs at the upper critical field, H_{C2}. Type I superconductors are usually metals or metalloids with a finite conductivity at room temperature. The highest known transition temperature of any Type I superconductor at atmospheric pressure is currently Pb at 7.2 K. At higher pressures the record for the critical temperature of metallic superconductors is 17 K for sulphur at 157 GPa [87] [88].

2.6.3. Theories explaining superconducting behaviour

BCS theory

In 1957 a theory explaining the behaviour of superconductors was proposed by Bardeen, Cooper and Schreiffer (BCS theory). The theory is a microscopic formulation of superconductivity, capable of describing the behaviour of conventional superconductors extremely well [12]. It postulates that a weak attraction binds electrons into Cooper pairs at the Fermi surface. The binding energy between the two electrons in the Cooper pair can be written as $2\Delta(T)$. The energy required to break the bond between electrons opens a gap in the band structure at the Fermi energy. The gap energy is temperature dependent and at zero Kelvin can be expressed as [89]

$$\Delta(0) = 2\hbar\omega_D \exp\left(-\frac{1}{N(0)V}\right) \qquad (2.40)$$

where ω_D is the Debye frequency, $N(0)$ is the density of states at the Fermi energy and V is the electron-phonon interaction potential. The gap energy is typically in the milli electron volt range equating to the IR region of the optical spectrum.

The superconducting critical temperature, T_C, is expressed in terms of the gap energy as [90]

$$k_B T_c = 1.14\hbar\omega_D \exp\left(-\frac{1}{N(0)V}\right) = \frac{2\Delta(0)}{3.52} . \qquad (2.41)$$

Ginzberg Landau theory

Extending the microscopic theory to describe the properties of superconductors in magnetic fields (in particular the spatially inhomogeneous mixed state of type II superconductors) is a formidable task. Rather, to predict the behaviour of superconductors in magnetic fields, the macroscopic Ginzburg Landau theory (GL) is applied. Work by Gor'kov in 1959 showed that GL theory could be derived from BCS theory [91].

The Ginzburg Landau theory is a macroscopic, phenomenological theory where it is assumed one can postulate a Gibbs energy functional in which the wavefunction, ψ, is a complex order parameter. The complex order parameter is directly related to the density of states of the superconducting electrons and is minimally coupled to the electromagnetic field. From the Gibbs energy functional, two so-called Ginzburg Landau equations are derived. The first Ginzburg Landau equation (GL-I) relates variation in the wavefunction to the vector potential **A** [92]:

$$\frac{1}{2m}(-i\hbar\nabla - 2e\mathbf{A})^2\psi + \alpha\psi + \beta|\psi|^2\psi = 0 , \qquad (2.42)$$

where α and β are functions of temperature and are related to the order parameter of the system. A full derivation of the Ginzburg Landau theory is given by Tinkham [93].

The second GL equation (GL-II) is the standard expression for quantum mechanical current, $\mathbf{J}_e$:

$$\mathbf{J}_e = -\frac{ie\hbar}{m}(\psi * \nabla \psi - \psi \nabla \psi*) - \frac{4e^2}{m}\psi * \psi \mathbf{A} . \qquad (2.43)$$

These two equations can be used to derive the properties of Type I and Type II superconductors. The magnetic response of these two types of superconductors are shown in Figure 2.13.

Ginzburg Landau theory leads to two characteristic lengths for superconductors; the coherence length and the penetration length. The coherence length, ξ, of a superconductor is the distance over which the complex order parameter varies without an increase in energy and can be expressed as

$$\xi^2(T) = \frac{\hbar^2}{2m|\alpha|} . \qquad (2.44)$$

Equation (2.44) holds true deep inside a bulk type I superconductor and away from surfaces within a bulk type II superconductor. The distance over which the magnetic flux density drops to zero at the surface of the superconductor is defined as the penetration length (λ_L) (Figure 2.13)

$$\lambda_L^2 = \frac{m\beta}{4e^2\mu_0|\alpha|} . \qquad (2.45)$$

The temperature dependence of the penetration depth is found from the temperature dependence of α and β.

The ratio of λ_L to ξ is defined as the Ginzburg Landau parameter, κ, which can be used to distinguish Type I and Type II superconductors
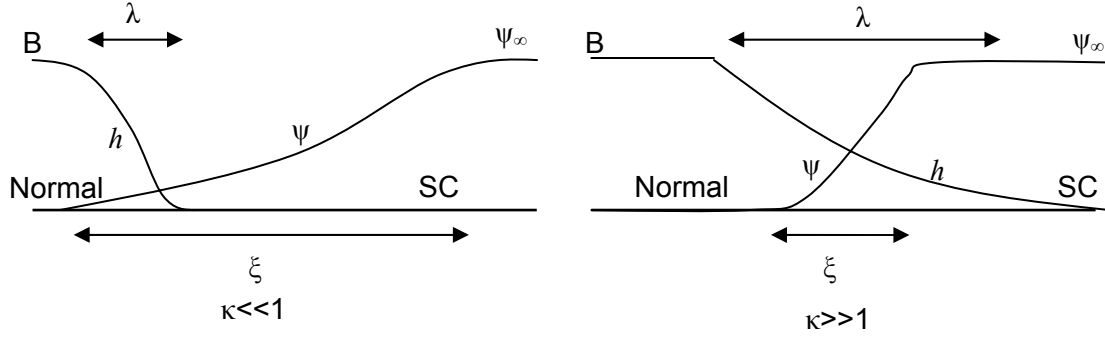
Figure 2.13 The variation of magnetic flux density, *B*, and the complex order parameter, ψ, at a superconducting – normal state boundary for $\kappa \ll 1$ (type I) and $\kappa \gg 1$ (type II) superconductors (adapted from reference [93]). λ is the penetration length of the superconducting material and ξ is the coherence length.

$$\kappa^2 = \frac{\lambda_L}{\xi} = \frac{m^2 \beta}{2\mu_0 e^2 \hbar^2}.$$
(2.46)

Type I superconductivity occurs in the region where $\kappa < 1/\sqrt{2}$ and Type II superconductivity when $\kappa > 1/\sqrt{2}$.

In a Type II superconductor the lower critical field, H_{C1}, is found by equating the free energy of a system with no flux to one with a single quantum of flux leading to an equation for H_{C1} given by

$$\mu_0 H_{C1} = \frac{\phi_0}{4\pi\lambda^2} \ln \kappa = \frac{\mu_0 H_C}{\sqrt{2}\kappa} \ln \kappa,$$
(2.47)

where ϕ_0 is the magnetic flux quantum and is defined as

$$\phi_0 = \frac{h}{2e} = 2.07 \times 10^{-15} \text{ Tm}^2.$$
(2.48)

At the upper critical field, H_{C2}, complete penetration of flux occurs and the superconductor becomes normal. In this regime $\mathbf{B} \approx \mu_0 \mathbf{H}_0$ and H_{C2} is defined as:

$$H_{C2} = \frac{\phi_0}{2\pi\mu_0 \xi^2(T)}.$$
(2.49)

Comparing H_{C2} to the equation for the critical field, H_C gives:

$$H_{C2} = \kappa\sqrt{2}H_C ,$$
(2.50)

which is shown schematically in Figure 2.14.

Abrikosov introduced the spatial variation of the macroscopic wavefunction, ψ, in the mixed state region of type II superconductors by considering a lattice of penetrating flux lines [94]. Further work by Kleiner et al. recreated the experimentally observed triangular flux line lattice [95]. The nearest neighbour distance in the triangular flux line lattice suggested by Kleiner is represented by [93]

$$a_{triangular} = \left(\frac{4}{3}\right)^{\frac{1}{4}}\left(\frac{\phi_0}{B}\right)^{\frac{1}{2}} = 1.075\left(\frac{\phi_0}{B}\right)^{\frac{1}{2}} .$$
(2.51)

2.6.4. Band structure of superconductors

The band structure of a material is extremely important in understanding its optical properties as was seen in section 2.5.2. for the gold and copper. The following section will review the band structure of the metallic superconductor; niobium, the Chevrel phase superconductors and certain high temperature cuprate superconductors.

The band structure of niobium consists of widely spaced d-bands and hybridised sp-bands close to the Fermi energy. This is similar to the band structure observed in gold and copper. However, the d-bands of niobium are more widely spaced and are only partially filled, unlike the filled bands of gold and copper [96, 97].
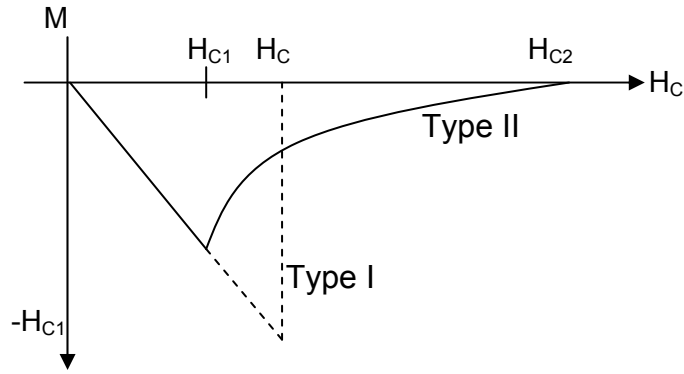
Figure 2.14 Critical fields in type I and type II superconductors. Diagram modified from reference [98].

The structure of the Chevrel phase materials is of the form $M(RE)Mo_6X_8$, where X is a chalcogen atom, M is an alkali metal and RE is a rare earth dopant [99, 100]. There is a large charge transfer between the M site and the Mo_6X_8 cluster which leads to the energy bands associated with the M atom being located well above the energy probed by optical techniques. The Fermi energy in Chevrel phase materials falls within the Mo 4d bands which lie within approximately 5 eV either side of the Fermi energy [99, 101, 102]. When large elements such as Sn or Pb are entered in the alkali metal position, the distance between the Mo_6X_8 clusters is increased, decreasing the position of the Fermi energy. A high density of states is observed at the Fermi energy due to the flat nature of the Mo 4d bands. Just above the Fermi energy a band gap of approximately 1 eV is present with the exact location determined by the electronic structure of the Mo_6X_8 cluster.

Band structure calculations and measurements of the cuprate superconductors are strongly dependent upon the oxygen content of the sample. Cuprate superconductors have a perovskite structure where planes of copper oxide are separated by rare earth atoms. High temperature cuprate superconductors with a majority of hole carriers (p-type) show a flat band close to the Fermi energy with extended saddle points corresponding to Van Hove singularities in the density of states [103].

2.6.5. Optical and electronic properties of superconductors

The following section considers the optical and electronic transport properties of three types of superconductor: the elemental superconductor, niobium; the Chevrel phase superconductors and the high temperature cuprate superconductors, focussing where data is available on YBCO and DyBCO.

The optical and electronic properties of a sample are of great importance to the understanding its photoluminescence emission. Reviewing these properties can give a strong indication as to the expected photoluminescence emission yields and energy ranges of interest. The effect of absorption and band structure on the probability of exciting an electron - hole pair and the free carrier density were discussed in detail in sections 2.4.2. and 2.5.2. The following sections consider measurements on superconducting materials to determine their optical properties. The data is presented via measurements of optical conductivity, absorption and reflectivity spectra, electrical resistivity (conductivity), Hall effect measurements and photoemission studies.

Optical data for the cuprate superconductors are often contradictory as the measurements are strongly dependent upon the quality of the sample, preparation method and defect concentration and disorder. An excellent series of reviews are available which give in depth detail about the measurement of optical and electronic properties of superconductors [104-109].

Optical properties

Optical conductivity

Infrared spectroscopy measurements of ordinary metals can be described using a Drude-like optical conductivity (σ) which can be expressed as [110]

$$\sigma = \frac{Ne^2}{m} \frac{\omega^2 \gamma}{\left(\omega_0^2 - \omega^2\right)^2 + \gamma^2 \omega^2}, \tag{2.52}$$

where m is the electron rest mass, N, is the density of free electrons and γ is the damping parameter described in the Drude-Lorentz model. The damping parameter can be described in terms of the electrical conductivity of the metal σ_0 by [111]

$$\gamma = \frac{Ne^2}{m\sigma_0}. \tag{2.53}$$

The Drude optical conductivity can be used with moderate success to describe the behaviour of BCS superconductors such as Pb and the Chevrel phase superconductors [99, 105]. However, the high temperature cuprate superconductors show a dramatic deviation from the Drude relationship showing damping which is linear in frequency above the region of electron-phonon coupling [105].

Absorption and reflectivity

The absorption spectrum of a material is an important means of identifying its optical properties. This section describes the main optical regions experimentally observed in the literature for niobium, the Chevrel phase materials and the cuprate superconductors.

Two distinct regions are identifiable in the absorption spectrum of niobium; a low frequency region dominated by intra-band transitions and a region of inter-band transitions at visible wavelengths. Peaks in the optical spectrum of niobium are attributed to transitions between the valence d-bands at 1.04 eV, 2.20 eV and 4.04 eV [112]. The specific bands are identified in the paper by Romaniello [96]. The optical properties of niobium are isotropic due to the BCC structure of the unit cell. Measurements on the low

temperature superconducting alloy, Nb_3Sn show no change in reflectivity between 7 K and 50 K [16].

A sharp increase in reflectivity to almost 100 % is observed from the Chevrel phase materials below 1 eV [99]. This behaviour is indicative of metallic behaviour, however, a small free carrier concentration means that the Chevrel phase materials are generally considered to be poor metals. Between 1 eV and 8 eV interband transitions are evident primarily due to transitions between the S_6p and Mo_6d bands [99]. Above 8 eV the reflectivity is constant. Reflectivity spectra are similar for all Chevrel phase materials confirming the assumption that absorption in the visible region is due to transitions within the Mo_6S_8 clusters [99].

Absorption in the mid infrared region of the optical spectrum of cuprate superconductors is attributed to charge transfer between free carriers within the CuO_2 planes [15, 113]. As for the Chevrel phase materials, below 1 eV a sharp increase in reflectivity is observed [113]. The transmission spectrum of YBCO between 0.25 eV and 3 eV is largely featureless [114].

Electronic properties

Transport properties

For most superconductors, resistivity, ρ, in the normal state at temperatures close to T_C is given by the Bloch-Gruneisen relation [115]:

$$\rho(T \geq T_C) = BT^n, \qquad\qquad (2.54)$$

where B and n are constants with n known as the resistivity exponent.

In simple metals, at temperature between a tenth and twentieth of the Debye temperature, standard theory attributes an n = 5 dependence to standard phonon damping, an n = 3 dependence to s–d electron transitions and an n = 2 relationship to electron-

electron interactions [115]. Optimally doped high temperature cuprates have a linear relationship with temperature (n = 1 dependence). Organic superconductors, Fullerenes, non-optimally doped cuprates and Nd based cuprates show an n = 2 dependence [116]. A review of the relationship between superconducting critical temperatures and the resistivity exponent can be found in the paper by Ruvalds [105].

The sign of the Hall coefficient in Hall effect measurements gives information about the charge carriers in the material. A positive sign indicates that the majority carriers are holes and a negative sign that they are electrons. In a system with only one type of carrier, the Hall coefficient (R_H) can be written in its simplest form

$$R_H = -\frac{1}{ne},$$ (2.55)

where n is the density of the majority carriers and e is the charge of the electron. In normal metals, the Hall coefficient is temperature independent. For the high temperature cuprates the change in the temperature dependence of the Hall coefficient exactly follows the temperature dependence of the resistivity. The Hall coefficient is also strongly dependent on oxygen content in the high temperature cuprates [117].

A universal correlation between T_C and the superconducting carrier density (n_s) divided by effective mass (m^*) has been demonstrated by Uemura and Schneider using muon spin relaxation rate measurements [118-120]. The relationship has been shown to apply to the high temperature cuprates, bithmuthate, Chevrel phase, organic and some heavy fermion superconductors [119-121]. These materials have been termed 'exotic' superconductors and show n_s/m^* initially increasing with relaxation rate before saturation followed by suppression. The initial linear increase has an identical slope for all of the exotic superconductors.

One of the first pieces of evidence for the superconducting energy gap (2Δ) was the observation of an exponential decay in specific heat below a sharp jump at the

superconducting transition temperature [122]. Raman spectroscopy and Angle Resolved Photoemission Spectroscopy (ARPES) measurements of high temperature cuprates have shown the superconducting gap to have d-type symmetry [105, 123, 124]. The Raman intensity varies as ω^3 in the low frequency part of the spectra of high temperature superconductors and as ω in BCS superconductors. ARPES measurements of optimally doped cuprate samples have shown the superconducting gap magnitude to scale linearly with T_C [123].

2.6.6. Photoluminescence measurements of superconductors from the literature

Studies of the photoluminescence emission of superconductors have to date measured the conventional superconductors; Nb_3Sn and MgB_2 and the high temperature superconductors; La_2CuO_4, $YBa_2Cu_3O_{7-\delta}$, $Bi_2Sr_2CaCu_2O_{8-\delta}$, and $YBa_2Cu_3O_{8-\delta}$ [13-18]. An excellent review of luminescence measurements of high temperature superconductors has been written by Pawar [19].

Sample quality and the method of sample fabrication strongly affect the measured photoluminescence spectra [13]. The form of the superconductor, i.e. thin film or bulk, is also found to be significant in influencing the measured luminescence spectra [19].

Room temperature spectra

Photoluminescence emission from cuprate superconductors is complex, with almost all studies on nominally identical samples displaying peaks at different energies. The mechanisms used to explain the transitions also vary greatly. Table 2.3 summarises the many different processes attributed to photoluminescence emission in the literature

for YBCO. Photoluminescence emission from cuprate superconductors has been shown to have a strong dependence upon defect concentration, oxygen content, surface contamination, sample fabrication and excitation energy [13, 14, 19].

λ(nm)	E (eV)	Process	Reference
660 nm	1.88 eV	Transitions from electrons trapped at oxygen vacancies - Not possible in optimally doped YBCO as there are no oxygen vacancies	[20]
611 nm	2.03 eV	Emission not associated with defects – No alternative explanation given	[20]
580 nm	2.14 eV	Transitions between holes in the oxygen derived $3d^{10}$ and $3d^9$ valence bands	[19]
571 nm	2.17 eV	Band gap of Cu_2O at 2 K	[125]
540 nm	2.3 eV	Transitions between holes in the oxygen derived $3d^{10}$ and $3d^9$ valence bands	[19]
530 nm	2.34 eV	Transitions from oxygen depleted zones	[13]
517 eV	2.4 eV	Transitions from oxygen vacancies and photoexcitation in the CuO_2 plane	[14, 15, 20]
443 nm	2.8 eV	Transitions between Cu2+ (Cu+) ions in the CuO_2 planes and Cu-O-Cu chains	[14, 15]
365 nm	3.4 eV	Luminescence from Y_2O_3	[13]

Table 2.3. Peak photoluminescence emission energies and assigned mechanisms from the literature for the cuprate superconductor YBCO.

Emission at 2.4 eV is attributed to photogeneration of electron-hole pairs in CuO_2 planes [14, 15]. Electrons are excited into the unoccupied p-levels of the oxygen ions in the Cu1-O4-Cu1 chains while the holes remain in the CuO_2 plane. Radiative recombination then takes place within the chain. Emission at 2.8 eV is attributed to photoinduced charge transfer where an electron is excited into the conduction band, which then travels to the Cu1-O4-Cu1 chain and is trapped by an oxygen ion or F centre with the chains acting as a charge reservoir. In materials where the Cu ions are only present in the CuO_2 planes, only a single peak has been observed at 2.4 eV [15]. Photoluminescence from Y_2O_3 has been observed at 3.4 eV under UV excitation energies [13].

When the photoexcitation density is high enough, persistent photoconductivity (PPC) is observed in underdoped cuprate superconductors. The process photodopes the superconductor and is analogous to chemical doping, increasing the oxygen content of the underdoped YBCO. The process is able to change the sample from an insulator to a metal and can lead to photoinduced superconductivity (PISC) [20, 126]. PPC cannot occur in optimally doped YBCO as there are no oxygen vacancies.

Photoluminescence of Nb_3Sn displays a peak at 2.33 eV (532 nm) [16]. The luminescence is attributed to transitions between the 4d-band of niobium (located between 2 to 3 eV below the Fermi energy) and the sp-bands of niobium and tin near the Fermi energy. The process of photoluminescence emission in Nb_3Sn is considered to be analogous to the emission seen in gold and copper.

The low temperature superconducting alloy, MgB_2, displays a photoluminescence emission peak between 2.75 – 3.1 eV (400 – 450 nm) which is attributed to Mg based impurity phases in the superconductor [18].

Variable temperature measurements

Results for the variation in luminescence across the superconducting transition between the normal and superconducting state vary greatly. A sharp increase in the intensity of the main 2.33 eV peak of Nb_3Sn is reported below T_C in measurements by Tominaga (Figure 2.15) [16]. The increase is attributed to an increased probability of relaxation of electrons and holes from excited states to emitting states below T_C [16]. The initial and final luminescence states are not affected upon entering the superconducting state as their energies are far from the superconducting gap at the Fermi level. Thus, since reflectivity does not change as a function of temperature, it is suggested that the only remaining variable is relaxation rate.

Evidence for the change in photoluminescence across T_C in YBCO is inconclusive. No change at T_C is reported by Garcia (Figure 2.16) [13]. However, the relative intensity and peak position of the 2.4 eV and 2.8 eV peaks are reported to change across the superconducting transition in the work by Eremenko (Figure 2.17) [14]. The change is attributed to the hindering of recombination of excited states with the superconducting condensate [14].
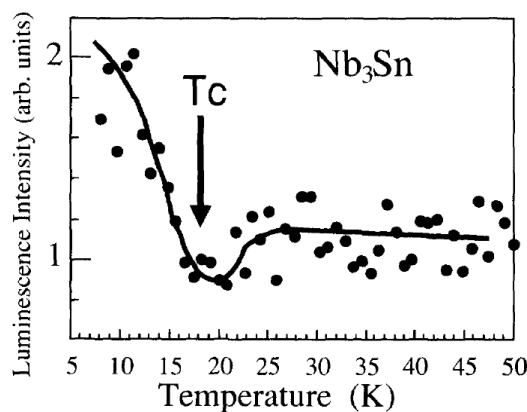
Figure 2.15 The change in the multiphoton induced photoluminescence intensity at 2.33 eV for Nb_3Sn measured using a 1 mJ/pulse laser excitation source as measured by Tominaga [16].

a)

b)
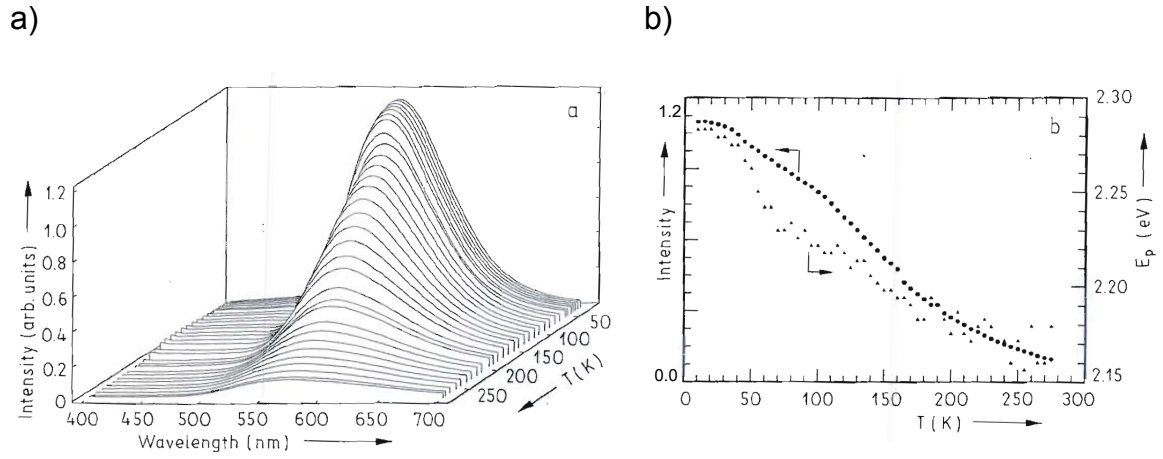
Figure 2.16 a) Photoluminescence emission spectra of YBCO as a function of temperature as measured by Garcia b) Peak photoluminescence emission intensity and peak position plotted as a function of temperature [13].

a)

b)
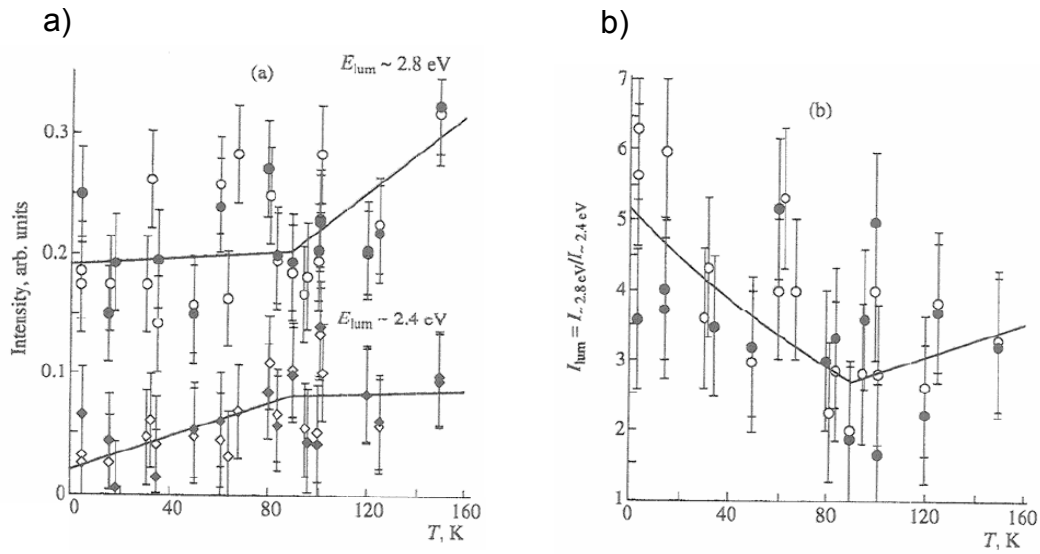
Figure 2.17 a) Temperature dependence of the absolute band intensities for the 2.8 eV and 2.4 eV photoluminescence emission peaks in YBCO single crystal as measured by Eremenko b) temperature dependence of the ratio of intensities for the 2.8 eV and 2.4 eV peaks [14].

Time dependent light emission

Another interesting phenomenon observed in the photoluminescence emission of oxygen deficient YBCO is a variation in peak photoluminescence intensity over a period of hours. The variation is attributed to persistent photoconductivity (PPC) where excited photodoped states gradually recombine radiatively by overcoming a distribution of energy barriers and relaxation times [20, 126]. A detailed review of PPC is given by Gilabert [127]. Persistent photoconductivity is only observed in underdoped YBCO, where oxygen vacancies are present [126]. In optimally doped YBCO the process cannot occur as there are no defect states to trap the excited electrons.

A second process commonly associated with the delayed radiative recombination of electrons is phosphorescence [128]. Electrons in an excited metastable state (commonly a triplet state) recombine with a singlet ground state. Transitions between the two states are forbidden by quantum mechanical selection rules and hence have a low probability of occurring leading to the delayed emission. Transitions between the ground singlet state to the excited triplet state are faster than the reverse triplet to singlet transition. Phosphorescent materials (phosphors) are typically rare earth compounds, transition metal ions, alkali halides or ns^2 type ions (including Cu^-, Au^- and Ag^-)[129].

2.7. Considerations for photoluminescence measurements

Measurement of photoluminescence emission requires three components; an excitation source matched to the absorption region of the sample, optics to condition the luminescence emission (to remove the elastically scattered excitation light) and instrumentation to detect the luminescence emission. Standard photoluminescence emission measurements are made using one of four methods: darkfield, episcopic,

confocal and multiphoton excitation spectroscopy (Figure 2.18). Each of these techniques will be briefly discussed below. Two key features in the experimental setup are of vital importance for the measurement of low yield photoluminescence emission from metals and superconductors. These are the reduction and removal of unwanted photoluminescence emission from optical components and the excitation and collection of the highest possible intensities of photoluminescence emission from the sample. Measurements of photoluminescence emission from gold, copper and superconductors are most commonly carried out using darkfield and multiphoton techniques [3, 9, 10, 13-16, 66, 130].

2.7.1. Experimental geometries

Darkfield luminescence microscopy

Darkfield luminescence microscopy excites the sample through an independent optical pathway to the emission collection pathway (Figure 2.18a). The collection optics are angled off-axis so only a minimal amount of elastically scattered light from the excitation source directly enters the post excitation optics. However, the non normal angle of incidence on the sample surface increases scattering from the sample making removal of the scattered excitation light more complex than other luminescence techniques.

Episcopic luminescence microscopy

Episcopic luminescence microscopy uses the same optical pathway for luminescence excitation and emission collection (Figure 2.18b). The focussing and collection objective is located closer to the sample surface as the scattered excitation light passes through the collection optics rather than being avoided. Since the optics can be

located close to the sample, the intensity of the measured luminescence is significantly increased. The reflected excitation light is removed from the emission spectrum using a dichroic filter. The main disadvantage of episcopic luminescence spectroscopy is luminescence from within the objective lens which is subjected to the full excitation intensity and is part of in the emission pathway.

Confocal luminescence microscopy

Confocal fluorescence microscopy uses an experimental arrangement similar to that of episcopic luminescence microscopy with the addition of two pinhole apertures (Figure 2.18c). The pinholes reduce the luminescence detected from optical components by limiting the measured luminescence to the focal the point of the excitation optics. The
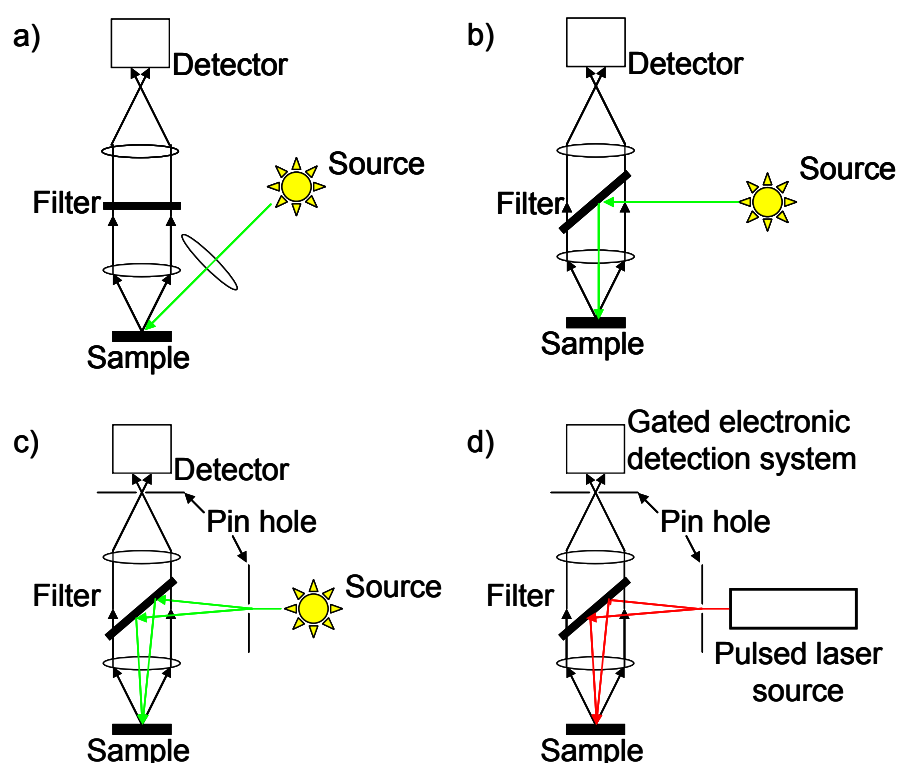

Figure 2.18 Schematic diagram of a) darkfield b) episcopic c) confocal and d) multiphoton photoluminescence emission spectroscopy experimental geometries for single photon excitation.

technique increases spatial resolution but reduces the intensity of the measured luminescence from the sample due to the reduced intensity of the excitation source after passing through the pinholes.

Multiphoton excitation spectroscopy

Multiphoton excitation spectroscopy typically uses a pulsed infrared laser to excite luminescence at green or ultraviolet energies. The pulse length of the laser is such that two photons from neighbouring pulses are simultaneously absorbed, exciting the photon via an intermediate state to an energy which is twice that of the laser wavelength. The experimental setup for multiphoton spectroscopy is shown in Figure 2.18d.

Experimental alignment and timing are extremely important in multiphoton spectroscopy as two-photon excitation can only occur if pulses from the laser both spatially and temporally overlap. If there is a mismatch in either of these requirements only single photon excitation at IR wavelengths is possible. This technique is advantageous for samples with low luminescence yields as excitation at higher energies only occurs at the focal point of the laser, thus reducing the problem of luminescence from optical components, sample holders or contaminated regions of the sample.

2.7.2. Optical materials for low luminescence intensity systems

All four photoluminescence spectroscopy techniques described above require the highest quality of optical materials to perform measurements on samples with low photoluminescence emission yields. Luminescence from optical components increases as a function of absorption within the lens. The absorption coefficient of the lens is dependent upon the type and density of defects and impurities. The choice of optical

materials for lenses and filters is therefore crucial in ensuring a low background to the sample luminescence emission.

Typical impurities in optical materials include straie, bubbles and inclusions. Straie are small thread-like structures between 0.1 and 10 mm long that lead to deviations in the refractive index over a small area. Inclusions are formed from stones and crystals with cross sections greater than 30 microns [131, 132].

Schott glass (high quality optical glass) is highly homogeneous with low bubble content giving high (90 – 95 %) transmissivity in the range 380 – 2100 nm. This material is the most commonly used material for IR and UV applications [131, 132].

Of even greater purity is synthetic fused silica (SiO_2) which contains negligible striae and inclusions [131, 133-135]. The material is non crystalline with an impurity content of 1 part per million. UV grade fused silica has the highest transmission coefficient of any optical material with an absorption loss two orders of magnitude less than Schott glass. This leads to fluorescence levels approximately 0.1 % that of natural quartz. However, there is a large dip in transmittance at 950 nm for UV grade fused silica.

For measurements in the IR region, calcium fluoride (CaF_2) is commonly used as it displays high transmittance out to 10 μm [131, 133, 135]. In high temperature environments, low-expansion borosilicate glass (e.g. Pyrex) displays excellent thermal stability. However, it contains many striae and bubbles reducing the lens homogeneity [131, 133]. The most common material for mirror substrates is low index commercial grade optical crown glass.

Sapphire (Al_2O_3) has lower transmittance than fused silica at approximately 85 % between 150 nm – 6000 nm [131, 135]. However, its high strength makes it an excellent

material for windows in cryostats and vacuum chambers. The application of antireflection coatings can increase transmission to 98%.

Windows for use in cryostats and vacuum chambers experience a substantial pressure differential across their surface. The recommended minimum window thickness, $T,$ for a clamped circular window under maximum stress is given by [136]

$$T = 0.866D\sqrt{\frac{P}{F_a}} \, , \tag{2.56}$$

where P is the pressure difference across the window, F_a is the apparent elastic limit of the material and D is the unsupported diameter of the window. The numerical constant takes into account the safety factor and the method of support for the window (i.e. clamped or unclamped).

For the instrument designed and commissioned in this thesis, UV grade fused silica was used for all standalone lenses and in the cryostat window as the priority was to reduce potential sources of luminescence whilst maximising emission collected from the sample.

2.7.3. Optical filters

Optical filters operate by either absorption or reflection of incident light. Absorbing filters are commonly fabricated from coloured glass. Longpass coloured glass filters absorb almost 100 % of light incident at wavelengths shorter than the specified cut off. However, due to their high absorbance they display strong luminescence under laser illumination.

Dichroic filters are formed from a series of thin film layers which reflect light for all but the required pass band wavelength range. Light rejection is highly dependent upon

the angle of incidence. Little or no luminescence is excited in the filter as they reflect rather than absorb the incident light.

Preliminary measurements showed that coloured glass filters could not be used for the measurement of photoluminescence emission from metals and superconductors. The strong luminescence emission from the glass filter dominated the measured emission spectra even when the filter was only subjected to low levels of scattered excitation laser illumination. Therefore, a reflecting dichroic filter matched to the excitation laser wavelength was selected to condition the optical pathway of the collected photoluminescence emission.

2.7.4. Detection methods

The choice of detector and measurement technique for samples with low yield photoluminescence emission is extremely important as the emission is weak. In the case of our measurements, the emission intensity could not be increased by increasing excitation power due to heating of the sample by the laser when under vacuum inside the cryostat.

Two methods are commonly used for the detection of luminescence. In the first technique, a monochromator is scanned incrementally across a range of wavelengths and the intensity of the detector signal measured at each wavelength. The detector in this case requires no spatial resolution and photomultiplier tubes or photodiodes are commonly used for this purpose. The second method uses a dispersing monochromator coupled to a spatially resolved detector. Commonly a CCD array detector is used with this technique, where each of the pixels in the CCD array corresponds to a small range of wavelengths. The details of the operation of the three main types of detector (PMT, photodiode and

CCD array) will not be given here, however, an excellent review has been written by Hungerford [137].

For low yield photoluminescence emission measurements, the signal to noise ratio of the detector is of greatest importance. It can be assessed through the consideration of the detectors ability to produce charge compared to the number of incident photons detected (quantum efficiency) and the dark noise of the detector generated by the thermal motion of electrons.

Photodiode detectors have excellent quantum efficiencies in the region of $80 - 90$ %, whilst photomultiplier tubes have much lower efficiencies at 20 - 40 % [138-140]. The quantum efficiencies of each type of detector are quoted for their maximum value across the whole wavelength range. The sensitivity of each detector decreases rapidly outside their operating range with photodiode detector sensitivity commonly dropping below 30 % below 700 nm and PMT sensitivity dropping below 10 % above 850 nm. Therefore, for measurements below 600 nm, PMT are the optimum single channel detector and above 850 nm, photodiode detectors are preferential.

Dependent upon the design on the device, CCD array detectors have quantum efficiencies above 90 % in the visible region [141]. Detector sensitivity is relatively constant across its region of operation, however, most CCD detector sensitivies drop below 10 % above 1000 nm. Dark noise from the detector is strongly temperature dependent and cooling the detector by only $20^{o}C$ can decrease dark noise by an order of magnitude. The most common means of cooling the detector is via a peltier stage or liquid nitrogen which can reduce dark noise to less than 1 electron per pixel per hour in the case of modern CCD detectors [141, 142].

The dynamic range (maximum count rate) of the detector is not a limiting factor for the measurement of low yield emission since the detector is unlikely to be saturated.

The time lag in the removal of charge from the detector is also not a concern, since the measurements are carried out on a time frame of seconds to minutes rather than nanoseconds or even picoseconds as would be required for time resolved spectroscopy.

A CCD array detector was chosen for this study as it was capable of measuring a 60 s exposure across the complete wavelength range of interest in a single reading with 0.3 nm wavelength resolution. The equivalent time for a measurement of this exposure time using a PMT or photodiode would have been impractical as a complete scan of the 550 nm measurement range would have been in the region of 15 hours, assuming a detector efficiency twice that of the CCD array.

2.7.5. Optical cryostats

Common designs of cryostat include dipper probes, liquid and gas flow cryostats and cryocoolers. Dipper probes immerse the sample directly into the cryogenic liquid. This limits the temperature of the sample to a range close to that of the cryogen. Although optical access through the cryogenic liquid is difficult, the technique is documented as having been used in the measurement of photoluminescence of the low temperature superconductor, Nb_3Sn, where the sample was immersed in superfluid liquid helium [17].

Liquid flow cryostats continuously exchange liquid helium or nitrogen between the cold finger of the sample holder inside the cryostat and a dewar. Temperature control is excellent using this technique, however, the geography of the experimental setup in the laboratory can be difficult is due to the requirement for a continuous supply of cryogenic liquid.

Gas flow cryostats, operate by pumping a flow of cold gas past the sample from a bath of cryogenic liquid surrounding the sample chamber. Temperature control is again

excellent and vibrations within the cryostat are minimal as there is only a single moving valve controlling gas flow. The requirement for a continuous supply of cryogenic liquid again increases the complexity of the laboratory setup.

Cryocoolers compress helium gas using a moving displacer within the cold head of the cryostat. Using this technique the sample stage is cooled to temperatures as low as 10 K without the requirement for a dewar of cryogenic liquid. Conventional cryocoolers suffer from large vibrations created by the movement of the displacer. However, modern cryocoolers use a pulse tube refrigerator, reducing vibrations and producing cooling to 2 K. A thorough discussion of the operation of pulse tube refrigerators can be found in reference [143].

For this study an optical cryostat with a pulse tube refrigerator was chosen as this provided the potential to reach the lowest base temperature without the requirement for a supply of liquid helium in the laboratory, which was not practical due to the geography of the laboratory arrangement.

2.8. Conclusion

This chapter has considered theoretical and experimental approaches relating to the measurement of photoluminescence emission from metals and superconductors. The optical properties in the component processes of photoluminescence emission have been discussed using a classical optics approach which looked at the absorption, reflection and transmission characteristics of light in simple metals. Photoluminescence emission has been discussed in detail, firstly, in the case of a conventional sample, such as a semiconductor, before considering the processes occurring in metals and superconductors. Experimental data from the literature for the measurement of

photoluminescence emission from metals and superconductors has also been discussed and its reliability assessed. The variation of photoluminescence emission across the superconducting transition has been discussed and the discrepancy between different studies considered.

This chapter has also presented a review of the experimental considerations for photoluminescence measurements with its focus on the optimum components for the measurement of low yield photoluminescence emission. The section concludes that a darkfield luminescence spectroscopy setup with fused silica lenses and reflecting rather than absorbing filters will offer the best arrangement for measuring low yield samples. The detector of choice is a CCD array detector with a dispersing monochromator as this setup would allow measurement of the full wavelength range of interest in a single long exposure measurement. Finally, the cryostat which best suits the experimental requirements of this study is a pulse tube refrigerator due to its ability to produce cooling to 2 K without the need for liquid helium in the laboratory. Chapter 4 will discuss how these components have been optimised further for the measurement of low yield photoluminescence from metals and superconductors.

Chapter 3. Commercial Equipment

3.1. Introduction

In Chapter 3 data are presented for the optical and electronic characterisation of the metals (gold and copper), the low temperature superconductors (niobium, $PbMo_6S_8$, $Pb_{1-x}Gd_xMo_6S_8$ $x = 0.3$, $SnMo_6S_8$, $Sn_{1-x}Eu_xMo_6S_8$ $x = 0.35$) and the high temperature superconductors (YBCO and DyBCO). For the superconducting materials, the superconducting transition temperatures are also identified using resistivity, heat capacity and AC susceptibility measurements as a function of temperature. Preliminary investigations are also presented for the measurement of photoluminescence emission from low yield samples using commercial spectroscopy apparatus. This is followed by a discussion of the advantages and disadvantages of commercial systems. Commercial systems have the benefit of unrivalled development time, pre-calibration and system reliability. However, care must be taken to ensure that the equipment is performing to specification. Preliminary measurements were carried out for the three instruments and self consistency of data confirmed in addition to cross checking with results from the literature. When operating to specification, commercial equipment offers ease of use, fast data acquisition times, automated data collection and versatility of measurement modes.

In section 3.2, a Jobin Yvon Fluorolog 3-22 spectrofluorometer is considered for the measurement of photoluminescence excitation and emission spectra. The system's strengths and weaknesses are analysed for the measurement of metals and

superconductors. In section 3.3, the operation of a J. A. Woollam VASE series ellipsometer is discussed and data analysis techniques considered for the measurement of refractive index, n, and extinction coefficient, κ. The limitations of the equipment are considered for the measurement of bulk samples with rough surfaces. Finally, a Quantum Design physical properties measurement system (PPMS) is examined and data presented for resistivity, heat capacity and magnetic moment measurements of superconducting samples.

3.2. Jobin Yvon Fluorolog 3-22 spectrofluorometer

The Jobin Yvon Fluorolog 3-22 spectrofluorometer (Fluorolog) is a commercial photoluminescence spectrometer capable of excitation and emission measurements between 250 nm and 800 nm. The advantage of the Fluorolog design is its modular form allowing for the integration of extra units such as time correlated single photon counting (TCSPC) and fibre optic excitation and emission collection. Additional polarisation and low temperature measurement options are also available for the instrument discussed below.

The following section considers the system configuration of the Fluorolog and specifications for the excitation source. Preliminary photoluminescence measurements of the Chevrel phase superconductor $PbMo_6S_8$ are compared with measurements of black card and an organic polymer to determine the accuracy of the Fluorolog for the measurement of samples with low photoluminescence emission intensities. The limitations of commercial photoluminescence equipment are then discussed and the strengths and weaknesses of the system examined with consideration for the design of an instrument for the measurement of low yield photoluminescence emission.

3.2.1. System configuration

Figure 3.1 is a schematic representation of the Jobin Yvon Fluorolog 3-22 spectrofluorometer showing the excitation source, double grating excitation and emission spectrometers, sample compartment and photomultiplier tube detector.

Optical excitation is carried out using a 450 W xenon lamp. Figure 3.2 shows the xenon lamp emission spectrum measured as part of the recalibration of the Fluorolog after replacement of the xenon lamp bulb. Table 3.1 lists the specification of the xenon lamp and slit width for the Fluorolog. The intensity of light emitted by the xenon lamp changed as a function of wavelength and time. Therefore, to correct for changes in lamp intensity the monochromated lamp emission was measured coincidentally with the sample photoluminescence emission. The corrected sample photoluminescence emission
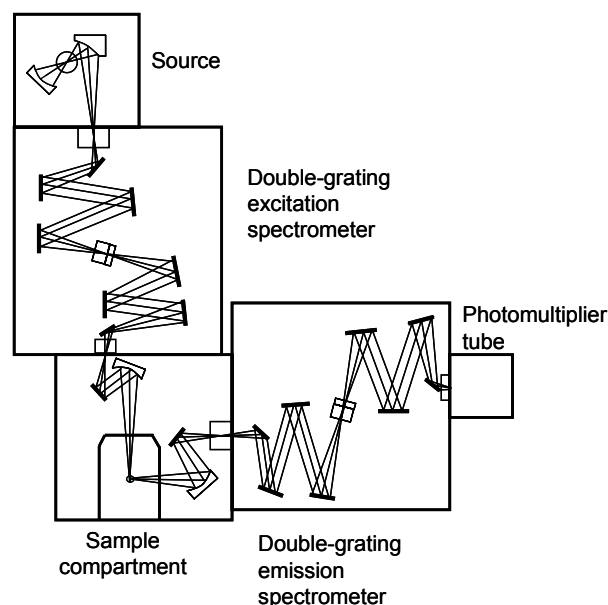

Figure 3.1 Schematic diagram of the Jobin Yvon Fluorolog 3-22 spectrofluorometer with double grating excitation and emission spectrometers. The source is a 450 W xenon lamp which is focussed onto the sample using mirrors to reduce chromatic aberration. A Cryomech PT405 pulse tube refrigerator was suspended within the sample compartment for variable temperature measurements. Figure adapted from reference [144].

Component	Specification
Xenon lamp	450 W power
Power at the sample at 514 nm excitation wavelength	< 1 mW
Monochromator slit width	1 – 5 nm

Table 3.1 Specification of the Jobin Yvon Fluorolog 3-22 system components

intensity (S_c) was calculated by dividing the raw sample emission intensity (S_m) by the lamp intensity (R) [145]

$$S_c = \frac{S_m}{R}.$$

(3.1)

The emission from the xenon lamp passes through an excitation double grating spectrometer which monochromates the source and maximises stray light rejection. The double grating design has a high rejection of unwanted excitation wavelengths. An additional benefit of the double grating design is the doubling of slit width for the same stray light rejection compared to a single grating. An increase in slit width at the entrance and exit to the sample compartment increases the excitation power and the proportion of photoluminescence emission collected.

Mirrors rather than lenses are used to focus the excitation source on to the sample and to collect luminescence emission. This design reduces chromatic aberration and ensures that all parts of the sample are at the focal point of the excitation and emission optics.

The collection optics in the Fluorolog are positioned at 90° to the excitation pathway. This geometry is best suited to transparent or highly absorbing samples, where reflection of light from the sample surface is minimal. For highly reflective samples such as metals, greater than 80 % of the excitation light is reflected into the collection optics.
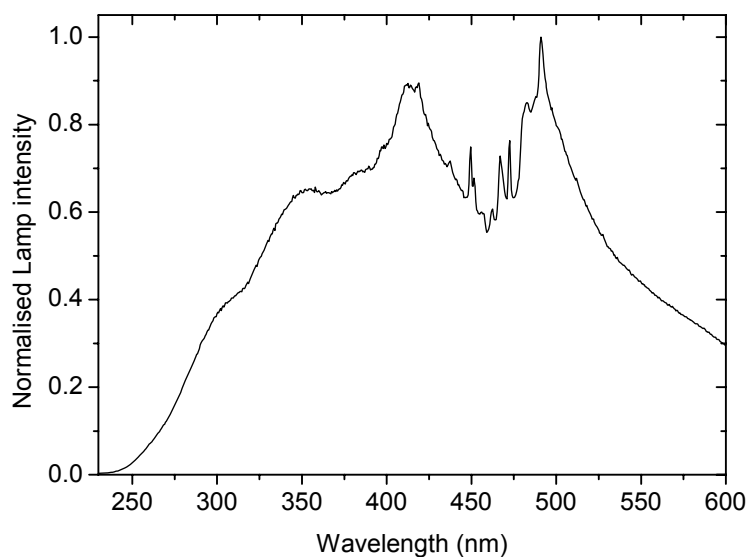
Figure 3.2. Xenon lamp emission spectrum measured after lamp replacement for the Jobin Yvon Flurolog 3-22 spectrofluorometer.

In this case, the double grating emission spectrometer is essential for the removal of stray light, allowing measurement of spectra 5 nm above the excitation wavelength.

For accurate measurements within 5 nm of the excitation wavelength, an additional module is available from the manufacturer with a front face collection option. In this design, the collection optics are positioned at 30° to the excitation pathway so only scattered light from the samples passes through the collection optics, greatly increasing stray light rejection. Front face optics were tested for superconductor samples in a second Fluorolog 3 system but the additional rejection did not change the measured spectra.

To ensure complete isolation of the sample compartment from external light sources, the sample chamber was sealed using a fitted lid and covered with a blackout cloth.

A Cryomech PT405 pulse tube refrigerator cryostat was suspended within the sample chamber for variable temperature measurements. The cryostat was capable of

controlling sample temperature between 10 K and 300 K with the sample mounted on copper sample holder in the centre of the sample chamber.

3.2.2. Example spectra

Figure 3.3 shows the normalised photoluminescence emission spectra of the organic polymer Polyfluorene 2/6, the nominal photoluminescence spectra of the Chevrel phase superconductor $PbMo_6S_8$ and a section of black card. For the measurement the $PbMo_6S_8$ sample was mounted on a copper wire on a nickel plated copper sample holder using GE varnish whilst the black card was mounted on an aluminium holder using bluetak. Figure 3.3 shows the normalised photoluminescence emission spectra of the $PbMo_6S_8$ sample and the black card overlaying one another.

We conclude that the nominal luminescence spectra originated from the Fluorolog sample chamber and not from the samples since there were no components in common between the two measurements. The luminescence spectrum was only observable when light was reflected off an object in the sample position and not from the empty chamber. Examination of the Fluorolog sample chamber using a handheld UV lamp showed visible luminescence emission from multiple locations where an organic polymer solution had been spilt. An effort was made to remove the residue completely but even a small quantity of the polymer produced a luminescence intensity great enough to mask emission from the metals and superconductors.

The composition of the polymer in the sample chamber was not known, however the similarity between the spectra of the polyfluorene 2/6 and the unknown polymer sample suggested that they were both polyfluorene based. Differences between the polyfluorene 2/6 and the unknown polymer could be due to sample composition and self-

absorption of the primary luminescence peak in the thicker unknown polymer sample. The polyfluorene 2/6 spectrum was provided courtesy of Helen Vaughan in the Organic Electroactive Materials Group at Durham University.
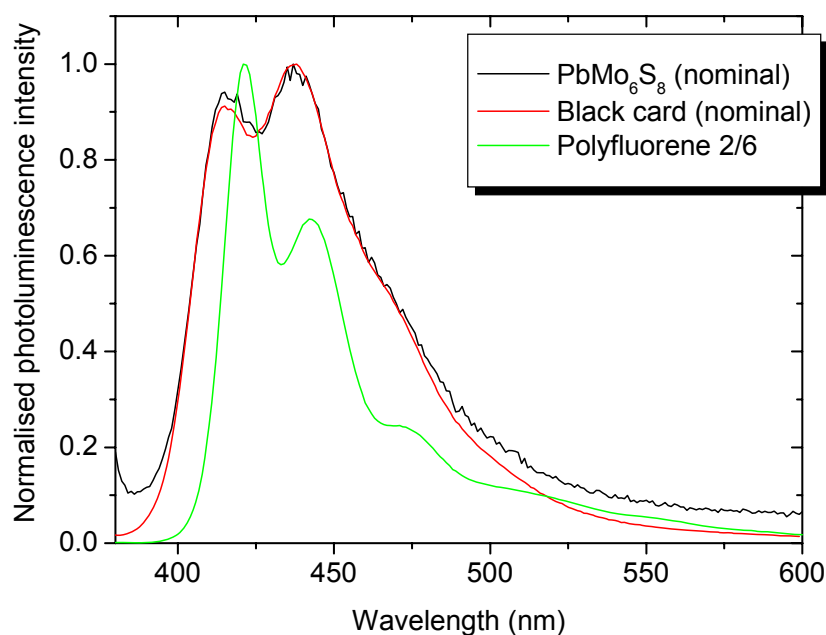

Figure 3.3. Normalised photoluminescence emission spectra for polyfluorene 2/6 (green line) and nominally the Chevrel phase superconductor PbMo$_6$S$_8$ (black line) and black card (red line). The PbMo$_6$S$_8$ sample was mounted on a copper wire on a nickel plated sample holder using GE varnish. The black card was mounted to an aluminium holder using bluetak and the polyfluorene 2/6 was mounted on a glass slide in an aluminium sample holder. Peak intensity of the polyfluorene spectrum was approximately 10^5 times higher than the PbMo$_6$S$_8$ superconductor and 10^3 times greater than the black card. Polyfluorene 2/6 spectrum provided courtesy of Helen Vaughan.

3.2.3. Limitations of commercial photoluminescence systems

Measurements of the photoluminescence emission spectra of metals and superconductors were not possible using the Jobin Yvon Fluorolog 3-22 spectrofluorometer for the two main reasons outlined below.

The polymer residue in the sample chamber could not be physically removed nor its photoluminescence emission spectrum mathematically subtracted from the sample spectrum due to the variable intensity of the polymer luminescence depending on sample roughness and reflectivity. This ruled out the use of this instrument for measurements samples with high surface reflectivity or low photoluminescence emission intensities.

Measurements in a second Fluorolog in the Chemistry Department (with front face optics and no polymer residue) recorded a background spectrum from the anodised sample holder. Although the sample holder spectrum was a much lower intensity than the polymer luminescence in the first Fluorolog, no change in the emission spectra was measured when different samples were mounted to the holder. This indicated that the intensity of the photoluminescence emission from the metals and superconductors was below the resolution of the Fluorolog detector. Increasing the power of the excitation source would have increased the intensity of photoluminescence emission from the samples, however, this was not possible in the existing commercial Fluorolog setup.

3.3. J.A. Woollam variable angle spectroscopic ellipsometry (WVASE®) series ellipsometer

3.3.1. Introduction

Ellipsometry is commonly used to measure the optical constants and/or layer thicknesses of thin film and bulk samples. The technique measures the ratio of the reflection coefficients for s and p polarised light, $\tilde{R}_s$ and $\tilde{R}_p$, respectively. The s and p directions of polarisation (also commonly referred to as the o and e directions of polarisation respectively) are defined in terms of the oscillation of the electric field of the light wave relative to the optical axis of the sample [78]. In the case of s polarised light the electric field oscillates perpendicular to the optical axis and p polarised light parallel to the axis. The ratio between the reflection coefficients is known as the complex ellipsometric parameter, $\tilde{\rho}$, is expressed as [146]

$$\tilde{\rho} = \frac{\tilde{R}_p}{\tilde{R}_s} \tag{3.2}$$

where

$$\tilde{\rho} \equiv \tan\left(\Psi\right)e^{i\Delta}. \tag{3.3}$$

Ψ is the magnitude of the complex refraction coefficient between the p and s direction and Δ is the phase difference. Measurement of the ratio of reflected polarised light is advantageous as the absolute intensity of the incident and reflected light is not required, making the method more reliable than standard reflectivity techniques.

The following sections give details of the system configuration of the J.A. Woollam WVASE ellipsometer and the theory behind its operation. Equations for the analysis of data are presented followed by the measured refractive index, extinction

coefficient and calculated reflectivity spectra. Finally, there is a discussion of the limitations of commercial ellipsometry equipment for the measurement of the optical properties of bulk metals and superconductors.

3.3.2. System configuration and operation

Figure 3.4 is a schematic diagram of the J.A. Woollam variable angle spectroscopic ellipsometry (WVASE) series ellipsometer. Unpolarised emission from a xenon lamp is monochromated before passing through a calcite or quartz crystal polariser which linearly polarisers the light at an angle, P, relative to the plane of incidence of the sample. The linearly polarised light is focussed on the surface of the sample where it is elliptically polarised upon reflection from the surface.

The sample is mounted to the sample stage of the ellipsometer using a small vacuum located behind the sample. Initial alignment of the sample on the ellipsometer is
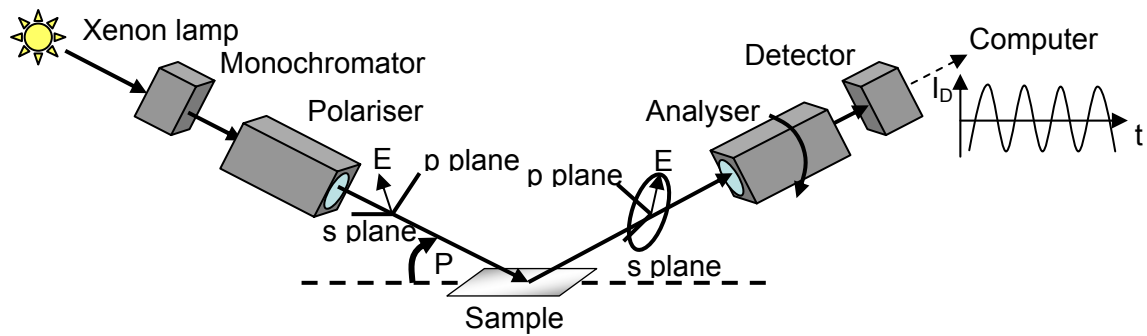

Figure 3.4 Typical system configuration of a rotating analyser ellipsometer. Light from the xenon lamp is monochromated and linearly polarised before reflecting off the surface of the sample which is at an angle of incidence, P. The reflected light passes through a rotating analyser before entering the detector. Measurements are made as a function of wavelength and angle of incidence on the sample. Adapted from reference [146]

carried out in two positions. Firstly, the sample stage is rotated and the plane of the sample surface aligned perpendicular to the incoming linearly polarised light. The sample is then rotated to an angle of 60° relative to the incoming light and the lateral position of the sample adjusted to maximise the intensity of light reflected from the sample surface falling on the detector located at 120° relative to the light source.

After reflection from the sample surface the elliptically polarised light passes through a second polariser (analyser) which continuously rotates at a fixed frequency between 10 – 60 Hz. The light enters the solid state detector as a sinusoidally oscillating intensity, I_D, and is logged and analysed by a computer.

Detector intensity measured as a function of time, I_D, is proportional to the magnitude of the electric field, E_D, squared [146]

$$I_D \propto |E_D|^2. \tag{3.4}$$

The magnitude of the electric field can be expressed as a combination of Jones matrices so that

$$E_D = [analyser.matrix][sample.matrix][Polariser.matrix][Input.beam]. \tag{3.5}$$

Expansion and normalisation of the matrices leads to an equation for I_D in terms of measurable quantities

$$I_D \propto \frac{\left|\dfrac{\tilde{R}_p}{\tilde{R}_s}\right|^2 - \tan^2 P}{\left|\dfrac{\tilde{R}_p}{\tilde{R}_s}\right|^2 + \tan^2 P}\cos(2A) + \frac{2\operatorname{Re}\left(\dfrac{\tilde{R}_p}{\tilde{R}_s}\right)\tan P}{\left|\dfrac{\tilde{R}_p}{\tilde{R}_s}\right|^2 + \tan^2 P}\sin(2A) \tag{3.6}$$

where, A is the analyser azimuthal angle and $\tilde{\rho}$ is the complex ellipsometric parameter as defined in equations (3.2) and (3.3). Substituting into equation (3.6) gives an expression for I_D as a function of Ψ, Δ, A and P

$$I_D \propto 1 + \frac{\tan^2 \Psi - \tan^2 P}{\tan^2 \Psi + \tan^2 P} \cos(2A) + \frac{2 \tan \Psi \cos \Delta \tan P}{\tan^2 \Psi + \tan^2 P} \sin(2A), \qquad (3.7)$$

which can be rewritten as a Fourier series in twice the analyser angle

$$I_D \propto 1 + \alpha \cos(2A) + \beta \sin(2A), \qquad (3.8)$$

where α and β are the normalised Fourier coefficients. The analyser angle can be expressed as a function of time as

$$A(t) = 2\pi f_0 t, \qquad (3.9)$$

where f_0 is the frequency of rotation. Therefore, α and β can be determined by performing a Fourier transform on the experimentally measured detector intensity.

Finally, rearranging equations (3.7) and (3.8) leads to expressions for Ψ and Δ in terms of α, β and P [146]

$$\tan \Psi = \sqrt{\frac{1+\alpha}{1-\alpha}} \left| \tan P \right| \qquad (3.10)$$

$$\cos \Delta = \frac{\beta}{\sqrt{1-\alpha^2}} \cdot \frac{\tan P}{\left| \tan P \right|} \qquad (3.11)$$

3.3.3. Determination of optical constants and film thickness

A four stage process is used to calculate the optical constants, film thickness and reflectivity using the data obtained for Ψ and Δ. Firstly, the refractive index, n, and extinction coefficient, κ, are calculated using the relationship [147]

$$n^2 = \kappa^2 + \frac{\sin^2 P \tan^2 P (\cos^2 2\Psi - \sin^2 2\Psi \sin^2 \Delta)}{(1 + \sin 2\Psi \cos \Delta)^2}, \qquad (3.12)$$

$$\kappa = \frac{\sin^2 P \tan^2 P \sin 4\Psi \sin \Delta}{2n(1 + \sin 2\Psi \cos \Delta)^2}. \qquad (3.13)$$

To calculate film thickness a Cauchy fit is then performed to generate modelled values for n and κ using [146]

$$n(\lambda) = A + B / \lambda^2 + C / \lambda^4 + ..., \qquad (3.14)$$

where λ is the wavelength (in microns), and A, B and C are fitting parameters. An iterative process is carried out to fit the modelled data to the experimentally measured data for n and κ, leading to modified values for A, B and C which are re-entered into equation (3.14) and used to calculate film thickness

$$d = \frac{\delta}{\sqrt{n^2 - \sin^2 P}} \left(\frac{\lambda}{360} \right), \qquad (3.15)$$

where δ is the change in phase of the beam of vacuum wavelength, λ. The measure of how closely the generated data fits the experimental data is given in the software by the mean squared error (MSE) value [148]. The value is calculated by the summation of the squares of the differences between the modelled and experimental data points divided by the standard deviation of the experimental data. The closer the MSE value is to unity, the better the fit.

Finally, reflectivity, R, is calculated using [149]

$$R = \frac{(n-1)^2 + \kappa^2}{(n+1)^2 + \kappa^2}. \qquad (3.16)$$

3.3.4. Optical constants of copper and gold

The following section presents data for the refractive index, extinction coefficient and reflectivity spectra for copper and gold measured using the J.A. Woollam WVASE series ellipsometer. The data are plotted along with values from the literature [150].
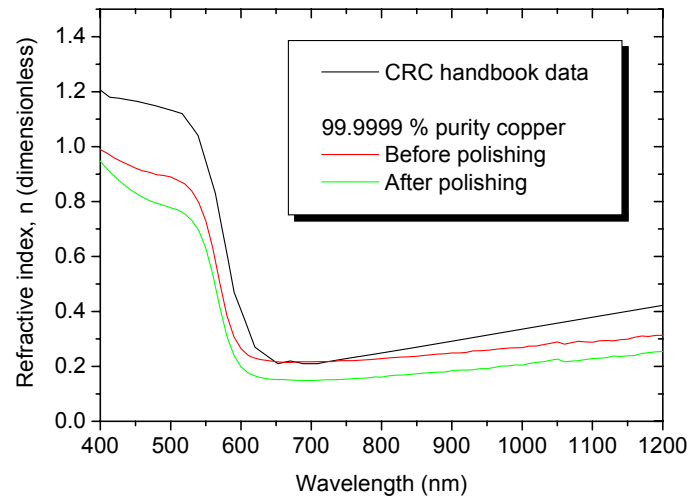
Copper

Figure 3.5 Refractive index, *n*, as a function of wavelength for copper from the CRC handbook (black line) and measured for 99.9999 % purity copper before polishing (red line) and 94 days after polishing (green line) using the J. A. Woollam ellipsometer [150].
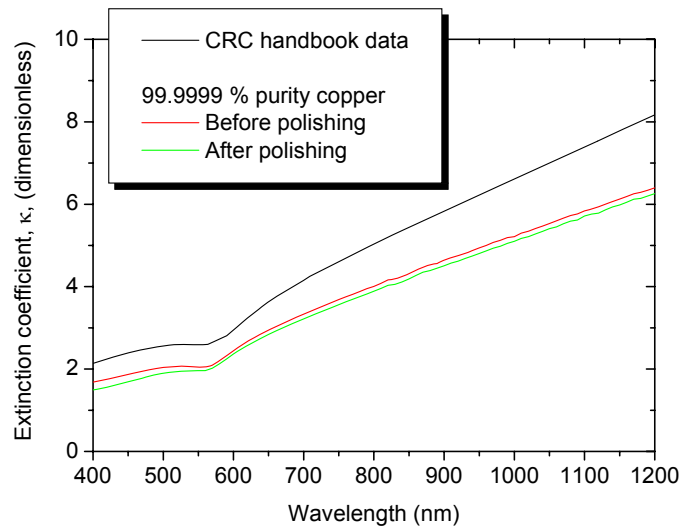

Figure 3.6 Comparison of the extinction coefficient, *κ*, as a function of wavelength for copper from the CRC handbook (black line) and measured for 99.9999 % purity copper before polishing (red line) and 94 days after polishing (green line) using the J. A. Woollam ellipsometer [150].
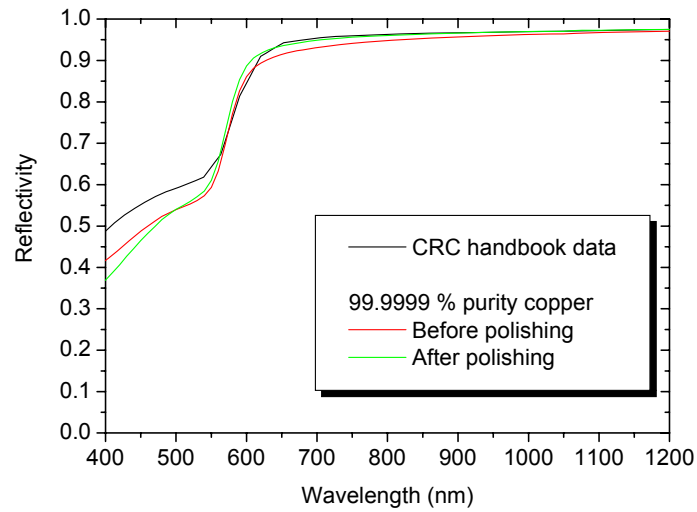
Figure 3.7 Reflectivity as a function of wavelength for copper calculated using the data for the refractive index, *n*, and extinction coefficient, *κ* from the CRC handbook (black line) and measured for 99.9999 % purity copper before polishing (red line) and 94 days after polishing (green line) using the J. A. Woollam ellipsometer [150]
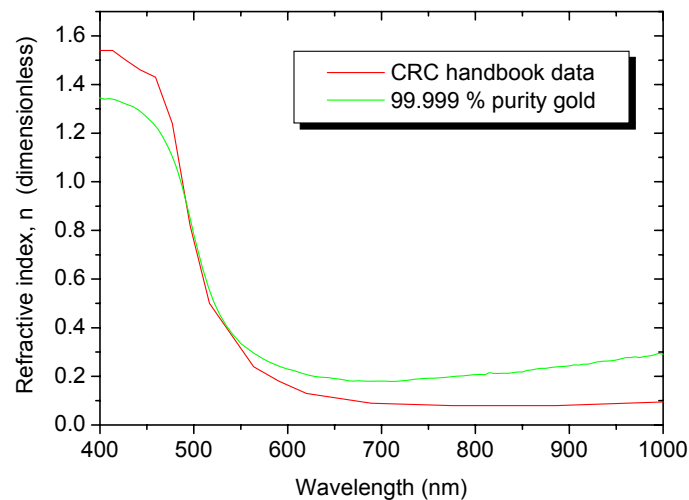
Gold

Figure 3.8 The refractive index, *n*, as a function of wavelength for gold measured using the J. A. Woollam ellipsometer [150]. For comparison there are also data taken from the CRC handbook. The sample was polished on the same day as the measurement.
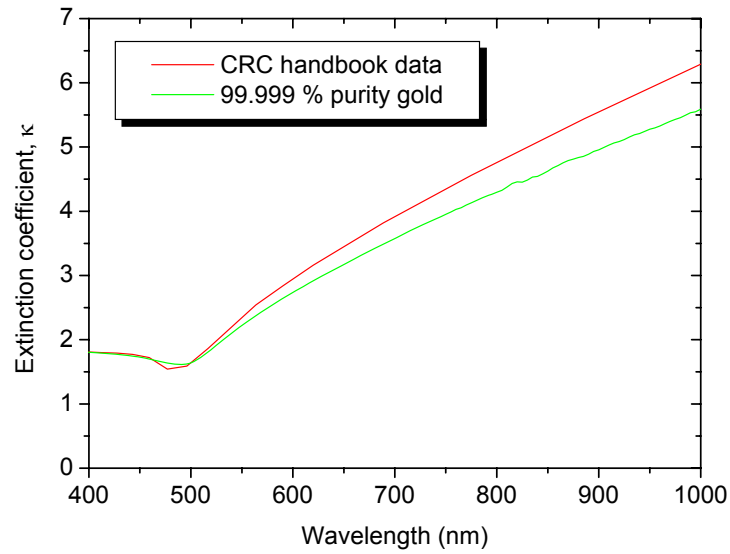
Figure 3.9 Comparison of the extinction coefficient, κ, as a function of wavelength for gold from the CRC handbook and measured using the J. A. Woollam ellipsometer [150]. The sample was polished on the same day as the measurement.
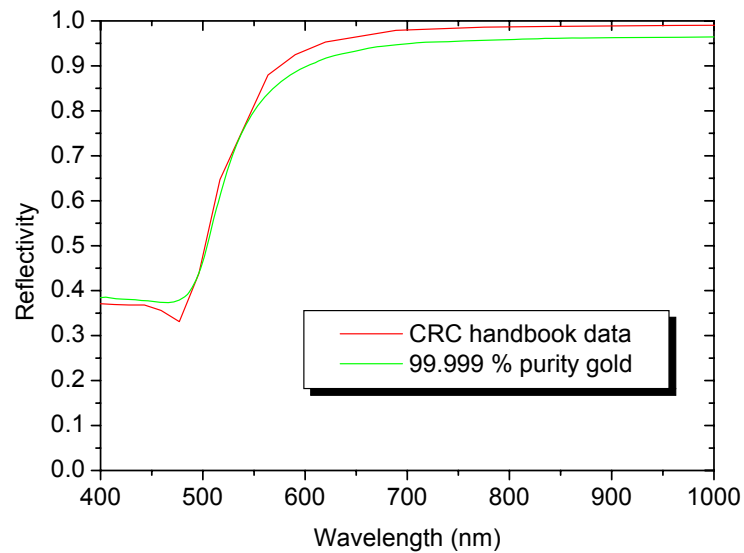

Figure 3.10 Reflectivity calculated as a function of wavelength for gold using data for the refractive index, *n*, and extinction coefficient, κ. Data for *n* and κ were sourced from the CRC handbook and from measurements using the J. A. Woollam ellipsometer [150]. The sample was polished on the same day as the measurement.

3.3.5. Optical constants of superconductors

Refractive index, extinction coefficient and reflectivity spectra are presented below for the high temperature superconductors YBCO and DyBCO and the Chevrel phase superconductors $PbMo_6S_8$ and $SnMo_6S_8$ measured using the J.A. Woollam WVASE series ellipsometer. Also shown are literature data for niobium. We could not measure optical properties of the niobium sample probably because our samples had an inhomogeneous sample surface.
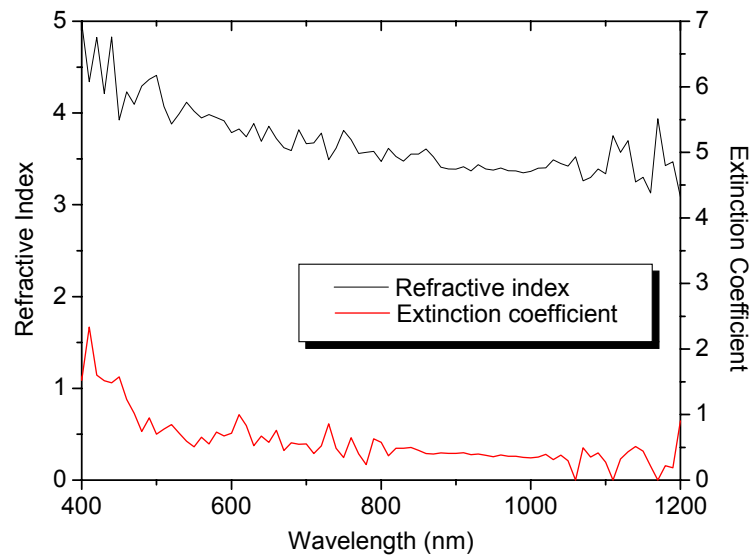
YBCO

Figure 3.11 Refractive index, *n*, and extinction coefficient, *κ*, as a function of wavelength for the YBCO single crystal measured using the J. A. Woollam ellipsometer.

Figure 3.12 Reflectivity as a function of wavelength for the YBCO single crystal calculated using data for the refractive index and extinction coefficient measured using the J. A. Woollam ellipsometer.

DyBCO

Figure 3.13 Refractive index, *n*, and extinction coefficient, *κ*, as a function of wavelength for the DyBCO single crystal measured using the J. A. Woollam ellipsometer.
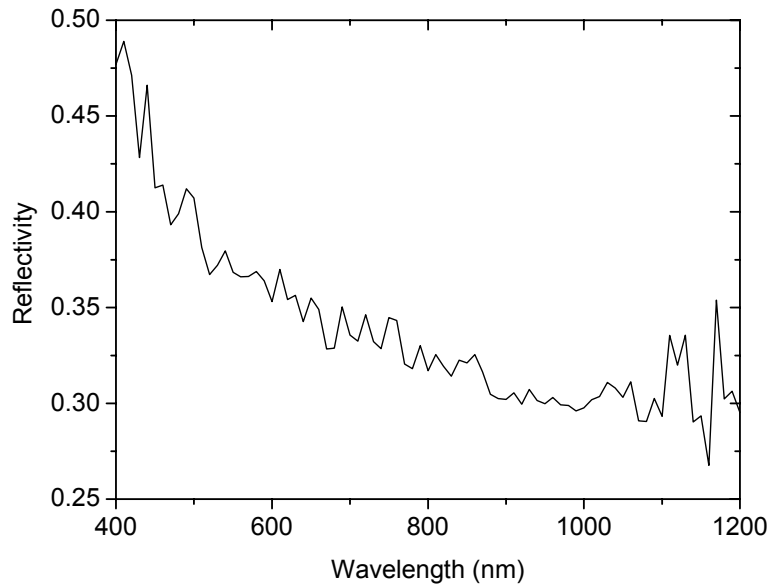
Figure 3.14 Reflectivity as a function of wavelength for the DyBCO single crystal calculated using data for the refractive index and extinction coefficient measured using the J. A. Woollam ellipsometer.
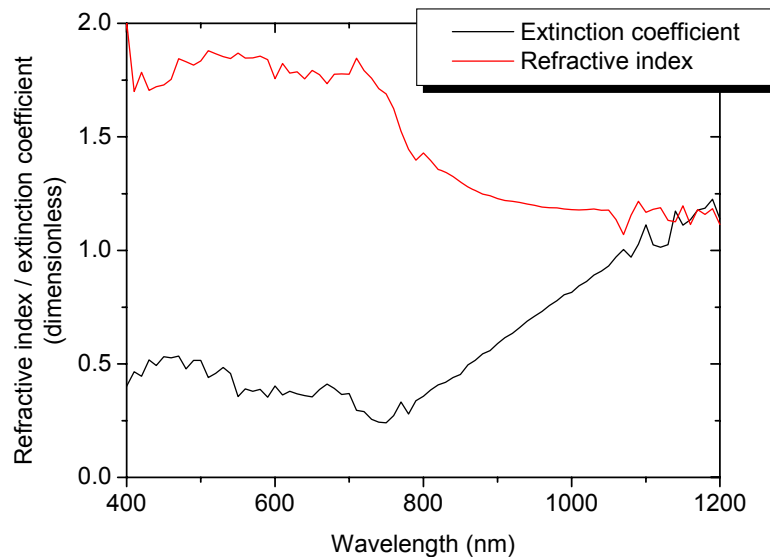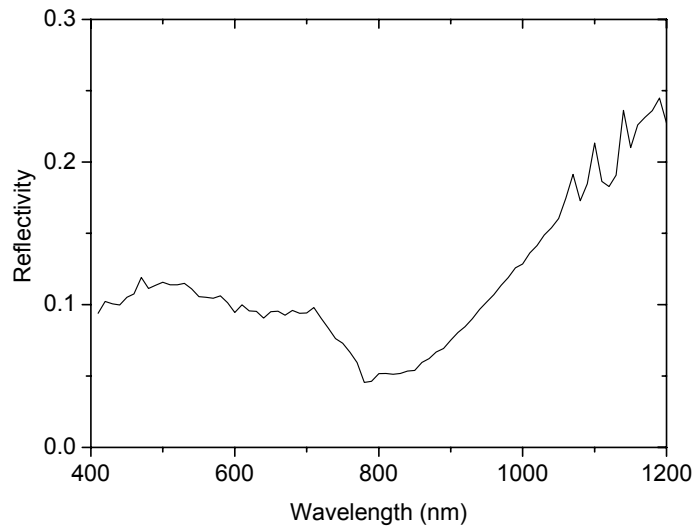
PbMo₆S₈

Figure 3.15 Refractive index, *n*, and extinction coefficient, *κ*, as a function of wavelength for the Chevrel phase superconductor PbMo₆S₈ measured using the J. A. Woollam ellipsometer.

Figure 3.16 Reflectivity as a function of wavelength for the Chevrel phase superconductor PbMo$_6$S$_8$ calculated using data for the refractive index and extinction coefficient measured using the J. A. Woollam ellipsometer.
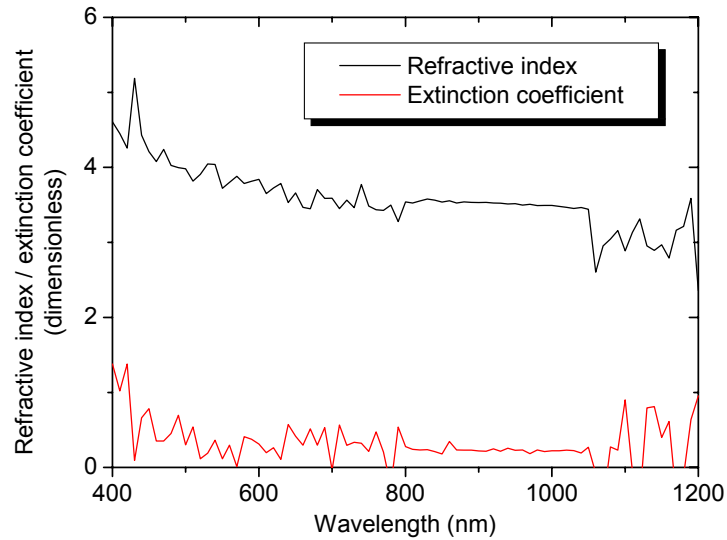
SnMo$_6$S$_8$

Figure 3.17 Refractive index, *n*, and extinction coefficient, *κ*, as a function of wavelength for the Chevrel phase superconductor SnMo$_6$S$_8$ measured using the J. A. Woollam ellipsometer.
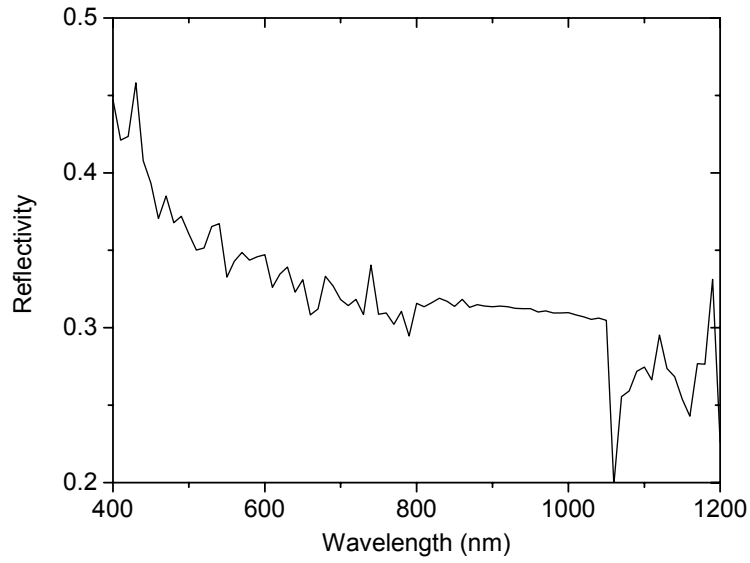
Figure 3.18 Reflectivity as a function of wavelength for the Chevrel phase superconductor $SnMo_6S_8$ calculated using data for the refractive index and extinction coefficient measured using the J. A. Woollam ellipsometer.
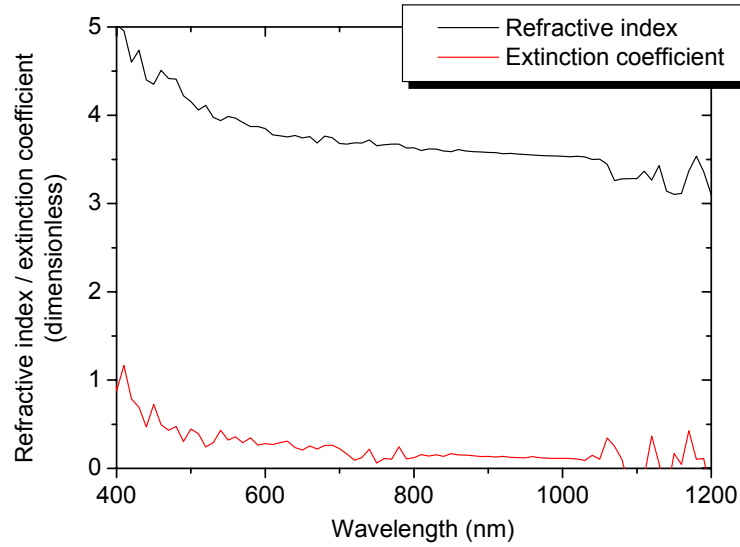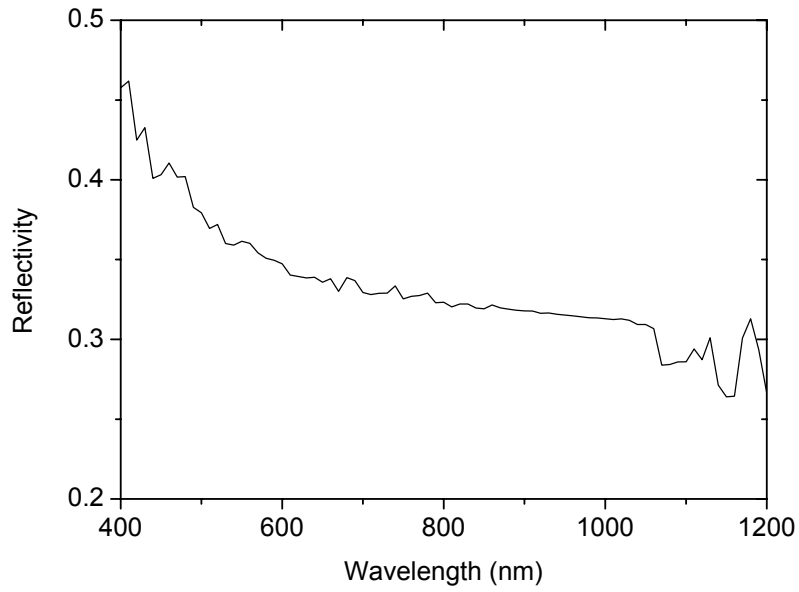
Niobium
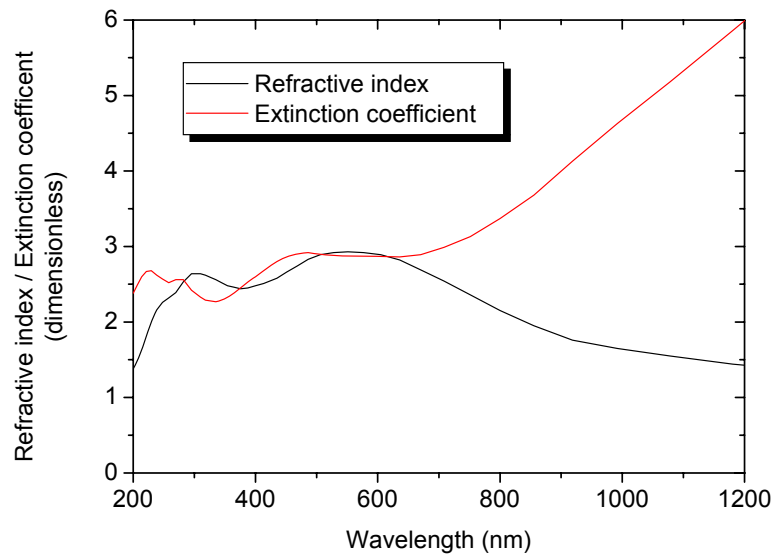
Figure 3.19 Refractive index, *n*, and extinction coefficient, *κ*, as a function of wavelength for niobium from the CRC handbook [150].
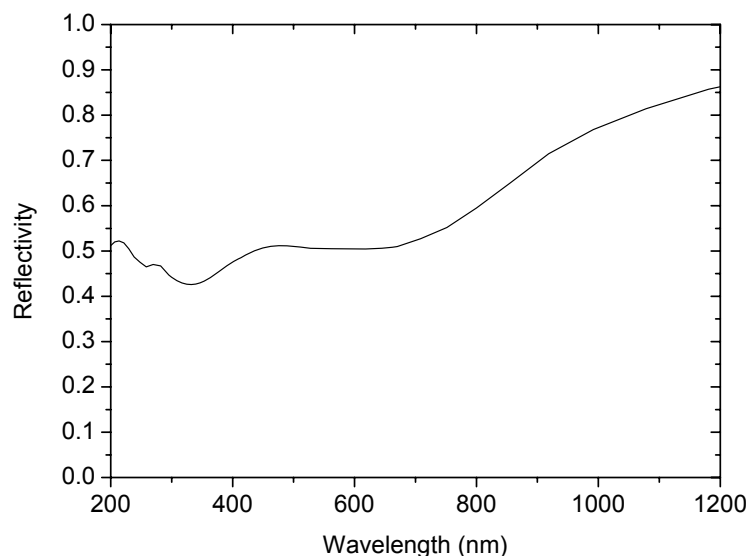
Figure 3.20 Reflectivity as a function of wavelength for niobium from the CRC handbook [150].

3.3.6. Discussion of ellipsometry measurements and analysis

Accurate calculation of refractive index, extinction coefficient and layer thickness using ellipsometry requires careful modelling based on assumptions about the sample composition and layering. If the assumptions are inaccurate then the model used to determine the optical constants will calculate incorrect values for the refractive index and extinction coefficient. Common inaccuracies in modelling involve of a lack of inclusion of oxide layers, unknown surface coatings, patterned sample surfaces and the anisotropy of the sample [146].

A high intensity of reflected light at the detector is required for accurate measurement of the optical properties of the sample. Reflectivity from the sample surface in the visible region must be high enough to give an acceptable signal to noise ratio with a surface roughness recommended by the manufacturer to be less than 10 % of the

wavelength of the incident light. The copper, gold, niobium and DyBCO samples were polished using a 1 μm grade diamond paste. Although the samples had a visible mirror finish, the roughness was an order of magnitude greater than the recommended value, leading to increased scattering from the sample surface. The polycrystalline Chevrel phase samples and the single crystal YBCO sample were too delicate to be polished and had their surfaces cleaned using 1200 grade abrasive paper giving a surface roughness two orders of magnitude above the recommended limit. The doped Chevrel phase samples $Pb_{1-x}Gd_xMo_6S_8$ x = 0.3 and $Sn_{1-x}Eu_xMo_6S_8$ x = 0.35 had absorption coefficients greater than 90 % in the visible region, reducing the intensity of reflected light below the measurable limit of the detector. Reflectivity data in the literature for Chevrel phase compounds and YBCO have comparable values to our measurements of between 10 – 30 % in the visible region [113] [99].

A comparison of the data in the literature and the measured optical constants for copper showed a small difference which suggested the presence of an oxide layer on the sample surface. Modelling of the ellipsometry data for the polished 99.9999 % purity copper sample was carried out for three conditions 1) an infinitely thick layer of copper with no oxide layer, 2) the addition of a thin CuO layer and 3) a thin Cu_2O layer. The lowest mean squared error (MSE) was produced for an 8.4 nm thick CuO layer above the infinitely thick copper layer giving an MSE of 14.07. This was compared to an MSE of 81.85 for the model of the single infinitely thick copper layer. Performing the same fit on the 99.999 % purity gold ellipsometry data gave an MSE of 14.98 for a single infinitely thick layer of gold with no oxide layer. This is consistent with data in the literature which reports that no oxide layer is formed on gold [83, 84].

3.4. Quantum Design physical properties measurement system (PPMS)

3.4.1. Introduction

The Quantum Design physical properties measurement system (PPMS) is a variable temperature (1.8 – 350 K), variable magnetic field (0 – 9 T) environment for the measurement of electrical, magnetic and thermal properties of samples. The system contains multiple, interchangeable measurement modes including; resistivity, AC transport, heat capacity, AC susceptibility, torque magnetometry, and vibrating sample magnetometry.

The following section gives details of the resistivity, heat capacity and magnetic moment measurement modes of the PPMS for the measurement of the superconducting samples. The methods used to determine the superconducting transition temperature, T_C, from the data are explained and the measured transition temperatures presented.

3.4.2. General overview

Figure 3.21 is a schematic diagram of the Quantum Design PPMS. The left figure shows the magnet assembly with the variable temperature insert (VTI) mounted vertically through its centre. The right figure shows a cross section through the magnet and sample space. The location of the thermometers, heaters and sample stage (puck) are labelled. Pucks of specific designs are inserted into the base of the variable temperature insert for resistivity, AC transport and heat capacity measurements. Pins at the base of the sample space contact with the base of the puck to give a robust electrical connection.
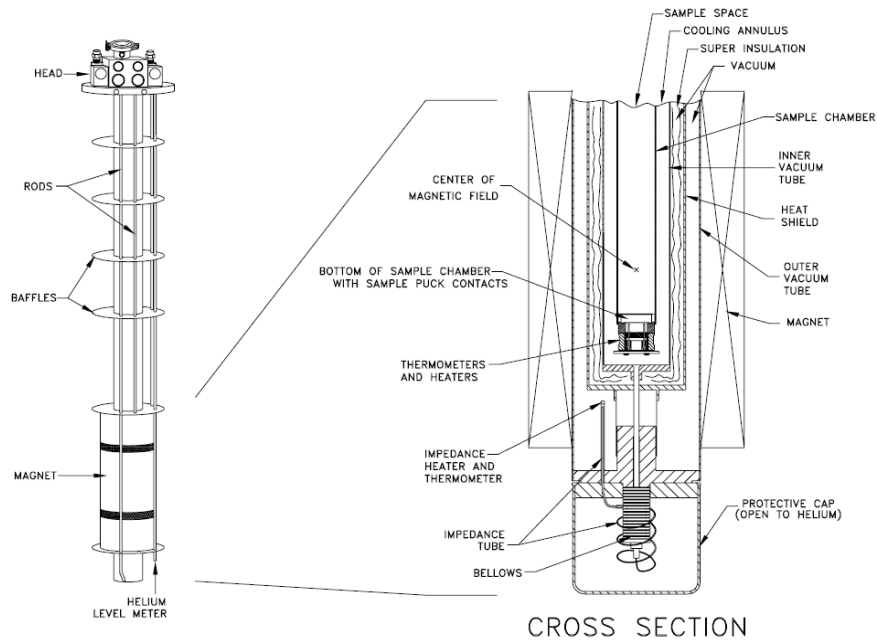
Figure 3.21 Cross-sectional schematic diagram of the Quantum Design Physical Properties Measurement System (PPMS) probe. The left hand diagram shows the magnet assembly with the variable temperature sample space located vertically through its centre. The right hand diagram is a cross section through the magnet and sample space showing the location of thermometers, heaters and sample puck. The figure is reproduced from the Quantum Design PPMS manual [151].

A thermometer and heater are positioned at the base of the chamber, close to the puck for accurate temperature monitoring and control.

3.4.3. Measurement options

Resistivity

Resistivity measurements were made using the four point geometry shown in the inset diagram in Figure 3.22. A current was applied to the outer two contacts and voltage measured across the inner contacts. Electrical connections were made using solder to

connect to the puck and conductive silver paint or two part conductive epoxy on the sample to minimise contact resistances.

Samples with extremely low resistivities (e.g. copper) were measured using a custom resistivity probe which was inserted into the variable temperature bore of the PPMS. The precision of the probe was 60 nΩ which was achieved through a series of improvements to the probe including; the use of single lengths of wire for the current and voltage leads which were twisted together in pairs to reduce thermal voltages, polarity switching of the stable current source with concurrent voltage measurements and amplification of the voltage signal through a nanovolt amplifier.

The ideal sample geometry for a resistivity measurement is a semi-infinite plane in the lateral dimension with the gap between the voltage contacts equal to or greater than the thickness of the sample. This minimises the effect of a voltage drop across the width or thickness of the sample. Since the photoluminescence measurements required the largest sample size possible, a compromise was made with the samples having lengths approximately twice their width and thicknesses of between $0.1 - 1.5$ mm thickness.

Resistivity, ρ, was calculated using

$$R = \frac{V}{I}, \tag{3.17}$$

$$\rho = \frac{RA}{L}, \tag{3.18}$$

where R is the resistance of the sample, V is the measured voltage, I is the applied current, A is the cross sectional area and L, the distance between the voltage contacts measured using a vernier micrometer.

The superconducting transition temperature, T_C, is commonly identified by four values; T_C (onset), T_C (90%), T_C (50 %) and T_C (10%). Figure 3.22 shows how the four values are determined. Figure 3.23 shows the resistivity data for the Chevrel Phase
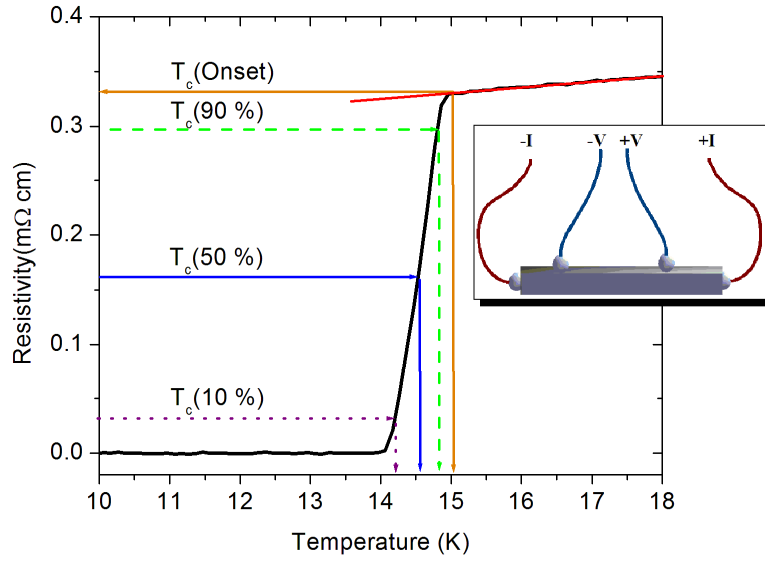
Figure 3.22 Determination of the superconducting critical temperature (T_C) from resistivity measured as a function of temperature. The graph shows the method of determining the commonly stated values of T_C(onset), T_C(90%), T_C(50%) and T_C(10%). The inset figure shows the geometry of the current (I) and voltage (V) contacts on the sample.
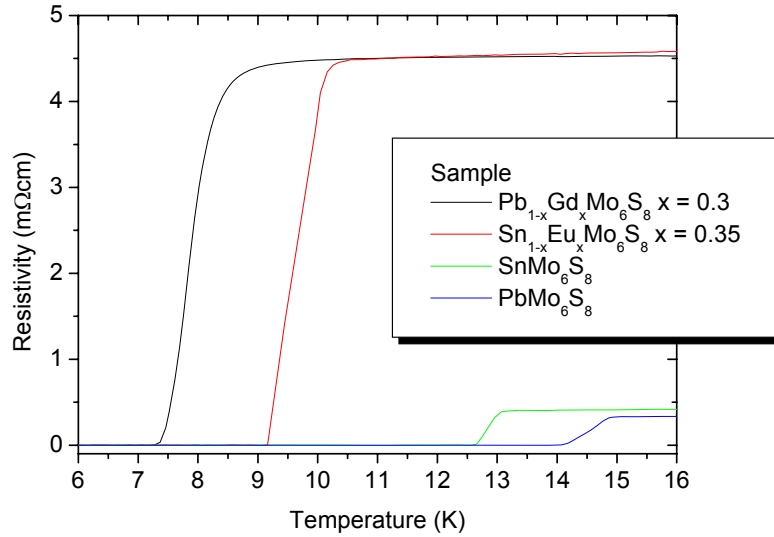
Figure 3.23 Measurement of resistivity as a function of temperature for $Pb_{1-x}Gd_xMo_6S_8$ x = 0.3, $Sn_{1-x}Eu_xMo_6S_8$ x = 0.35, $SnMo_6S_8$, $PbMo_6S_8$. Data were collected using the resistivity mode of the Quantum Design physical properties measurement system (PPMS). Data were collected as a function of temperature in zero field.

superconductors $PbMo_6S_8$, $Pb_{1-x}Gd_xMo_6S_8$ x = 0.3, $SnMo_6S_8$ and $Sn_{1-x}Eu_xMo_6S_8$ x = 0.35 at zero applied external magnetic field. A summary of the transition temperatures are given in Table 3.2.

Heat capacity

Heat capacity, C_p, is defined as the increase in temperature, T, of a sample under the application of a known quantity of heat, Q, at a constant pressure, P,

$$C_p = \left(\frac{\delta Q}{\delta T} \right)_P .$$
(3.19)

A schematic diagram of the heat capacity stage in the PPMS is shown in Figure 3.24. The sample platform is suspended on eight gold wires which are connected to the sample holder (puck) frame acting as a thermal bath for the sample. The sample is in close thermal contact with the platform through a thin layer of Apiezon N grease. To
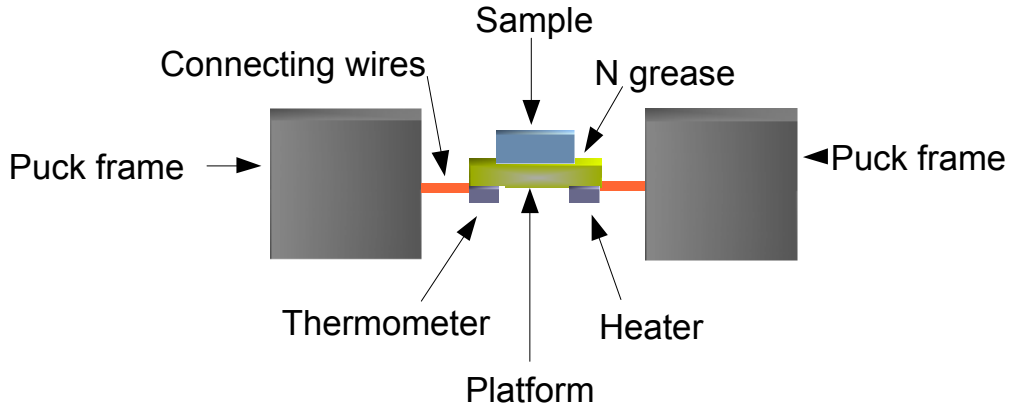
Figure 3.24 Schematic diagram of the sample stage (puck) for the measurement of heat capacity in the Quantum Design physical properties measurement system (PPMS). The sample is mounted on a suspended platform using Apiezon N grease. The grease ensures excellent thermal contact between the sample and platform. The platform is connected to the measurement puck (thermal bath) by 8 thin gold wires. The puck and sample sit in a high vacuum with the heater and thermometer mounted to the underside of the sample platform. Diagram adapted from reference [152].

ensure that no external heat sources influence the measurement, the puck and sample are surrounded by a high vacuum of between 10^{-3} to 10^{-5} mbar generated by the standard system vacuum pump and a charcoal sorption pump [153].

Heat capacity is measured by the application of a small pulse of heat from the heater on the underside of the sample platform. The time for the temperature to return to thermal equilibrium with the bath is measured by a thermometer also located on the underside of the platform. For variable temperature measurements the temperature of the thermal bath is swept slowly across the desired measurement range, in this case from 300 K to approximately 10 K below T_{C}. An addenda measurement of the puck with Apiezon N grease is run without the sample before the main sample measurement. The addenda data is subtracted from the measurement with the sample giving accurate heat capacity data for the sample.

At the superconducting transition temperature, heat capacity as a function of temperature deviates from its normal state trend. Determination of the superconducting critical temperature is carried out by fitting the heat capacity data above and below the superconducting transition using a modified version of [154]

$$\frac{C}{T} = a + bT + cT^{2} + dT^{4} + eT^{6},$$ (3.20)

where a, b, c, d and e are constants. The fits are extrapolated across the transition and the difference between the fit and measured data are calculated (Figure 3.25a). The difference between the fits and the data are integrated with respect to temperature (to find the change in entropy, ΔS) using [154]

$$S = \int \frac{C(T)}{T} dT,$$ (3.21)

before being plotted against one another. The superconducting transition (T_{c} (50%)) is taken to be the point where the two plots cross (Figure 3.25b).
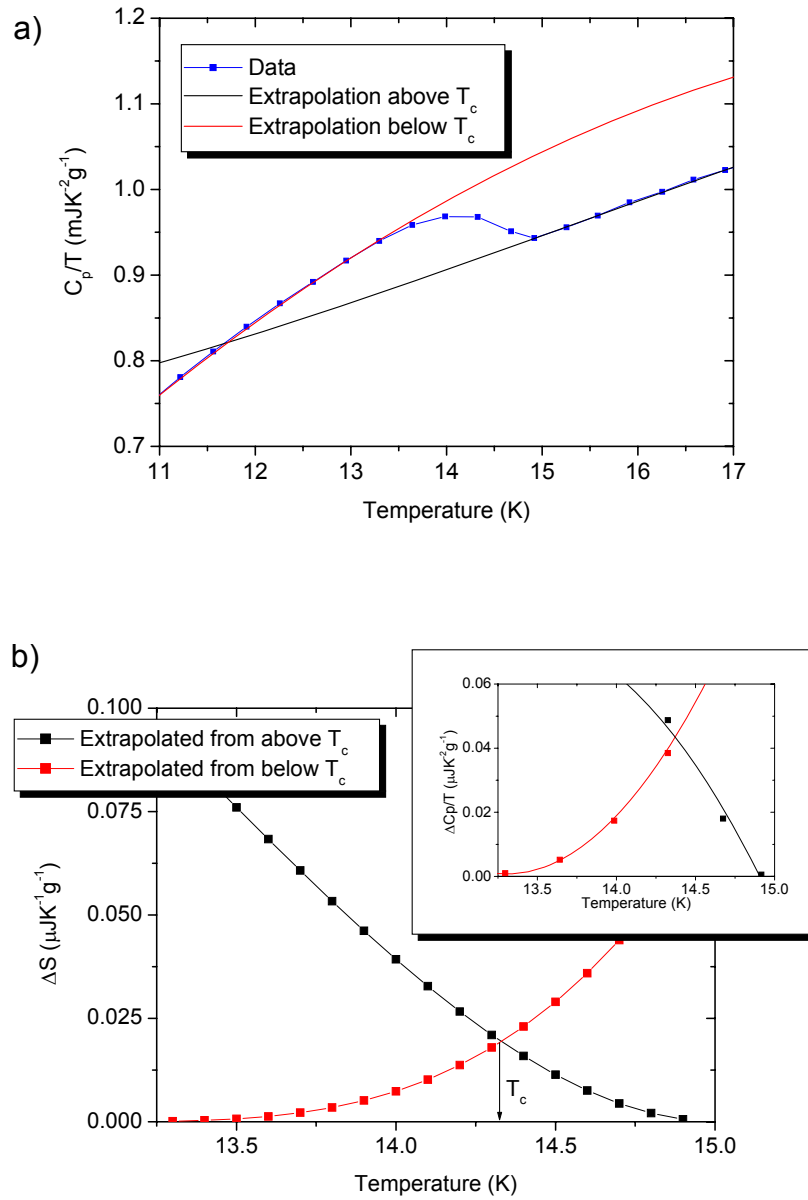
Figure 3.25 Method for the determination of the superconducting critical temperature (T_C) from heat capacity (C_p) measurements of the Chevrel phase superconductor PbMo$_6$S$_8$. Two fits are made to the measured C_p/T data above and below T_C. Part a) shows how the fits are extrapolated across the transition. The inset graph in part b) demonstrates the calculated difference between the fits and measured data. The differences are then integrated to find the change in entropy (ΔS) across the transition (part b main graph). The mid point of the superconducting transition is at the point at which the two curves for the change in entropy cross [154].

Figure 3.26, Figure 3.27 and Figure 3.28 show the measured heat capacity curves for the Chevrel phase superconductors $PbMo_6S_8$, $Pb_{1-x}Gd_xMo_6S_8$ x = 0.3 and the high temperature superconductor YBCO respectively. The values for T_C obtained for these samples are given in Table 3.2.
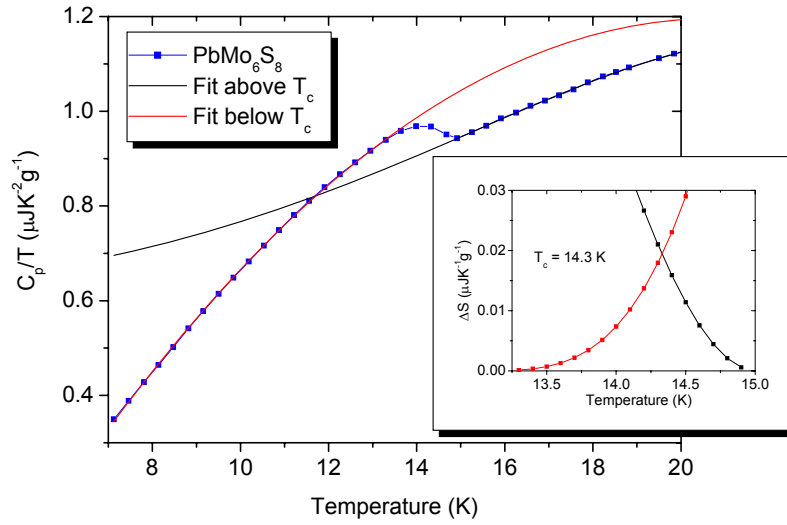
Figure 3.26 Heat capacity, C_p, of PbMo$_6$S$_8$ measured as a function of temperature using the heat capacity mode of the Quantum Design physical properties measurement system (PPMS). Data are collected as a function of temperature in zero field.
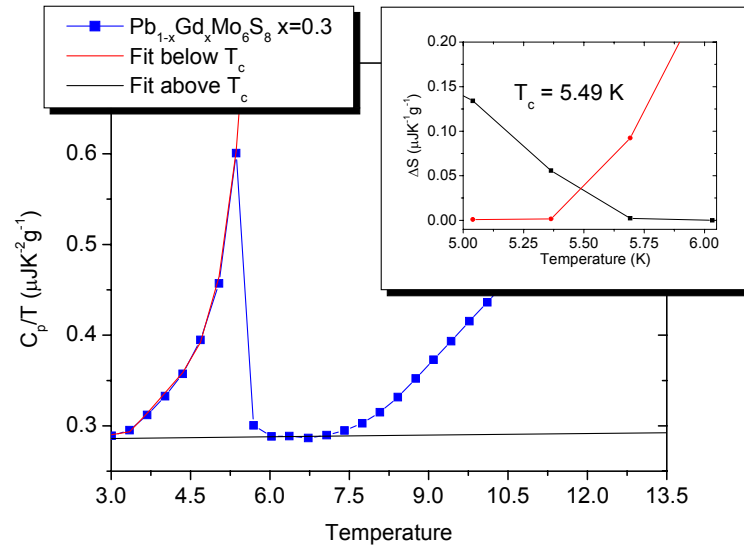
Figure 3.27 Heat capacity, C_p, of Pb$_{1-x}$Gd$_x$Mo$_6$S$_8$ x = 0.3 measured as a function of temperature using the heat capacity mode of the Quantum Design physical properties measurement system (PPMS). Data are collected as a function of temperature in zero field.
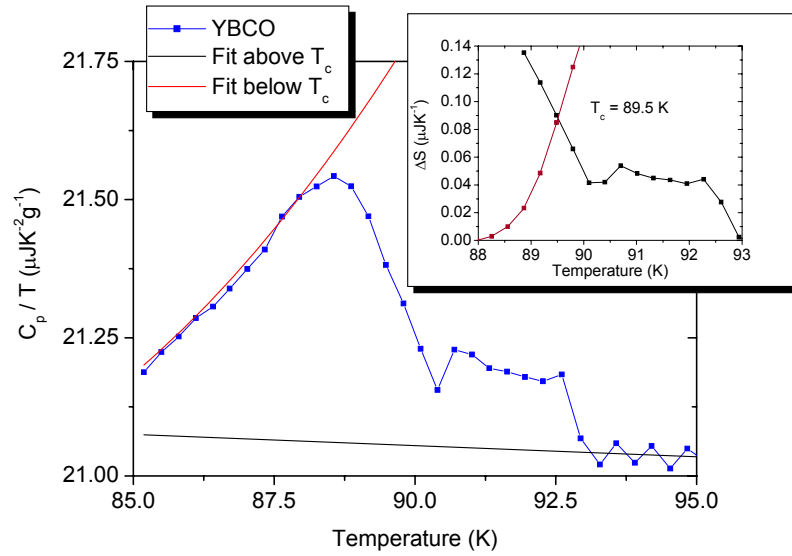
Figure 3.28 Heat capacity, C_p, measured as a function of temperature of the YBCO single crystal across the superconducting transition using the heat capacity mode of the Quantum Design physical properties measurement system (PPMS). Data are collected as a function of temperature in zero field.

AC susceptibility

Figure 3.29 is a schematic diagram of the AC susceptibility insert for measurement of magnetic moment in the Quantum Design PPMS. Drive and detection coils surround the sample which is mounted inside a gelatine capsule in a plastic straw. The AC drive coils induce an opposing magnetic field in the sample according to Lenz's
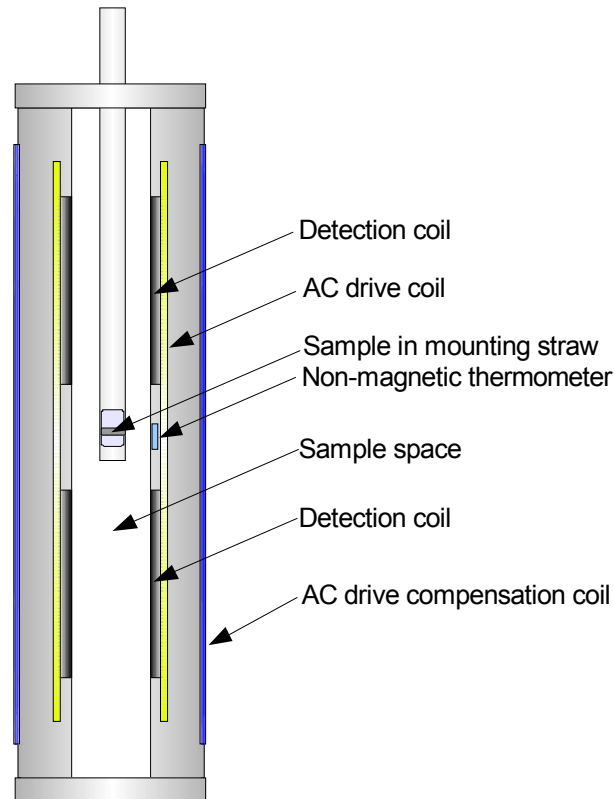
Figure 3.29 Schematic diagram of the coil arrangement for the measurement of magnetic moment in the Quantum Design physical properties measurement system (PPMS). The sample is surrounded by a series of coils within the variable temperature sample space. The AC drive coils induce a magnetic field within the sample due to Lenz' law. The detection coils measure the amplitude of the induced field, which is the sample's magnetic moment. The sample is mounted inside a plastic straw and gelatine capsule and located centrally between the two detection coils. The sample space is located within the main 9 T magnet coils which are shielded from the AC drive coils by an AC drive compensation coil. Temperature is measured using a field independent thermometer. Diagram adapted from reference [155].

Law. In the superconducting state currents are set up in the surface of the sample which expel magnetic flux within the sample. The currents induce a magnetic field in the detection coils with amplitude directly equivalent to the magnetic moment of the sample.

For measurements in an external magnetic field, the main superconducting magnet coil is shielded from the AC drive coils by an AC drive compensation coil. The temperature inside the variable temperature insert is measured using a field independent thermometer to ensure accurate measurement of temperature in high external magnetic fields.

Figure 3.30 demonstrates the method for determining the four most commonly stated values of T_C in a susceptibility measurement. Figure 3.31 shows the susceptibility for the Chevrel phase superconductors $PbMo_6S_8$, $Pb_{1-x}Gd_xMo_6S_8$ x = 0.3, $SnMo_6S_8$ and $Sn_{1-x}Eu_xMo_6S_8$ x = 0.35 and Figure 3.32 shows the data for the high temperature single crystal superconductors YBCO and DyBCO. A summary of the transition temperatures found are shown in Table 3.2.

Summary of superconducting transition temperatures

Table 3.2 summarises the superconducting transition temperatures at T_C (10%), T_C (50%) and T_C (90%) for the single crystal elementary superconductor Nb, the polycrystalline Chevrel phase superconductors $PbMo_6S_8$, $Pb_{1-x}Gd_xMo_6S_8$ x = 0.3, $SnMo_6S_8$ and $Sn_{1-x}Eu_xMo_6S_8$ x = 0.35 and the high temperature single crystal superconductors YBCO and DyBCO measured using the resistivity, heat capacity and magnetic moment modes of the Quantum Design PPMS.
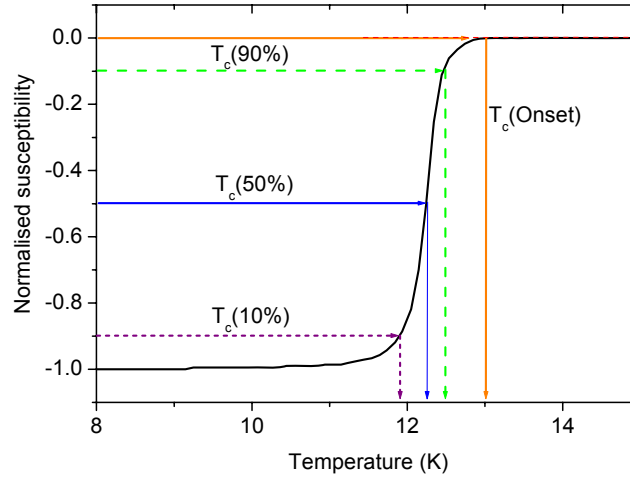
Figure 3.30 Determination of the superconducting critical temperature (T_C) from measurements of magnetic moment as a function of temperature. The graph shows the method of determining the commonly stated values of T_C(onset), T_C(90%), T_C(50%) and T_C(10%).
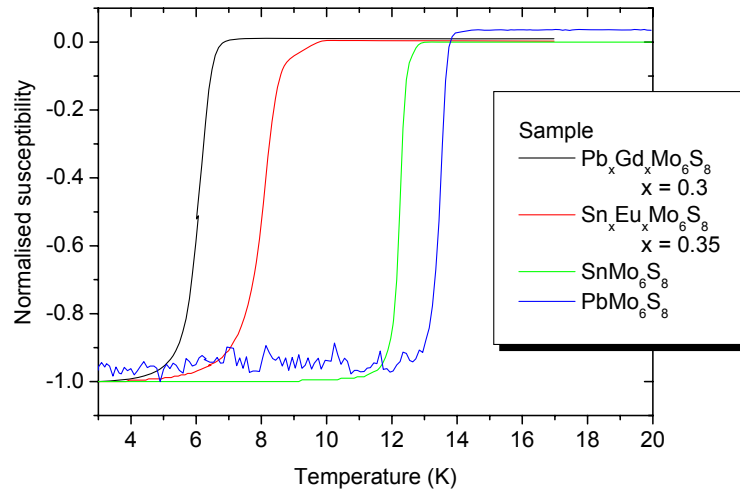
Figure 3.31 Normalised magnetic moment as a function of temperature of the Chevrel phase superconductors $Pb_{1-x}Gd_xMo_6S_8$ x = 0.3, $Sn_{1-x}Eu_xMo_6S_8$ x = 0.35, $SnMo_6S_8$ and $PbMo_6S_8$. Samples were measured using the AC susceptibility (ACMS) mode of a Quantum Design physical properties measurement system (PPMS). Data are normalised and were collected as a function of temperature in zero external field.
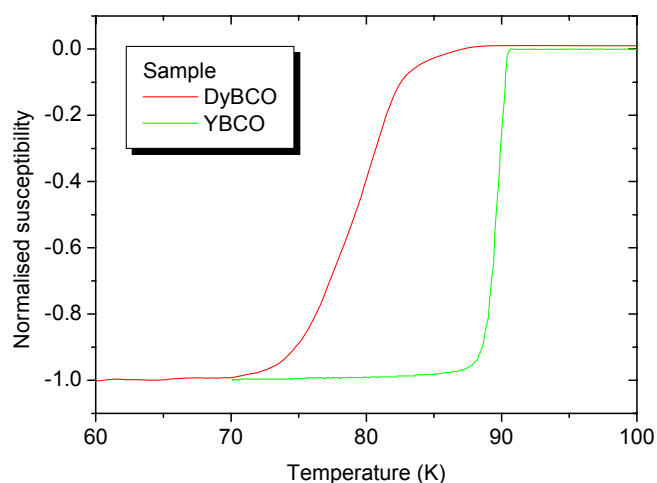
Figure 3.32 Normalised magnetic moment as a function of temperature of YBCO and DyBCO single crystal samples. Samples were measured using the AC susceptibility (ACMS) mode of the Quantum Design physical properties measurement system (PPMS). Data were collected as a function of temperature in zero external field.

Sample	Resistivity			Heat Capacity	Magnetic Moment		
	10%	**50%**	**90%**	**50%**	**10%**	**50%**	**90%**
Nb	8.1 K	8.6 K	8.8 K	-		-	-
YBCO	-	-	-	89.5 K	88.6 K	89.7 K	90.3 K
DyBCO	-	-	-	-	74.8 K	79.1 K	82.6 K
$PbMo_6S_8$	14.2 K	14.5 K	14.8 K	14.3 K	13.0 K	13.5 K	13.6 K
$Pb_{1-x}Gd_xMo_6S_8$ x=0.3	7.5 K	7.9 K	8.4 K	5.49 K	5.4 K	6.03 K	6.5 K
$SnMo_6S_8$	12.7 K	12.8 K	13.0 K	-	11.9 K	12.2 K	12.4 K
$Sn_{1-x}Eu_xMo_6S_8$ x=0.35	9.2 K	9.6 K	10.0 K	-	7.0 K	8.0 K	8.6 K

Table 3.2 Summary of superconducting transition temperatures, T_C, measured by resistivity, heat capacity and AC susceptibility techniques. Temperatures are stated for T_C (10%), the midpoint of the transition, T_C(50%) and T_C(90%).

The critical temperatures measured using the three techniques are within 2 K for all samples. The differences result predominantly from inhomogeneities in the sample. Heat capacity and magnetic moment techniques measure the bulk properties of the superconductor. Resistivity measures a percolative path through the superconductor which results in a higher critical temperature being observed using this technique.

3.5. Conclusions

This chapter has given details of the operation of three pieces of commercial hardware for the measurement of optical, electrical and magnetic properties of metals and superconductors. The advantages and disadvantages of the Jobin Yvon Flurolog 3-22 spectrofluorometer and J.W. WVASE series ellipsometer have been discussed and the reliability of data examined.

The Jobin Yvon Fluorolog 3-22 spectrofluorometer was found not to be suitable for the measurement of photoluminescence from samples with low intensity photoluminescence emission due to its low excitation power and large background.

Optical constants for gold and copper, the high temperature superconductors YBCO and DyBCO and the Chevrel phase superconductors $PbMo_6S_8$ and $SnMo_6S_8$ were measured using the J.A. Woollam WVASE series ellipsometer. The limitations of the technique for the measurement of rough, bulk samples with low reflectivities and unknown surface structure have been discussed.

Finally, the critical temperatures of a range of superconducting samples have been measured and confirmed using the resistivity, heat capacity and AC susceptibility modes of the Quantum Design PPMS – prior to the detailed optical measurements that are the basis of this thesis.

Chapter 4. Design of an instrument for measuring low intensity, variable temperature photoluminescence emission

4.1. Introduction

Chapter 3 discussed the failure of commercial spectroscopy equipment to measure the photoluminescence emission spectra of metals and superconductors. Their limitation was the requirement for higher excitation powers and carefully selected optical components to measure the weak emission spectra. This chapter discusses the design, commissioning and calibration of an instrument capable of measuring low intensity photoluminescence emission spectra as a function of temperature.

The following sections consider the experimental set-up, excitation source, components and detector selection for low intensity emission spectra, where sample luminescence intensity must be maximised without producing significant luminescence from sources other than the sample. The cryogenic hardware and optimisation of sample cooling and thermometry is examined and considerations for sample holder designs are discussed in terms of thermal and optical requirements. Detailed analysis and measurement of the sample temperature and the effect of laser heating are presented. External hardware and software is summarised before different techniques for mounting the sample are investigated for their thermal and optical benefits. Finally, calibration tests and measurements are carried out to enable measurement accuracy to be determined.

4.2. Optical hardware

4.2.1. Experimental Setup

Figure 4.1 is a schematic representation of the experimental set-up for the variable temperature photoluminescence instrument. Optical excitation of the sample was carried out using an argon ion (Ar^+) laser capable of lasing at 488 nm and 514 nm. Using the 488 nm wavelength, excitation powers of up to 120 mW were achievable at the sample. The laser was focussed onto the sample using a series of mirrors and a fused silica lens (L_1 in Figure 4.1). Light was incident on the samples at approximately 30 degrees to the normal. The sample was attached to a custom designed copper sample holder inside a pulse tube refrigerator cryostat for variable temperature measurements.

Photoluminescence (PL) emission was collected by optics aligned along an axis perpendicular to the sample surface. This configuration reduced the intensity of elastically scattered light entering the collection optics. A microscope objective (labelled Ob in Figure 4.1) positioned directly outside the cryostat collected and collimated PL emission. Once collimated, the emission passed through a dichroic filter (F_1 in Figure 4.1), removing any remaining elastically scattered laser light. The collimated PL emission was subsequently focussed on to the spectrometer and silicon photodiode array detector (Figure 4.1).

Prior to measuring photoluminescence emission spectra, a mirror (M_1 in Figure 4.1) was inserted between the focussing lens and spectrometer. The mirror reflected the sample image onto a CCD camera which was used to reposition the sample to correct for thermal contraction during variable temperature measurements.
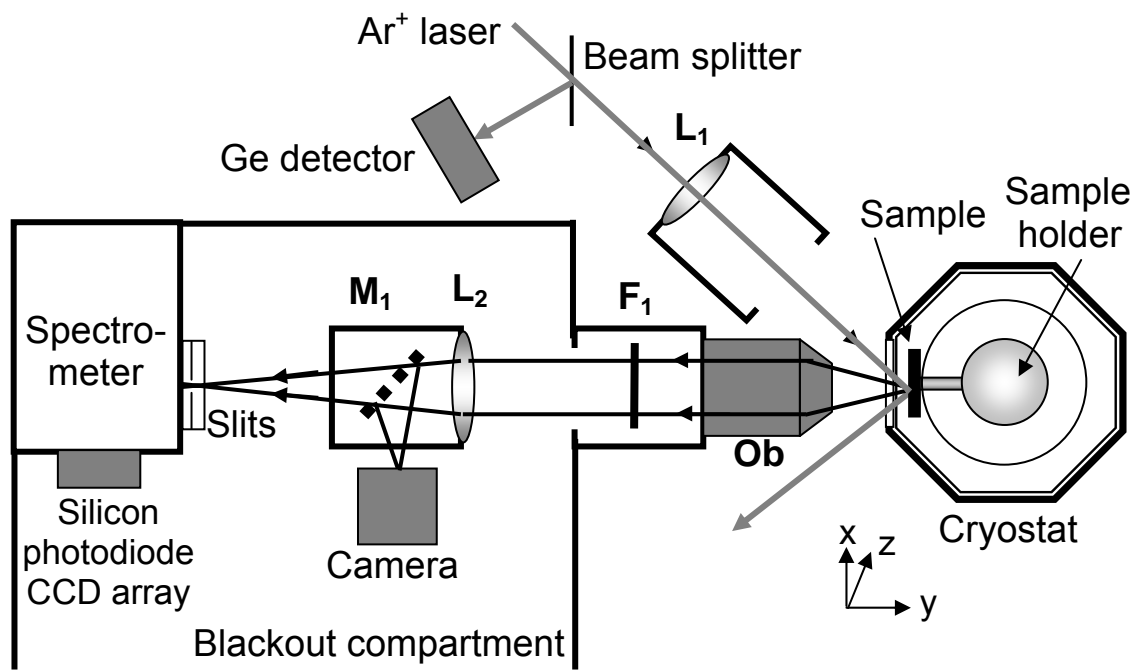
Figure 4.1 Schematic diagram of the instrument for measuring low intensity photoluminescence emission. Light from the argon ion laser (Ar$^+$) passes through a beam splitter where part of the beam is diverted on to the germanium detector (Ge detector). The light then passes through a fused silica lens (L_1) and is focussed through the cryostat window on to the sample. Emission from the sample is collected by the microscope objective (Ob) and collimated. The emission then passes through a dichroic filter (F_1) and is focussed on to the slits of the spectrometer by a second fused silica lens (L_2) where it is monochromated by the spectrometer and measured by the silicon photodiode CCD array. For alignment of the sample during variable temperature measurements, a mirror (M_1) is placed between lens L_2 and the spectrometer slits to image the sample using a CCD camera.

Data were collected using National Instruments LabVIEW software on a PC. The original software was written by a previous student (Martin Archbald) but was significantly modified for the purposes of this work. Figure 4.2 shows the component parts of the photoluminescence experimental setup broken down into the areas which will be discussed below.
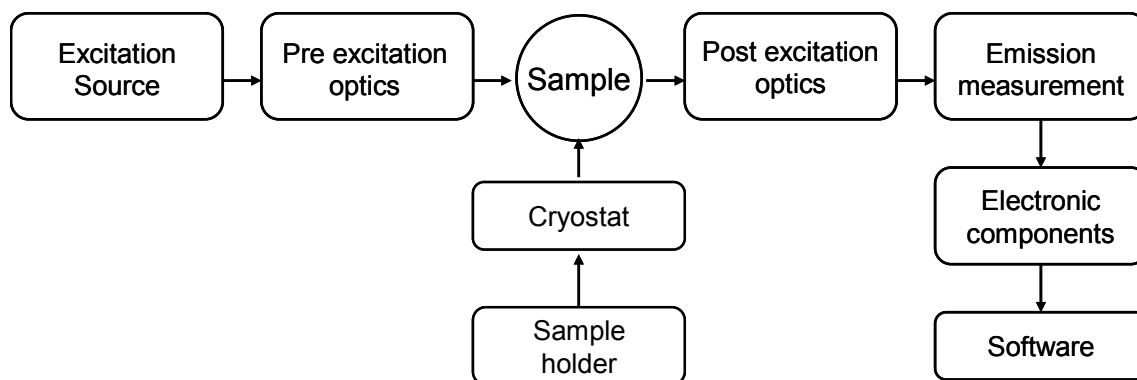
Figure 4.2 Component parts of the instrument for measuring low intensity, variable temperature photoluminescence emission.

4.2.2. Excitation source

Excitation source selection

Three key specifications were required from the excitation source: The excitation energy of the source had to be greater than the interband transition energy; The power of the source had to be sufficient to produce luminescence of an intensity great enough to be detectable but not so high as to damage the sample; Finally, the shape of the light emitted from the source had to be capable of being focussed on to the sample.

We considered excitation sources at UV wavelengths for samples with larger interband transition energies. UV LED's from UltraLED.co.uk with peak emission at 410 nm were tested. However, the emission from the LED's was diffuse and the intensity was too low to excite observable emission intensities. A xenon lamp was also investigated but the power found to be too low for observable sample photoluminescence emission intensities. A third choice considered was a UV laser emitting at 405 nm with 30 mW power at the diode. However, the only effective method found for eliminating elastically scattered laser light in the emission spectrum was using a double monochromator which

reduced the intensity of the samples' photoluminescence emission to below the resolution of the detector.

A Coherent Innova 90 argon ion (Ar+) laser was eventually chosen as the excitation source as it satisfied all requirements. Up to 120 mW of power was obtainable from the laser at either 488 nm or 514 nm. The laser was retuned between each batch of measurements to maintain optimum power output.

Optimisation of laser power, stability and wavelength

The stability of the power of the Ar^+ laser was strongly dependent upon the temperature of the laboratory and the duration of operation. Laser power varied on two time scales. The first was a gradual change over a period of hours, which was shown to be strongly dependent upon room temperature. The second was over a period of minutes or seconds and was dependent upon the tuning and duration of operation of the laser.

Variation in laser power due to changes in room temperature was almost completely removed by setting the central heating and air conditioning in the laboratory to constant. Short time period fluctuations were reduced, but not removed, by regular tuning of the laser and operation of the laser in light regulating mode rather than current regulating mode. To correct for any remaining fluctuations, laser power was continuously monitored using a germanium photodiode detector (Ge detector in Figure 4.1). The voltage output from the Ge detector was calibrated for laser power on each day of measurements by manually increasing laser power and measuring power using a Melles Griot Handheld Power Meter located between the fused silica lens (L_1 in Figure 4.1) and cryostat window. All variable temperature photoluminescence data in this thesis have been corrected for changes in laser power and are presented in units of counts s^{-1} W^{-1}.

4.2.3. Optical Components

High intensity laser light passing through the optical components inevitably produces luminescence. This emission can be of high enough intensity to mask or be confused with the sample photoluminescence emission. The optical components in the instrument discussed below were chosen to minimise photoluminescence of the components themselves, particularly those directly in the path of the collection optics.

Pre-excitation optical components

The excitation laser beam was focussed to a tight spot on the sample using a 25 mm focal length fused silica lens (labelled L_1 in Figure 4.1). A beam splitter positioned before L_1 redirected a fraction of the laser beam on to a germanium detector (c.f. Figure 4.1). Laser power was continuously monitored using the voltage output of the germanium photodiode detector.

Post excitation collection optics

Photoluminescence emission was collected along the normal axis of the sample surface. This geometry maximised rejection of the scattered laser line in the collected photoluminescence emission. The post excitation optical pathway was enclosed to reduce the influence of external light sources on the photoluminescence emission spectrum.

Photoluminescence emission from the samples was collected using an Olympus UPLSAPO 4 x microscope objective of numerical aperture 0.16 and a working distance of 13 mm. The objective was selected for the low fluorescence of its component materials [156], however, the optics still luminesced if laser light directly reflected from the cryostat window entered the objective. A working distance large enough to locate the objective lens beyond the region of reflected light was required, but was not

commercially available. Therefore, the collection optics were moved back from the cryostat window by a few millimetres, away from the optimum working distance of the objective, when measuring photoluminescence emission spectra. To confirm that this did not affect the measured photoluminescence emission spectra, the sample spectrum was measured at the optimum working distance of the microscope objective without the cryostat window in place, with the objective moved away from the sample without the cryostat window, and with the window in place. All spectra were found to be identical other than a slight decrease in photoluminescence emission intensity at the defocused position and with the cryostat window in place.

Dichroic filter

Because the samples were not perfectly smooth, the intensity of the elastically scatted laser light passing through the collection optics was high, and many thousands of times stronger than the photoluminescence emission intensity of the samples. Therefore, the laser light was of high enough intensity to saturate the detector. To solve this problem, a filter (F_1 in Figure 4.1) was placed in the post excitation optical pathway to remove the remaining laser light.

In preliminary work, low-pass coloured glass filters were used to remove the scattered laser light. These filters absorb incident light at wavelengths shorter than their cut off energy. However, due to the almost perfect absorption at the laser excitation wavelength, these filters display high luminescence intensities which completely obscured the sample photoluminescence signal. Therefore, to minimise external luminescence sources, a reflecting rather than absorbing filter was selected.

A Semrock RazorEdge® Long Wave Pass Raman dichroic filter was chosen to reject the laser light as it has a sharp cut off wavelength (Figure 4.3). The filter is
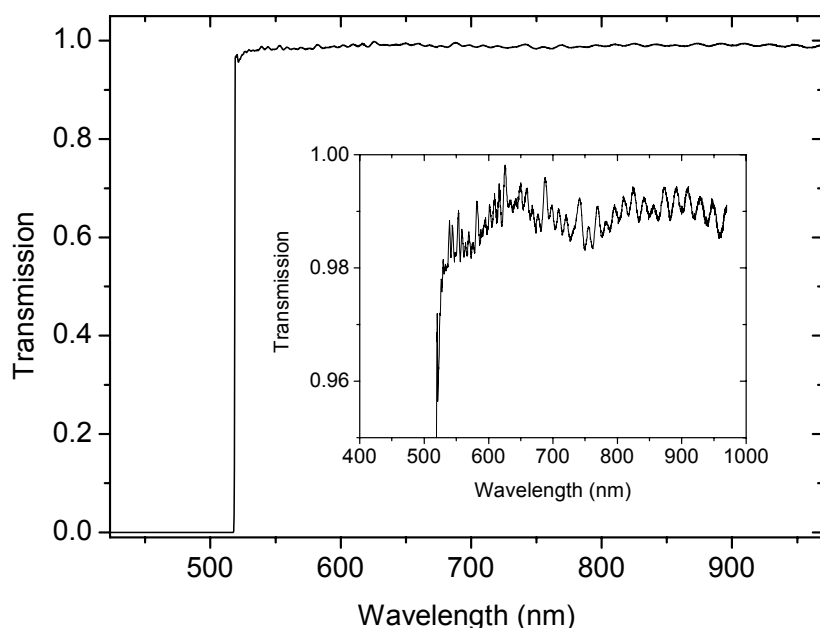
Figure 4.3 Transmission spectrum of the Semrock RazorEdge® Long Wave Pass Raman dichroic filter. Transmission spectrum data quoted from the manufacturer's website. [157]

composed of a series of thin film layers deposited by ion beam sputtering onto a fused silica substrate [158, 159]. The disadvantage of such a filter is that the maximum angle of incidence for light rejection is 5°, which in some cases was less than the angular distribution of scattered light from the sample surface. The only method of reducing this effect was to place the filter directly after the collimating objective. However, this increased the potential for luminescence from the objective lens.

Focussing optics

Photoluminescence emission was focussed onto the spectrometer slits using a UV grade fused silica lens (Labelled L_2 in Figure 4.1). The f number of the lens was matched to the spectrometer dimensions to ensure complete filling of the spectrometer grating (aperture ratio f/4.1) [160].

4.2.4. Emission measurement

Spectrometer

After collection and collimation of the photoluminescence emission, the light was focussed onto the entrance slits of the Bentham TM300V multiple grating monochromating spectrometer (labelled spectrometer in Figure 4.1). The grating within the spectrometer dispersed the spectrum of the photoluminescence emission across the width of the 25 mm silicon photodiode CCD array (labelled silicon photodiode CCD array in Figure 4.1) which was mounted to the exit slits of the spectrometer.

Three array gratings were available within the spectrometer with 150, 400 or 1200 lines per inch. The greater the number of lines per inch, the smaller the spectral range dispersed across the 25 mm CCD array. The 150 line grating was used in preference to the 400 and 1200 line gratings as a single photoluminescence emission spectrum could be measured which covered the full wavelength range of interest. The wavelength response of the grating was taken into account in the correction factors during the analysis of the data.

The separation between the slits at the entrance to the spectrometer (slit width) affected the intensity of light collected (and hence signal to noise ratio) and resolution of the peaks in the spectra. Wider slits gave better signal to noise ratio but poorer wavelength resolution. The slit width of the spectrometer was kept constant at 1.50 mm for all measurements.

A filter wheel at the entrance to the spectrometer rotated a shutter into the optical pathway for background measurements of detector noise.

Silicon diode CCD array

Photoluminescence spectra were measured using an EG&G PARC 1024 element large aperture silicon photodiode CCD array with specified detection limits of 180 nm to 1100 nm. The manufacturer's specification stated a typical efficiency of 1960 photons per count at 550 nm. A maximum of 32 768 counts in any one reading was measurable before saturation of the detector. A dark count of 100 counts per second was achieved with the detector cooled to -20$^\text{o}$C. Cooling was provided by a two-stage Peltier-effect thermoelectric cooler which required a continuous flow of dry nitrogen and chilled water. Increasing measurement time linearly increased count rate, however, the detector dark noise also scaled linearly with detection time. A background scan of detector dark noise was measured then subtracted from each PL spectrum. The non linear spectral response of the detector was corrected for during analysis of the data.

Dark conditions

Due to the low photoluminescence emission intensities of metals and superconductors, even minimal background light was prominent in the measured spectra. Several important changes were made to the equipment to ensure dark conditions for the measurement; an enclosure was constructed surrounding the collection optics and entrance to the spectrometer, all measurements were run with the computer monitor and room lights off and instrument dials and switches were positioned out of the line of sight of the detector

Optimisation of photoluminescence emission intensity

Photoluminescence intensity was maximised at each temperature by removing the dichroic filter and focusing the laser light scattered from the surface of the sample on to

the slits of the spectrometer. The filter was then replaced and the horizontal and vertical alignment of the collection optics adjusted to maximise the intensity of the measured photoluminescence emission.

4.3. The Cryomech Cryostat

4.3.1. Cryostat design and improvements

Hardware

Measurements of PL emission spectra as a function of temperature were conducted using a cryogen free Cryomech ST405 pulse tube refrigerator (Figure 4.4). The cryostat provides approximately 0.3 W of cooling power at a base temperature of 3 K. Optical access to the sample space is via a 50 mm diameter, 3mm thick, Spectrosil 2000 fused quartz window. The sample chamber of the cryostat is under vacuum so that the cryostat walls remain at room temperature throughout the experiment with the sample holder thermally shielded from room temperature radiation using multiple layers of superinsulation and an aluminium radiation shield.

Vacuum system

A rotary pump and diffusion pump were connected to the cryostat and were capable of reaching a base pressure of 2×10^{-4} mbar when connected to the sample space. Extensive tests were carried out to ensure that there were no leaks within the vacuum system and o-ring seals and valves were maintained on a regular basis to ensure that perishing of rubber components did not degrade the vacuum. It is essential to have a good vacuum or three problems arise: an increase in sample base temperature due to the

thermal link between the walls and the sample holder increasing the heat load on the cryocooler; the layers of superinsulation are not thermally insulated from one another at pressures higher than 6 x 10^{-4} mbar [161] and the possibility of condensation of gases onto the surface of the sample at low temperatures. We note that it was important to ensure that sufficient time was given for the spaces between the superinsulation layers to be evacuated and all of the layers to reach thermal equilibrium whilst cooling samples.
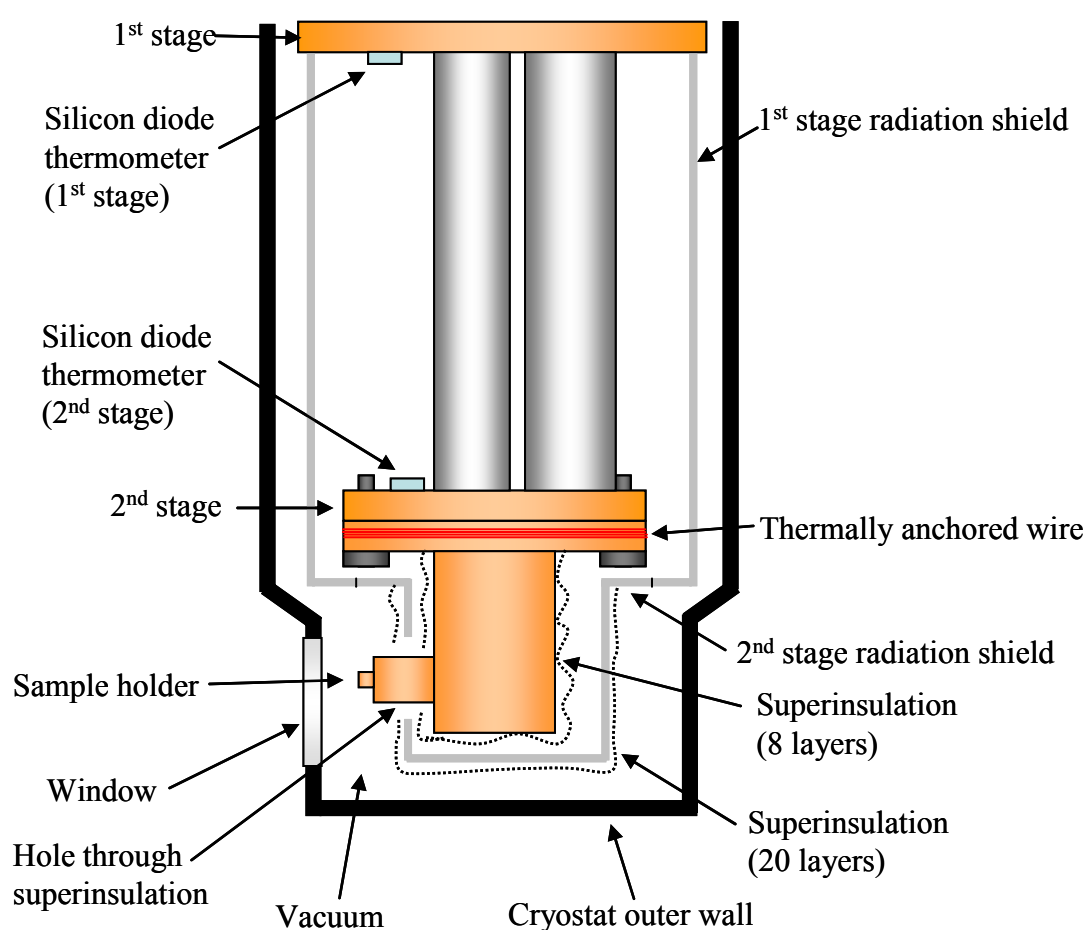

Figure 4.4. Schematic diagram of the components within the Cryomech cryostat and sample holder. The diagram shows the sample holder in vacuum surrounded by superinsulation and a radiation shield. Wiring for thermometry and resistance measurements is thermally anchored into a groove in the sample holder filled with GE varnish.

Radiation shielding improvements

Two cold stages are present within the cryostat (Figure 4.4). The 1st stage typically operates at temperatures between 65 K and 35 K and the 2nd stage between 300 K and 3 K. A two section polished aluminium radiation shield is attached to the 1st stage. The first section covers the area between the 1st and 2nd stage cold head and the second section surrounds the sample space area at the base of the cryostat.

We added additional shielding by inserting layers of single sided aluminiumised Mylar superinsulation. Twenty layers of superinsulation were added between the outer wall of the cryostat and the outside of the radiation shield with an additional 8 layers between the sample holder and radiation shield. A hole was produced between the sample holder, radiation shield and outer superinsulation so that the arm of the sample holder protruded through the radiation shield (Figure 4.4). The superinsulation was wrapped loosely and crinkled to minimise surface contact between layers, reducing thermal conduction between layers. The maximum recommended density of superinsulation layers was 30 layers per centimetre [162]. We found an increase in base temperature of 5 K when the superinsulation was wrapped too tightly.

Vibration of the cryostat

Motion of the sample from vibrations created by the pulse tube refrigerator was observable through the alignment CCD camera. Although, the pulse tube produces the lowest mechanical vibration of all cryogen-free cooling techniques, movement of the sample in a circular motion of approximately 100 μm diameter was observable. Vibrations from the pulse tube did not significantly affect the accuracy of the measurements since the distance moved during the vibration was less than the diameter of the laser spot on the sample.

Thermal anchoring of thermometers and wiring

The silicon diode thermometers were thermally anchored to the 1st and 2nd stage cold heads using a small bobbin of thermometer wire wrapped and epoxied around the thermometer. A small layer of grease was placed between the thermometer bobbin and the cryostat cold head and the bobbin screwed into place to ensure optimum contact. Good practice was followed for thermally anchoring wiring. For example, wiring for the sample temperature calibration resistivity measurements was thermally anchored using GE varnish in a groove in the bulk of the copper sample holder. This method ensured that the wiring was in thermal equilibrium with the local environment.

4.4. Sample holder design

4.4.1. Considerations for sample holder design

Standard commercial sample holders for cryogenic applications clamp the sample between metal plates which are anodised or coated in a layer of paint. Preliminary measurements found that photoluminescence emission from these materials was excited by scattered laser light within the cryostat. The intensity of photoluminescence emission from the holder, paints, plastics and adhesives was several orders of magnitude greater than that of the metals and superconductors and masked the sample signal.

To prevent excitation and measurement of photoluminescence from the sample holder, a shield was constructed from a silicon wafer to block scattered light from the region around the sample. Silicon was chosen as the shield as it was readily available, rigid, flat and luminesced at 1000 nm, which was outside of the wavelength measurement range. Unless directly illuminated, the luminescence spectrum of silicon showed no

signal at energies other than the band gap. Two samples holders were designed – one for angular measurements at room temperature and one for cryogenic measurements which are considered below in turn.

4.4.2. Room temperature sample holder for angular measurements

To determine the contribution of photoluminescence of optical components to the sample photoluminescence emission spectrum, a rotating sample holder with degree precision was constructed. The design consisted of an aluminium post with inset step mounted to a rotatable optics holder with degree gradations. The sample was mounted to a silicon wafer and attached to the step as shown in Figure 4.5. The sample was rotated through $\sim 30^o$ in 1 degree increments until laser light was reflected from the sample surface directly into the microscope objective. The change in the measured photoluminescence emission spectrum was attributed to the luminescence of the optical components.
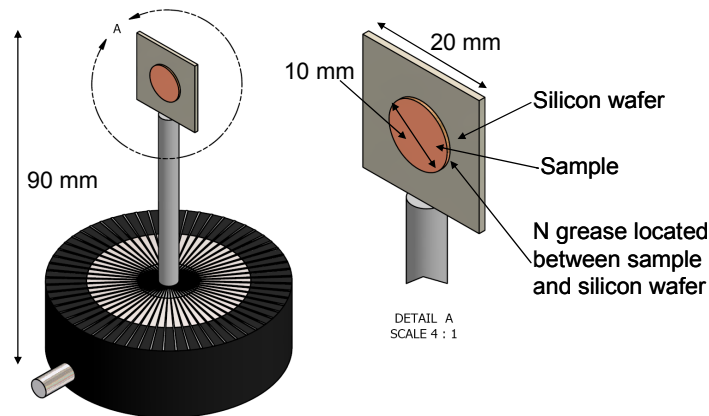

Figure 4.5. Room temperature sample holder designed for photoluminescence measurements as a function of angular rotation. The sample is attached to the silicon wafer using Apiezon N grease or double sided copper adhesive tape. The silicon wafer is then attached to the aluminium rod using adhesive tape. The sample can be rotated with 1 degree precision using the markings on the base.

4.4.3. Sample holder for cryogenic measurements

Thermal requirements

The standard design of cryostat sample holders positions the sample in the centre of the cryostat. However, the low intensity photoluminescence emission from metals and superconductors required the collection optics positioning within the working distance of the microscope objective, 13 mm from the sample surface. This means that the sample is located outside the radiation shield where it absorbs both the intense laser power and room temperature radiation. Therefore, a new sample holder was necessarily designed and commissioned for these measurements.

Thermal contact between the cold stage and the sample

Heat conduction across joints between the cold head, sample holder and sample is a very significant factor in determining the base temperature of the sample. As is standard good practice, Apiezon N grease or GE varnish were used to attach the samples and thermometers to the sample holder, although their thermal conductivity is 10^5 times lower than copper. In order to maximise the thermal contact between the sample and the cold stage the number of joints was minimised, surface area of contact faces was increased and the different components at joints were connected as well as possible.

The joint between the 2nd stage cold head and the sample holder was bolted together to ensure tight contact between the copper plates. A thin layer of silicone grease ensured that any small imperfections in the smoothness of the surface would not significantly affect contact area.

The thermal conductance of the sample holder was maximised by minimising the number of joints between the 2nd stage cold head and the sample, maximising the bulk of the sample holder and matching the contact area between the sample holder and the cold

head. Copper was chosen as the sample holder material for its excellent thermal conductivity. The maximum weight of the sample holder could not exceed 2.26 kg (as specified by the manufacturer [161]) before damage occurred to the pulse tube. A protrusion of copper through the silicon shield directly contacted the sample with the sample holder (Figure 4.6). This design reduced the number of joints to two, one between the cold head and top of the sample holder and one between the sample and sample holder. A thin layer of grease was applied at each joint to optimise thermal contact.

Table 4.1 and Figure 4.7 detail the improvements to the base temperature of the sample holder using the different designs of sample holder. Temperature was measured using a platinum resistance thermometer attached in the position of a sample.
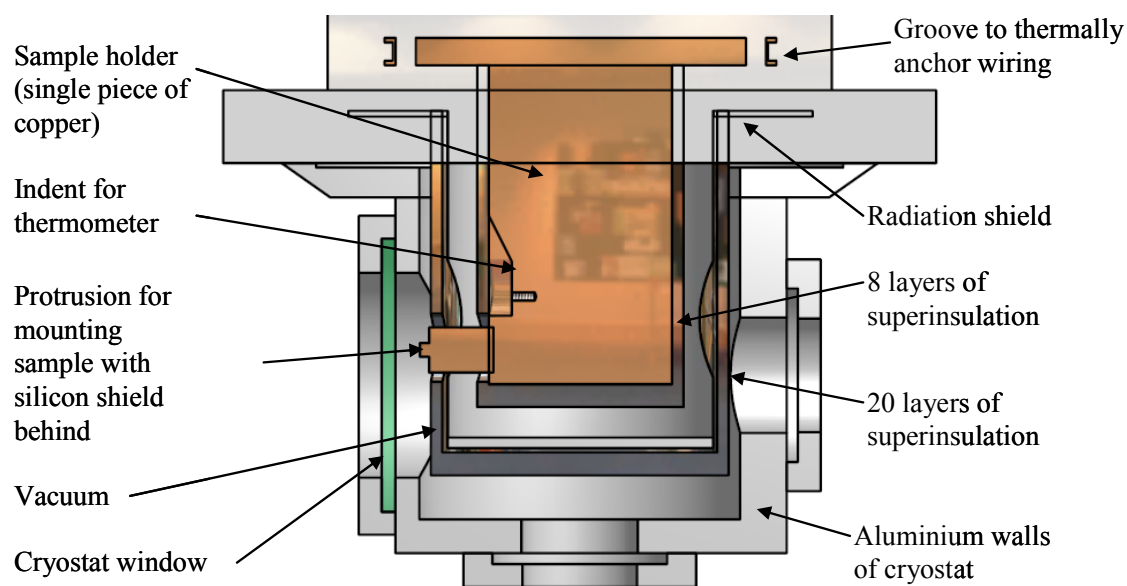

Figure 4.6. Final design of the sample holder for measurement of photoluminescence as a function of temperature. The drawing shows the position of the sample holder relative to the cryostat window and walls inside the Cryomech cryostat. The radiation shield and superinsulation are also shown on the diagram.
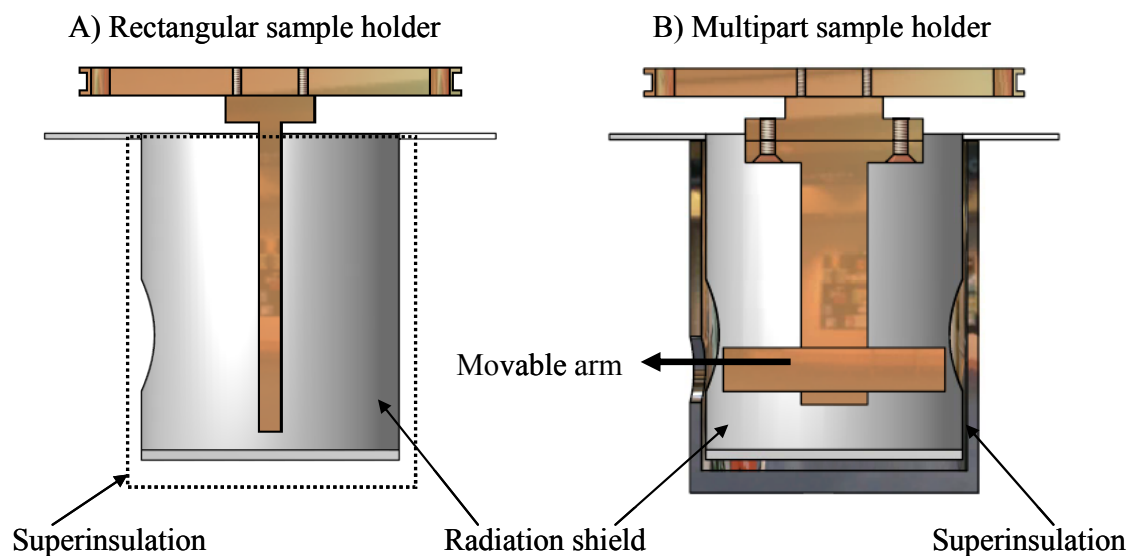
Figure 4.7. Schematic diagram of sample holder designs. A) Rectangular sample holder, B) Multipart sample holder. Also shown on the diagram is the location of the superinsulation and radiation shield.

Thermal contraction and repositioning of the sample

Thermal contraction of the copper sample holder during cool down led to movement of the sample by up to 1 mm between 300 K and 3 K. This changed the alignment of the luminescence emission relative to the collection optics. The effect was observable over a 300 K temperature range as a 5 mm horizontal movement of the focussed spot of the unfiltered scattered laser light across the slits of the spectrometer.

Alignment of the sample was maintained using a QImaging Retiga 1300 CCD camera (labelled camera in Figure 4.1) focussed backwards through the collection optics using a removable mirror (labelled M_1 in Figure 4.1). For repositioning the sample at each temperature, the post-excitation optics were aligned at the optimum working distance of the microscope objective, where the image of the sample on the camera was in focus.

Figure 4.7 Drawing reference		Experimental setup	Base temperature
A		**Rectangular sample holder**	
	i	No optical access – 4 layers of superinsulation and radiation shield	14 K
	ii	No optical access – 20 layers of superinsulation and radiation shield	10 K
	iii	Superinsulation removed – only radiation shield with wide optical access	39 K
B		**Multiple section sample holder – bolted + greased connection to Cryomech cryostat 2nd cooling stage**	
	i	No optical access - 20 layers superinsulation and radiation shield	5 K
	ii	1.5 cm diameter optical access – thermometer inside radiation shield and 20 layers of superinsulation	10 K
	iii	1 cm diameter optical access – thermometer outside radiation shield and 20 layers of superinsulation	15 K
	iv	Thermometer wiring inset in groove - 1 cm diameter optical access – thermometer outside radiation shield and 20 layers of superinsulation	12 K

Table 4.1 Changes in sample base temperature for various sample holder designs. The base temperature was measured by a platinum resistance thermometer in the location of the sample.

Manual repositioning of the sample to within a few microns was accomplished using a mask over the CCD camera image on the computer monitor showing features on the sample surface. The sample position was adjusted using an x – z translation stage to bring the camera image of the sample back into alignment with the mask on the monitor.

Contraction of the sample holder was primarily in the y direction between 300 K and 250 K. A translation stage located inside the cryostat was trialled to correct for motion in the y direction (Figure 4.8). However, the thermal load of the control rod, which protruded through the cryostat casing, increased the base temperature of the cryostat to 100 K. Therefore, although the sample holder constructed of a single piece of copper lacked the flexibility of the y translation stage design, the improved base temperature was preferable.
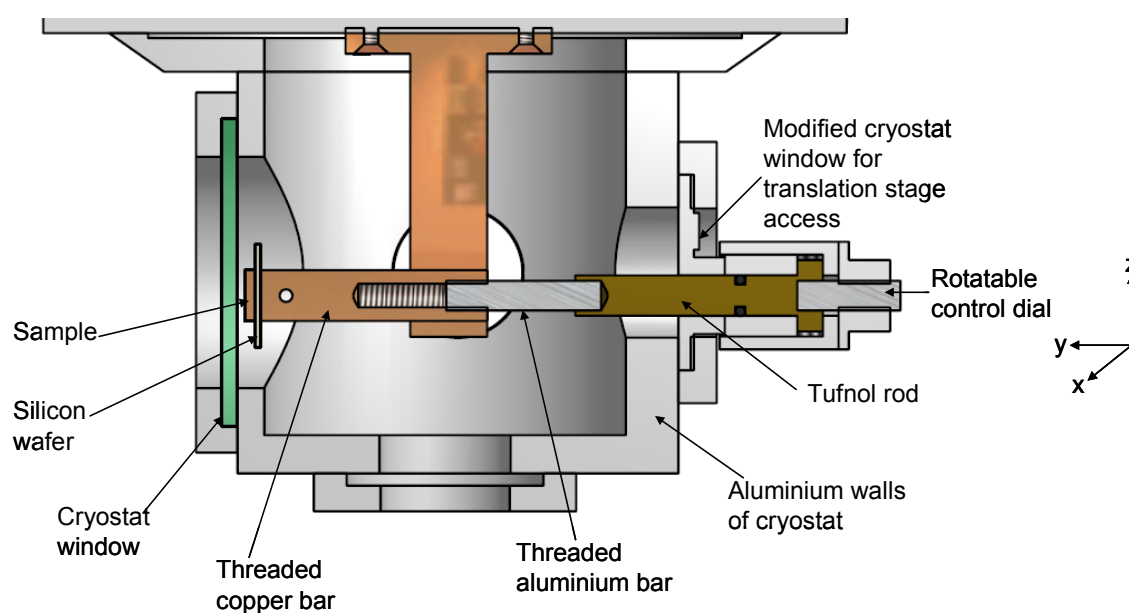
Figure 4.8. Design of the y direction translation stage located within the Cryomech cryostat. The translation stage arm was constructed from aluminium, tufnol and copper. Rotation of the end of the arm, outside the cryostat moved the sample towards or away from the cryostat window within a hole through the vertical section of the sample holder. Silicone grease between the vertical section and the movable threaded copper bar improved thermal conduction through the holder.

4.5. Thermometry

Sample temperature measurement

Calibration of sample temperature was carried out by comparing electrical resistance measurements as a function of temperature in the variable temperature bore of the Quantum Design Physical Properties Measurement System (PPMS) and the Cryomech optical cryostat with and without laser illumination. Accurate measurement of resistance as a function of temperature for niobium, DyBCO and $PbMo_6S_8$ was carried out using the AC Transport mode of the PPMS. However, the low resistance of copper required a custom nanovolt precision probe which was constructed to enable measurement of resistances down to 1×10^{-7} Ω.

The custom nanovolt precision probe used twisted pairs of current and voltage wires. Each wire was a single piece with no joints between the sample and a nanovolt amplifier. Application of current in a delta mode pattern (alternating positive and negative current) eliminated the effects of thermal voltages.

The nanovolt precision measurements were repeated in the Cryomech optical cryostat for all four samples using the sample holder arrangement used for photoluminescence measurements. All wiring was thermally anchored to the sample holder to ensure that the wiring was in thermal equilibrium with the sample. Resistance was measured as a function of the cryostat's second stage cold head temperature. The resistance vs temperature scans with and without laser illumination were then compared to the measurements made in the PPMS to calibrate actual sample temperature against the Cryomech optical cryostat second stage cold head temperature.

To eliminate the possibility of contamination of the luminescence signal with remnants of voltage and current contacts, all photoluminescence measurements were made prior to the resistance measurements.

4.6. External hardware and software

4.6.1. External hardware

Function of the electronics

Figure 4.9 is a schematic representation of the electronic components interfacing the PC to the cryostat and detectors. One Keithley 2000 Digital Multimeter was used to measure the output from the Ge detector. A second Keithley 2000 Digital Multimeter together with Keithley 220 current source was used to make the four point resistance measurement of the samples for temperature calibration.

The cryostat temperature was controlled and measured by a Model 9650 Scientific Instruments Digital Temperature Controller which provided a voltage output to heaters in the cold head which worked against the cooling power of the pulse tube refrigerator.

The output from the silicon diode array CCD detector was detected using an EG&G PARC model 1471A detector which was monitored by the PC. A Bentham Mono Stepping Drive set the central wavelength of the spectrometer grating and hence fixed the wavelength range measured by the silicon diode array CCD detector. Two stepper motors were each driven by PDFX series drives to position the x – z translation stage of the cryostat. General Purpose Interface BUS (GPIB) and Recommended Standard 232 (RS232) connections coupled all the hardware to the PC. A National

```
                    ┌─────────────────────────────┐
                    │   Equipment on optical bench │
                    └─────────────────────────────┘
                                   │
                                   ▼
┌──────────────────────────┬──────────────────────────┬──────────────────────────┐
│      Thermometry         │    Detector interface    │    Translation stage     │
│  ┌────────────────────┐  │  ┌────────────────────┐  │  ┌────────────────────┐  │
│  │   Keithley 2000    │  │  │   EG&G Princeton   │  │  │  Parker PDFX Series │  │
│  │       DMM          │  │  │ Applied Research   │  │  │ Stepper motor driver│  │
│  ├────────────────────┤  │  │ Detector Interface │  │  └────────────────────┘  │
│  │   Keithley 220     │  │  │    Model 1471A     │  │  ┌────────────────────┐  │
│  │  Current supply    │  │  └────────────────────┘  │  │  Parker PDFX Series │  │
│  └────────────────────┘  │  ┌────────────────────┐  │  │ Stepper motor driver│  │
│  ┌────────────────────┐  │  │   Bentham Mono     │  │  └────────────────────┘  │
│  │    Keithley        │  │  │  Stepping Drive    │  ├──────────────────────────┤
│  │   2000 DMM         │  │  └────────────────────┘  │    Laser monitoring      │
│  └────────────────────┘  │                          │  ┌────────────────────┐  │
│  ┌────────────────────┐  │                          │  │     Keithley       │  │
│  │Scientific Instruments│ │                          │  │    2000 DMM        │  │
│  │Digital Temperature │  │                          │  └────────────────────┘  │
│  │   controller       │  │                          │                          │
│  │   Model 9650       │  │                          │                          │
│  └────────────────────┘  │                          │                          │
└──────────────────────────┴──────────────────────────┴──────────────────────────┘
                                   │
                                   ▼
                    ┌─────────────────────────────┐
                    │ PC via GPIB or RS232 interface │
                    └─────────────────────────────┘
```
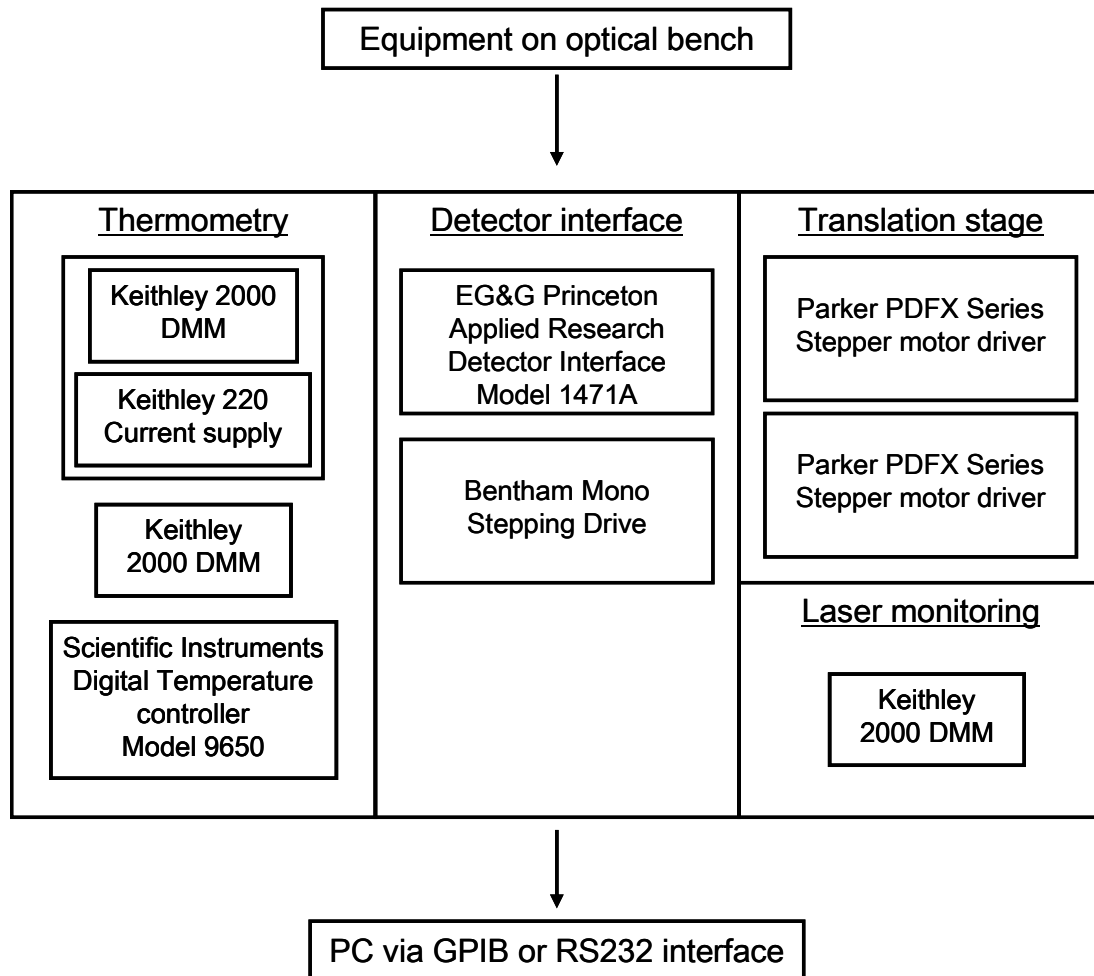
Figure 4.9 Schematic diagram of electronic equipment for interfacing between optical bench equipment and computer control software. DMM stands for Digital Multimeter.

Instruments GPIB card was installed in a PCI slot on the PC to enable control of the hardware and data logging in LabVIEW software.

4.6.2. Software

LabVIEW

Control and logging of data from the experiment was conducted using National Instruments LabVIEW 7 software. The easy adaptability of the program with simple interfacing of hardware meant that the software could be modified quickly to automate

the experiment and log data to file with the benefit of a visual representation of data in the front end of the software (Figure 4.10).

Additions to the original program included; temperature batch scanning, laser power measurement, measurement of laboratory temperature, automatic background scanning during batch measurements and the ability to make repeat measurements with set waiting times between scans.
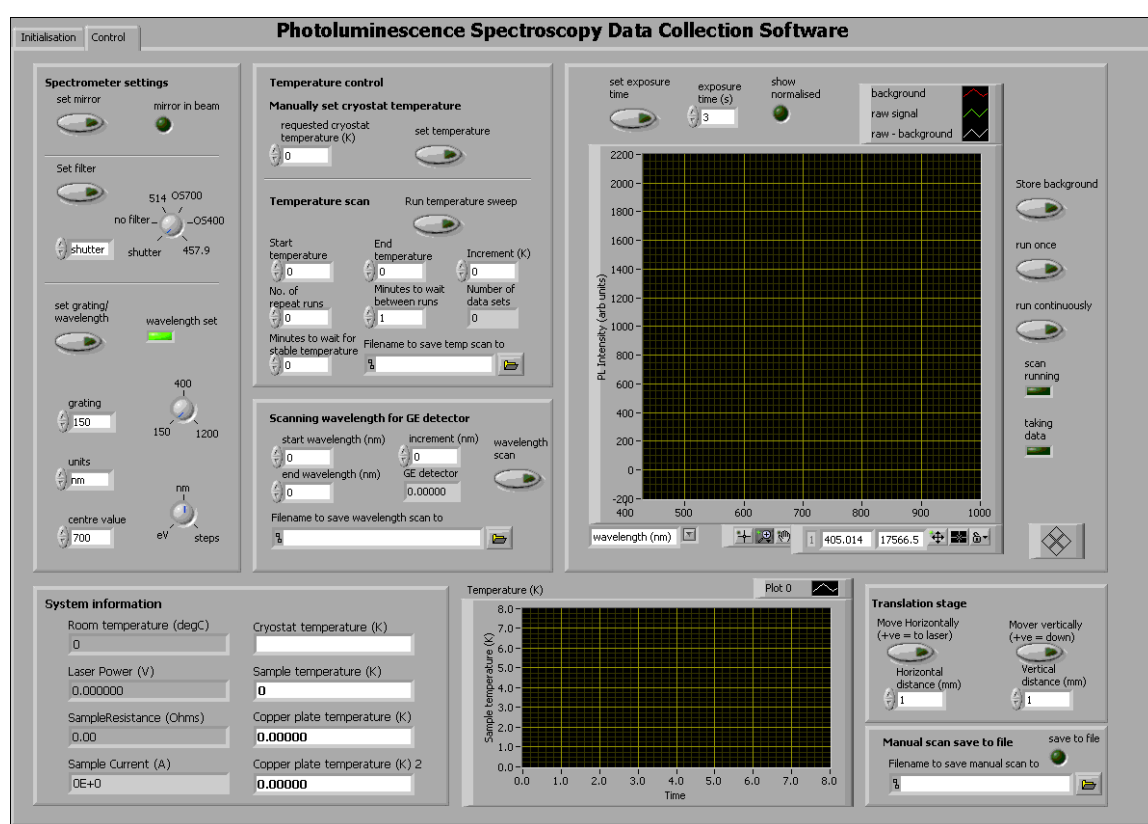

Figure 4.10. Example of the front panel of the LabVIEW 7 photoluminescence control and data logging software. The diagram shows the spectrometer settings including shutter, central wavelength, line grating control and sample measurement time. Cryostat temperature is controlled by an instant set temperature function or a batch scan option. Positioning of the translation stage in the x – z direction can be set in millimetre steps. The screen also displays the background scan and photoluminescence spectra as well as cryostat temperature, laser power and room temperature.

4.7. Sample preparation

4.7.1. Samples

Sample dimensions

Sample size varied from 2mm x 2mm to 10 mm x 10 mm and sample thickness between 0.1 mm to 1 mm. A selection of samples can be seen in Figure 4.11 below.

Preparation of samples

Samples were prepared in two stages. Firstly, the Cu, Au, Nb, YBCO and DyBCO single crystal samples were polished to a visible mirror finish of 1 μm smoothness using a polishing and lapping machine. The machine used 1200 grade abrasive paper followed by liquid diamond paste (6 μm, 3 μm, 1μm grade) on Kemet Pan-W self adhesive cloths for precision lapping and polishing. The samples were then

4mm
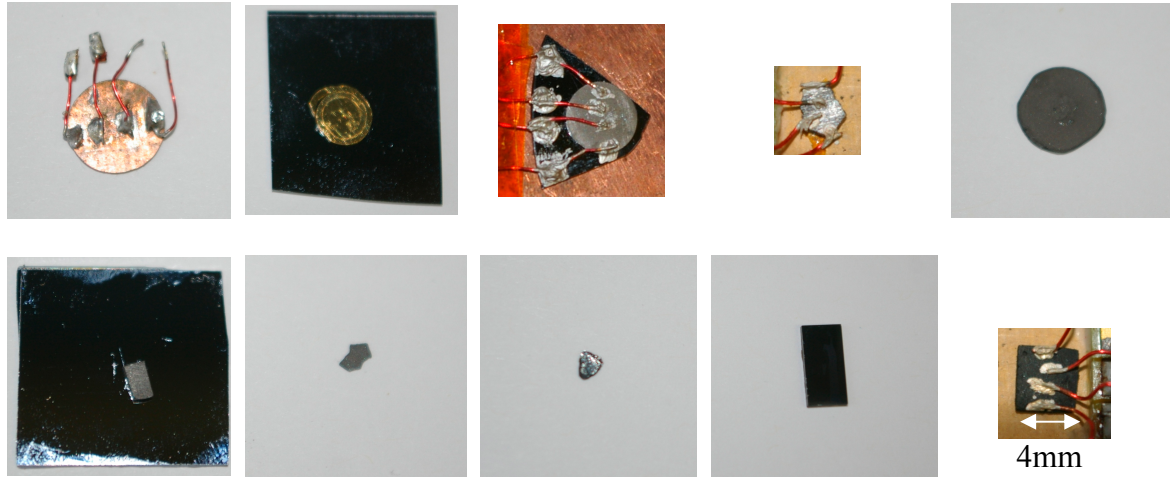
Figure 4.11. Photograph of a selection of samples mounted on silicon wafers. Top row -from left to right: copper, gold, niobium, $PbMo_6S_8$, $Pb_{1-x}Gd_xMo_6S_8$ x = 0.3, bottom row – left to right: $SnMo_6S_8$, $Sn_{1-x}Eu_xMo_6S_8$ x = 0.35, YBCO (single crystal), YBCO (thin film), DyBCO (single crystal). The copper, niobium, $PbMo_6S_8$, and DyBCO samples are shown with the contacts for resistivity measurements. The scale on all of the photographs is the same.

cleaned in acetone and isopropanol to remove any glue or grease from the polishing process. Polycrystalline samples ($PbMo_6S_8$, $Pb_{1-x}Gd_xMo_6S_8$ x = 0.3, $SnMo_6S_8$, $Sn_{1-x}Eu_xMo_6S_8$ x = 0.35) were not polished due to their granular nature, but the top layer of the surface was removed using abrasive paper and the samples cleaned using acetone and isopropanol in an ultrasonic bath. Mounting of the 99.999 % purity gold sample in the cryostat was not possible in its original wire form. Therefore, the sample was pressed into a disk by winding the wire into a spiral and compressing in a hydraulic press. The sample was then polished and cleaned as above.

Mounting techniques

Preliminary tests mounting samples and thermometers using GE varnish gave poor thermal contact between the components and sample holder. This was attributed to bubbles forming in the GE varnish during evacuation of the cryostat which increased the joint width and hence temperature gradient. Samples were mounted using Apiezon N grease as a very thin layer could be applied which calculations confirmed was crucial in reducing the temperature gradient across the joint between the sample and holder (section 4.8.1. below).

Care had to be taken to ensure that adhesives were located behind the sample as the photoluminescence intensity of the N grease was 10^5 times greater than luminescence from the samples. The $PbMo_6S_8$ and YBCO samples were smaller than the protrusion of copper on the sample holder. Therefore, the samples were mounted to a 300 μm thick silicon wafer to prevent luminescence from the sample holder or N grease being measured.

4.8. Data collection and corrections

4.8.1. Data correction

Four corrections were applied in the analysis of raw photoluminescence emission spectra. These accounted for; variation in laser power as a function of time, the response as a function of wavelength of the silicon photodiode CCD array detector and spectrometer, a lower wavelength limit due to the dichroic filter and calibration of sample temperature. Example data analysis is shown in the following sections.

Correction of photoluminescence intensity due to changes in laser power

Correction for fluctuation in laser excitation power was carried out by dividing the measured photoluminescence intensity (in counts s^{-1}) by the laser power (in W) as measured by the calibrated germanium detector. This gave a final photoluminescence intensity in counts s^{-1} W^{-1}. Figure 4.12 shows the PL emission intensity of copper as a function of excitation power.

Silicon photodiode detector and spectrometer response

The spectrometer and silicon photodiode CCD array displayed a wavelength dependent sensitivity response. The manufacturers' stated sensitivities for the two instruments were combined to create a normalised overall response (Figure 4.13). This response was then inverted to give a wavelength dependent correction factor which was applied to all photoluminescence emission spectra during data analysis. Figure 4.14 shows a corrected photoluminescence emission spectrum for gold.
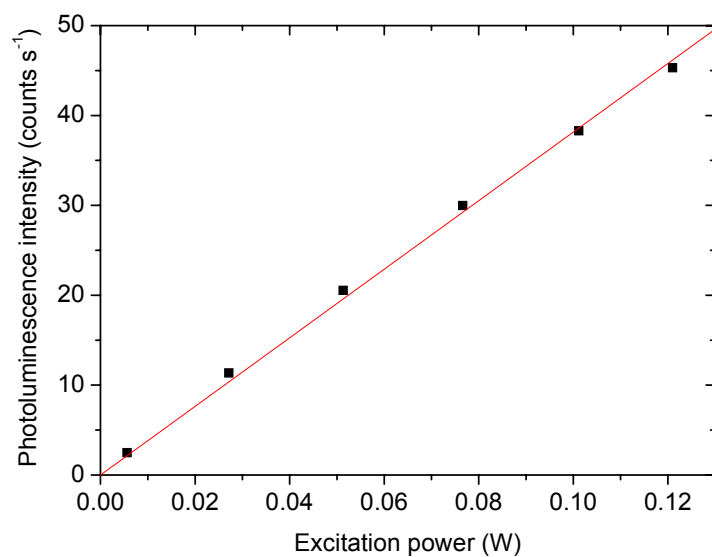
Figure 4.12. Photoluminescence intensity as a function of excitation power for copper. Excitation power (at 488 nm) was measured using the Ge detector calibrated against a Melles Griot Power Meter positioned between the focussing lens and the cryostat window.
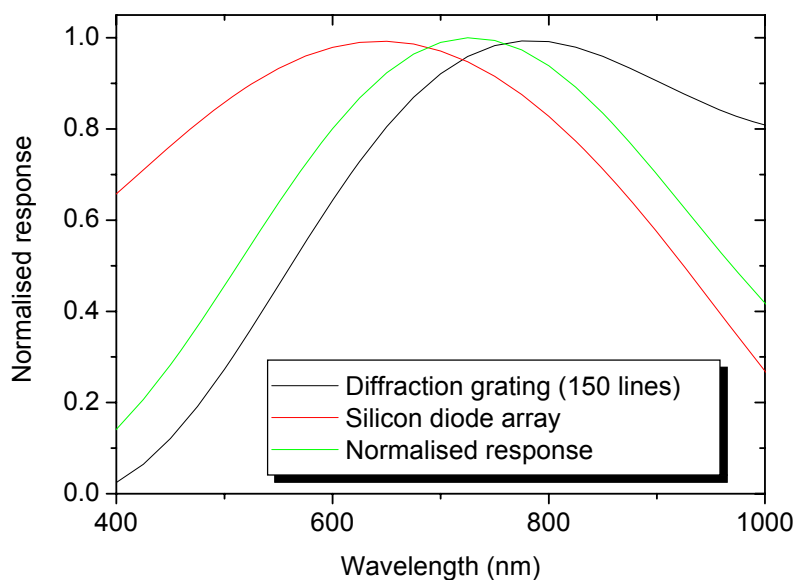

Figure 4.13 Wavelength dependent response for the 150 line spectrometer diffraction grating (black) and silicon photodiode CCD array detector (red). The overall system response has been calculated and normalised (green) before being used as a correction factor for measured photoluminescence emission spectra.
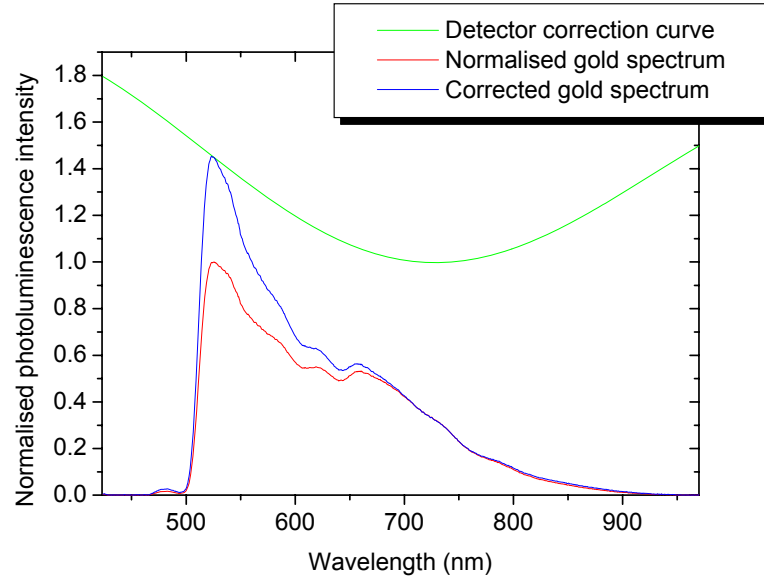
Figure 4.14. Example of the correction of the photoluminescence emission spectrum of gold for the wavelength dependence of the spectrometer and silicon photodiode array detector. The green line shows the correction curve for the spectrometer and silicon diode CCD array detector as a function of wavelength, the red line is the normalised photoluminescence emission spectrum of gold and the blue line shows the corrected photoluminescence emission spectrum of gold. The detector correction curve was calculated from the combined wavelength dependence of the spectrometer grating and silicon diode CCD array.

Angular dependence of the Raman RazorEdge® long wave pass dichroic filter

The dependence upon angle of incidence for the Raman RazorEdge® long wave pass dichroic filter is given by the manufacturer as [157]

$$\lambda(\theta) = \lambda_0 \sqrt{1 - \left(\sin\theta / n_{eff}\right)^2}$$ (4.1)

Where λ is the wavelength of the feature in the spectrum with the filter at an angle θ to the normal, λ_0 is the wavelength with the filter at normal angle of incidence. n_{eff} is the effective refractive index of the filter and varies for s and p polarised light from 2.08 and

1.62, respectively. Figure 4.15 shows a schematic diagram of the geometry of angles relative to the filter surface and a comparison of measured and calculated shift in wavelengths. The measured shift is for unpolarised light.

Figure 4.16 is an example of the change in the photoluminescence emission spectra of copper with rotation of the dichroic filter. Measured photoluminescence emission intensity was reduced below 535 nm by the dichroic filter and this wavelength was taken to be the lower limit for photoluminescence spectra during data analysis.
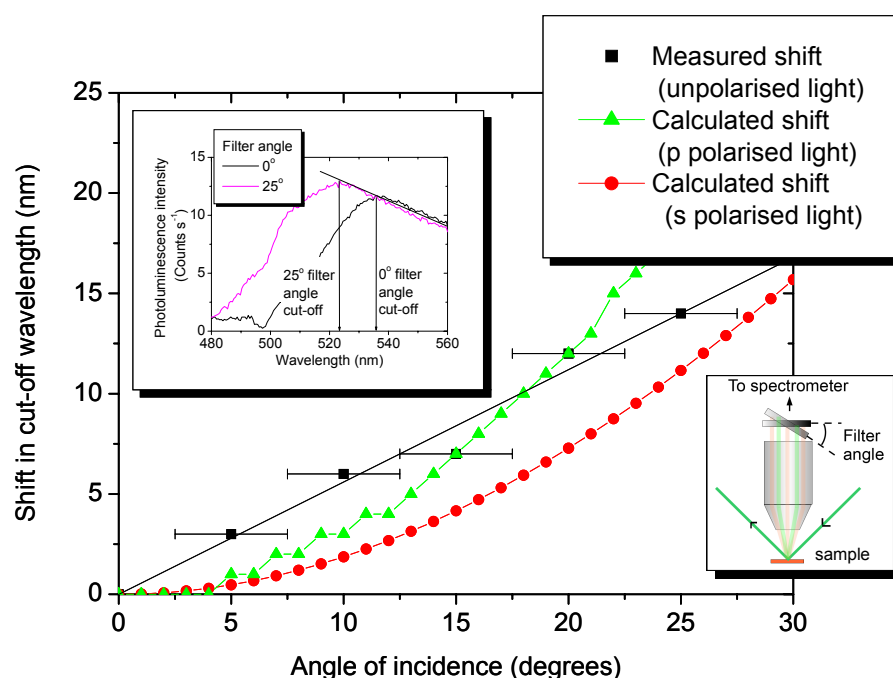
Figure 4.15 Comparison of calculated and measured shift in wavelength as a function of angle of incidence at the dichroic filter between 0 and 25° for s, p and un-polarised light. The measured wavelength is the cut off edge of the gold spectrum (535 nm at 0 degrees angle of incidence). The inset diagram shows how filter angle was measured relative to the sample surface. The calculated shift is for data calculated using equation (4.1).
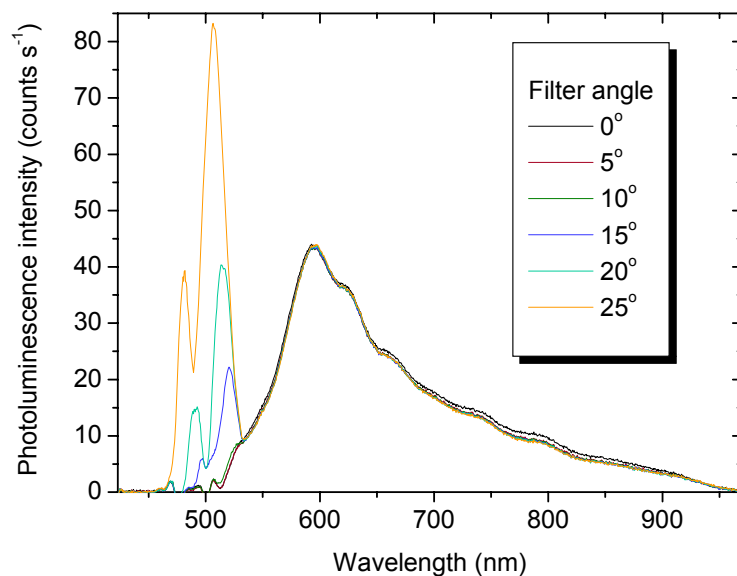
Figure 4.16. Photoluminescence emission spectra of copper after rotation of the dichroic filter between 0° and 25°.

Sample temperature

As discussed in section 4.5. (Thermometry), sample temperatures were calibrated using measurements of resistance as a function of temperature using the AC Transport mode or custom nanovolt precision probe in the Quantum Design PPMS and Cryomech optical cryostat.

Solder provided the most mechanically robust joint between the sample and current and voltage leads and, as such, was used to attach the contacts to the copper sample. It was not possible to use solder with the niobium, DyBCO and $PbMo_6S_8$ samples so silver conductive paint was used to make the contacts to these samples. The paint did not have the mechanical strength necessary to be able to move the samples between the PPMS and Cryomech optical cryostat and the contacts had to be remade once the sample was mounted in the Cryomech cryostat. The change of contacts led to a corresponding change in resistance. Therefore, all resistance measurements on these

samples were normalised to 1 at 300 K to allow comparison of the resistance vs temperature data.

Figure 4.17, Figure 4.18, Figure 4.19 and Figure 4.20 show resistances as a function of temperature for copper, niobium, DyBCO and $PbMo_6S_8$ respectively. Figure 4.17 shows critical features for copper including: that in the worst case the base temperature of the sample can vary by up to 75 K; the laser typically heats the sample by 50 K at the cryostat base temperature; and even in the best case (where the sample mounting techniques were most developed), the base temperature of the sample under laser illumination was 75 K. These data are used to identify a conversion from the
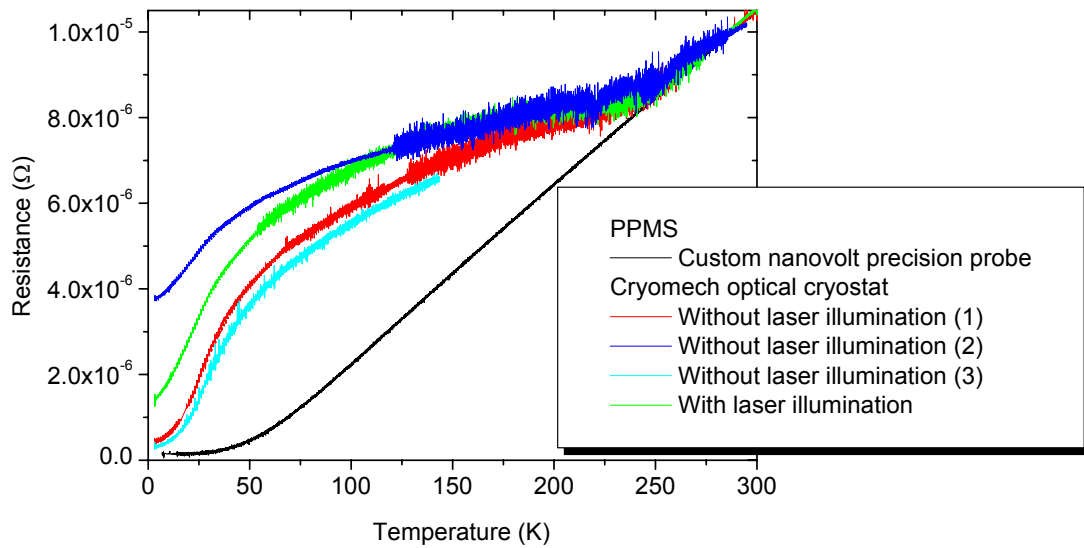

Figure 4.17. Resistance as a function of temperature measured by the Cryomech optical cryostat second stage thermometer and Physical Properties Measurement System (PPMS) variable temperature insert for copper. Measurements were made using the custom resistivity probe in the Physical Properties Measurement System (PPMS) and in the Cryomech optical cryostat with and without laser illumination of the sample for increasing and decreasing temperatures. The measurement in the Cryomech optical cryostat was repeated three times to assess the reproducibility of the sample mounting.
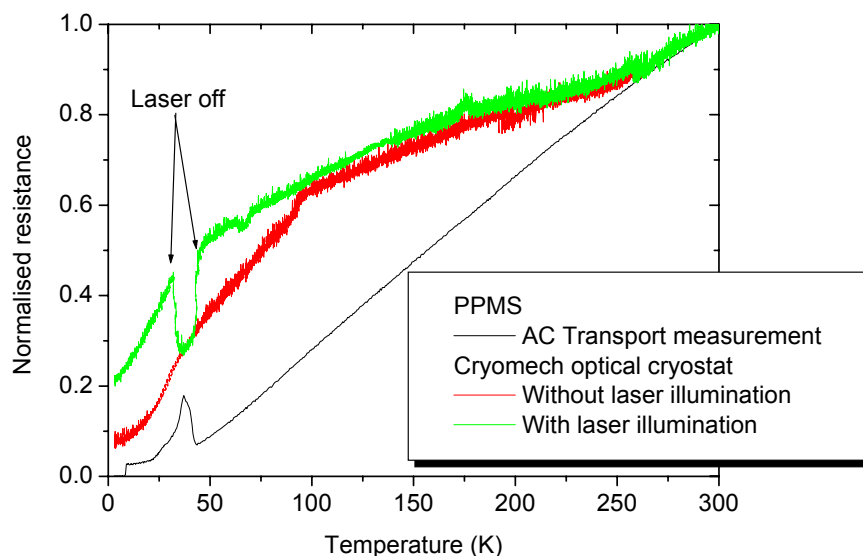
Figure 4.18. Resistance as a function of temperature for niobium. Measurements were made using the custom resistivity probe in the Physical Properties Measurement System (PPMS) and in the Cryomech optical cryostat with and without laser illumination for increasing and decreasing temperatures (as measured by the Cryomech cryostat second stage cold head thermometer).

temperature of the Cryomech 2nd stage thermometer to the temperature of the sample under laser illumination. The decrease in resistance between 25 and 50 K in the measurement of niobium under laser illumination in Figure 4.18 was due to the temporary removal of laser illumination. During this period the resistance decreased to the value measured in the scan without laser illumination. The second feature to note is the increase in resistance between 25 and 50 K in the AC Transport measurement. This increase is due to an electrical fault in the AC mode of the PPMS and was not present in measurements carried out using the custom nanovolt precision probe.

Due to failure of the laser during the final series of measurements, resistance as a function of temperature for $PbMo_6S_8$ under laser illumination was estimated from calculations using measurements without illumination. The relationship between the
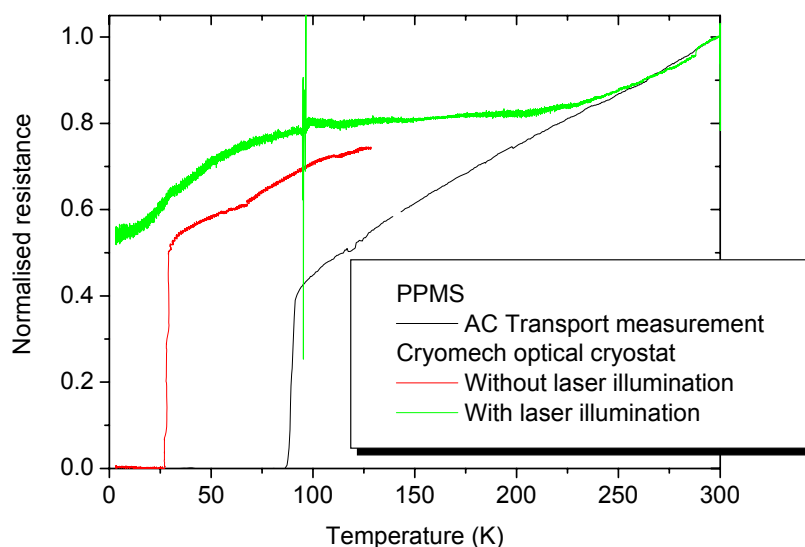
Figure 4.19. Resistance as a function of temperature for DyBCO. Measurements were made using the custom resistivity probe in the Physical Properties Measurement System (PPMS) and in the Cryomech optical cryostat with and without laser illumination of the sample for increasing and decreasing temperatures (as measured by the Cryomech cryostat second stage cold head thermometer).

sample resistance with and without sample illumination was similar for all samples. In all cases the largest increase in the sample resistance due to laser illumination was measured at the cryostat base temperature and decreased with increasing cryostat second stage cold head temperature to an almost negligible difference at room temperature. To determine the expected temperature increase of the $PbMo_6S_8$ sample under laser illumination, the difference in sample temperature with and without laser illumination calibrated from the resistance measurements of the copper, niobium and DyBCO samples were plotted as a function of the Cryomech cryostat second stage cold head temperature (Figure 4.21). A fit was then made to the data and the average temperature increase from the three samples added to the $PbMo_6S_8$ sample temperature data without laser illumination.
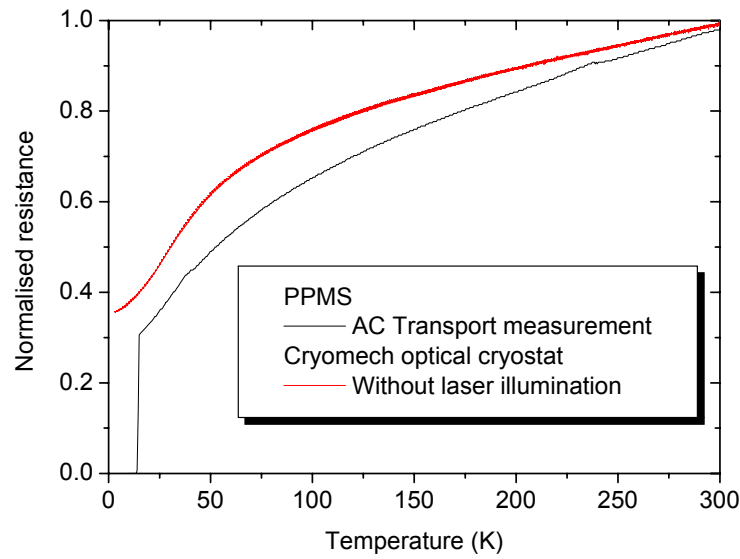
Figure 4.20. Resistance as a function of temperature for PbMo$_6$S$_8$. Measurements were made using the custom resistivity probe in the Physical Properties Measurement System (PPMS) and in the Cryomech optical cryostat without laser illumination of the sample for increasing and decreasing temperatures (as measured by the Cryomech cryostat second stage cold head thermometer).

The reproducibility shown in Figure 4.18 when laser illumination was removed from the sample is good, +/- 5 K, during each temperature run, which was typical of those samples where the grease was not compromised and the sample did not fall off the holder.

Figure 4.22 shows the calibrated sample temperature vs the Cryomech optical cryostat second stage temperature for copper, niobium, DyBCO and PbMo$_6$S$_8$. The data in Figure 4.22 have been used throughout this thesis to convert from the temperature of the Cryomech second stage cold head thermometer to the temperature of the sample under laser illumination. Temperature conversion data of this type was not obtained for all samples due to the similar electrical and thermal properties of certain materials.
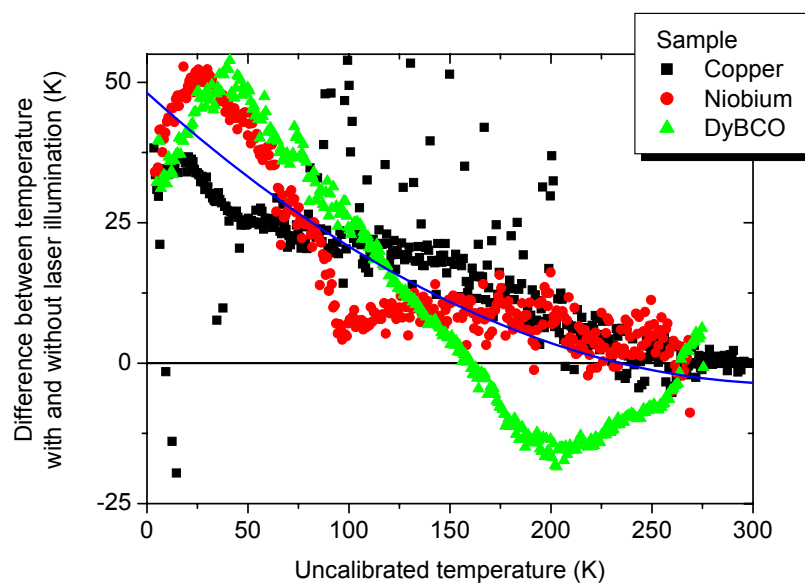
Figure 4.21. Calibrated temperature increase due to laser illumination of the sample vs the uncalibrated Cryomech optical cryostat second stage cold head temperature for copper, niobium and DyBCO. The blue line is a second order polynomial fit to the data.
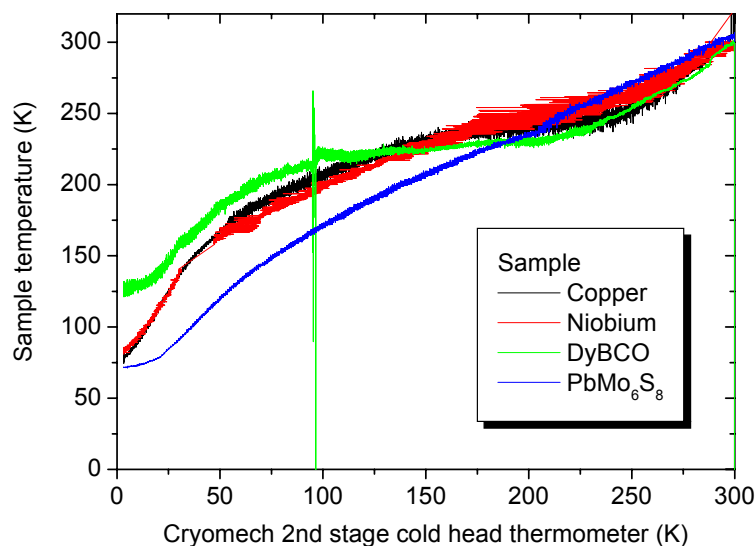

Figure 4.22. Calibrated sample temperature under laser illumination as a function of the Cryomech optical cryostat second stage cold head temperature for copper, niobium, PbMo$_6$S$_8$ and DyBCO. Calculated values for resistance under laser illumination were used as calibration data for PbMo$_6$S$_8$ due to failure of the laser.

The copper data have been used to estimate the temperature of the gold sample, the DyBCO data used to calibrate the YBCO sample and the PbMo$_6$S$_8$ data used to calibrate the SnMo$_6$S$_8$ sample.

Calculation of sample temperature

The effect of laser illumination, Apiezon N grease thickness and the addition of a silicon wafer for sample mounting was calculated using the equation for thermal conduction

$$P_{Total} = kA\frac{\Delta T}{x}$$
(4.2)

where P_{Total} is the total power flowing along the temperature gradient for a material of thermal conductivity, k, area A and length, x for a temperature increase, ΔT.

Figure 4.23 part a) shows a schematic representation of the arrangement in the Cryomech optical cryostat. Part b) and c) are simplified representations of the sample holder without and with a silicon wafer, respectively. A silicon wafer was required for both the photoluminescence measurements of small samples and to electrically insulate the sample from the copper holder during temperature calibration resistance measurements. Preliminary calculations showed that the temperature drop across the sample and the copper components is very small. In principle, if no Apiezon grease were required, the elemental samples would reach a base temperature below 3 K, the high temperature cuprates less than 4 K and the Chevrel phase samples less than 6.5 K. Unfortunately, as we shall see below, the Apiezon N grease increases the temperature difference between the surface of the sample absorbing the laser light and the cryostat second stage cold head very markedly.

The base heat load on the sample (due to radiation from the walls and window of the cryostat) was estimated by comparing the base temperature of the Cryomech optical
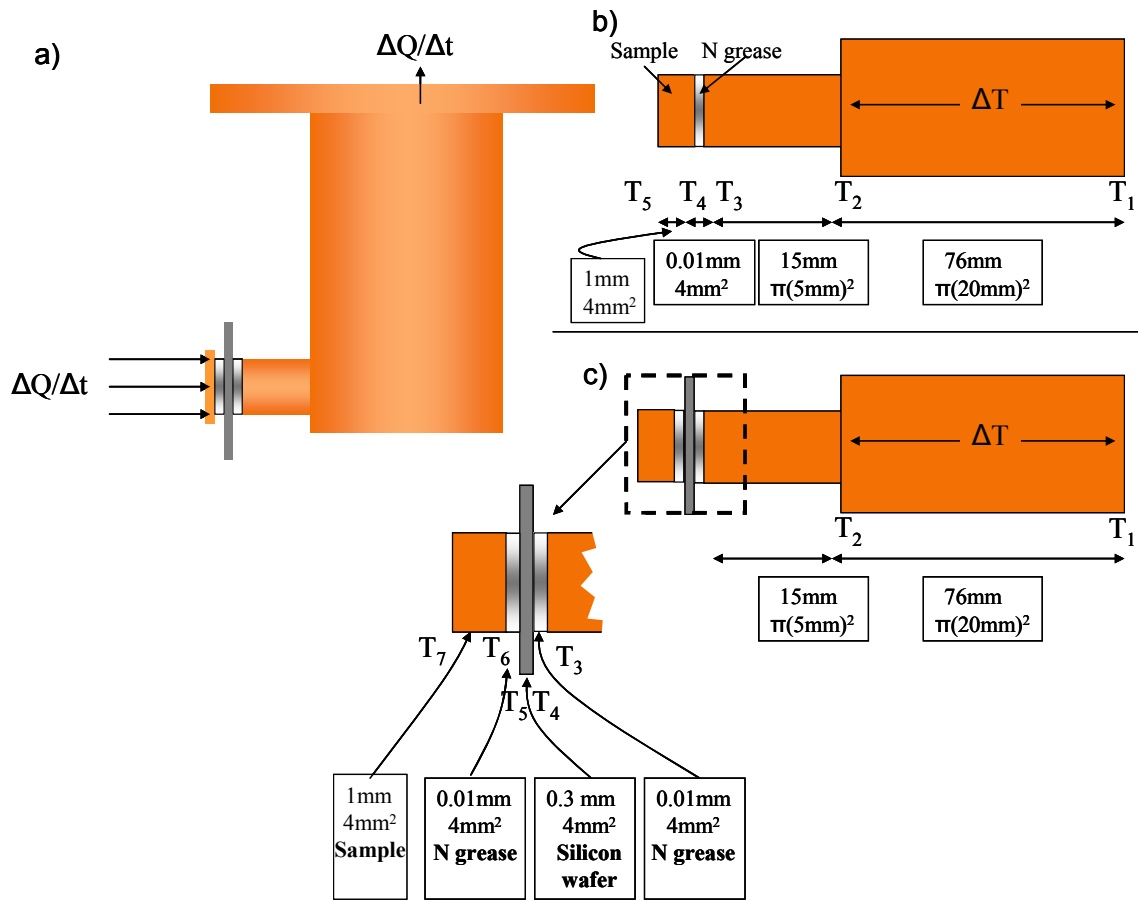
Figure 4.23. Schematic diagram of a) the single piece sample holder, the sample holder simplified for heat conduction calculations b) without and c) with the silicon wafer between the sample and sample holder.

cryostat second stage cold head to the manufacturer's specification for the cooling power. For a base temperature of 3.35 K the manufacturer's specification stated that the cooling power of the cryostat was 0.28 W. By increasing the heat load on the cryostat through the application of 120 mW of laser illumination to the sample, the base temperature increased to 3.66 K. This was in broad agreement with the manufacturer's specification of at total of 0.4 W heat load for a base temperature of 3.66 K.

Table 4.2 shows the calculated temperature increase relative to the base temperature for copper, niobium, DyBCO and $PbMo_6S_8$. The measured sample thickness

and cross sectional area were entered into the calculation along with the thermal conductivity at 4.2 K from the literature.

The power through the system was dependent upon the base heat load on the sample (P_{base}) and the power of the laser on the sample (P_{laser}). The power of the laser was measured between the final focussing lens and the cryostat window before the laser beam was fully focussed. The decrease in spot diameter between the measurement position and the sample has been accounted for in the value of P_{laser} used in the calculation. The best fit to the data was found when the total power was calculated using

$$P_{Total} = P_{base} + \alpha P_{laser} \tag{4.3}$$

where α is the absorption coefficient of the sample measured at 488 nm using ellipsometry as presented in Chapter 3.

The only variable in the calculations in Table 4.2 was the thickness of Apiezon N grease. The thickness was varied to give the measured sample temperature under laser illumination in the optical cryostat with a silicon wafer present. In the case of $PbMo_6S_8$ the thickness of N grease was varied to fit the measured temperature without laser illumination. The calculation was then repeated under identical conditions but with the removal of the silicon wafer and one layer of N grease.

The calculation generates values for the sample temperature without laser illumination which are within 3 K of the measured values for copper and niobium and 12 K of the estimated temperature under laser illumination for $PbMo_6S_8$. A comparison between calculation and experiment could not be made for DyBCO without laser illumination as the sample had entered the superconducting state. However, the N grease thickness is consistent with the values used in the calculation for copper and niobium.

| Sample | | N grease thickness (µm) | Temperature increase relative to the cryostat base temperature of 3.66 K | | | | Thermal conductivity (W/(m.K)) @ 4.2 K |
| | | | Silicon | | No silicon | | |
			No laser	Laser	No laser	Laser	
Copper	**C**	104	41 K	79 K	21 K	39 K	630
	M		43 K	79 K			
Niobium	**C**	108	43 K	84 K	22 K	42 K	7.8
	M		46 K	84 K			
DyBCO	**C**	102	41 K	126 K	21 K	65 K	10
	M		Below T_C	126 K			
PbMo$_6$S$_8$	**C**	58	24 K	59 K	13 K	32 K	15
	M		24 K	71 K*			

Table 4.2. Calculated and measured sample base temperatures. The temperature increase is stated relative to the base temperature of the cryostat, 3.35 K (measured value). The thermal conductivity of N grease is quoted by the manufacturer as 0.095 W/(m.K) [163]. An average value of 150 W/(m.K) from references is used for the thermal conductivity of the silicon wafer[164] [165]. References for copper, gold, niobium, DyBCO and PbMo$_6$S$_8$ thermal conductivities are found in references [166-169] respectively. C indicates calculated data and M measured temperatures. * PbMo$_6$S$_8$ temperature under laser illumination was calculated from unilluminated calibration data.

Table 4.2 clearly demonstrates that the dominant factor in the temperature increase along the length of the sample holder is the thickness of the low thermal conductivity Apiezon N grease. The thermal conductivity of Apiezon N grease is two

orders of magnitude lower than the value for $PbMo_6S_8$ and nearly 4 orders of magnitude smaller than the value for copper.

The calculations in Table 4.2 are consistent with the variability in the sample temperature observed experimentally and attribute the variability to the changes in the thickness of the two layers of Apiezon N grease. The calculations give a difference in N grease thickness of ~50 μm across the four samples. If these differences are uncontrolled and are applied to the calculation for each sample, a reproducibility for the lowest temperature of the sample under laser illumination is +/- 20 K for copper and niobium, +/- 30 K for DyBCO and +/- 40 K for $PbMo_6S_8$. In practice the thickness of the Apiezon grease is specific to the roughness of the sample. We have found that the base temperature of the copper sample was 43 K, 46 K and 135 K for each of the three measurements without laser illumination (Figure 4.17). By simply adding the upper temperature into the calculation above we find an N grease thickness of 178 μm. Considering the measured base temperatures in Table 4.2, we estimate that the reproducibility of the lowest sample temperatures between separate mounting of the sample are of the order of +/- 45 K for copper and niobium, +/- 65 K for DyBCO and +/- 60 K for $PbMo_6S_8$.

Photoluminescence emission measurements of copper, gold, niobium and DyBCO were carried out without the silicon wafer present in the experimental setup. In this case, the calculation predicts that the removal of the second layer of N grease reduces the temperature increase by 39 K, 42 K and 62 K for copper, niobium and DyBCO respectively, compared to the measurement with the silicon wafer present. Photoluminescence measurements of YBCO, $PbMo_6S_8$ and $SnMo_6S_8$ were all carried out with a silicon wafer between the sample and holder to act as a shield to the excitation of photoluminescence from the sample holder and Apiezon N grease.

4.8.2. Accuracy of measurements

Luminescence of optical components

Figure 4.24 shows the PL emission spectrum of copper after rotation of the sample to directly reflect the laser into the microscope objective. The laser light is incident on the edge of the objective lens at 21° and is central to the microscope objective at 26°. A peak at 800 nm is observable in the PL emission spectrum at 26° rotation which is not present in the 0° spectrum. The peak is attributed to the luminescence of the optical components and is taken as confirmation that there is no contribution to the sample PL emission spectrum from luminescence of optical components for the standard (0°) experimental geometry.
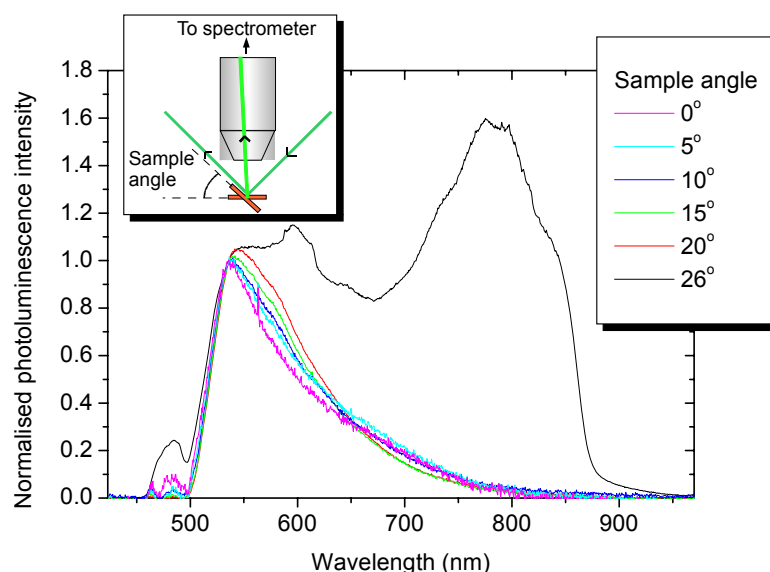

Figure 4.24. Contribution of the optical components to the normalised photoluminescence emission spectrum of gold. The sample is rotated from an angle normal to the collection optical pathway to 26° when the sample directly reflects the laser from the sample surface into the microscope objective. The inset figure shows the angle of sample rotation relative to the collection optics. The reflected laser light is not directly incident on the microscope objective until 21° and is central on the microscope objective at 26°.

4.9. Conclusions

This chapter has detailed the design, commissioning and calibration of an instrument to measure low intensity photoluminescence emission spectra as a function of temperature. A discussion of optical hardware suitable for the measurement of samples with low photoluminescence emission intensities was carried out and cryogenic apparatus and sample holder designs discussed. Best practice for accurate thermometry has been considered and calibration of sample temperature thoroughly examined. The temperatures quoted are reproducible during an individual run to within +/- 5 K. Sample mounting leads to a reproducibility of the sample base temperature of +/- 45 K for copper and niobium, +/- 65 K for DyBCO and +/- 60 K for $PbMo_6S_8$, which is caused by variations in the thickness of Apiezon N grease between the sample, silicon wafer and holder.

A considerable amount of work has been completed to develop an instrument for the measurement of low yield photoluminescence emission. In this chapter we have discussed how we have achieved the very high sensitivity required to measure metallic samples and the following chapters will present the successful measurement of sample spectra and the difficulties encountered in obtaining reliable results. The reliability of the measured spectra will be discussed through comparison of data with calculated spectra and data in the published literature. In this work, we have achieved good signal to noise for samples with low luminescence yields but unfortunately achieving sample base temperatures below 70 K has not proven possible.

Chapter 5. Photoluminescence of gold and copper

5.1. Introduction

The measurement of the room temperature photoluminescence emission spectra of gold and copper has been reported in the literature by several authors and was discussed in detail in Chapter 2 [9, 10, 64]. However, little work has been carried out into the measurement of their photoluminescence emission spectra at low temperatures and no results have been published on measurements made as a function of temperature [9]. Study of the photoluminescence emission spectra as a function of temperature has the potential to provide important information regarding changes in the density of states and optical constants at low temperatures, which are difficult to measure by conventional techniques. The aim of the work presented in this chapter is to provide the first systematic study of the photoluminescence emission spectra of gold and copper as a function of temperature.

Section 5.2. gives details of the samples and their preparation for measurement with sections 5.3. and 5.4. presenting the data for photoluminescence emission from gold and copper, respectively. Spatially resolved spectra from across the sample surface are shown along with the dependence of the photoluminescence emission of each sample on excitation power, the variation in peak photoluminescence emission intensity as a function of time and measurements as a function of temperature. Photoluminescence emission spectra of gold and copper have been calculated and compared to data in the

literature and the experimentally measured spectra in section 5.5. Finally, section 5.6. gives a discussion of the data followed by conclusions in section 5.7.

5.2. Samples

5.2.1. Sample purity and form

The gold and copper samples of various purities and forms measured using the low yield photoluminescence instrument and are listed in Table 5.1 below. Preliminary spatial mapping measurements of low purity gold samples showed an additional peak in the emission spectrum at certain locations on the sample surface when compared to the photoluminescence emission spectrum of the high purity sample. Therefore, the highest purity samples commercially available were selected for measurements as a function of temperature.

The 99.999 % purity gold sample was supplied by the manufacturer in wire form. In order to make photoluminescence measurements the wire was wound into a flat coil and compressed using a hydraulic press before polishing. The process increased the surface area of the sample and reduced scattering of the laser light compared to the curved surface of the gold in wire form. In its pressed form the sample was not required to be mounted on a silicon wafer as pressing increased the sample surface area to greater than the dimensions of the mounting protrusion on the sample holder. Pressing the sample also ensured that locating the Apiezon N grease behind the sample was less problematic than for a sample in wire form.

Sample purity	Form	Supplier	Impurities as stated by the supplier (ppm)
Au 99.999 %	Wire – pressed	Sigma-Aldrich	Ca 5.0, Fe 3.3, Ag 2.8, Zn 2.4, Ni 0.4, Mg 0.3
99.999 %	Wire	Advent Research Materials	Ag 9, Fe 1 all other content < 1 ppm
99.99 %	Foil	Sigma-Aldrich	Pt 7, Ag 5, Pd 3, Cu 2, Fe 2, Ni 1, all other content < 1 ppm
Cu 99.9999 %	Rod	Sigma-Aldrich	Unknown impurities
99.95 %	Rod	Smiths Metals Centres	Ag 100, Ca 3, Pb 3, Si 2, Sn 2, Fe 2, Bi 1, Al 1, Cd 1, Mg 1 all other content < 1 ppm

Table 5.1 Purity and form of the gold and copper samples. Supplier information is listed along with the stated impurities as supplied by the manufacturer.

5.2.2. Sample preparation

The gold and copper samples were polished then cleaned in an ultrasonic bath with acetone and isopropanol to ensure a clean, flat surface for measurements. Photoluminescence emission spectra were measured before and after polishing for both samples. In both cases the photoluminescence emission intensity of the spectra decreased after polishing with the same ratio of decrease measured for both samples (Table 5.2). Figure 5.1 shows the spectra before and after polishing. The shape of the photoluminescence emission spectrum of gold changed only minimally after polishing, however, the copper sample showed a disappearance of the peak at 850 nm after polishing.

147

Sample	Before polishing	After polishing	Ratio
			Before : After
Gold	3.6×10^3 counts s^{-1} W^{-1}	0.3×10^3 counts s^{-1} W^{-1}	12:1
Copper	1.2×10^3 counts s^{-1} W^{-1}	0.1×10^3 counts s^{-1} W^{-1}	12:1

Table 5.2. Peak photoluminescence emission intensities of gold and copper measured before and after polishing. Samples were polished using 1200 grade abrasive paper followed by 6 μm, 3 μm and finally 1 μm liquid diamond paste. All measurements were made within 24 hours of polishing.

5.3. Photoluminescence of gold

The following section presents data for the 99.999 % purity gold wire purchased from Sigma Aldrich. The sample thickness after pressing was 0.3 mm with a surface area
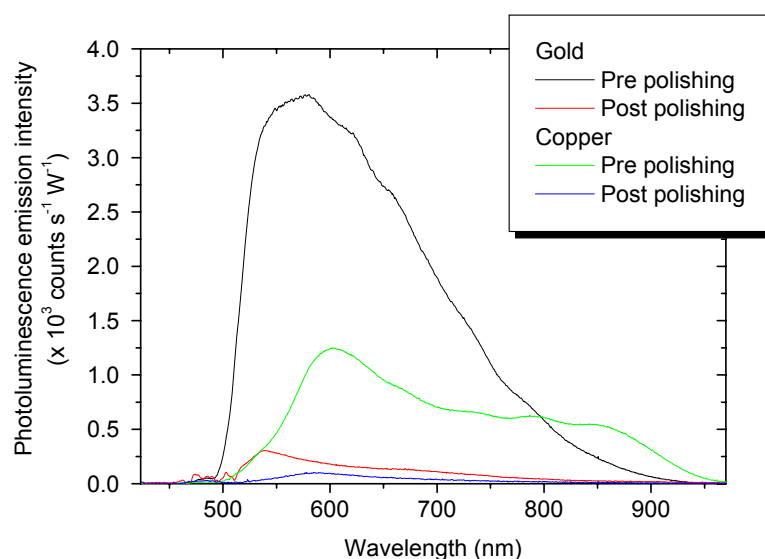
Figure 5.1. Photoluminescence spectra of gold and copper before and after polishing. Post polishing measurements were made with the cryostat window in place in the optical setup. Measurements were made within 24 hours of polishing with a typical excitation power of 55 mW.

of 5.78 mm x 6.59 mm. The sample was characterised by the measurement of photoluminescence emission spectra as a function of position on the sample surface, excitation power and time. The photoluminescence emission spectra, peak photoluminescence emission intensity and full width half maximum (FWHM) were then measured as a function of increasing, decreasing and a random order of temperatures.

5.3.1. Spatially resolved measurements across the sample surface

Figure 5.2 shows the spatially resolved normalised photoluminescence emission spectra of 99.999 % purity gold. Measurements were made at 1 mm intervals in the
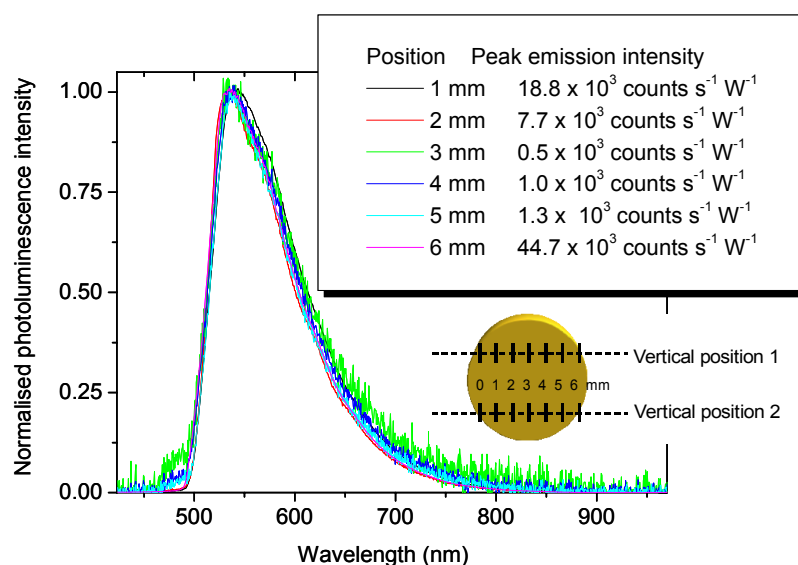
Figure 5.2 Normalised photoluminescence emission spectra of 99.999 % purity gold wire measured across the sample surface. The inset figure is a schematic diagram of the location of measurements on the sample. Measurements were made along the horizontal direction at 1mm intervals in one of two vertical positions. The spectra shown in the main graph are taken in vertical position 1. The edge of the sample was located at 0 mm and 6 mm. Typical excitation powers were 55 mW.

horizontal direction at vertical position 1 (inset figure). The peak photoluminescence emission intensity at each position is stated in the legend.
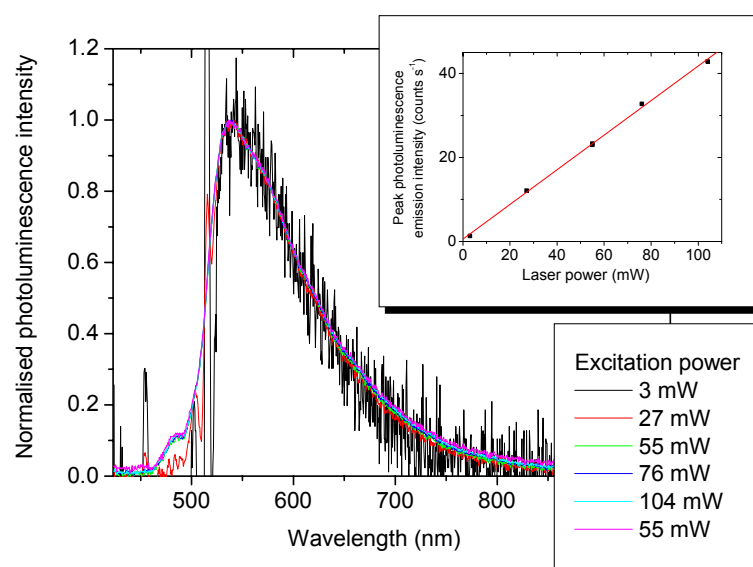
5.3.2. Photoluminescence spectra as a function of excitation power

Figure 5.3 shows the normalised photoluminescence emission spectra of 99.999 % purity gold for increasing excitation power. Excitation power was manually increased to a maximum of 104 mW before being decreased back to 55 mW to confirm reproducibility of the spectra. Excitation power was measured using a handheld Melles Griot power level meter positioned between the final focussing lens and the cryostat window.

Figure 5.3. The normalised photoluminescence emission spectra of 99.999 % purity gold measured for increasing excitation power at 304 K. The inset graph shows peak photoluminescence emission intensity as a function of excitation power. Laser power was manually increased from 0 to 104 mW before the power was reduced and the measurement at 55 mW repeated.

5.3.3. Time dependent measurements

Variation of photoluminescence intensity over a period of days

Figure 5.4 shows the peak photoluminescence emission intensity plotted as a function of time for gold. A change in peak photoluminescence intensity of approximately 10 counts s^{-1} (200 counts s^{-1} W^{-1}) over the course of 8 days is observed with the spectral shape remaining the same throughout the measurements.

Variation of photoluminescence spectra over a period of hours

Figure 5.5 shows a selection of seven normalised photoluminescence emission spectra from measurements made at 2 minute intervals over the course of a 9 hour period
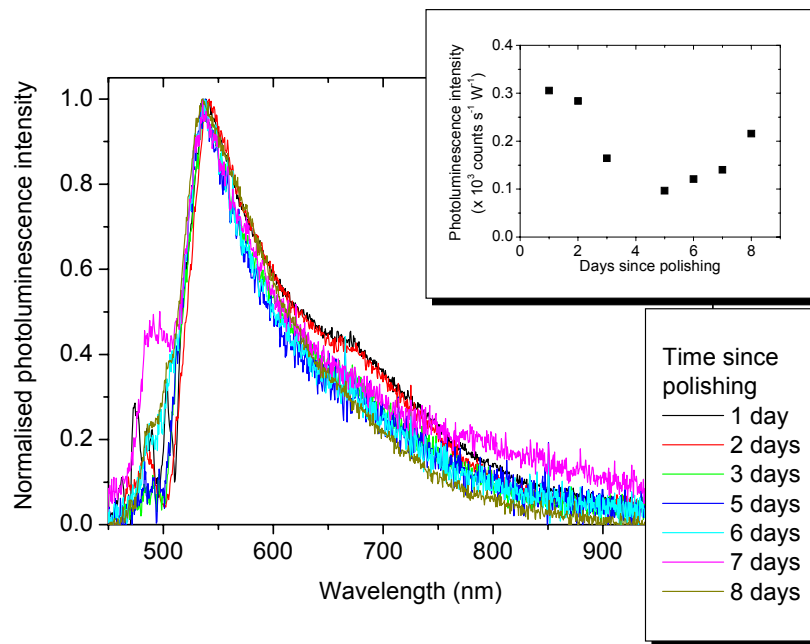
Figure 5.4. Normalised photoluminescence emission spectra of gold measured over a period of 8 days. The inset graph shows the peak photoluminescence emission intensity as a function of time. Spectra are measured at 300 K with the cryostat window present in the optical setup. Typical excitation powers were 55 mW.

at a set temperature of 206 K. The inset figure shows the variation in peak photoluminescence emission intensity during this period. The location of the laser excitation spot was moved to a new position on the sample as the first photoluminescence measurement was started.

A decrease in peak photoluminescence emission intensity is observed over the first 30 minutes after excitation at a new position on the sample. This is followed by an oscillation in intensity with a period of approximately 500 minutes. As well as a change in the main peak photoluminescence emission intensity at 535 nm, the intensity at ~575 nm was also observed to change over the 9 hour measurement. However, the changes did not correlate with those observed at 535 nm.
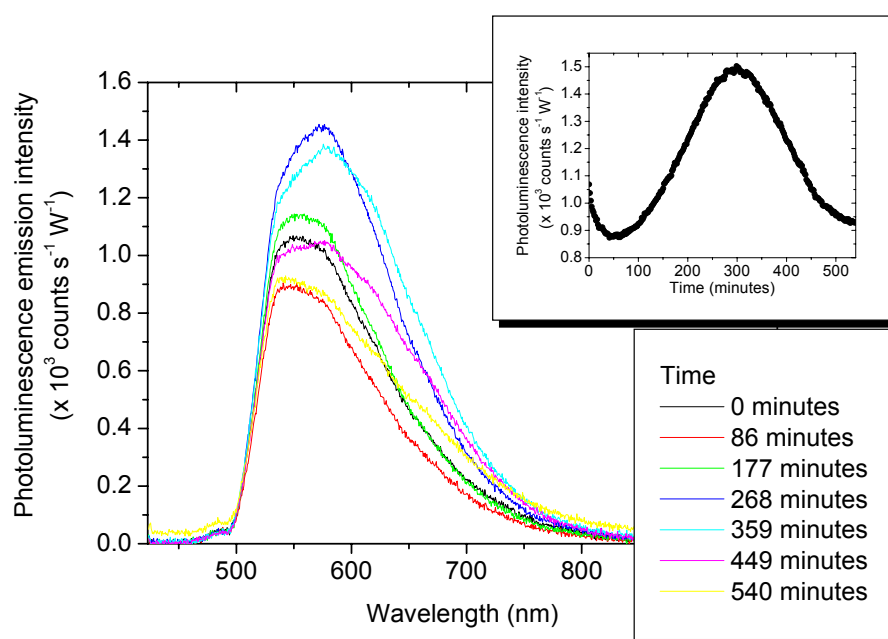
Figure 5.5. Photoluminescence emission spectra of gold measured over a 9 hour period. Each spectrum was measured at 206 K at 2 minute intervals. The main graph shows 7 normalised spectra measured at various times throughout the 9 hour period. The inset graph shows the variation in the photoluminescence emission intensity at 535 nm corrected for fluctuations in laser power (in counts s^{-1} W^{-1}) as a function of time. Typical photoluminescence excitation power was 55 mW.

5.3.4. Temperature dependent measurements

The photoluminescence emission spectrum of 99.999 % purity gold was measured as a function of increasing, decreasing and a random order of temperatures. Measurements were made over the course of a 9 day period with polishing of the sample indicating zero days. Photoluminescence emission spectra were measured 30 minutes after the cryostat temperature had settled at the set temperature and the sample had been repositioned to account for thermal contraction. The 30 minute period ensured that the sample had reached thermal equilibrium with the cryostat and that the initial period of rapid decrease in photoluminescence emission intensity had passed. The photoluminescence emission spectra, peak photoluminescence emission intensity and full width half maximum (FWHM) of 99.999 % purity gold measured as a function of temperature are presented in Figure 5.6 to Figure 5.8.

Variation of spectral shape with temperature

Figure 5.6 shows the photoluminescence emission spectra of 99.999 % purity gold measured as a function of decreasing temperature 4 days after sample polishing.

Variation in peak intensity with temperature

Figure 5.7 shows the peak photoluminescence emission intensity of 99.999 % purity gold as a function of increasing, decreasing and a random order of temperatures. Measurements were made 4, 6 and 9 days respectively after the sample had been polished. In Figure 5.7 the peak photoluminescence emission intensity is corrected for changes in excitation power and is given in counts s^{-1} W^{-1}.
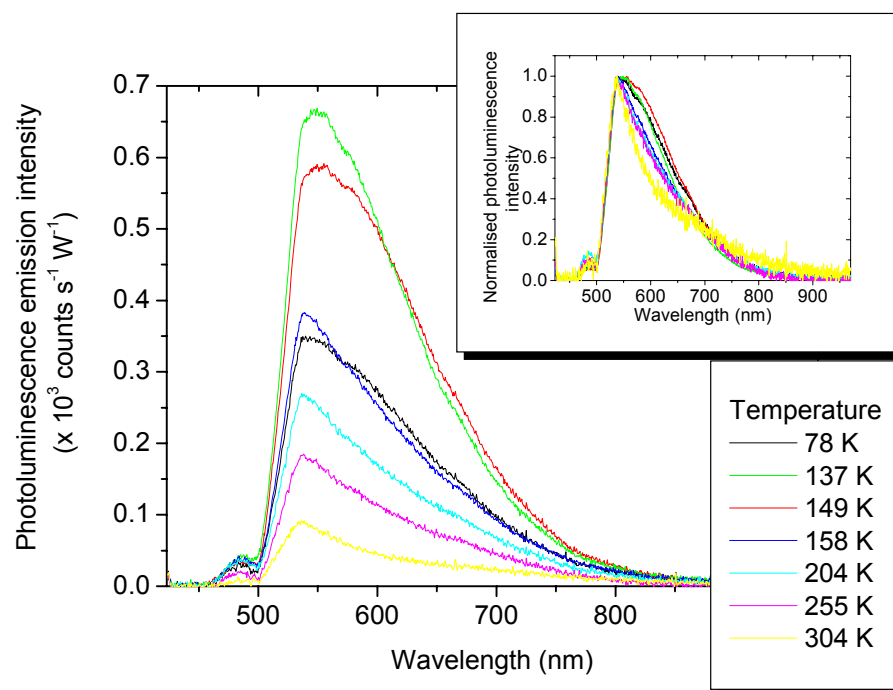
Figure 5.6. Photoluminescence emission spectra of gold measured as a function of temperature. Spectra were measured for decreasing temperatures from 304 K four days after the sample was polished. The inset graph shows the normalised spectra. All spectra were measured after a 30 minute period which began once the sample had been repositioned to correct for thermal contraction. Typical photoluminescence excitation power was 55 mW.
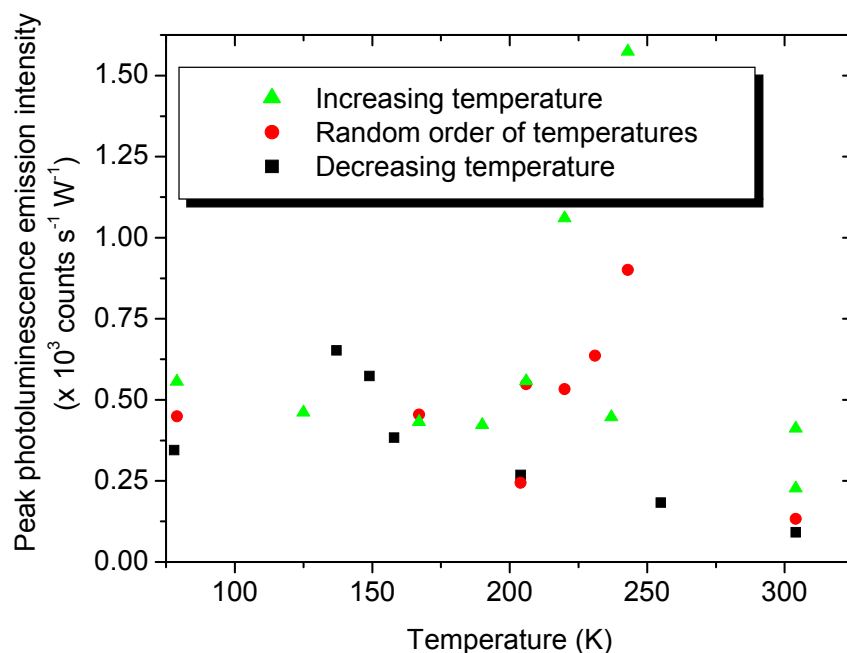
Figure 5.7. Peak photoluminescence emission intensity measured as a function of temperature for 99.999 % purity gold. The measurements were made over a five day period for increasing temperatures (green), a random order of temperatures (red) and decreasing temperatures (black). Data were collected 4, 6 and 9 days after polishing for decreasing, random order and increasing temperatures respectively. Typical photoluminescence excitation powers were 55 mW.

Variation of full width half maximum with temperature

Figure 5.8 displays the full width half maximum of the photoluminescence emission spectra of 99.999 % purity gold measured for increasing, decreasing and a random order of temperatures. Measurements were made 4, 6 and 9 days after polishing for the decreasing, random order and increasing temperatures respectively.
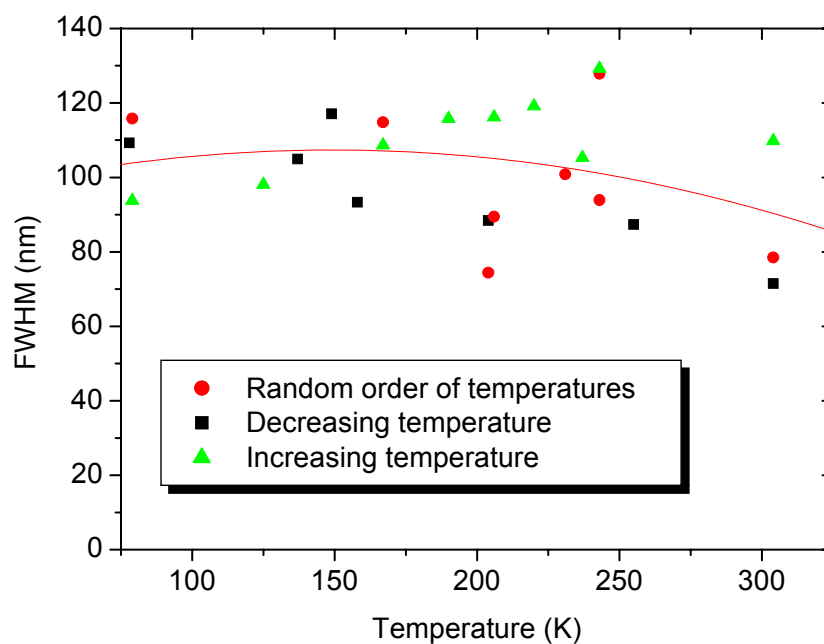
Figure 5.8. Variation in the full width half maximum (FWHM) of the photoluminescence emission spectra of 99.999 % purity gold measured as a function of temperature. The measurements were made over a five day period for a random order of temperatures (red), decreasing temperatures (black) and increasing temperatures (green). Data were collected 4, 6 and 9 days after polishing for the decreasing, random order and increasing temperatures respectively. The red line is displayed as a guide to the eye. Typical excitation powers were 55 mW.

5.4. Photoluminescence of copper

The following section presents data collected for a 0.6 mm thick, 8.9 mm diameter cross section of the 99.9999 % purity copper sample purchased from Sigma Aldrich. The sample was characterised by measuring photoluminescence emission spectra as a function of position on the sample surface, excitation power and time. A systematic study of the photoluminescence emission spectra, peak photoluminescence emission intensity and full width half maximum (FWHM) as a function of increasing, decreasing and a random order of temperatures was then carried out.

5.4.1. Spatially resolved measurements across the sample surface

Figure 5.9 shows data for the spatially resolved photoluminescence emission spectra of 99.9999 % purity copper. Figure 5.9a is a 2D representation of the photoluminescence emission spectra measured in 1 mm intervals along the horizontal direction at vertical position 2 (shown in Figure 5.9c). Figure 5.9b shows the normalised photoluminescence emission spectra. Note the changes in spectral shape which are observed for copper which were not observed for gold (c.f. Figure 5.2).
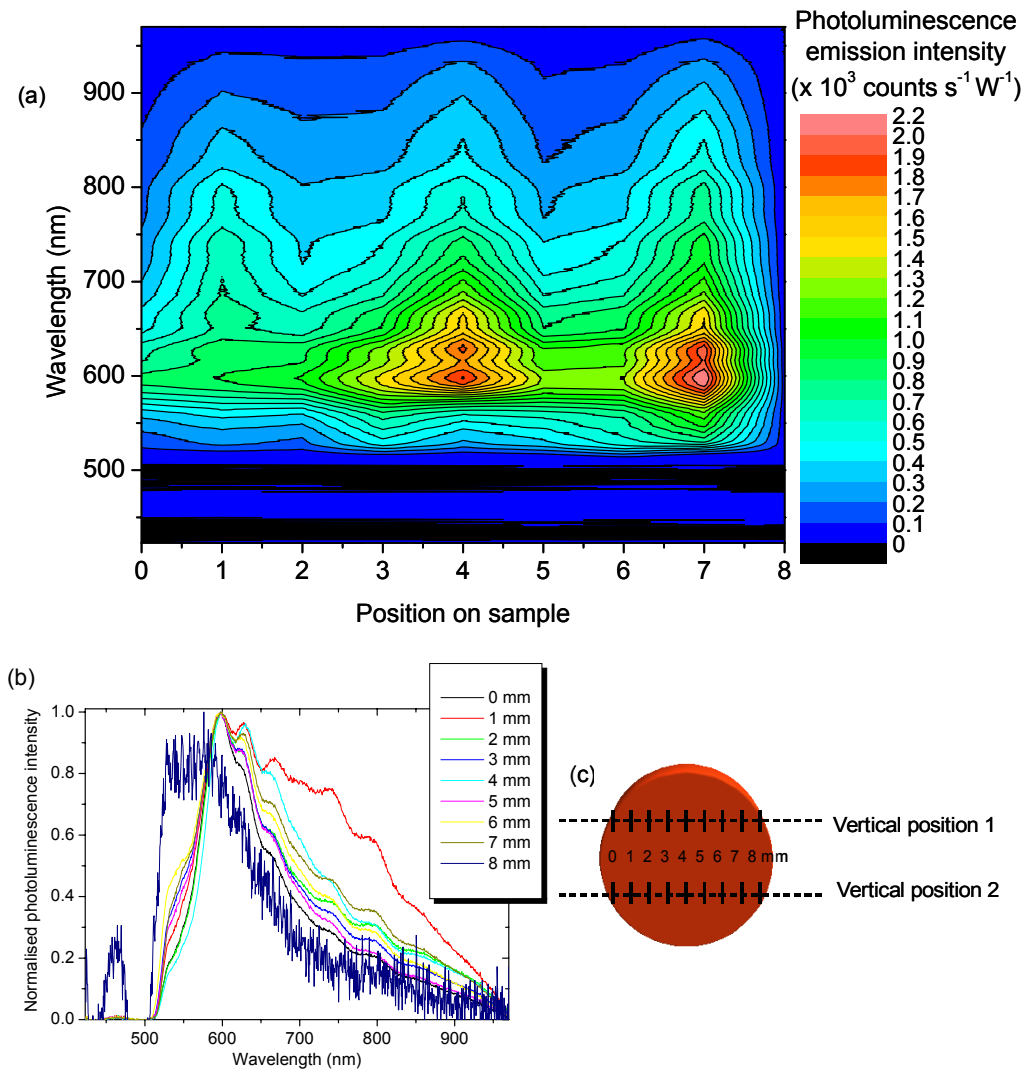
Figure 5.9 (a) 2D projection of the photoluminescence emission spectra of copper measured at different positions across the sample surface (b) Normalised photoluminescence emission spectra (c) Schematic diagram of the location of measurements on the sample. Measurements were made along the horizontal direction at 1mm intervals in one of two vertical positions. The spectra in parts (a) and (b) are measured in vertical position 2. The edge of the sample was at 0 mm and 8 mm. At 8 mm the laser spot was on both the silicon and sample. Typical excitation powers were 50 mW.

5.4.2. Excitation power dependence

Figure 5.10 presents the normalised photoluminescence emission spectrum of copper as a function of excitation power. Excitation power was manually increased to a maximum value of 113 mW before the measurement at 51 mW was repeated to confirm reproducibility of the spectra. Excitation power was measured between the final focussing lens and cryostat window using a handheld Melles Griot power level meter.
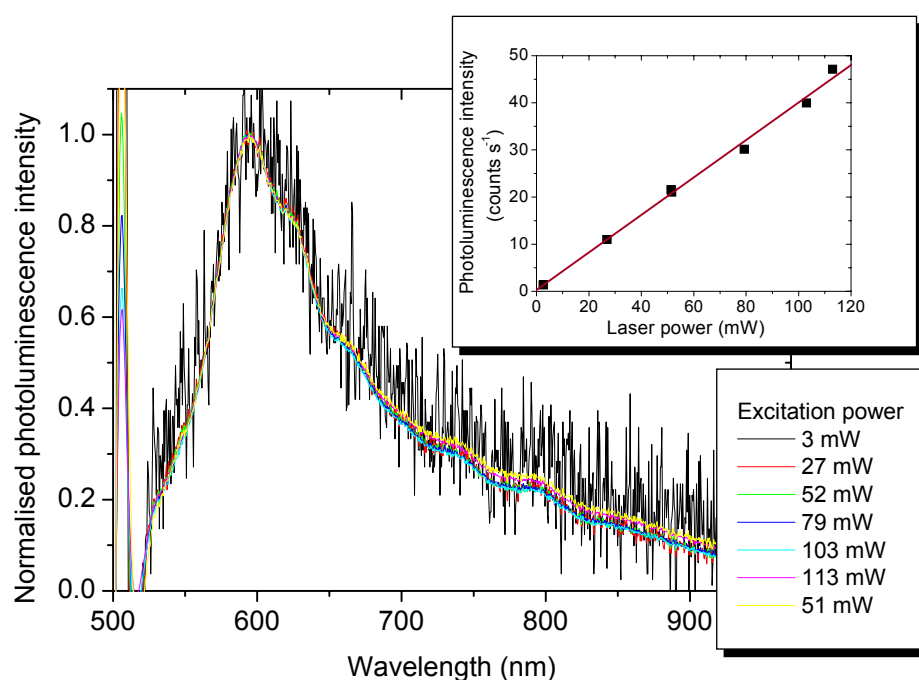

Figure 5.10. The normalised photoluminescence emission spectra of copper measured for increasing excitation powers at 304 K. The inset graph shows the peak photoluminescence emission intensity as a function of excitation power. Laser power was manually increased from 0 to 113 mW before the power was reduced and the measurement at 51 mW repeated.

5.4.3. Time dependent measurements

Variation of photoluminescence over a period of days

Figure 5.11 shows peak photoluminescence emission intensity plotted as a function of time for copper with polishing of the sample indicating zero days. The peak photoluminescence emission intensity of the copper sample increased by a factor of 35 (180 counts s^{-1}) over a 22 day period (Figure 5.11). A second peak at 800 nm was also observable after approximately one week. The relative intensity of the 800 nm peak increased by 40 % relative to the main 600 nm photoluminescence peak during the three week period. The increase in intensity of the 800 nm peak relative to the 600 nm peak was not proportional to the overall increase in luminescence intensity.
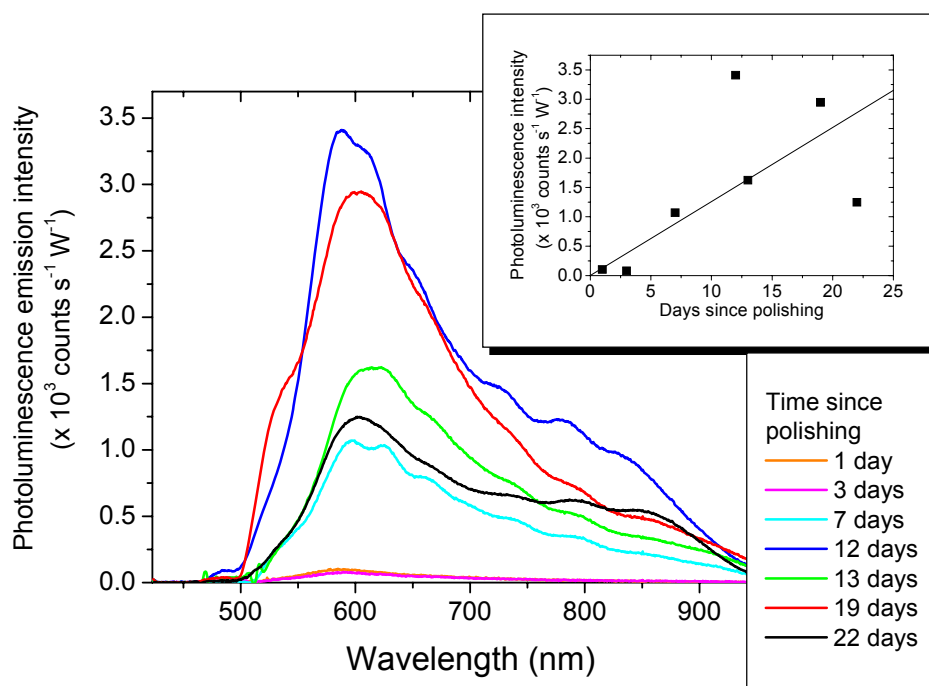

Figure 5.11. Photoluminescence emission spectra of copper measured over a period of 22 days. The inset graph shows the peak photoluminescence emission intensity as a function of time. Spectra are measured at 300 K with the cryostat window in the optical setup. Typical excitation power was 50 mW.

Variation of photoluminescence spectra over a period of hours

Figure 5.12 shows a selection of five photoluminescence emission spectra measured over the course of a 12 hour period at 2 minute intervals. The measurements were made at a temperature of 206 K. The inset figure shows the variation in peak photoluminescence emission intensity over this period. The location of the focussed excitation laser spot was moved to a new position on the sample at the beginning of 12 hour period but was not repositioned at any point during the measurement.

As was observed for the gold sample, there was a rapid, reproducible decrease in peak photoluminescence emission intensity during the first 30 minutes. There then
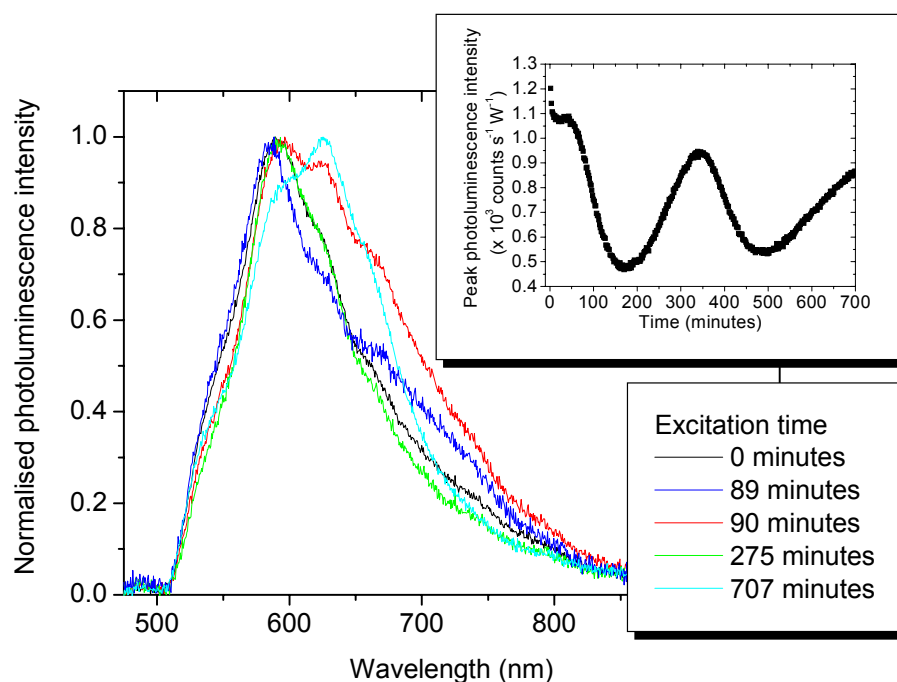

Figure 5.12. The normalised photoluminescence emission spectra of copper measured over a 12 hour period. Each spectrum was measured at 206 K in 2 minute intervals. The main graph shows 5 normalised spectra measured at various times throughout the 12 hour period. The inset graph shows the change in the peak photoluminescence emission intensity (in counts s^{-1} W^{-1}) as a function of time. Typical photoluminescence excitation power was 50 mW.

followed an oscillation in peak photoluminescence emission intensity with a period of approximately 300 minutes. Spectral shape varied over the 12 hour period but did not correlate to the period of oscillation in peak photoluminescence emission intensity. The measurement was repeated at 79 K for a 13 hour period and a 1 hour period. The repeated measurements showed the same initial rapid decrease in peak intensity but differed in their period of oscillation.

5.4.4. Temperature dependent measurements

Photoluminescence emission spectra were measured as a function of increasing, decreasing and a random order of temperatures. The measurements were made over the course of a 21 day period with polishing of the sample indicating zero days. The sample was polished again 21 days after the first polish and the number of days since polishing reset to zero.

Measurements of photoluminescence emission were made 30 minutes after the cryostat temperature had settled at the set temperature and the sample had been repositioned to account for thermal contraction. The 30 minute wait ensured that the sample had reached thermal equilibrium with the cryostat and that the period of rapid decrease in photoluminescence emission intensity observed in Figure 5.12 had passed.

The photoluminescence emission spectra, peak photoluminescence emission intensity and full width half maximum (FWHM) of 99.9999 % purity copper measured as a function of temperature are presented in Figure 5.13 to Figure 5.16 below.

Variation of spectral shape with temperature

Figure 5.13 shows the photoluminescence emission spectra of 99.9999 % purity copper measured as a function of decreasing temperature 3 days after the sample was polished. The inset figure shows the normalised spectra.
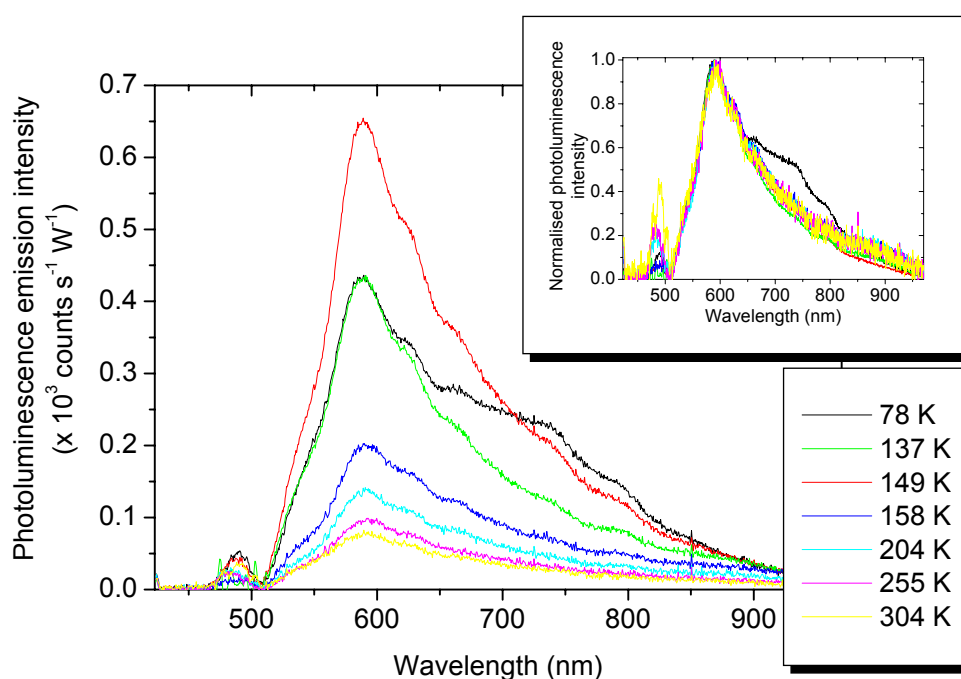

Figure 5.13. Photoluminescence emission spectra of copper measured as a function of temperature. Spectra were collected for decreasing temperatures starting from 304 K, 3 days after the sample was polished. The inset graph shows the normalised spectra. All spectra were measured after a 30 minute period which began once the sample had been repositioned to correct for thermal contraction. In all but the 78 K measurement realignment occurred immediately after cooling to the set temperature. The 78 K spectrum was measured after the sample had been at 78 K for 2 hours prior to realignment. Typical photoluminescence excitation power was 50 mW.

Variation in peak intensity with temperature

Figure 5.14 and Figure 5.15 show peak photoluminescence emission intensity as a function of decreasing, increasing and a random order of temperatures. Measurements were made 3, 19 and 21 days after sample polishing, respectively. Peak photoluminescence emission intensity has been corrected for fluctuations in excitation power and is given in counts s^{-1} W^{-1} in Figure 5.14. Figure 5.15 shows the data normalised at 78 K.
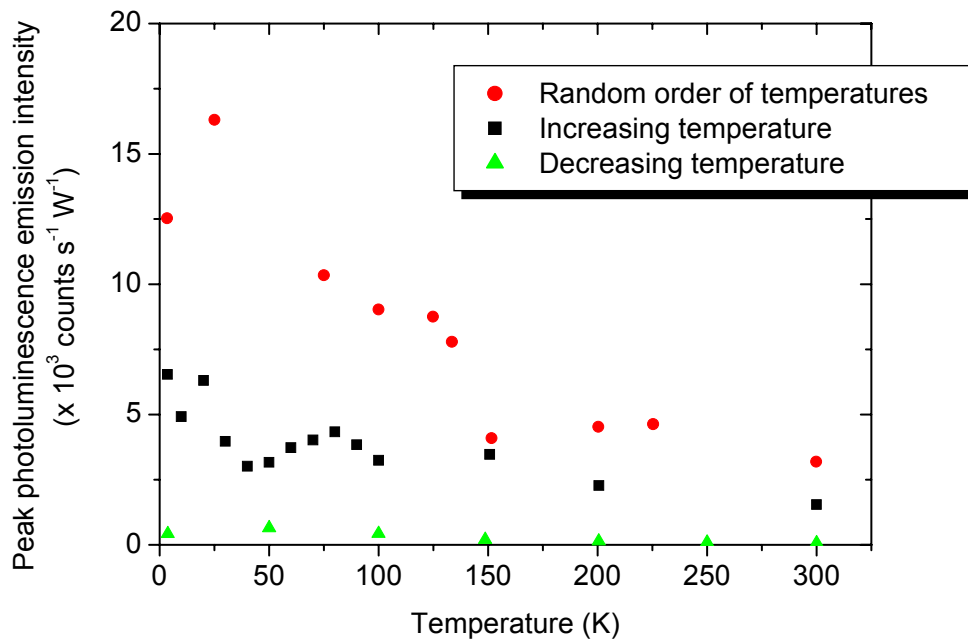

Figure 5.14. Peak photoluminescence emission intensity as a function of temperature for 99.9999 % purity copper. The measurements were made over a three week period for a random order of temperatures (red), increasing temperatures (black) and decreasing temperatures (green). Data were collected 3, 19 and 21 days after polishing for the decreasing, increasing and the random order of temperatures respectively. Typical photoluminescence excitation power was 50 mW.
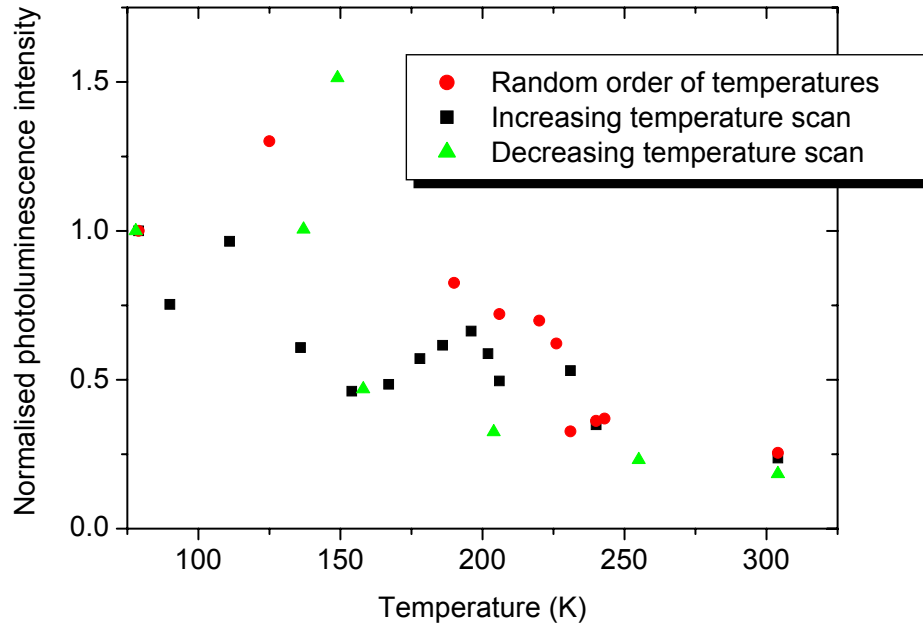
Figure 5.15. The normalised peak photoluminescence emission intensity of copper measured as a function of temperature and normalised to 1 at 79 K. The measurements were made over a three week period for a random order of temperatures (red), increasing temperatures (black) and decreasing temperatures (green). Data were collected 3, 19 and 21 days after polishing for the decreasing, increasing and random order temperatures respectively. Typical excitation powers were 50 mW.

Variation of full width half maximum with temperature

Figure 5.16 presents the full width half maximum (in nanometres) for the photoluminescence emission spectra of 99.9999 % purity copper for increasing, decreasing and a random order of temperatures.
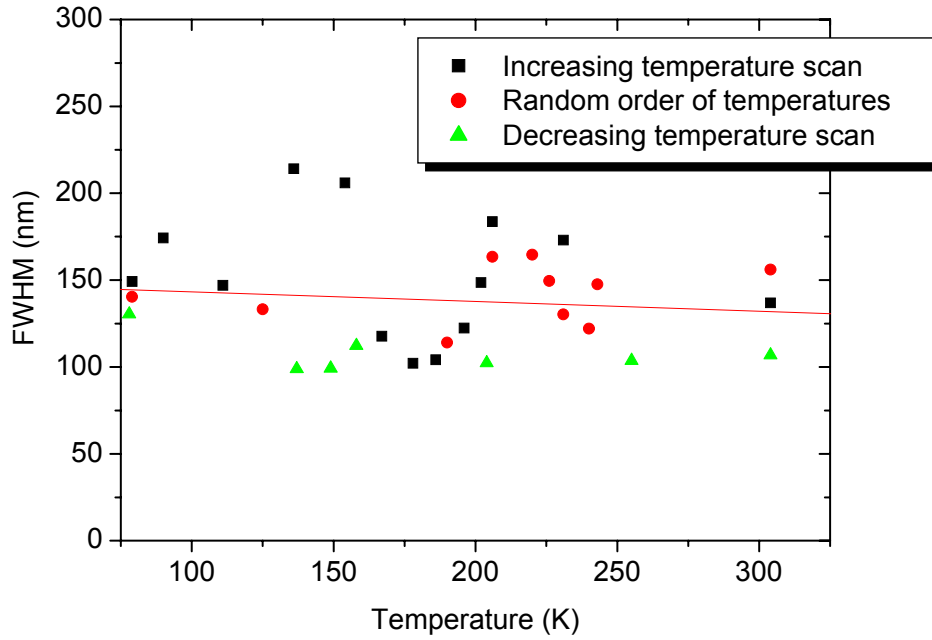
Figure 5.16. Variation in full width half maximum (FWHM) of the photoluminescence emission spectra measured as a function of temperature for 99.9999 % purity copper. The measurements were made over a three week period for increasing temperatures (black), a random order of temperatures (red) and decreasing temperatures (green). Data were collected 3, 19 and 21 days after polishing for the decreasing, increasing and random order temperatures respectively. The red line is displayed as a guide to the eye. An anomalous point at 240 K in the increasing temperature run is not displayed on the graph. Typical excitation powers were 55 mW.

5.5. Calculation of photoluminescence spectra

Figure 5.20 and Figure 5.21 present the photoluminescence emission spectra of gold and copper calculated using equation (2.37) based on the work of Apell [64]. Data for the refractive index, extinction coefficient and absorption coefficient were obtained from the literature and density of states were calculated by Dr Stewart Clark using

CASTEP software (Figure 5.17) [150, 170]. A comparison of measured and calculated density of states data from the literature with the data calculated by Dr Stewart Clark for this study is given in Figure 5.18 and Figure 5.19.

In Figure 5.20 the calculated spectrum and literature spectra are compared with experimental data for 99.99 % and 99.999 % purity gold [9]. In Figure 5.21 the calculated spectrum is compared with data from the literature and experimentally measured spectra for 99.95 % and 99.9999 % purity copper.
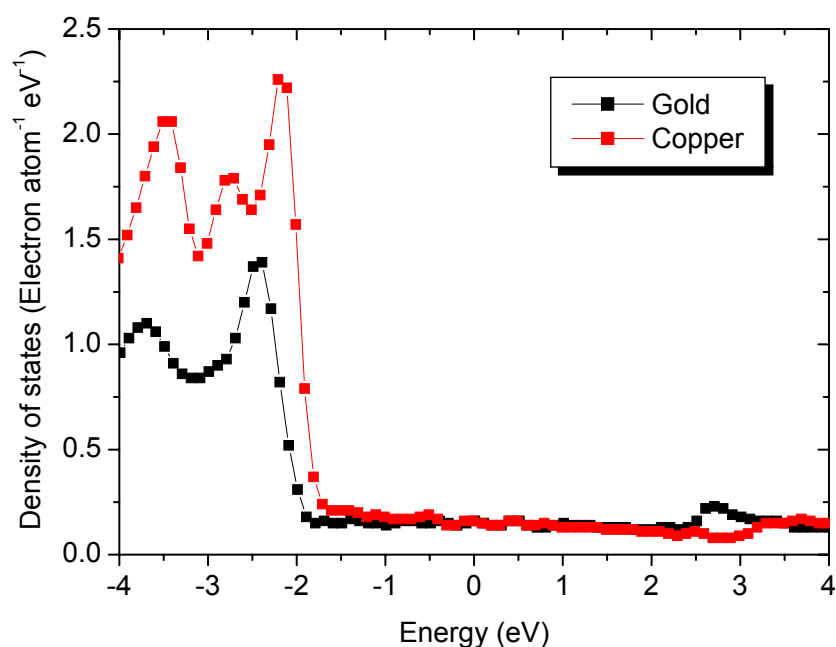

Figure 5.17. Calculated density of states as a function of energy for gold and copper. Calculations were performed by Dr Stewart Clark using a molecular dynamics technique in CASTEP software [170]. The Fermi energy is located at zero energy on the x axis scale.
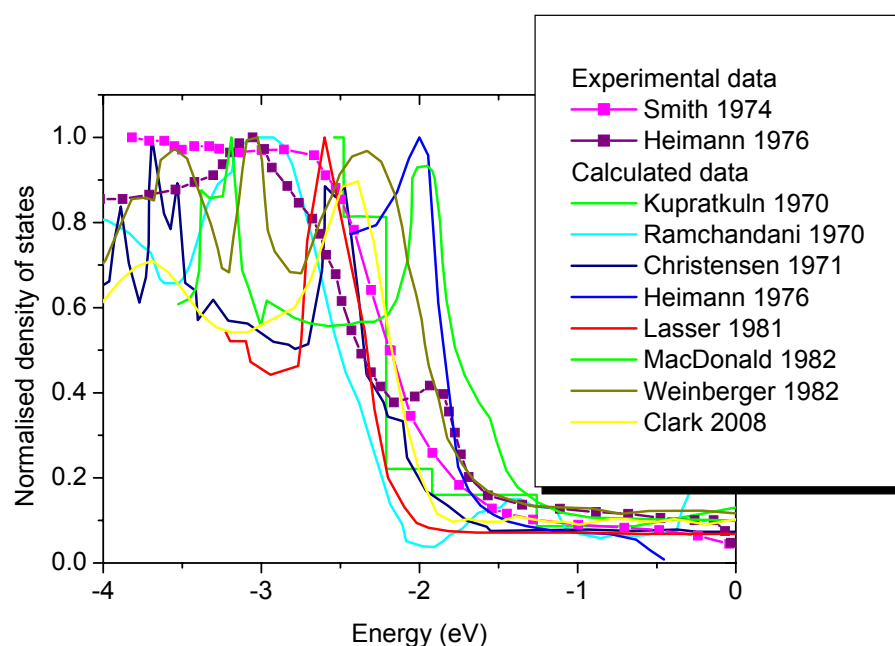
Figure 5.18. Comparison of the experimentally measured and calculated density of states of gold in the literature with the calculated density of states by Dr Stewart Clark [62, 170-177].
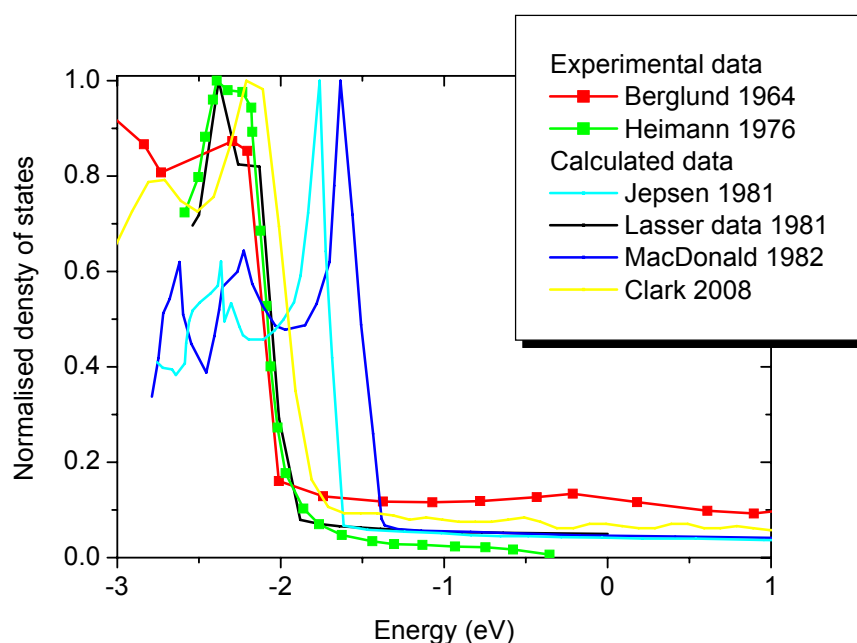

Figure 5.19. Comparison of the experimentally measured and calculated density of states of copper in the literature with the calculated density of states by Dr Stewart Clark [62, 170, 172, 176, 178, 179].
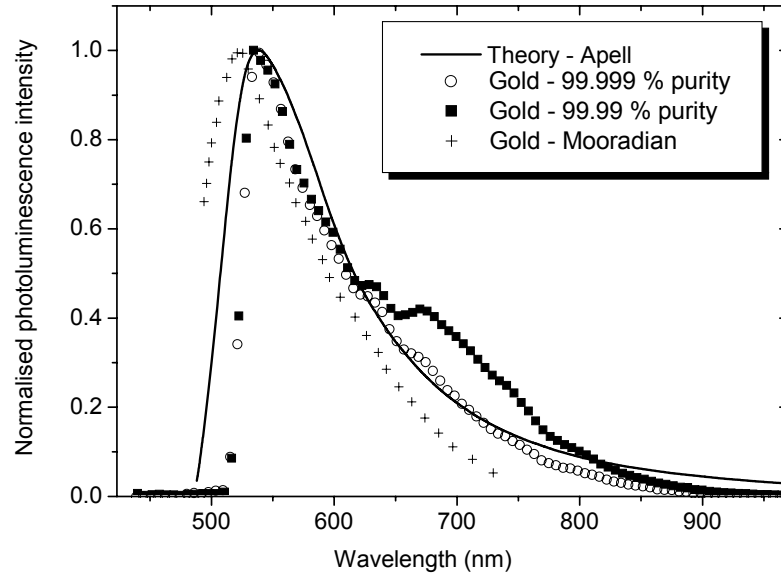
Figure 5.20. Comparison of the normalised photoluminescence emission spectra of 99.999 % (open circles) and 99.99 % (squares) purity gold measured at 300 K, the spectrum as measured by Mooradian (cross) [9] and the spectrum calculated using equation (2.37) (solid line). The calculated spectrum uses data for the refractive index, extinction coefficient and reflectivity from the CRC handbook of optical materials [150] and calculated density of states data. The spectra are normalised to their peak photoluminescence emission intensity.

5.6. Discussion

The processes occurring during photoluminescence emission from gold and copper have been discussed in detail in Chapter 2. The broad agreement between the spectra measured for 99.999 % purity gold and 99.9999 % purity copper and those in the literature and calculated using equation (2.37) (Figure 5.20 and Figure 5.21) suggests that Apell's model is broadly an explanation of the processes occurring for our samples [9, 10, 64].
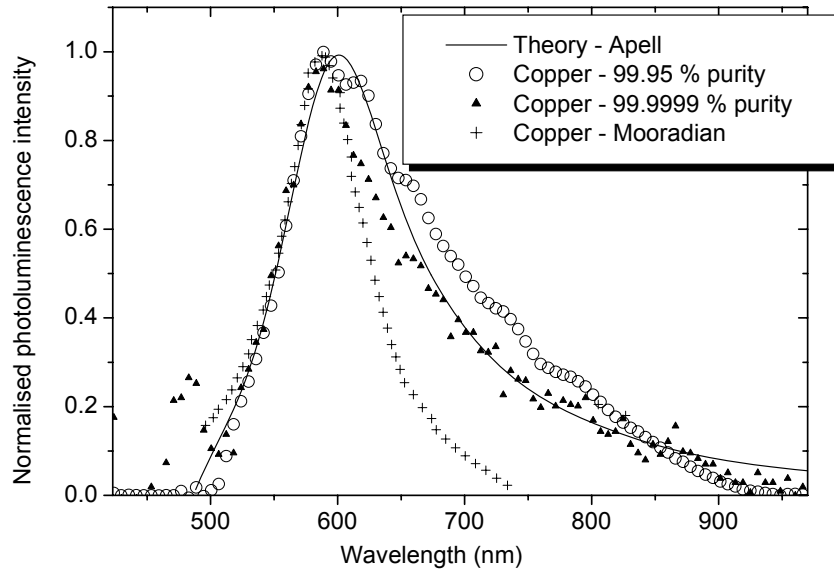
Figure 5.21. Comparison of the normalised photoluminescence emission spectra of 99.95 % (open circles) and 99.9999 % (solid triangles) copper measured at 304 K, the spectrum as measured by Mooradian (cross) [9] and the spectrum calculated using equation (2.37) (solid line). The calculated spectrum uses data for the refractive index, extinction coefficient and reflectivity from the CRC handbook of optical materials [150] and calculated density of states data. The spectra are normalised to their peak photoluminescence emission intensity.

Room temperature data for Gold

A comparison between data in the literature and the calculated spectra for gold show an agreement within 3 nm for the full width half maxima of the spectra [9]. The offset in the peak photoluminescence emission wavelength for 99.999 % purity gold relative to data in the literature is due to the onset of the dichroic Raman Razoredge filter cut-off at 535 nm which also reduces the FWHM of the experimental spectra by 20 nm relative to the calculated and literature data [9, 10].

Figure 5.4 shows strong evidence for the photoluminescence emission spectrum of gold being that of the bulk sample. The shape of the emission spectrum of gold

170

remains the same throughout the measurements and the photoluminescence emission intensity does not change by more than 10 counts s^{-1} (200 counts s^{-1} W^{-1}) over the course of 8 days' measurements. This is consistent with the unreactive nature of gold as discussed in chapter 2 [83, 84].

Spatially resolved measurements of 99.999 % purity gold showed an invariant FWHM and peak photoluminescence emission wavelength across the sample surface. However, the peak photoluminescence emission intensity varied by two orders of magnitude across the surface (Figure 5.2). The change in peak intensity cannot be simply explained. Surface contamination is ruled out as the source of the increase as the spectral shape did not change. Enhancement of photoluminescence emission on roughened gold and copper surfaces has been shown to increase luminescence emission intensities by an order of magnitude. The enhancement can occur for samples with a roughness approximately the same as the wavelength of the incident light but has only been reported in the literature for samples with surface roughnesses two orders of magnitude lower than the polished surface of the 99.999 % purity gold sample [10, 66]. Further study of the microstructure of the sample surface may provide a clearer insight into the possible source of the inhomogeneity in peak photoluminescence emission intensity. An additional peak at 670 nm in the 99.99 % gold sample spectrum compared to the 99.999 % purity sample was observed at one position on the 99.99 % purity gold sample during the spatially resolved measurements (Figure 5.20). The emission is attributed to impurities, however, the chemical structure of the impurity cannot be identified without the use of complimentary analytical techniques.

The gold sample displayed a linear relationship between peak photoluminescence emission intensity and excitation power (Figure 5.3). This is consistent with the theoretical work of Boyd (equation (2.33) in chapter 2) who states that for gold and

copper samples, photoluminescence emission intensity is directly proportional to source intensity [10].

Room temperature data for copper

Figure 5.21 shows good agreement between the wavelength of the peak photoluminescence emission of 99.95 % and 99.9999 % purity copper and data in the literature [9]. The difference between the peak emission wavelength of the calculated spectrum and the experimental data for copper is most likely attributable to the uncertainty in the calculated density of states where a small change in the onset energy of the sp and d bands is squared then integrated.

The FWHM of the 99.95 % purity copper sample is 30 nm wider than the 99.9999 % purity sample (Figure 5.21). The additional width is attributed to the convolution of photoluminescence emission peaks from impurities combined with the emission from elemental copper.

The FWHM of our 99.9999 % purity copper spectrum and the calculated spectrum agree to within 5 nm (Figure 5.21). The FWHM of the copper spectrum measured by Mooradian is 40 nm narrower than the 99.9999 % purity sample [9]. According to Mooradian, ingots, single crystal slices and thin films all produced the same photoluminescence emission spectra, indicating that sample form is not the reason for the disparity between FWHM. Our data has shown that a narrower spectrum can be attributed to a higher purity of sample. Mooradian does not state the composition of their sample, however, it is unlikely that a sample with purity greater than 99.9999 % was studied in their work. Our experimental data has shown that the measured spectrum of copper broadens as a function of time which we attribute to oxidation of the sample (Figure 5.11). In Figure 5.21 we have presented the spectra for the 99.9999 % purity

copper sample measured 3 days after sample polishing as this was the narrowest FWHM, and hence least oxidised, of the copper spectra measured in our study. Although the work by Mooradian does not state the conditions of storage of their sample, they do not specify any special precautions taken, and the samples in their study appear to have been subject to the same storage conditions as our 99.9999 % purity sample. Therefore, the effect of oxidation would be expected to be equivalent in the two studies. We therefore, cannot explain the reason for the discrepancy in the FWHM between Mooradian's data and our 99.9999 % purity data.

Over the course of the 22 days' measurements the photoluminescence intensity of the 600 nm peak in the copper spectrum increased at a more rapid rate than the 800 nm peak (Figure 5.11). The increase in the intensity of the 600 nm peak is not consistent with an increase due the convolution of the newly polished copper luminescence spectrum and an increasing 800 nm peak. This leads us to the conclusion that the 800 nm peak originates from an oxide on the sample surface and that the 600 nm peak has a large component from an oxide layer [81, 82].

Spatially resolved measurements across the 99.9999 % purity copper sample surface were made 13 days after sample polishing and showed a broad similarity in the overall spectral shape and good agreement for the peak photoluminescence emission wavelength (Figure 5.9). The average variation in peak photoluminescence emission intensity across the sample was ~70 %. FWHM varied by a maximum of 53 % (excluding the spectrum at 1 mm). At 1 mm, a FWHM 141 % greater than the narrowest FWHM (at 0 mm) was observed. Subtraction of the normalised spectrum at 0 mm from the spectrum at 1 mm revealed a second peak centred around 800 nm. The spectral shape was consistent with the spectrum observed 22 days after sample polishing which was attributed to the formation of an oxide on the sample surface. Due to the measurement

being made 13 days after polishing of the sample, we attribute the spectrum at 1 mm to the formation of an inhomogeneous oxide layer on the copper surface.

Similar to the gold sample the copper sample displayed a linear relationship between photoluminescence emission intensity and excitation power (Figure 5.10) which is consistent with the theoretical work of Boyd (equation (2.33) in chapter 2) [10].

Oscillations in emission intensity for gold and copper over a period of hours

Peak photoluminescence emission intensity in both the 99.999 % purity gold and 99.9999 % purity copper samples oscillated over a period of several hours (Figure 5.5 and Figure 5.12). Spectral shape also varied over the course of the measurement but there was no obvious relationship with the variation in intensity. There are no reports in the literature of such a variation having been observed before. The possibility of the effect being due to the experimental setup is eliminated as, under identical conditions, no oscillations were observed in niobium, $SnMo_6S_8$ or YBCO (Chapter 6). Resistivity measurements, which were highly sensitive to changes in temperature, did not show the oscillation suggesting that thermal processes were not the source of the oscillation. The observed period of oscillation was different at 3 K and 100 K for both samples, however, a systematic study was not carried out to discover if the observed period of oscillation was reproducible at each temperature.

Data in the literature of persistent photoconductivity report an initial decrease in photoluminescence emission intensity over the course of several hours in oxygen depleted cuprate superconductors which is on a similar timeframe to the decrease we have observed [20, 126, 127]. However, they did not observe the oscillation we found for both gold and copper. At present we have no explanation as to the processes occurring to

create the oscillation in photoluminescence intensity over the course of several hours under continuous sample excitation.

Temperature dependent measurements

A systematic study of photoluminescence emission from gold and copper as a function of temperature has not been published in the literature. However, the work of Mooradian presents individual measurements at 300 K and 10 K for gold and copper. A decrease in peak photoluminescence emission wavelength from 520 nm to 500 nm is stated for gold and from 593 nm to 580 nm for copper. FWHM is reported to decrease for both gold and copper but a value is only given for gold where a decrease of 50 nm is presented [9]. No indication is given by Mooradian as to the change in peak photoluminescence emission intensity between 300 K and 10 K.

In our data, the peak photoluminescence emission wavelength of gold lay below the cut off wavelength of the Raman Razoredge filter and hence no observations could be made as to a change in the peak photoluminescence emission wavelength with temperature between 300 K and 79 K. No shift in peak wavelength was observable for copper. The FWHM of both gold and copper did not show a change as a function of temperature greater the noise on the data. We conclude that the differences between Mooradian's observations and our data can be attributed to changes in photoluminescence properties occurring below 79 K, which is below the range of our measurements.

A reproducible increase in peak photoluminescence emission intensity of approximately a factor of two was measured for the 99.999 % purity gold sample and a factor of five for 99.9999 % purity copper sample between 300 K and 79 K (Figure 5.7 and Figure 5.15). The larger increase in peak photoluminescence intensity for copper

compared to gold between 300 K and 79 K is consistent with the observation in the literature of the broadening of the 2 eV peak in the absorption spectrum of copper as a function of decreasing temperature which is not present for the corresponding 2.5 eV peak in gold [79, 80]. No indication is given by Mooradian as to the change in peak photoluminescence emission intensity between 300 K and 10 K and hence a comparison could not be made as to the relative intensities observed in their study.

5.7. Conclusions

This chapter has presented the first systematic study of the photoluminescence emission of gold and copper as a function of temperature between 300 K and 79 K along with measurements as a function of position on the sample surface, excitation power and time. A comparison has been made between measurements of high purity gold and copper with experimental and theoretical work in the literature. Good agreement has been found between these sets of data for gold and copper and the probable presence of an oxide on the copper sample discussed. No explanation has been found for the origin of variations in photoluminescence emission intensity and spectral shape as a function of time.

Our study of the photoluminescence emission of gold and copper as a function of temperature has shown a reproducible increase in peak photoluminescence emission intensity of approximately a factor of two for 99.999 % purity gold and a factor of five for 99.9999 % purity copper between 300 K and 79 K. Spectral shape (FWHM) and peak photoluminescence emission wavelength showed no change as a function of temperature for both gold and copper over the 220 K temperature range. The following chapter will

extend the study of photoluminescence emission as a function of temperature to metallic

and ceramic superconducting samples.

Chapter 6. Photoluminescence of superconducting materials in the normal state

6.1. Introduction

Data in the literature on the photoluminescence emission from superconductors gives conflicting results and interpretations for of the origin of the luminescence and the influence of the superconducting transition on photoluminescence emission. Studies have independently looked at emission from low temperature alloys (Nb_3Sn and MgB_2, [16-18]) and a range of high temperature cuprate materials [13-15]. However, to date, there has been no systematic study of emission from both low and high temperature superconductors by one author, which would allow differences due to experimental geometries to be eliminated from comparisons of the different classes of samples.

The following chapter presents data for low and high temperature superconductors in their normal state measured as a function of temperature. Data are given for spatially resolved measurements of the sample surfaces and the excitation power and temperature dependence of the photoluminescence emission. The variation in photoluminescence emission under continuous excitation over a period of hours is also presented for a selection of the samples. The structure of the chapter is presented as follows; in section 6.2. sample details are presented along with a brief summary of their fabrication procedures. Section 6.3. includes the density of states data which have been calculated for both the low and high temperature superconductors. The data have then

been used to calculate photoluminescence emission spectra for all the samples studied in this thesis. The calculated spectra have then been compared with experimentally measured spectra.

Sections 6.4. 6.5. and 6.6. present data for the work on niobium, the Chevrel phase superconductors ($PbMo_6S_8$, $SnMo_6S_8$, $Pb_{1-x}Gd_xMo_6S_8$ x = 0.3 and $Sn_{1-x}Eu_xMo_6S_8$ x = 035) and the high temperature cuprate superconductors (DyBCO and YBCO). Spatially resolved measurements from across the sample surface and the excitation power dependence of the photoluminescence spectra are presented for all samples apart from $Pb_{1-x}Gd_xMo_6S_8$ x = 0.3, where damage occurred to the sample surface upon application of the laser. The peak photoluminescence emission intensity and FWHM are presented as a function of temperature for niobium, $PbMo_6S_8$, $SnMo_6S_8$, DyBCO and YBCO. Measurements of photoluminescence emission spectra over a period of several hours are presented for niobium, $SnMo_6S_8$ and YBCO. The effect of heating and roughening of the polished niobium sample is also investigated to examine whether oxidation should be a consideration in the analysis of the data. After the data for each material has been presented, a comparison and discussion of relevant data in the literature is provided. Finally, a general discussion of the data is presented in section 6.7. followed by conclusions in section 6.8.

6.2. Samples

6.2.1. Sample purity and form

The purity and form of the samples measured using the high sensitivity photoluminescence equipment are listed in Table 6.1. Fabrication of the Chevrel phase

materials was carried out by Nigel Leigh in Durham. Detailed information on the fabrication process can be found in references [180, 181]. Single crystal DyBCO and YBCO were fabricated at Birmingham University and their structure confirmed to be single crystal in measurements made at the ESRF Xray Synchrotron Facility in Grenoble, France [182]. The thin film YBCO sample was fabricated at Cambridge University using pulsed laser deposition in an off-axis geometry [183].

The single crystal cuprates were prepared by polishing down to 1 μm roughness using liquid diamond paste (as detailed in Chapter 4) followed by cleaning using acetone and isopropanol. Polishing of the niobium sample led to the photoluminescence emission intensity decreasing below the limit of resolution of the detector and, as such, an unpolished sample was used for the variable temperature measurements presented below. The granular polycrystalline composition of the Chevrel phase materials meant that polishing was ineffective, therefore, these samples were simply cleaned in acetone and isopropanol before the measurement of the photoluminescence emission spectra. The thin film YBCO sample was also only cleaned in isopropanol and acetone as its roughness was already less than the minimum roughness achievable using diamond paste polishing.

Where possible, the samples were mounted directly to the copper sample holder in the cryostat using Apiezon N grease. However, in the case of $PbMo_6S_8$, $Sn_{1-x}Eu_xMo_6S_8$ x = 0.35 and the YBCO single crystal, the sample sizes were small and required a silicon wafer to be placed between the sample and sample holder to prevent the excitation of photoluminescence emission from the copper sample holder itself.

Sample purity	Form	Supplier
Nb	Single crystal	Sigma-Aldrich
$PbMo_6S_8$	Polycrystalline	Fabricated in Durham [180, 181]
$SnMo_6S_8$	Polycrystalline	Fabricated in Durham[180, 181]
$Pb_{1-x}Gd_xMo_6S_8$ x = 0.3	Polycrystalline	Fabricated in Durham [180, 181]
$Sn_{1-x}Eu_xMo_6S_8$ x = 0.35	Polycrystalline	Fabricated in Durham [180, 181]
DyBCO	Single crystal	Fabricated by Birmingham University[182]
YBCO	Single crystal	Fabricated by Birmingham University[182]
YBCO	Thin film	Fabricated by Cambridge University [183]

Table 6.1. Summary of the form of the elemental, Chevrel phase and cuprate superconductor samples and their suppliers.

6.3. Theoretical calculation of density of states

The density of states spectra for niobium, $PbMo_6S_8$, $SnMo_6S_8$, DyBCO and YBCO were calculated by Dr Stewart Clark using CASTEP software (Figure 6.1 and Figure 6.2) [170]. These data have been used along with the refractive index, extinction coefficient and absorption coefficient data presented in Chapter 3 to calculate the photoluminescence emission spectra for the samples. A comparison of the calculated spectra and experimentally measured data is given at the end of sections 6.4.1. to 6.6.2. for niobium, $PbMo_6S_8$, $SnMo_6S_8$, DyBCO and YBCO, respectively.
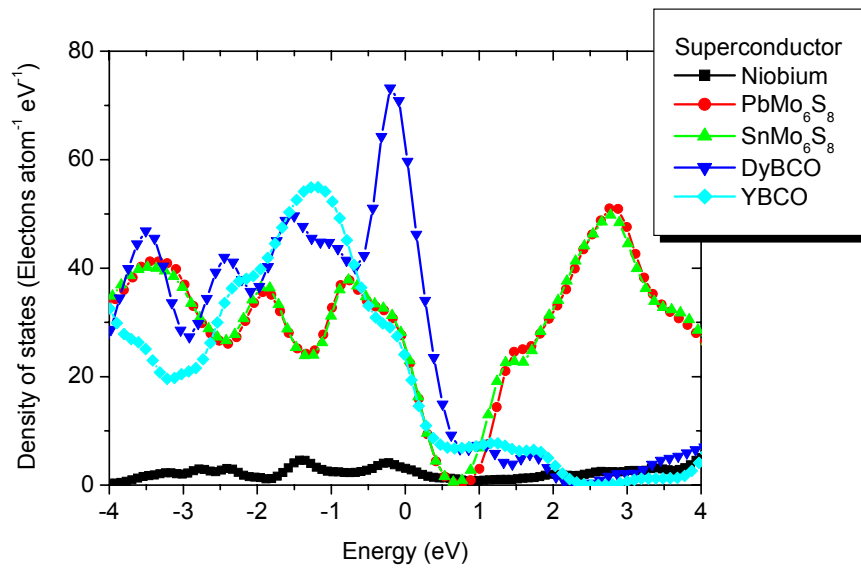
Figure 6.1 Calculated density of states as a function of energy for niobium, PbMo$_6$S$_8$, SnMo$_6$S$_8$, DyBCO and YBCO. Calculations were performed by Dr Stewart Clark using CASTEP software [170]. The Fermi energy is located at zero energy on the x axis scale.
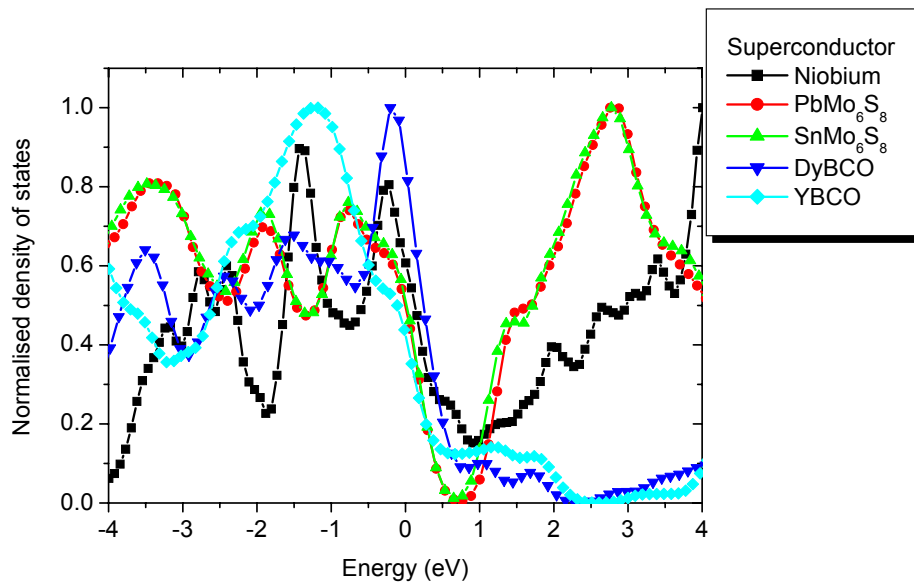

Figure 6.2 Normalised density of states as a function of energy for niobium, PbMo$_6$S$_8$, SnMo$_6$S$_8$, DyBCO and YBCO. Data is normalised to the peak density of states in the energy range -4 eV to +4 eV. Calculations were performed by Dr Stewart Clark using CASTEP software [170]. The Fermi energy is located at zero energy on the x axis scale.

A comparison between the calculated density of states of niobium and data from the literature is given in Figure 6.3 in the energy range +/- 3 eV from the Fermi energy [97, 184]. This energy range is important as it is the region probed by optical transitions. The three spectra compare extremely well in this region, however, only calculated density of states and no experimental data were available in the literature for comparison. Data for the density of states as a function of energy close to the Fermi level were not available in the literature for comparison with the CASTEP data for the Chevrel phase and high temperature cuprate superconductor materials.
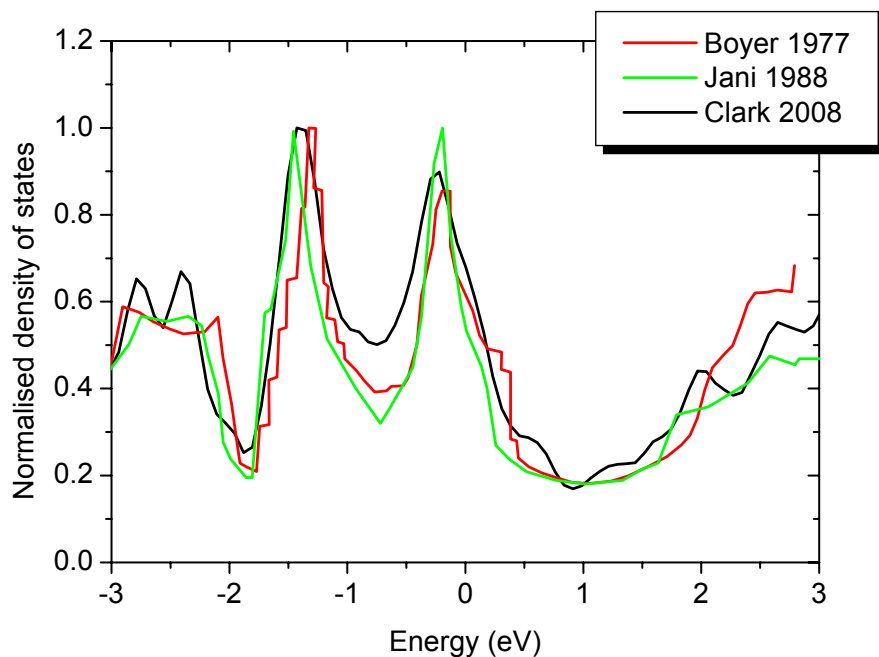

Figure 6.3. Comparison of the calculated density of states of niobium in the literature with the calculated density of states by Dr Stewart Clark [97, 184]

6.4. Niobium

6.4.1. Niobium – Experimental results

Spatially resolved measurements across the sample surface

Figure 6.4 shows the spatially resolved photoluminescence emission spectra of 99.99 % purity single crystal niobium. Measurements were made in 1 mm intervals along the horizontal direction across the vertical middle of the sample. The inset figure shows the normalised photoluminescence emission spectra.
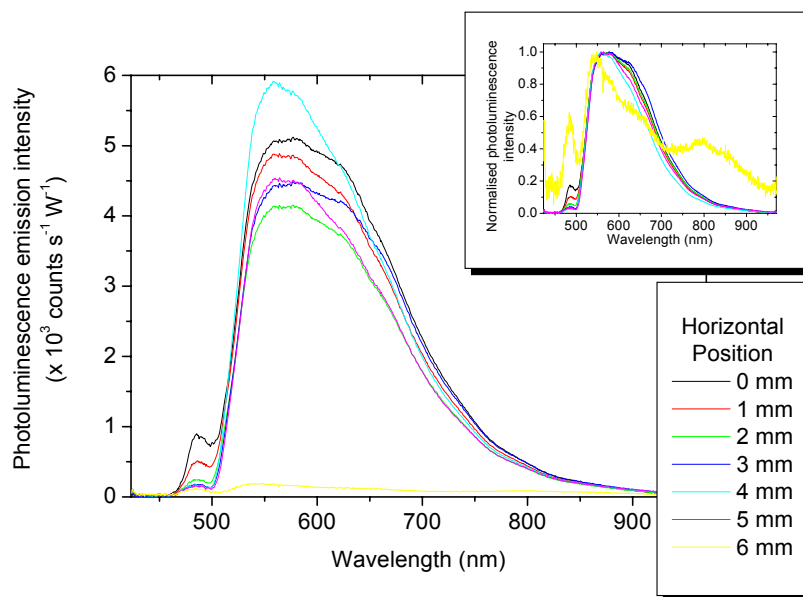

Figure 6.4 Photoluminescence emission spectra of 99.99 % purity single crystal niobium measured at different positions horizontally across the sample surface. The inset graph shows the normalised photoluminescence emission spectra. Measurements were made along the horizontal direction at 1mm intervals in one of three vertical positions (top, middle, bottom). The spectra were measured in the middle vertical position. The edge of the sample was at 0 mm and 6 mm. At 6 mm the laser spot was located on both the silicon and sample. Typical photoluminescence excitation power was 51 mW.

Excitation power dependence

Figure 6.5 displays the normalised photoluminescence emission spectra of 99.99 % single crystal niobium measured as a function of excitation power. The excitation power of the laser was manually increased from 0 to 102 mW before decreasing the power back to 55 mW. Measurement of excitation power was carried out using a handheld Melles Griot laser power meter which was positioned between the final focussing lens and the cryostat window.
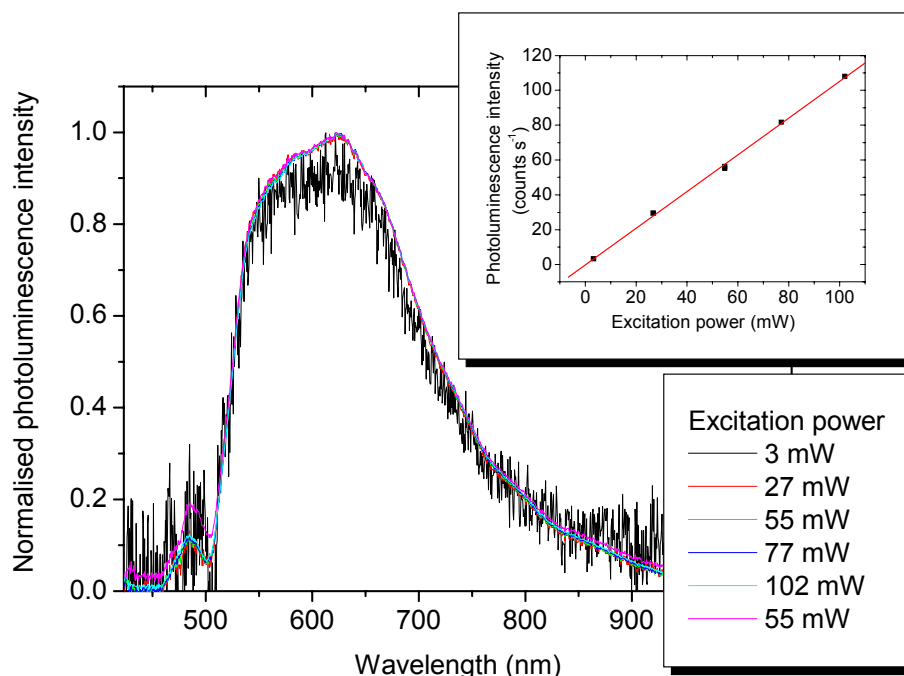

Figure 6.5. The normalised photoluminescence emission spectra of 99.99 % purity single crystal niobium measured for increasing excitation powers at 304 K. The inset graph shows the peak photoluminescence emission intensity as a function of excitation power. Laser power was manually increased from 0 to 102 mW before the power was reduced and the measurement at 55 mW repeated.

Variation of photoluminescence spectra over a period of hours

Figure 6.6 shows a selection of seven normalised photoluminescence emission spectra taken at three minute intervals over a 13 hour period at 101 K. The inset graph shows the variation in peak photoluminescence emission intensity over this period. The first measurement was made immediately after the focussed laser spot had been repositioned on the sample.
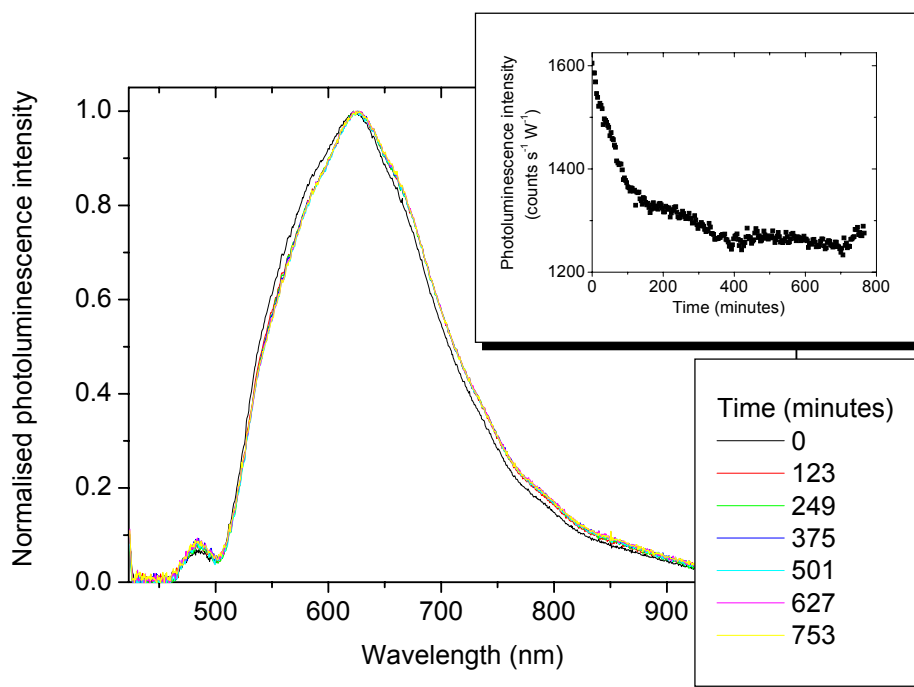

Figure 6.6. The normalised photoluminescence emission spectra of 99.99 % purity single crystal niobium measured over a 12 hour period. Each spectrum was measured at 101 K in 3 minute intervals. The main graph shows 7 normalised spectra measured at various times throughout the 12 hour period. The inset graph shows the change in the peak photoluminescence emission intensity (in counts s^{-1} W^{-1}) as a function of time. Typical photoluminescence excitation power was 51 mW.

Oxidation

In order to investigate the possibility that an oxide was present on the surface of the niobium samples, two identical sections of 99.99 % single crystal niobium were prepared using a diamond saw. A measurement of the photoluminescence emission spectrum was made of one of the sections before the sample was polished to 1 μm roughness using a polishing and lapping machine. A comparison of the pre- and post-polishing photoluminescence emission spectra showed a decrease in peak photoluminescence emission intensity from approximately 56 counts s^{-1} (1100 counts s^{-1} W^{-1}) to less than 2 count s^{-1} (< 40 counts s^{-1} W^{-1}) (Figure 5.1). The count rate of 2 counts s^{-1} was at the noise floor of the detector and hence a spectrum could not be resolved to any degree of accuracy. A repeat of the measurement on the polished sample after 20 weeks showed the intensity of the photoluminescence emission spectrum to still be below the resolution of the detector.
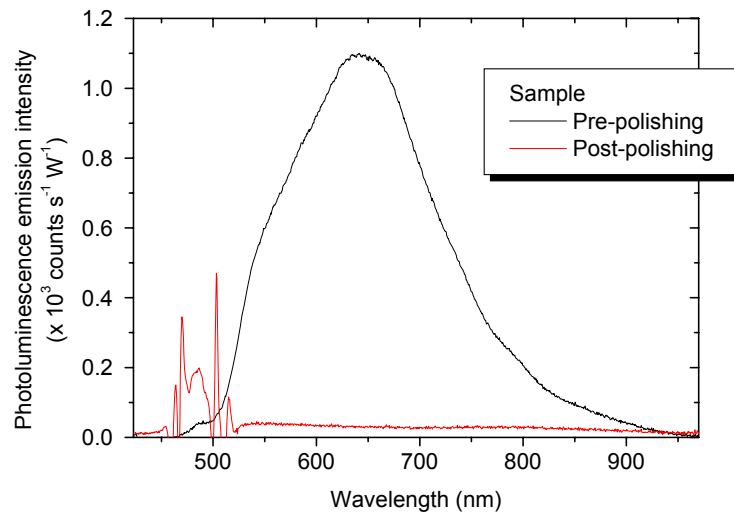

Figure 6.7. Photoluminescence emission spectra of niobium before and after polishing. Post polishing measurements were made with the cryostat window in place in the optical setup. Measurements were made within 24 hours of polishing. Typical photoluminescence excitation power was 51 mW.

The polished sample was then roughened using 1200 grade abrasive paper and cleaned in acetone and isopropanol in an ultrasonic bath. Figure 6.8 shows the pre- and post-polishing photoluminescence emission spectra along with the emission spectrum for the roughened sample. The peak photoluminescence emission intensity can be seen to have increased from < 2 count s^{-1} (20 counts s^{-1} W^{-1}) to ~9 counts s^{-1} (178 counts s^{-1} W^{-1}). The sample was then heated on a hot plate at 200 ^{o}C for 30 minutes leading to a further increase in peak photoluminescence intensity to ~100 counts s^{-1} (1960 counts s^{-1} W^{-1}).
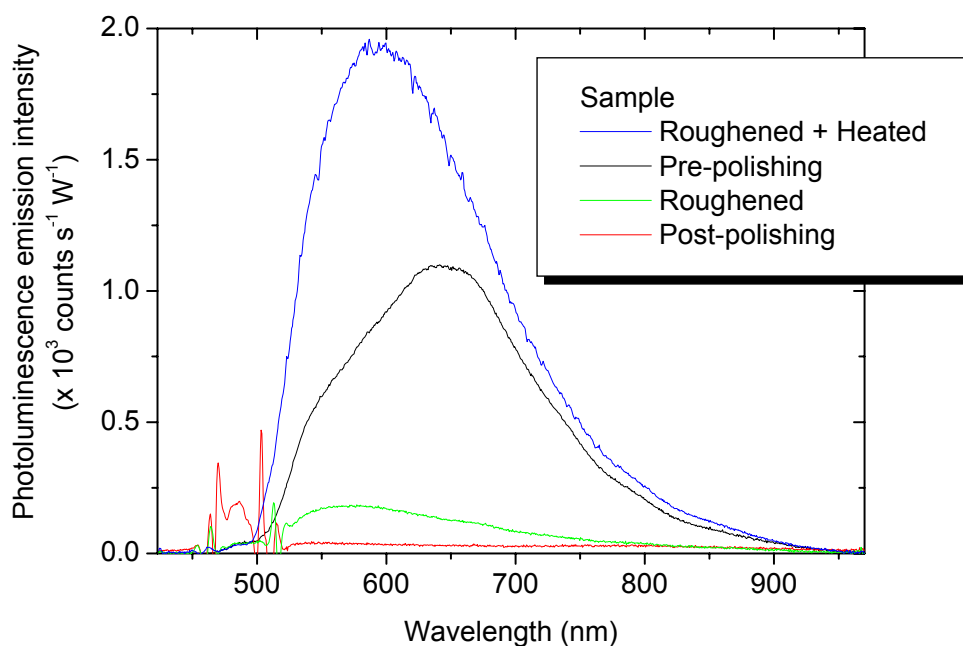

Figure 6.8. Photoluminescence emission spectra of 99.99 % purity single crystal niobium pre- and post-polishing and after roughening and heating. Polishing was carried out down to 1 μm diamond paste, the sample was then roughened using 1200 grade abrasive paper and cleaned with acetone and isopropanol. The roughened sample was then heated on a hotplate at 200°C for 30 minutes. Typical photoluminescence excitation power was 51 mW.

Due to the peak photoluminescence emission intensity of the polished sample lying below the resolution of the detector, all measurements presented for the niobium sample in this thesis were made on the second unpolished diamond saw cut section of 99.99 % purity single crystal niobium.

Temperature dependent measurements

The photoluminescence emission spectra of 99.99 % purity niobium measured as a function of temperature are presented below. Measurements were made for increasing, decreasing and a random order of temperatures. Figure 6.9 shows the photoluminescence
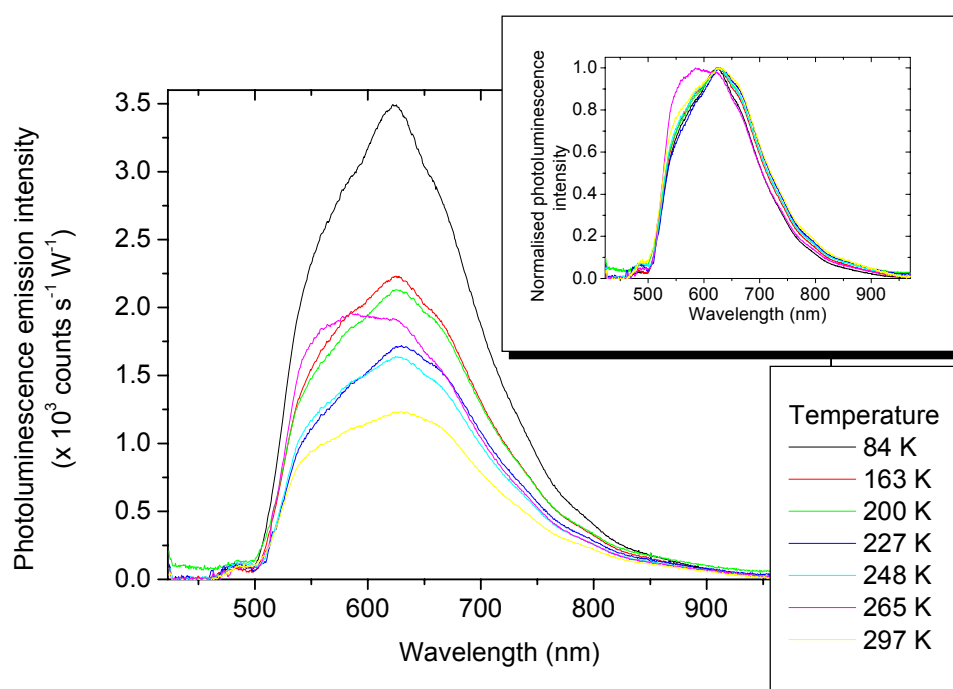

Figure 6.9. Photoluminescence emission spectra of 99.99 % purity single crystal niobium measured as a function of temperature. Spectra were collected for decreasing temperatures beginning at 304 K. The inset graph shows the normalised spectra. All spectra were measured after a 30 minute period which began once the sample had been repositioned at the set temperature to correct for thermal contraction of the sample holder. Typical photoluminescence excitation powers were 51 mW.

emission spectra measured for decreasing temperatures between 297 K and 84 K. Measurements were made 30 minutes after the sample had been repositioned to account for thermal contraction of the sample holder.

Peak photoluminescence emission intensity measured as a function of temperature is shown in Figure 6.10. The peak emission intensity is shown normalised to 1 at 110 K in Figure 6.11. The inset graph in Figure 6.11 shows the temperature region below 115 K in detail. The sharp increase in peak intensity below 100 K was reproducible in all measurements and was independent of the order of the measurement temperature. The full width half maximum of the photoluminescence emission spectra of 99.99 % single crystal niobium measured as a function of temperature is shown in Figure 6.12.
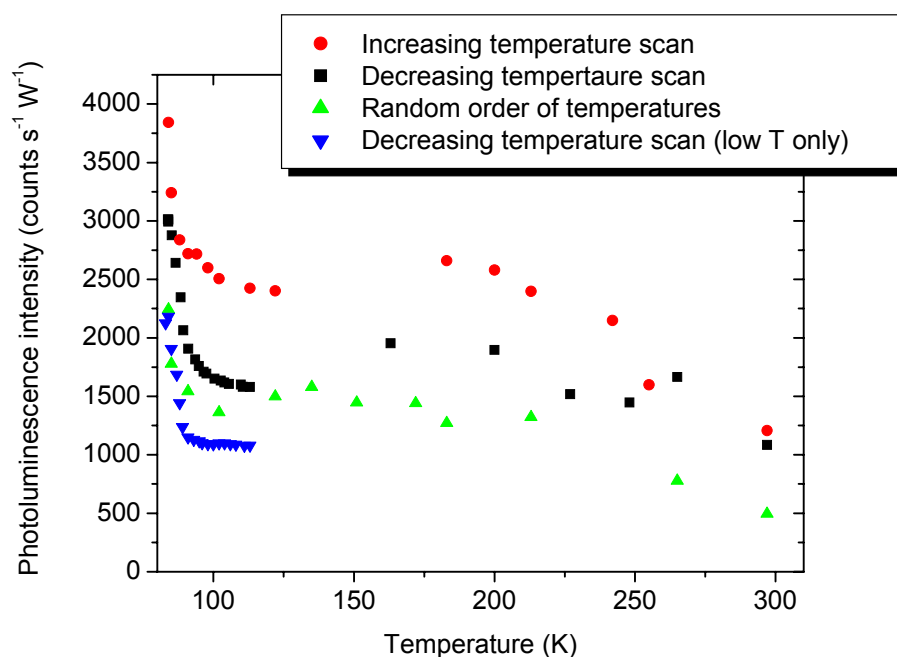

Figure 6.10. Peak photoluminescence emission intensity measured as a function of temperature for 99.99 % purity single crystal niobium. The measurements were made over a six day period for increasing (red), decreasing (black and blue) and a random order of temperatures (green). Typical photoluminescence excitation powers were 51 mW.
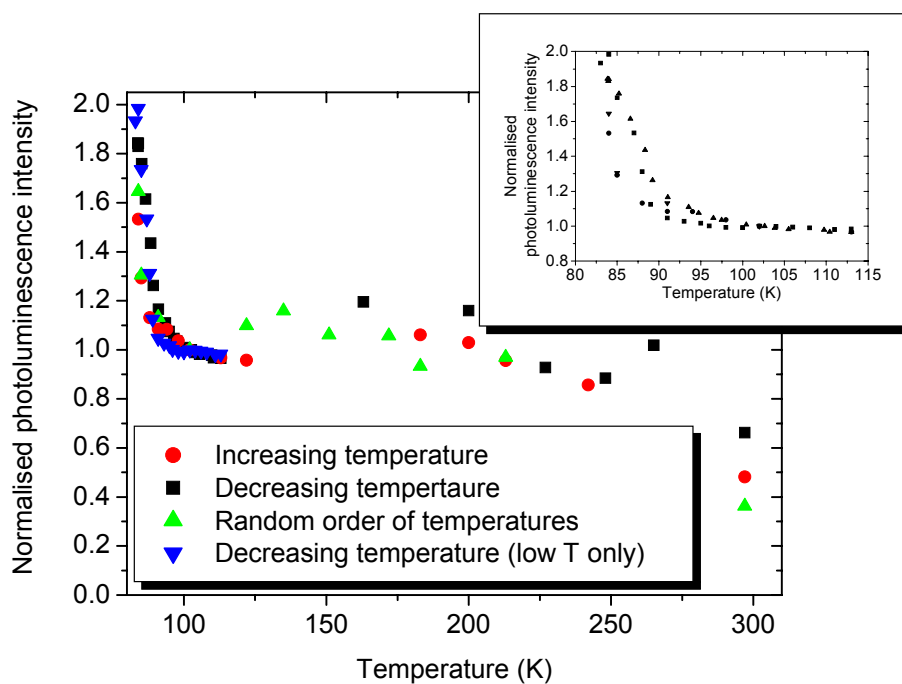
Figure 6.11. The peak photoluminescence emission intensity of 99.99 % purity single crystal niobium measured as a function of temperature and normalised to 1 at 110 K. The measurements were made over a six day period for increasing (red), decreasing (black and blue) and a random order of temperatures (green). Typical photoluminescence excitation powers were 51 mW.
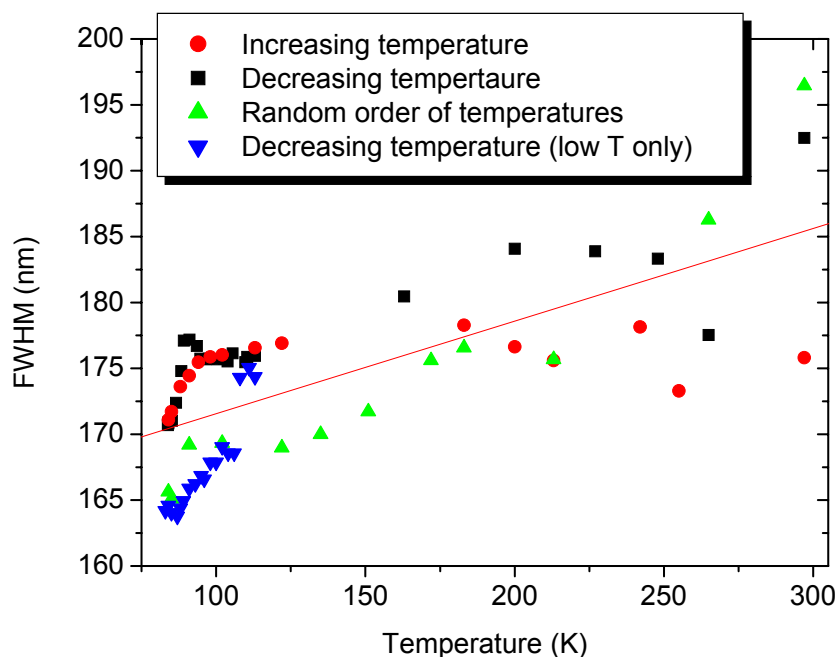
Figure 6.12. Full width half maximum (FWHM) of the photoluminescence emission spectra of 99.99 % purity single crystal niobium measured as a function of temperature. The measurements were made over a six day period for increasing (red), decreasing (black and blue) and a random order of temperatures (green). Typical photoluminescence excitation powers were 51 mW. The red line is displayed as a guide to the eye.

6.4.2. Niobium – Analysis and discussion

Niobium band structure

The band structure of niobium consists of widely spaced d-bands and hybridised sp-bands. This is similar to the band structure observed in gold and copper. However, the d-bands of niobium are more widely spaced and are only partially filled, unlike the filled bands of gold and copper [96, 97]. Transitions between the 3rd and 4th d-bands lead to a peak in the absorption spectrum of niobium at 2.2 eV [96].

Although there is no work in the literature measuring the photoluminescence emission from niobium, comparisons can be drawn with materials with similar band structures. Tominaga asserts that the mechanism for photoluminescence in the superconducting alloy Nb_3Sn can be assigned to transitions between d-holes and electrons below the Fermi surface due to the similarity between the band structure of the gold and copper and Nb_3Sn. Applying the same principle to niobium, suggests that a peak should therefore be observed at 2.2 eV (563 eV).

Room temperature data for niobium

The peak photoluminescence emission wavelength of niobium was measured at 625 nm. Spatially resolved measurements of the photoluminescence emission spectra of niobium showed a peak photoluminescence emission intensity which varied by less than 100 counts s^{-1} (2000 counts s^{-1} W^{-1}) across the surface (Figure 6.4) and a change in FWHM of 26 nm (~18 %). The small changes in the photoluminescence emission spectra are thought to be caused by scattering from the macroscopic roughness of the sample surface directing light into the spectrometer at slightly different angles, changing the relative intensity of the measured spectra. The linear dependence of the photoluminescence emission intensity with excitation power is consistent with a single photon excitation and emission process (Figure 6.5) [10].

Temperature dependent measurements for niobium

Between 304 K and 80 K the FWHM decreased by approximately 15 nm (Figure 6.12). The peak photoluminescence emission wavelength remained constant as a function of temperature (Figure 6.9), however, a reproducible increase in the peak photoluminescence emission intensity by a factor of two was measured for the 99.99 %

purity niobium sample between 304 K and 95 K (Figure 6.10, Figure 6.11). Below 95 K a sharp increase in peak photoluminescence emission intensity was observed, which will be discussed in section 6.7.

No work has been published in literature for the photoluminescence emission spectrum of niobium at room temperature or as a function of temperature. The photoluminescence emission intensity from Nb_3Sn between room temperature and 5 K has been measured by Tominaga and is reported to be almost constant down to approximately 25 K where there is a decrease then rapid increase in the photoluminescence intensity at the superconducting critical temperature (Figure 2.15) [16].

Oxidation of the sample surface

The fact that no photoluminescence emission spectrum could be measured for the newly polished niobium sample suggests that the emission spectrum from the pre-polished sample was due to an oxide on the sample surface (Figure 5.1). This is supported by the increase in peak photoluminescence emission intensity following roughening and heating of the sample (Figure 6.8). The similarity between the spectral shape of the roughened sample and the heated sample suggests that the increase in the luminescence intensity of the roughened sample was not due to the damage caused to the sample surface by roughening but to the beginning of the oxidation process.

The difference between the photoluminescence emission spectra of the pre-polished diamond saw cut sample and the same sample after polishing, roughening and heating is most likely due to the presence of oxides formed under different conditions (one from the heat of the cutting process and the other from heating on a hot plate) [185-187]. The photoluminescence emission spectrum of the niobium sample measured in this

work is therefore assumed to originate from an oxide layer on the surface of the sample and not from pure niobium.

Calculated spectra

Figure 6.13 shows a comparison between the measured photoluminescence emission spectrum of 99.99 % single crystal niobium and the spectrum calculated using equation (2.37). The calculated spectrum contains two peaks at approximately 550 nm and 900 nm which do not correspond to the single peak at 625 nm in the experimental spectrum.
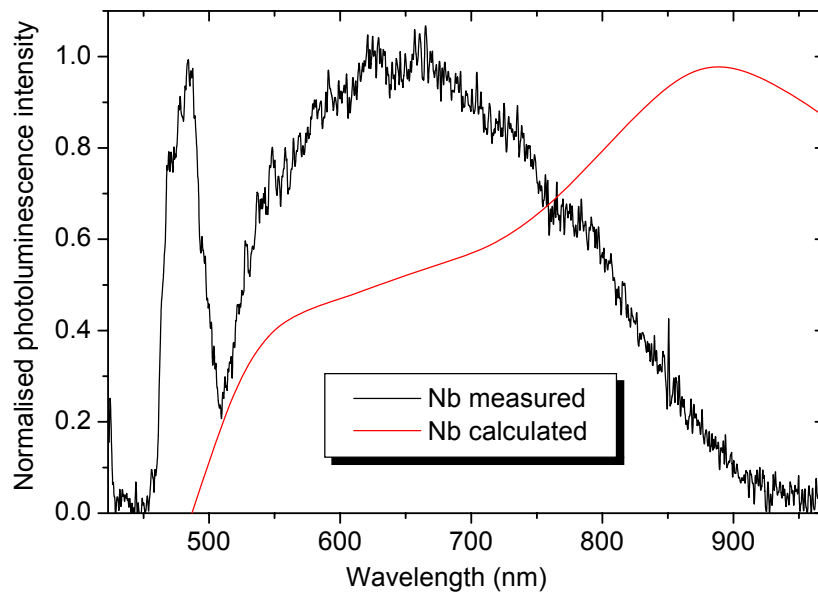

Figure 6.13 Comparison of the normalised room temperature photoluminescence emission spectra of niobium and the photoluminescence emission spectrum calculated using equation (2.37). The calculated spectrum used data for the refractive index and extinction coefficient from reference [150] and density of states calculated by Dr Stewart Clark.

As discussed above, the photoluminescence emission spectrum measured for niobium most likely originates from an oxide on the sample surface. Since the calculation uses density of states and optical data for pure niobium, the calculated spectrum is not representative of this sample.

6.5. Chevrel phase materials

6.5.1. Chevrel phase PbMo$_6$S$_8$

Spatially resolved measurements across the sample surface

Figure 6.14 shows the spatially resolved photoluminescence emission spectra of PbMo$_6$S$_8$ measured at 1 mm intervals across the sample surface. Spectra were measured in one of three vertical positions (top, middle and bottom) and data are shown for measurements made in the middle position. The inset figure shows the normalised photoluminescence emission spectra.

Excitation power dependence

Figure 6.15 presents the normalised photoluminescence emission spectra of PbMo$_6$S$_8$ measured as a function of photoluminescence excitation power. Excitation power was manually increased from 70 mW to 131 mW and was measured using a Melles Griot handheld power meter positioned between the final focussing lens and the cryostat window. The inset figure shows the relationship between photoluminescence peak intensity and excitation power.
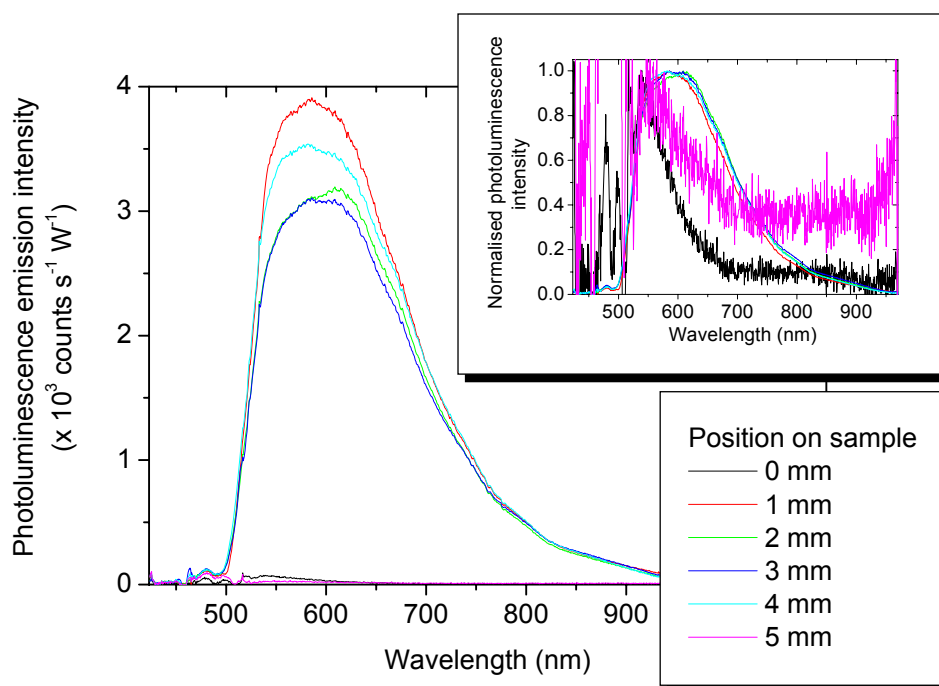
Figure 6.14 Photoluminescence emission spectra of polycrystalline PbMo$_6$S$_8$ measured at different positions across the sample surface. The inset graph shows the normalised photoluminescence emission spectra. Measurements were made along the horizontal direction at 1 mm intervals in one of three vertical positions (top, middle, bottom). The spectra displayed are measured in the middle vertical position. The edge of the sample was at 0 mm and 5 mm. At 0 mm and 5 mm the laser spot was on both the silicon and the edge of the sample. Typical photoluminescence excitation powers were 65 mW.
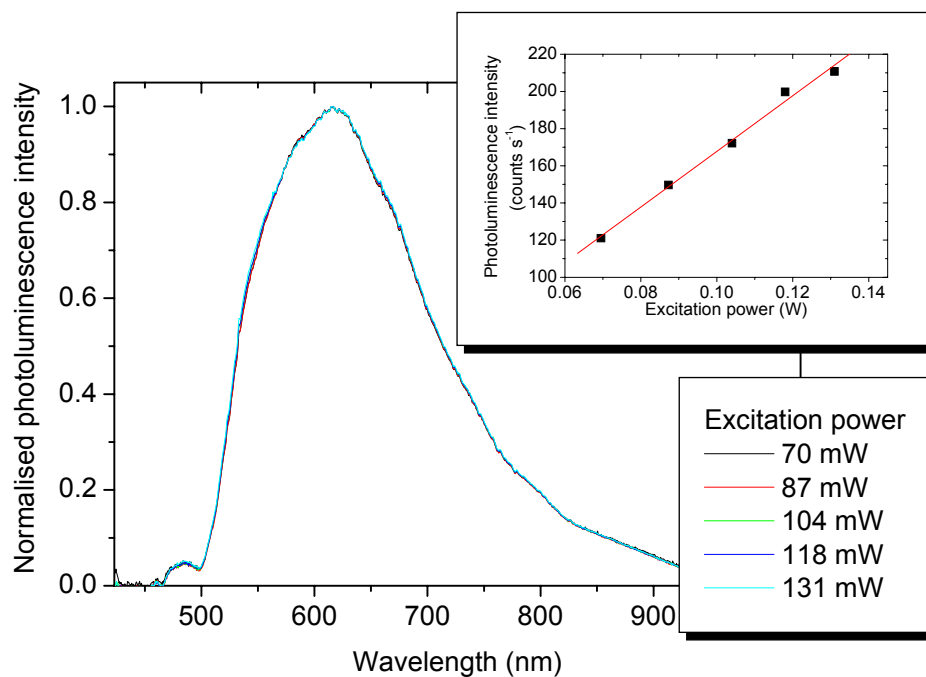
Figure 6.15. The normalised photoluminescence emission spectra of polycrystalline PbMo$_6$S$_8$ measured for increasing excitation powers at 79 K. The inset graph shows the peak photoluminescence emission intensity as a function of excitation power. Laser power was manually increased from 70 to 131 mW.

Temperature dependent measurements

Figure 6.16 shows the photoluminescence emission spectra of PbMo$_6$S$_8$ measured as a function of decreasing temperature between 304 K and 72 K. Spectra were measured after a 30 minute wait which began once the sample had been repositioned to account for thermal contraction of the sample holder.
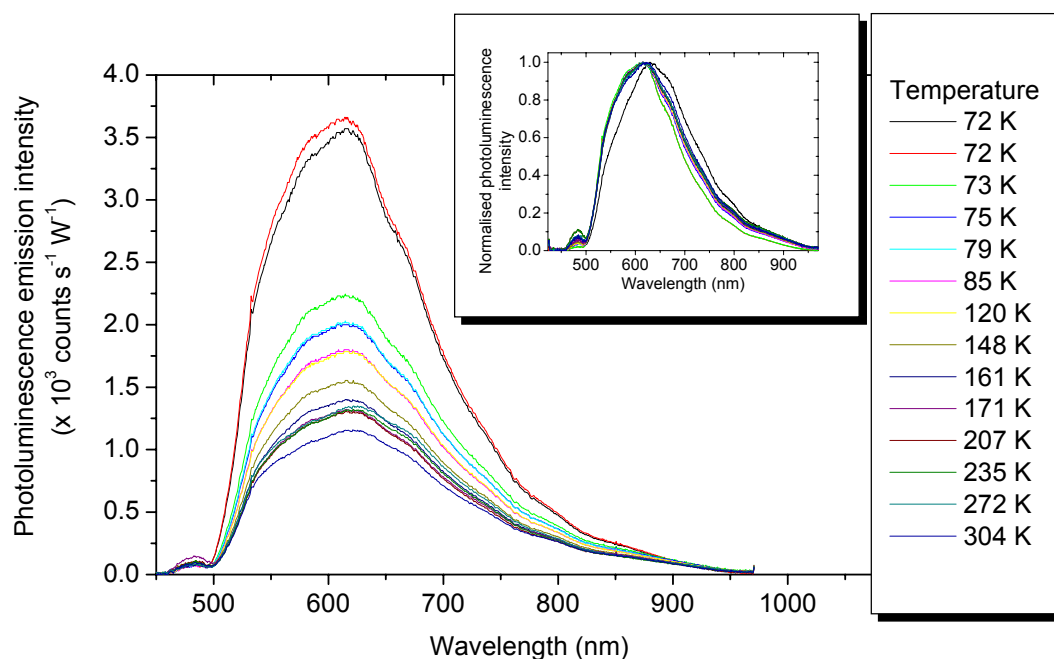
Figure 6.16. Photoluminescence emission spectra of polycrystalline PbMo$_6$S$_8$ measured as a function of temperature. Spectra were collected for decreasing temperatures between 304 K and 72 K. The inset graph shows the normalised spectra. All spectra were measured after a 30 minute period which began once the sample had been repositioned to correct for thermal contraction. Typical photoluminescence excitation powers were 65 mW.

Figure 6.17 and Figure 6.18 show the peak photoluminescence emission intensity measured as a function of temperature. In Figure 6.18 the intensity has been normalised to 1 at 79 K. The inset graph in both figures shows the region of rapid increased between 71 K and 78 K in detail. Measurements were made as a function of increasing, decreasing and a random order of temperatures. The rapid increase in photoluminescence intensity below 73 K was a reproducible feature which was observed even when a random order of temperatures was investigated.
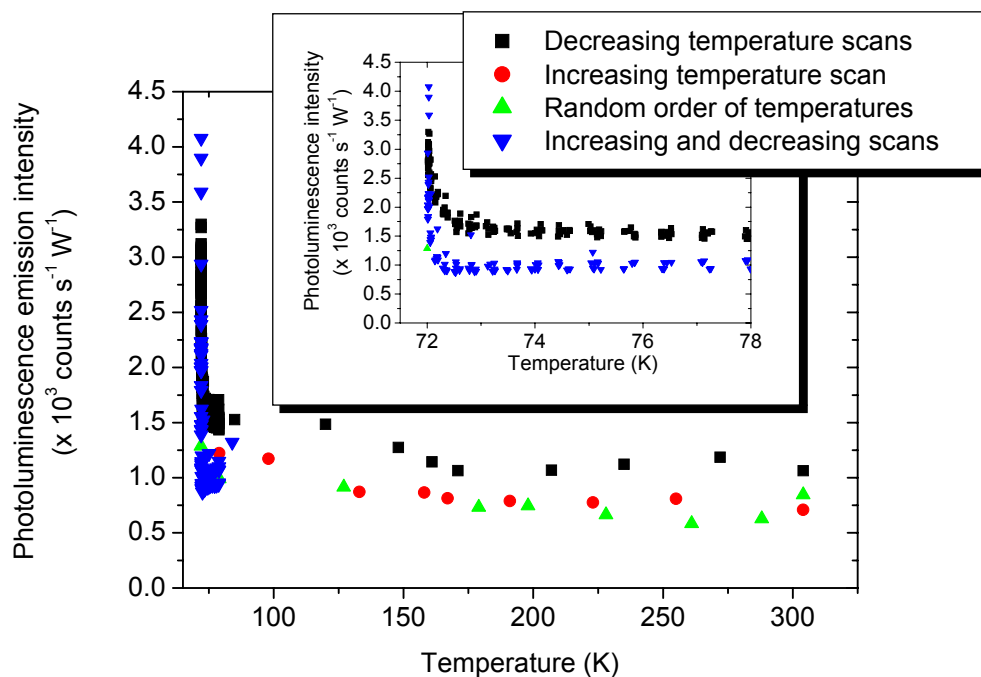
Figure 6.17. Peak photoluminescence emission intensity as a function of temperature for polycrystalline PbMo$_6$S$_8$. The measurements were made over a seven day period for decreasing (black), increasing (red and blue) and a random order of temperatures (green). Typical photoluminescence excitation powers were 65 mW.

Figure 6.18. Normalised peak photoluminescence emission intensity of polycrystalline PbMo₆S₈ measured as a function of temperature and normalised to 1 at 79 K. The measurements were made over a seven day period for decreasing (black), increasing (red and blue) and a random order of temperatures (green). Typical photoluminescence excitation powers were 65 mW.
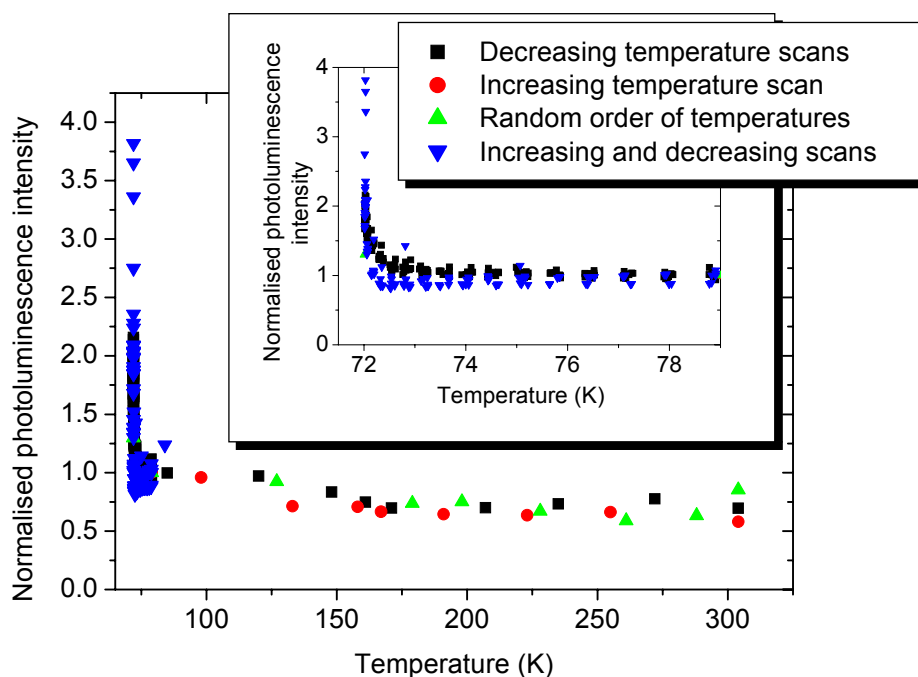
The FWHM of PbMo₆S₈ measured as a function of temperature is shown in Figure 6.19. Measurements were made for increasing, decreasing and a random order of temperatures.
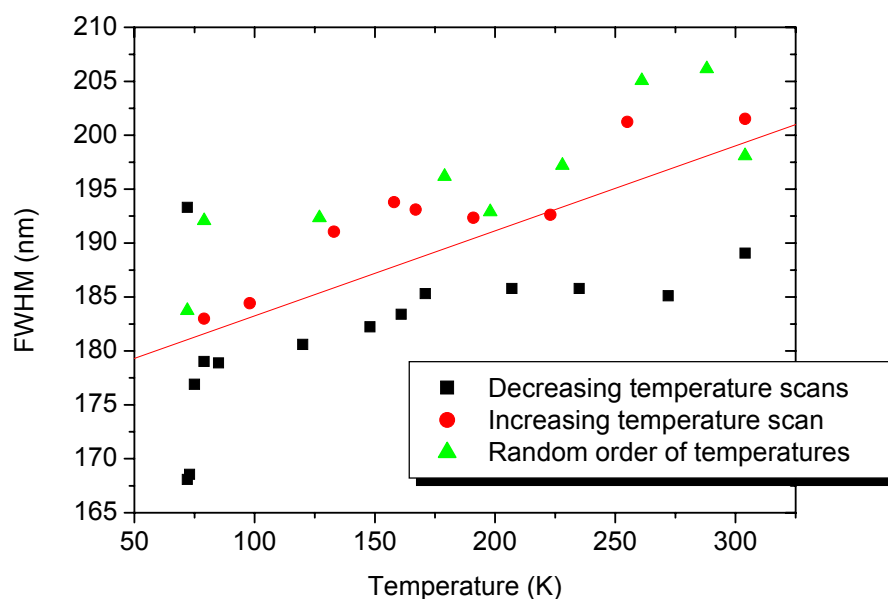
Figure 6.19. Variation in full width half maximum (FWHM) of the photoluminescence emission spectra of polycrystalline PbMo$_6$S$_8$ measured as a function of temperature. The measurements were made over a seven day period for decreasing (black), increasing (red) and a random order of temperatures (green). The red line is displayed as a guide to the eye. Typical photoluminescence excitation powers were 65 mW.

6.5.2. Chevrel phase SnMo$_6$S$_8$

Spatially resolved measurements across the sample surface

Figure 6.20 presents the spatially resolved photoluminescence emission spectra of SnMo$_6$S$_8$. Measurements were made at 1 mm intervals across the sample surface in a horizontal direction in one of three vertical positions (top, middle and bottom). The data displayed here were measured across the bottom position. The inset figure shows the normalised photoluminescence emission spectra. Measurements close to the edge of the sample showed evidence of luminescence from Apiezon N grease. Therefore, for all further measurements, spectra were excited from close to the centre of the sample.
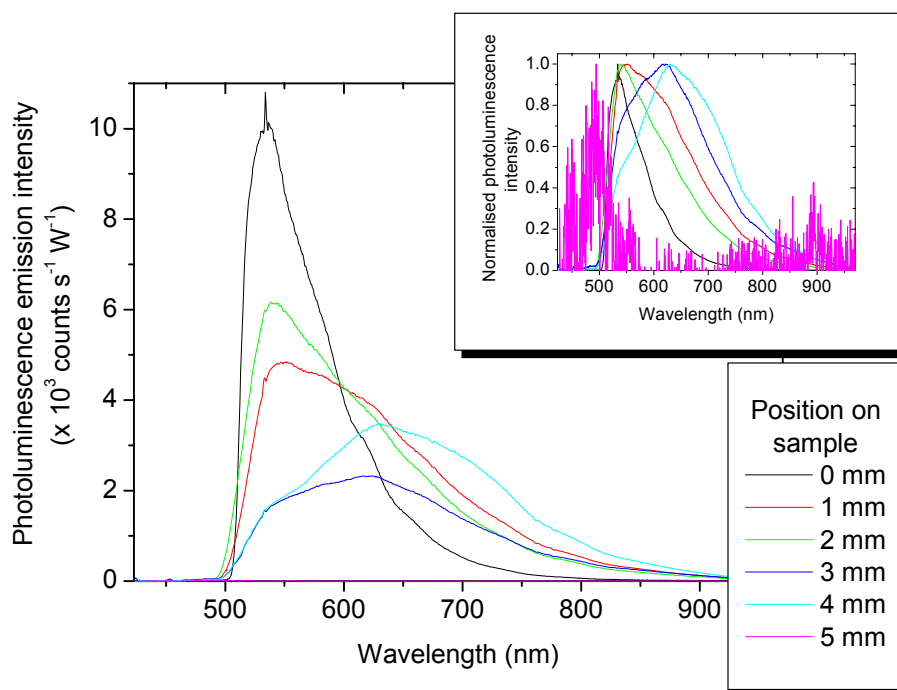
Figure 6.20 Photoluminescence emission spectra of polycrystalline SnMo$_6$S$_8$ measured at different positions across the sample surface. The inset graph shows the normalised photoluminescence emission spectra. Measurements were made along the horizontal direction at 1mm intervals in one of two vertical positions. The spectra displayed are measured across the bottom of the sample. At 0 mm and 5 mm the laser spot was on both the silicon and edge of the sample. Typical photoluminescence excitation powers were 65 mW.

Excitation power dependence

Figure 6.21 shows the normalised photoluminescence emission spectra of SnMo$_6$S$_8$ measured as a function of laser excitation power. Laser power was manually increased from 72 mW to 139 mW and power measured between the final focussing lens and the cryostat window using a handheld Melles Griot power meter. The inset figure shows peak photoluminescence emission intensity as a function of excitation power.
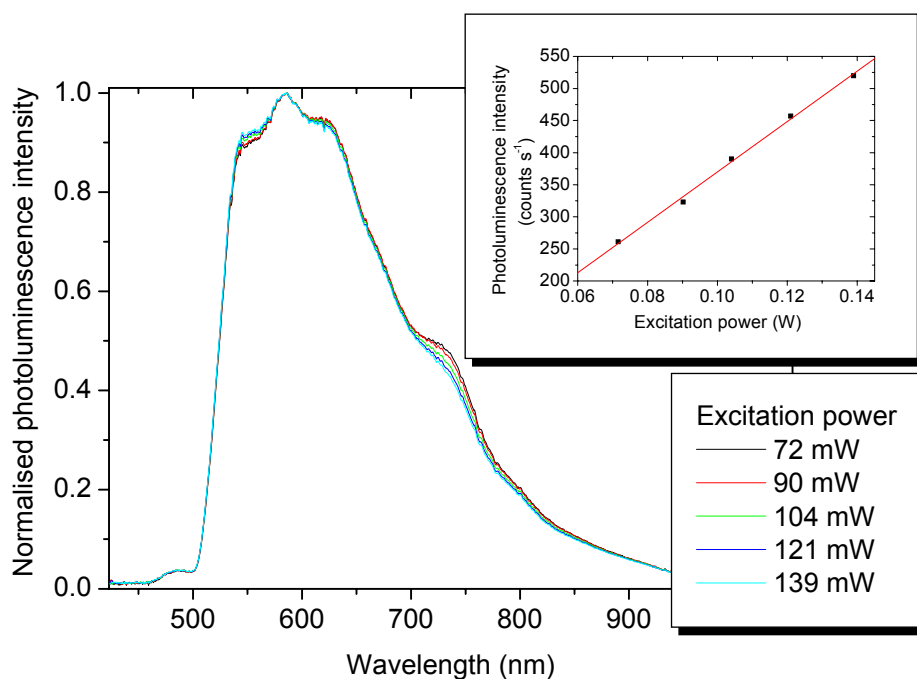
Figure 6.21. The normalised photoluminescence emission spectra of polycrystalline SnMo₆S₈ measured for increasing excitation powers at 76 K. The inset graph shows the peak photoluminescence emission intensity as a function of excitation power. Laser power was manually increased from 72 to 139 mW.

Variation of photoluminescence emission spectra over a period of hours

A selection of seven photoluminescence emission spectra measured over a 90 minute period at 72 K are shown in Figure 6.22. Spectra were recorded in three minute intervals and the inset graph shows the variation in peak photoluminescence emission intensity over the 90 minute period. The first measurement was made as the laser was repositioned on the sample surface. The position remained unchanged until the end of the run.
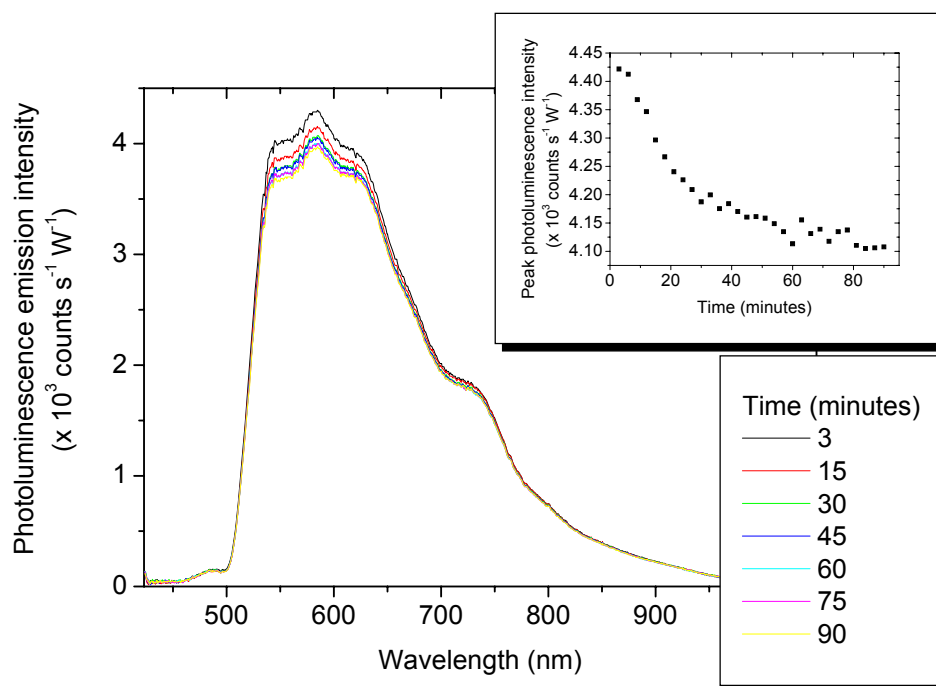
Figure 6.22. The photoluminescence emission spectra of polycrystalline SnMo$_6$S$_8$ measured over a 90 minute period. Each spectrum was measured at 72 K in 3 minute intervals. The main graph shows 7 normalised spectra measured at various times throughout the 90 minute period. The inset graph shows the change in the peak photoluminescence emission intensity (in counts s^{-1} W^{-1}) as a function of time. Typical photoluminescence excitation powers were 70 mW.

Temperature dependent measurements

Figure 6.23 and Figure 6.24 show the photoluminescence emission spectra of SnMo$_6$S$_8$ as a function of decreasing and increasing temperature, respectively. Spectra were measured 30 minutes after the sample had been realigned to correct for thermal contraction of the sample holder. In both cases, data were collected between 72 K and 304 K. Figure 6.24 shows the presence of a strong peak at 580 nm at 72 K which is not present in the spectra in Figure 6.23.
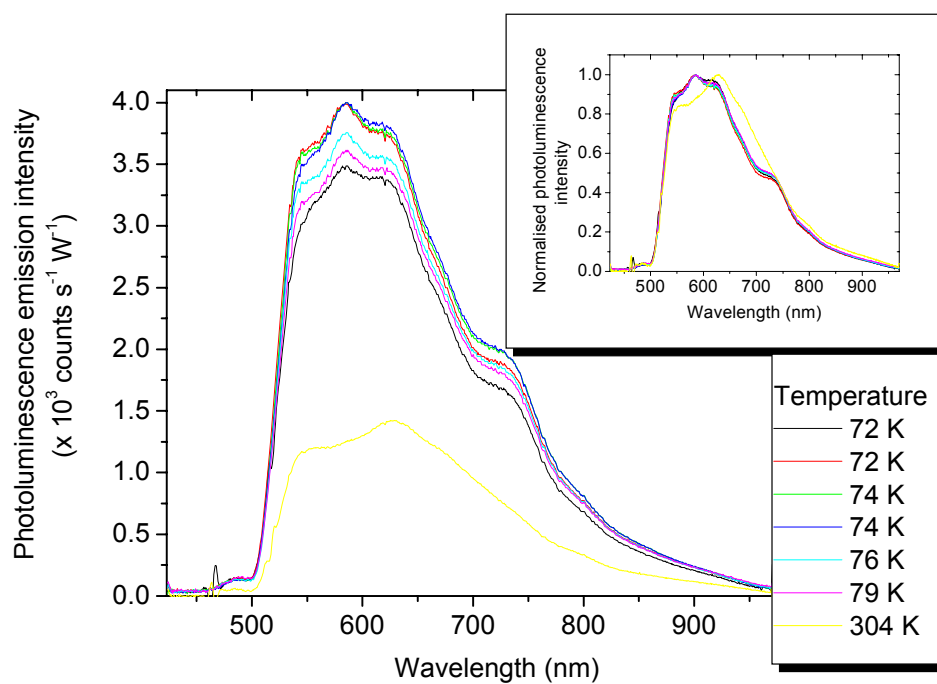
Figure 6.23. Photoluminescence emission spectra of polycrystalline SnMo₆S₈ measured as a function of temperature. Spectra were collected for decreasing temperatures beginning at 304 K. The inset graph shows the normalised spectra. All spectra were measured after a 30 minute period which began once the sample had been repositioned to correct for thermal contraction. Typical photoluminescence excitation powers were 70 mW.
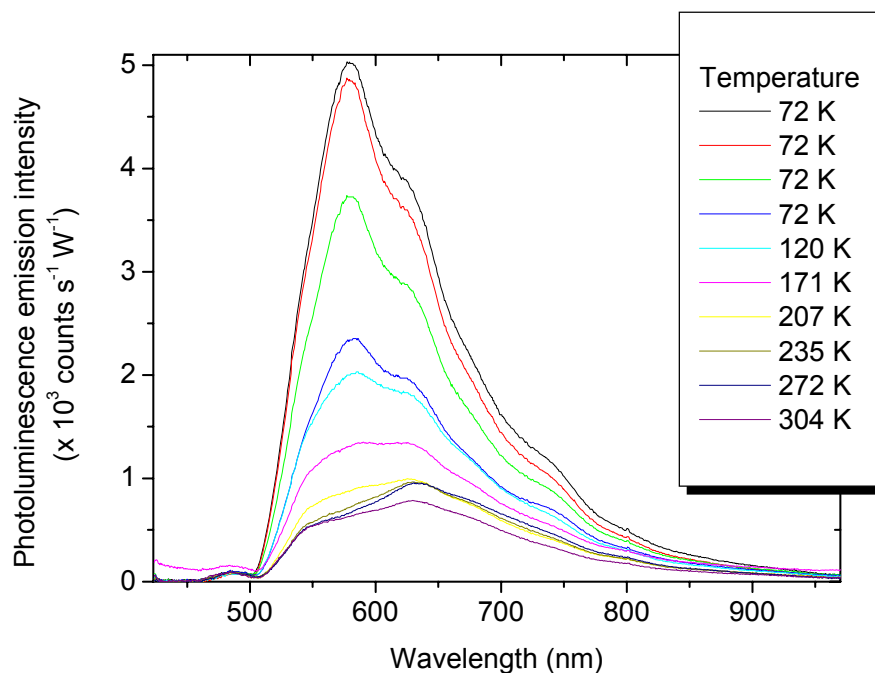
Figure 6.24. Photoluminescence emission spectra of polycrystalline SnMo$_6$S$_8$ measured as a function of temperature. Spectra were collected for increasing temperatures between 3 K and 304 K. All spectra were measured after a 30 minute period which began once the sample had been repositioned to correct for thermal contraction. Typical photoluminescence excitation powers were 65 mW.

An increase in peak photoluminescence emission intensity by a factor of two is measured between 300 K and 80 K in Figure 6.25 and Figure 6.26. Below 80 K, a sharp increase in the peak photoluminescence emission intensity of over 100 % is observed for the decreasing and increasing temperature runs. However, the increase is not observed in the random order temperature measurement.
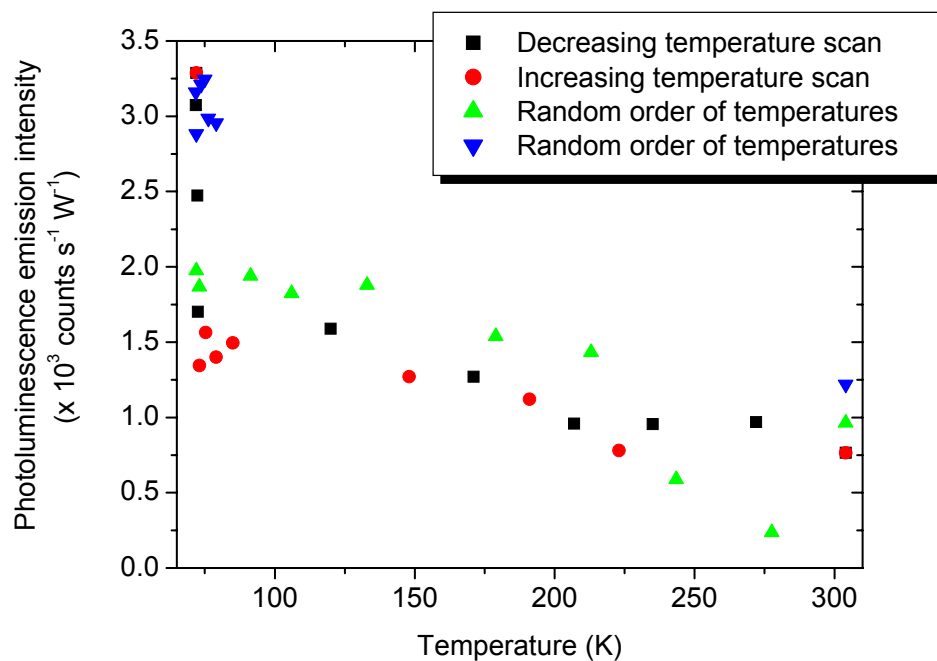
Figure 6.25. Photoluminescence emission intensity of the 630 nm peak as a function of temperature for polycrystalline SnMo$_6$S$_8$. The measurements were made over a five day period for decreasing (black), increasing (red) and a random order of temperatures (green and blue). Typical photoluminescence excitation powers were 70 mW.
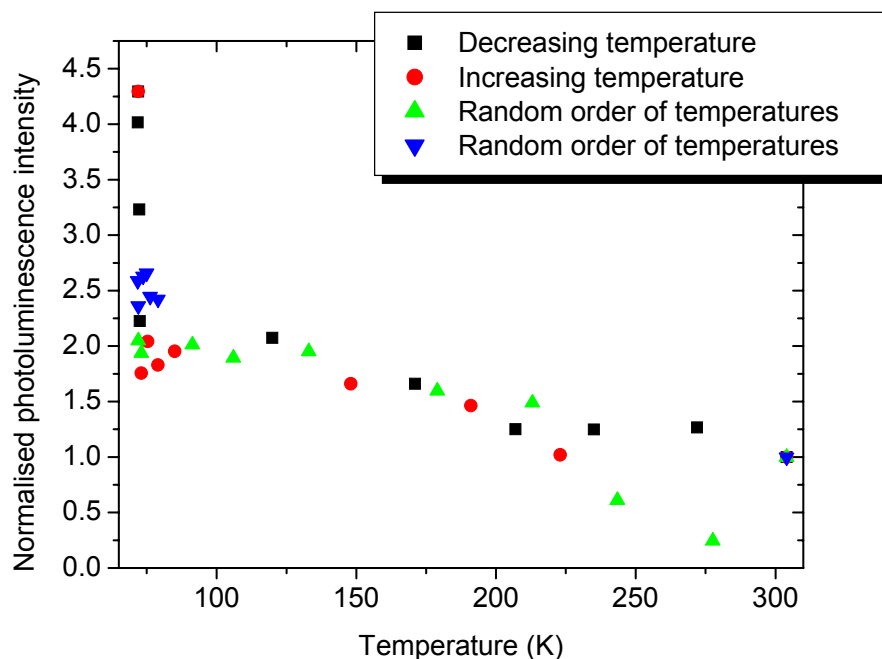
Figure 6.26. The normalised peak photoluminescence emission intensity of polycrystalline SnMo$_6$S$_8$ measured as a function of temperature and normalised to 1 at 304 K. The measurements were made over a five day period for decreasing (black), increasing (red) and a random order of temperatures (green and blue). Typical photoluminescence excitation powers were 70 mW.

Figure 6.27 presents data for the FWHM of SnMo$_6$S$_8$ measured for increasing, decreasing and a random order of temperatures. The decreasing (black), increasing (red) and one of two random order temperature measurements (blue) show a decrease in FWHM of 80 nm, 55 nm and 75 nm respectively, between 304 K and 72 K. However, the second random order temperature measurement (green) contradicts these measurements and shows an increase in FWHM of approximately 30 nm with decreasing temperature.
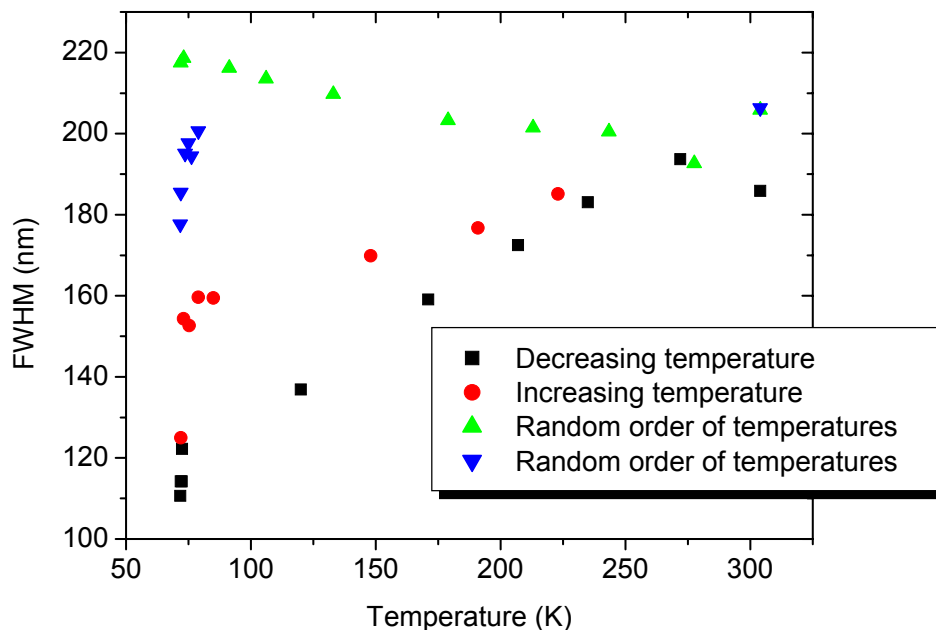
Figure 6.27. Variation in full width half maximum (FWHM) of the photoluminescence emission spectra measured as a function of temperature for polycrystalline SnMo$_6$S$_8$. The measurements were made over a five day period for decreasing (black), increasing (red) and a random order of temperatures (green and blue). Typical photoluminescence excitation powers were 70 mW.

6.5.3. Chevrel phase Sn$_{1-x}$Eu$_x$Mo$_6$S$_8$ x = 0.35 and Pb$_{1-x}$Gd$_x$Mo$_6$S$_8$ x = 0.3

Spatially resolved measurements across the sample surface - Sn$_{1-x}$Eu$_x$Mo$_6$S$_8$ x = 0.35

Figure 6.28 shows spatially resolved measurements of Sn$_{1-x}$Eu$_x$Mo$_6$S$_8$ x = 0.35. Measurements were made at 1 mm intervals across the sample surface in the top of three vertical positions on the sample (top, middle, bottom). Since the dimensions of the sample were small, the luminescence excited from the Apiezon N grease mounting the sample was observable as a contribution to the photoluminescence emission spectrum of the sample at all positions.
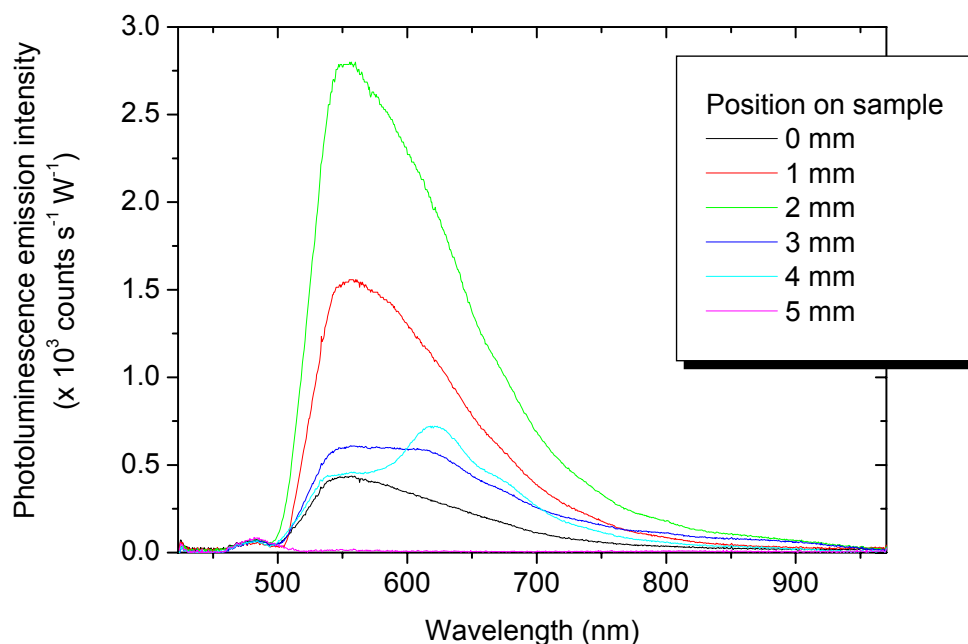
Figure 6.28 Photoluminescence emission spectra of polycrystalline $Sn_{1-x}Eu_xMo_6S_8$ x = 0.35 measured at different positions across the sample surface. Measurements were made along the horizontal direction at 1mm intervals in one of three vertical positions (top, middle, bottom). The spectra displayed are measured in the top vertical position. The edge of the sample was at 0 mm and 5 mm. At 5 mm the laser spot was on both the silicon and sample. Typical photoluminescence excitation powers were 70 mW.

Excitation power dependence - $Sn_{1-x}Eu_xMo_6S_8$ x = 0.35

Figure 6.29 presents the photoluminescence emission spectrum of $Sn_{1-x}Eu_xMo_6S_8$ x = 0.35 as a function of excitation power. Measurements were made in the centre of the sample (3 mm position in Figure 6.28). Laser power was manually increased from 70 mW to 100 mW before being reduced back to 70 mW. The measurement was carried out to identify if damage occurred to the sample under application of the laser. The inset
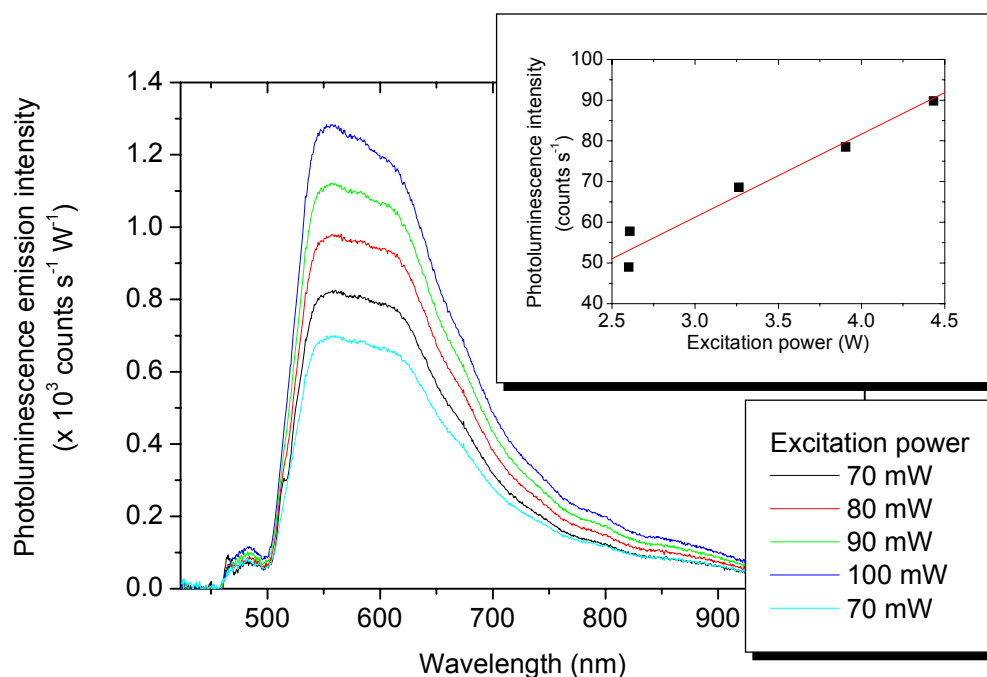
Figure 6.29. Photoluminescence emission spectra of polycrystalline $Sn_{1-x}Eu_xMo_6S_8$ x = 0.35 measured for increasing excitation powers at 304 K. The inset graph shows the peak photoluminescence emission intensity as a function of excitation power. Laser power was manually increased from 70 to 100 mW before the power was reduced and the measurement at 70 mW repeated.

figure shows the peak photoluminescence emission intensity as a function of excitation power.

The conclusion from the analysis of the spatially resolved measurements and measurements as a function of excitation power was that a reliable set of data could not be measured from the $Sn_{1-x}Eu_xMo_6S_8$ x = 0.35 sample (Figure 6.28 and Figure 6.29). This was due to the small size of the sample which led to difficulties in positioning the laser spot away from areas affected by Apiezon N grease and the apparent damage occurring under excitation by the laser. Therefore, no further measurements were made on this sample.

Room temperature spectrum - Pb$_{1-x}$Gd$_x$Mo$_6$S$_8$ x = 0.3

The photoluminescence emission spectrum of Pb$_{1-x}$Gd$_x$Mo$_6$S$_8$ x = 0.3 measured at 304 K is shown in Figure 6.30. This was the only spectrum measured for this sample as observations during preliminary measurements using the alignment camera showed the emission of a 'smoke-like' substance from the sample surface and a dark mark on the sample surface when laser illumination was removed. The 'smoke' led to problems with the collection of photoluminescence emission spectra and therefore no further measurements were made on the sample. No explanation has been found as to why the Pb$_{1-x}$Gd$_x$Mo$_6$S$_8$ x = 0.3 sample exhibited such different behaviour to the other Chevrel phase samples despite identical preparation, storage and excitation conditions.
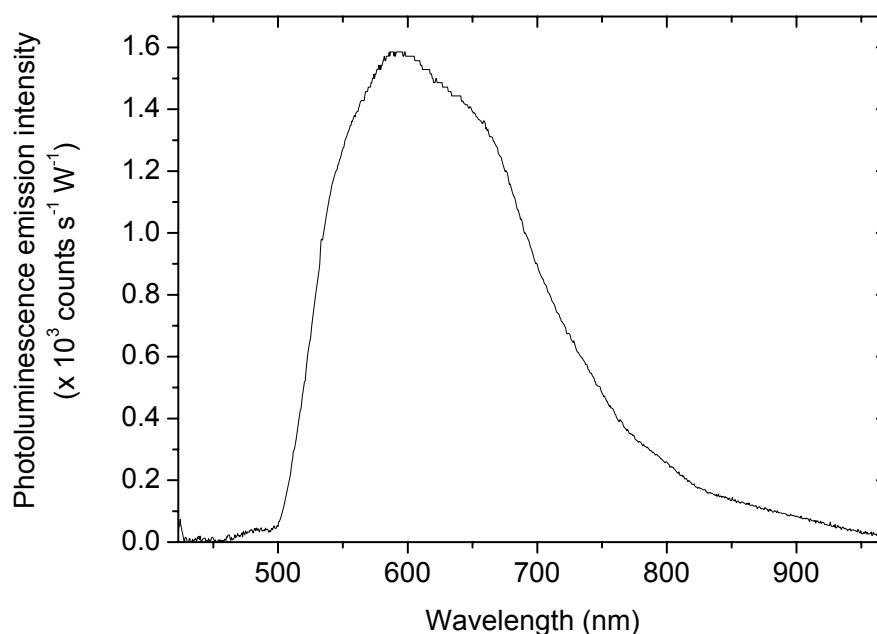
Figure 6.30 Photoluminescence emission spectrum of polycrystalline Pb$_{1-x}$Gd$_x$Mo$_6$S$_8$ x = 0.3 measured at 304 K. Photoluminescence excitation power was 70 mW.

6.5.4. Chevrel phase materials – Analysis and discussion

Unfortunately, the origin of photoluminescence emission in the Chevrel phase materials is at present unconfirmed. It is likely that the primary contribution to photoluminescence emission is from transitions between the S_6p to Mo_6d states as these are the primary processes contributing to the absorption spectrum in this energy range [99, 102]. However, further study using computational calculations should be conducted to confirm this.

Room temperature data for the Chevrel phase materials

Spatially resolved measurements of $PbMo_6S_8$ showed a homogeneous sample surface with a peak photoluminescence emission wavelength at 615 nm, an almost constant spectral shape and a peak photoluminescence emission intensity which varied by ~50 counts s^{-1} (~770 counts s^{-1} W^{-1}) (Figure 6.14). In contrast, spatially resolved measurements of $SnMo_6S_8$ showed photoluminescence emission spectra attributable to Apiezon N grease in all but the centre of the sample (Figure 6.20). Measurements as a function of temperature were therefore made only in this central location. Both the $PbMo_6S_8$ and $SnMo_6S_8$ samples showed a linear dependence of photoluminescence emission intensity on excitation power (Figure 6.15, Figure 6.21).

The $Sn_{1-x}Eu_xMo_6S_8$ x = 0.35 doped sample showed a decrease in photoluminescence emission intensity of 8.8 counts s^{-1} at 70 mW excitation power (125 counts s^{-1} W^{-1}) after the sample had been exposed to 100 mW excitation power. Due to the change in sample properties under laser excitation and the difficulty of finding a location on the small sample uncontaminated by Apiezon N grease, it was decided not to make any further measurements on this sample. Damage was also observed for the Pb_{1-}

$_x$Gd$_x$Mo$_6$S$_8$ x = 0.3 sample. In this case, the 'smoke-like' residue emitted from the sample under laser illumination meant that reproducible measurements could not be achieved.

Temperature dependent measurements for the Chevrel phase materials

FWHM decreased by 20 nm with decreasing temperature between 300 K and 70 K in PbMo$_6$S$_8$ (Figure 6.19) with peak photoluminescence emission wavelength remaining constant across the whole temperature range. An increase by a factor of 1.5 in peak photoluminescence emission intensity was measured as a function of decreasing temperature between 300 K and 80 K (Figure 6.17, Figure 6.18). Between 80 K and 70 K a reproducible increase in peak photoluminescence emission intensity by a factor of four was observed.

Measurements of the FWHM of SnMo$_6$S$_8$ as a function of temperature were inconclusive (Figure 6.27). Three out of the four measurements showed a decrease in FWHM with temperature with the fourth measurement showing an increase. The contradiction between the FWHM can be explained by the higher relative intensity of the 730 nm peak to the main emission peak in the spectrum of the anomalous random order measurement. In the spectra where the FWHM decreased as a function of temperature, the intensity of the 730 nm peak was approximately 50 % of the intensity of the main peak photoluminescence intensity. In the random order temperature measurement which showed and increase in FWHM, the 730 nm peak had an intensity which was up to 80 % of the main peak intensity. The 730 nm peak also showed a different dependence upon temperature to the main luminescence peak in this measurement and it was this dependence which dominated the value of FWHM. The 730 nm peak is thought to originate from an impurity on the sample surface with the relative intensity of the impurity peak determined by the distance of the excitation spot from the impurity.

The peak photoluminescence emission intensity of $SnMo_6S_8$ showed a factor of two increase in intensity as a function of decreasing temperature between 300 K and 80 K (Figure 6.25, Figure 6.26). Peak photoluminescence emission wavelength was observed not to change over this region. Below this temperature, the peak photoluminescence emission intensity rapidly increased with the peak photoluminescence emission wavelength shifting from the 630 nm peak to a peak at 580 nm (Figure 6.33). The region of increasing intensity below 80 K will be discussed in more detail in section 6.7.

Reliability of data

Photoluminescence emission measurements of $PbMo_6S_8$ have shown reproducible results with consistent spectra measured at all positions across the sample surface and as a function of temperature.

Reproducibility of data for the measurements on $SnMo_6S_8$, $Sn_{1-x}Eu_xMo_6S_8$ x = 0.35 and $Gd_{1-x}Gd_xMo_6S_8$ x = 0.3 was poor. Damage to the rare-earth doped Chevrel phase samples under laser illumination meant that a reliable data could not be collected for these materials. For the $SnMo_6S_8$ sample, the presence of an impurity peak combined with the difficulty in locating an area not contaminated by Apiezon N grease meant that data from this sample could not be considered to be reliable.

Calculated photoluminescence emission spectra

Figure 6.31 and Figure 6.32 show a comparison between the measured and calculated photoluminescence emission spectra for $PbMo_6S_8$ and $SnMo_6S_8$, respectively. Both calculations fail to reproduce any of the features observed in the measured spectra.

The discrepancy between the measured and calculated spectra could be due to failings in the model upon which equation (2.37) is based. The model only takes into account the density of states below the Fermi level. In the case of gold and copper (for which the model was designed) the density of states above the Fermi energy is low and invariant and a model for their photoluminescence emission would not require consideration of changes in the density of states in this region. However, in the Chevrel phase materials the density of states is high in the region > 1eV above the Fermi energy. The model also assumes the relaxation of excited electrons to the Fermi level before recombination. This is not possible in the Chevrel phase materials due to a gap in the density of states $0.5 - 1$ eV above the Fermi level.

Figure 6.31 Comparison of the normalised room temperature photoluminescence emission spectra of PbMo$_6$S$_8$ and the photoluminescence emission spectrum calculated using equation (2.37). The calculated spectrum used data for the refractive index and extinction coefficient measured using the J.A Woollam elipsometer and density of states calculated by Dr Stewart Clark.
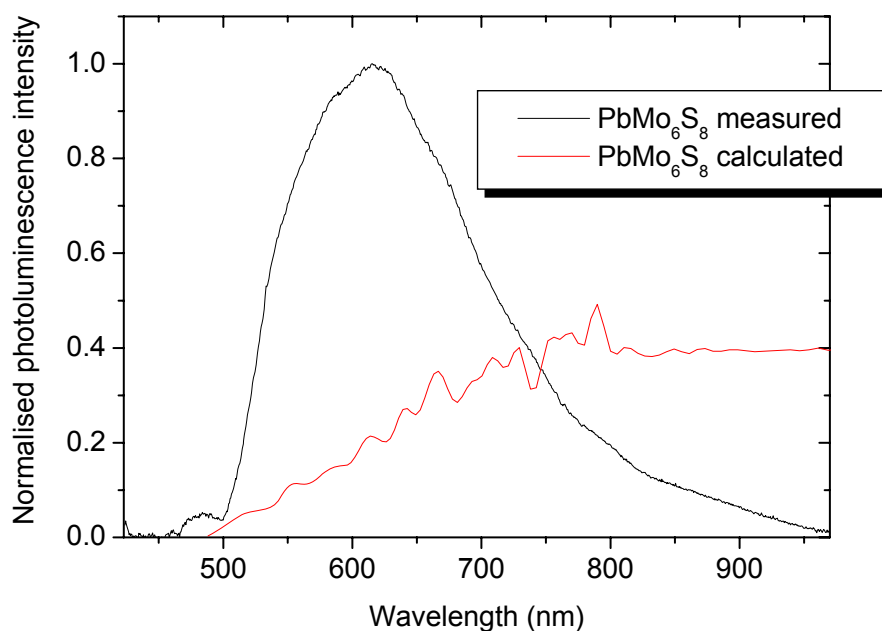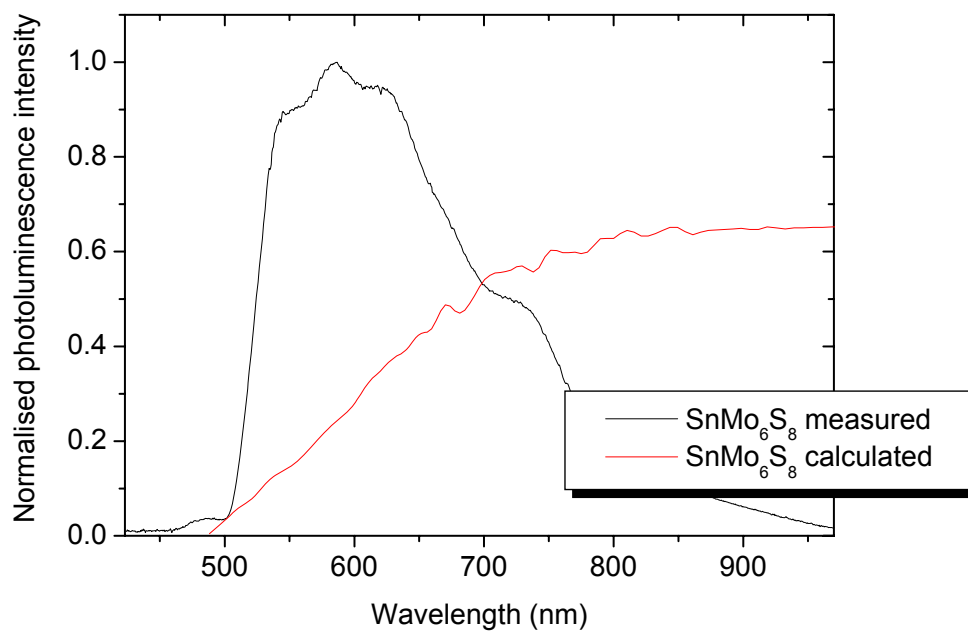
Figure 6.32 Comparison of the normalised room temperature photoluminescence emission spectra of SnMo₆S₈ and the photoluminescence emission spectrum calculated using equation (2.37). The calculated spectrum used data for the refractive index and extinction coefficient measured using the J.A Woollam elipsometer and density of states calculated by Dr Stewart Clark

6.6. Photoluminescence of high temperature superconductors

The following section presents data for photoluminescence emission spectra of the high temperature cuprate superconductors; DyBCO and YBCO. These materials are of interest due to their high superconducting transition temperatures and stable oxide chemical structures.

Spatially resolved photoluminescence emission spectra are presented along with measurements made as a function of excitation power and temperature. Data is also given for the excitation power dependence of photoluminescence emission of a thin film of YBCO and its spectrum compared with that of the single crystal YBCO sample.

Sample preparation for the DyBCO single crystal sample included the sample being cleaved and polished before cleaning in acetone and isopropanol. The YBCO sample was not cleaved but did go through the polishing and cleaning process. The thin film sample was only subjected to the final cleaning process.

6.6.1. Single crystal DyBCO

Spatially resolved measurements across the sample surface

Figure 6.33 presents data for spatially resolved photoluminescence emission spectra of DyBCO measured in 1 mm increments across the sample surface. Spectra are displayed for measurements in the top vertical position on the sample. Data was also measured in the bottom and middle position on the sample but are not shown here. The main graph shows the normalised photoluminescence emission spectra with the inset graph showing the spectra in counts s^{-1} W^{-1}.
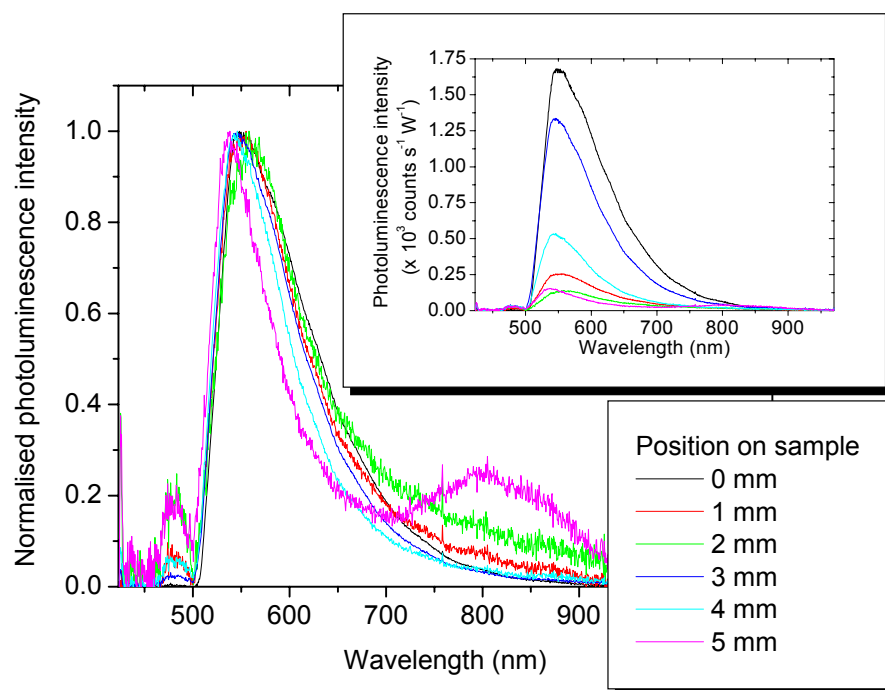
Figure 6.33 Normalised photoluminescence emission spectra of single crystal DyBCO measured at different positions across the sample surface. The inset graph shows the photoluminescence emission spectra in counts s^{-1} W^{-1}. Measurements were made along the horizontal direction at 1mm intervals in one of three vertical positions (top, middle, bottom). The spectra displayed are measured in the top vertical position. The edge of the sample was at 0 mm and 5 mm. At 5 mm the laser spot was on both the silicon and sample. Typical photoluminescence excitation powers were 72 mW.

Excitation power dependence

Figure 6.34 shows the photoluminescence emission spectrum of DyBCO measured as a function of excitation power. Excitation power was manually increased from 72 mW to 140 mW and power measured between the final focussing lens and the cryostat window using a handheld Melles Griot power meter. The inset graph shows peak photoluminescence intensity as a function of excitation power.
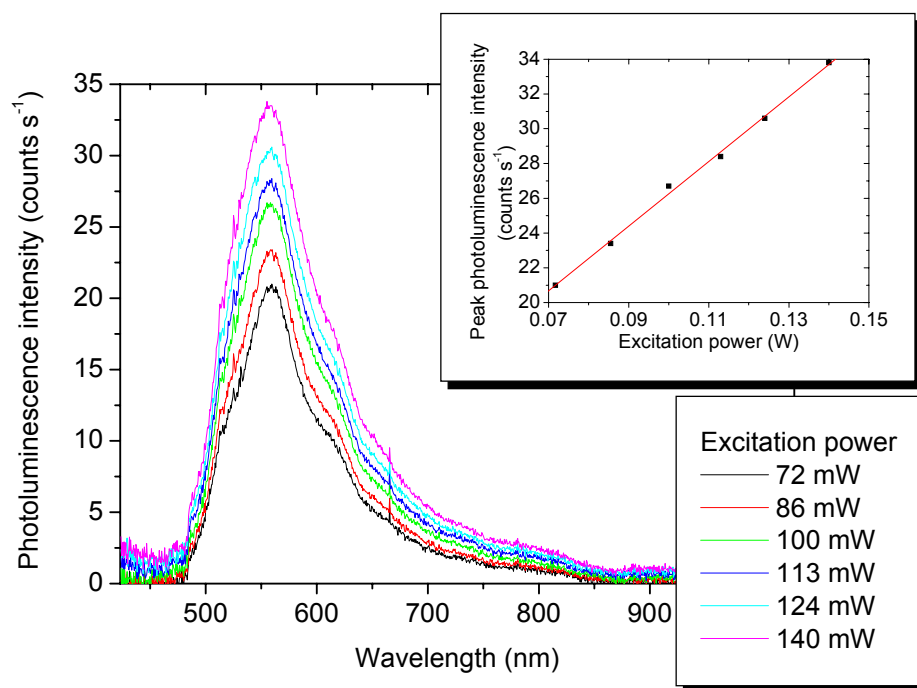
Figure 6.34. Photoluminescence emission spectra of single crystal DyBCO measured for increasing excitation powers at 304 K. The inset graph shows the peak photoluminescence emission intensity as a function of excitation power. Laser power was manually increased from 74 to 140 mW.

Temperature dependent measurements

Figure 6.35 presents the photoluminescence emission spectrum of DyBCO as a function of decreasing temperature between 296 K and 124 K. Measurements were made after a 30 minute wait commencing once the sample had been repositioned to correct for thermal contraction of the sample holder.
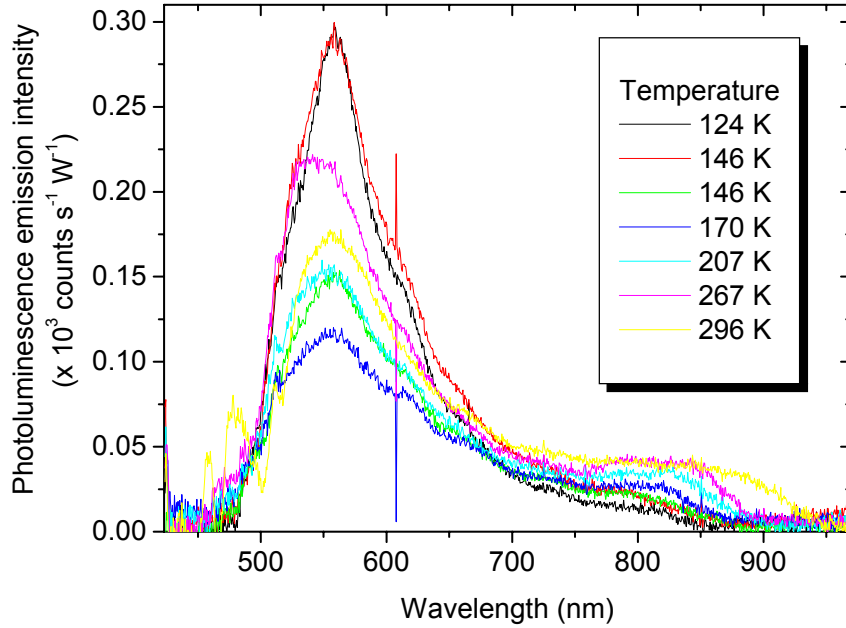
Figure 6.35. Photoluminescence emission spectra of single crystal DyBCO measured as a function of temperature. Spectra were collected for decreasing temperatures between 296 K and 124 K. All spectra were measured after a 30 minute period which began once the sample had been repositioned to correct for thermal contraction. Typical photoluminescence excitation powers were 72 mW.

Figure 6.36 shows the peak photoluminescence emission intensity as a function of temperature for DyBCO. Figure 6.37 shows the normalised peak intensity as a function of increasing, decreasing and a random order of temperatures. Measurements were made over a nine day period. The inset graph in Figure 6.36 plots the increase in peak photoluminescence emission intensity at 124 K over the nine day period.
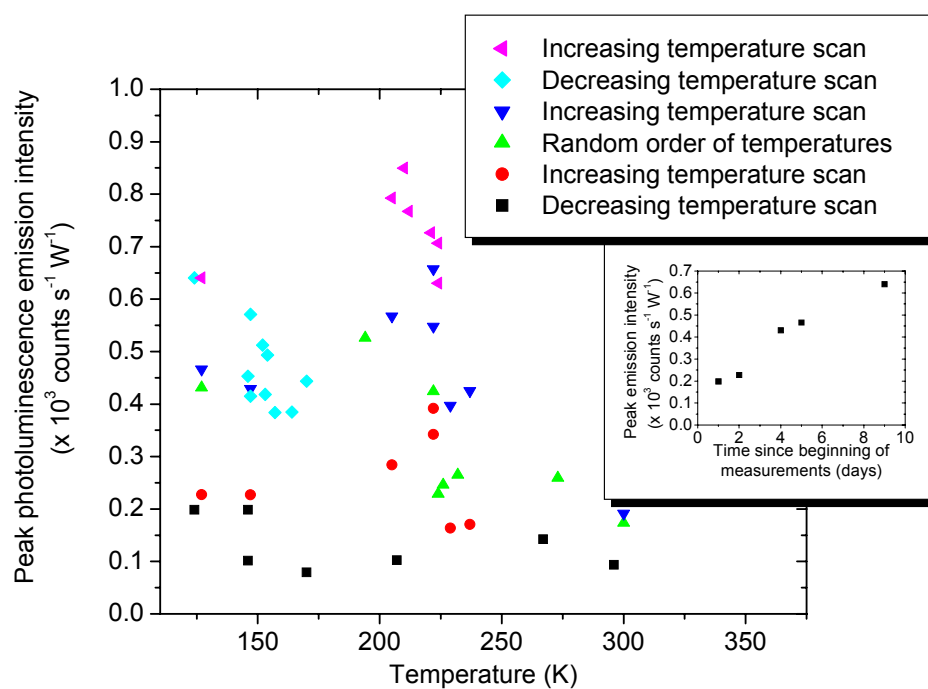
Figure 6.36. Peak photoluminescence emission intensity as a function of temperature for single crystal DyBCO. The measurements were made over a nine day period for decreasing (black and turquoise), increasing (red, black and blue) and a random order of temperatures (green). Typical photoluminescence excitation powers were 70 mW. The inset graph shows the change in peak photoluminescence emission intensity at 124 K over the nine day period
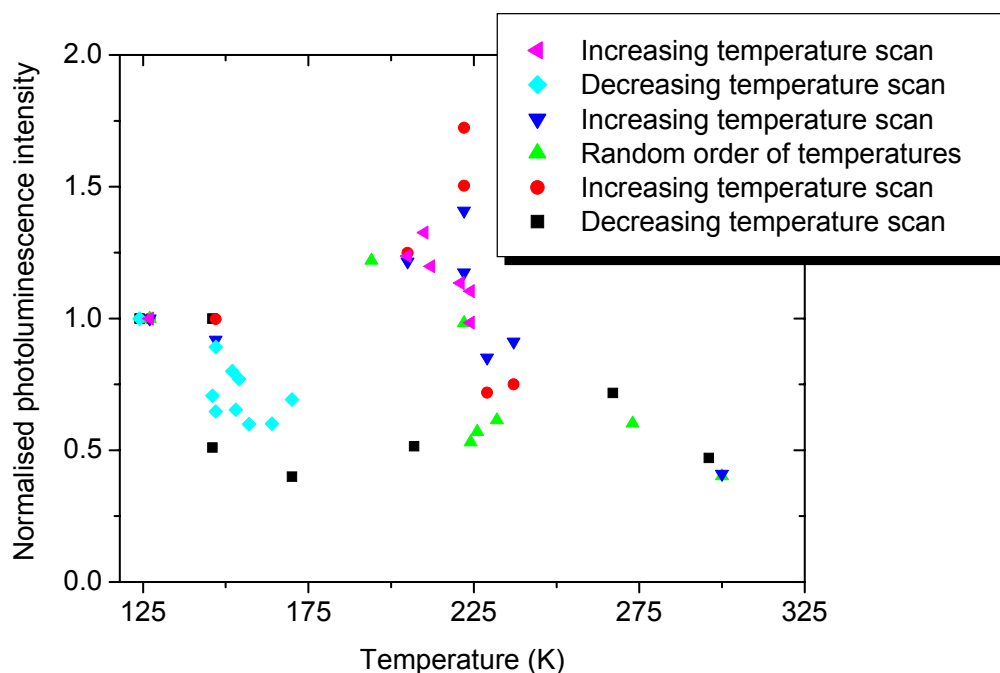
Figure 6.37. The normalised peak photoluminescence emission intensity of single crystal DyBCO measured as a function of temperature and normalised to 1 at 124 K. The measurements were made over a nine day period for decreasing (black and turquoise), increasing (red, black and blue) and a random order of temperatures (green). Typical photoluminescence excitation powers were 70 mW.

Figure 6.38 displays the FWHM of DyBCO measured as a function of increasing, decreasing and a random order of temperatures. No change is observed between 124 K and 300 K with the average FWHM remaining approximately constant.
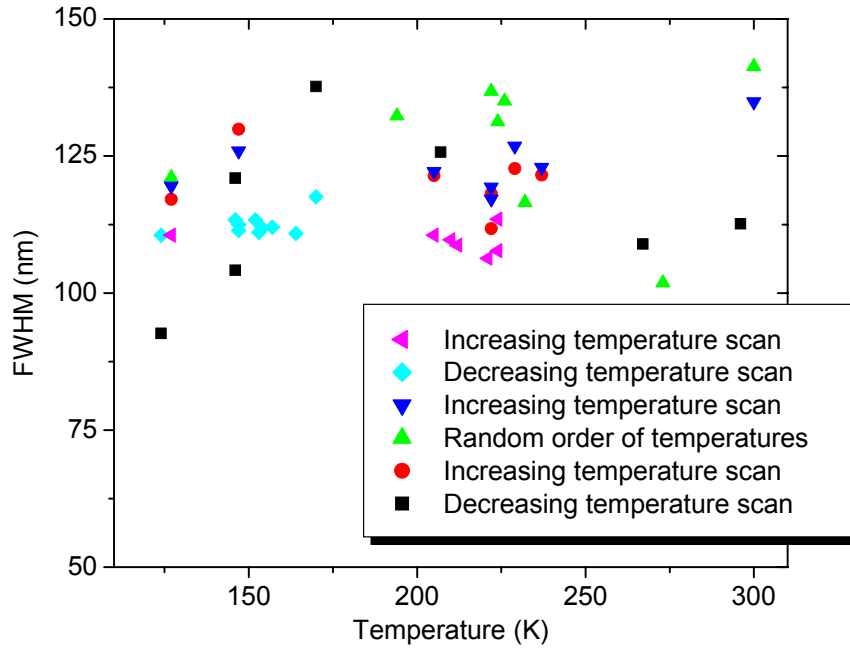
Figure 6.38. Variation in full width half maximum (FWHM) of the photoluminescence emission spectra measured as a function of temperature for single crystal DyBCO. The measurements were made over a nine day period for decreasing (green), increasing (black) and a random order of temperatures (red). Typical photoluminescence excitation powers were 70 mW.

6.6.2. Single crystal YBCO

Spatially resolved measurements across the sample surface

Figure 6.39 shows the spatially resolved photoluminescence emission spectra of single crystal YBCO measured in 1 mm increments across the sample surface. Measurements were made in three positions (top, middle and bottom) with the spectra shown here measured in the bottom vertical position on the sample.
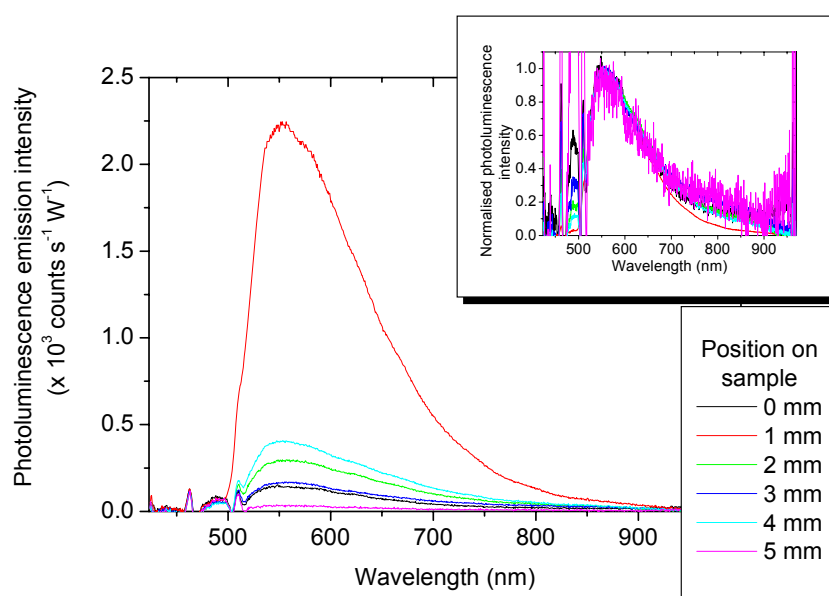
Figure 6.39 Photoluminescence emission spectra of single crystal YBCO measured at different positions horizontally across the sample surface. The inset graph shows the normalised photoluminescence emission spectra. Measurements were made along the horizontal direction at 1mm intervals in one of three vertical positions (top, middle, bottom). The spectra displayed are measured in the bottom vertical position. The edge of the sample was at 0 mm and 5 mm. At 5 mm the laser spot was on both the silicon and sample. Typical excitation powers were 53 mW.

Excitation power dependence

The excitation power dependence of single crystal YBCO is shown in Figure 6.40. The laser power was manually increased from 0 to 82 mW and was measured between the final focussing lens and the cryostat window using a handheld Melles Griot power meter. The main graph shows the normalised photoluminescence emission spectra with the inset graph showing the peak photoluminescence emission intensity as a function of excitation power.
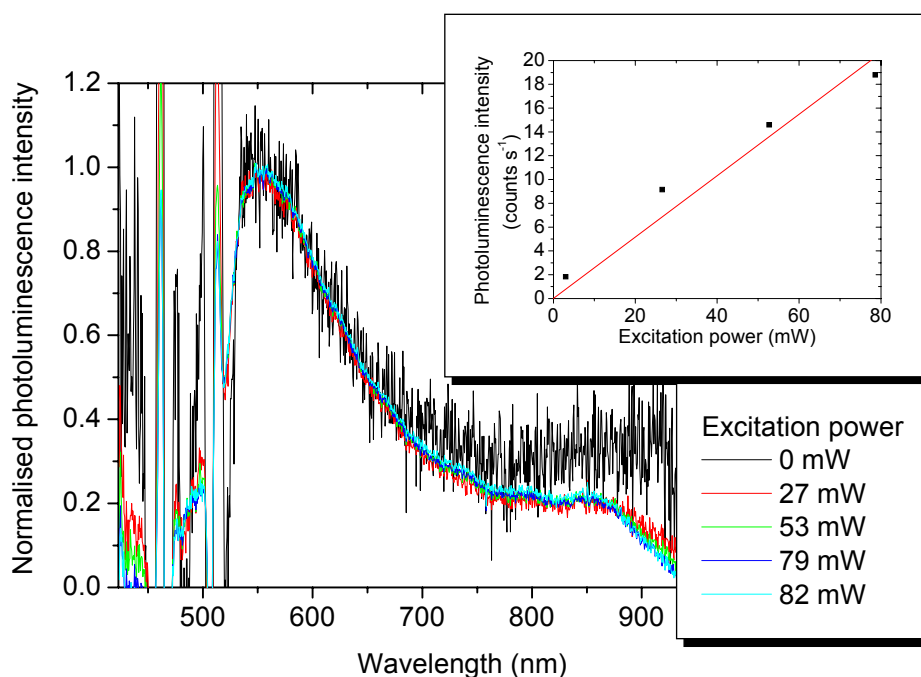
Figure 6.40. The normalised photoluminescence emission spectra of single crystal YBCO measured for increasing excitation powers at 304 K. The inset graph shows the peak photoluminescence emission intensity as a function of excitation power. Laser power was manually increased from 0 to 82 mW.

Variation in photoluminescence spectra over a period of hours

Figure 6.41 shows the variation in peak photoluminescence emission intensity measured over a 10 hour period. The measurements were made in 3 minute intervals at 127 K. The main graph shows a selection of 8 normalised photoluminescence emission spectra with the inset graph showing the variation in peak intensity with time. The first spectrum was measured immediately after the laser had been positioned at a new position on the sample and was not moved throughout the course of the 10 hour run.
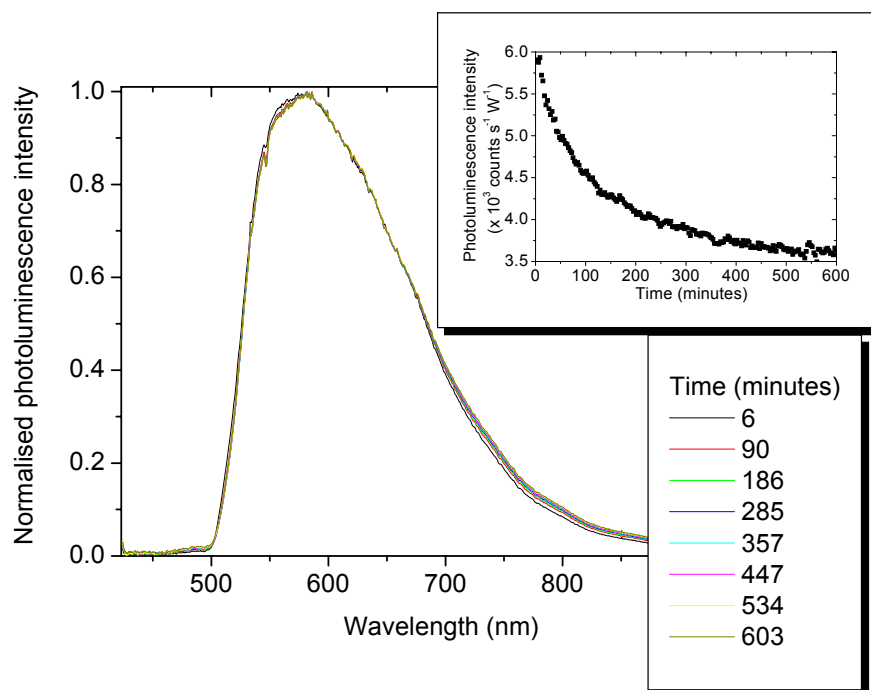
Figure 6.41. The photoluminescence emission spectra of single crystal YBCO measured over a 10 hour period. Each spectrum was measured at 127 K in 3 minute intervals. The main graph shows 8 normalised spectra measured at various times throughout the 10 hour period. The inset graph shows the change in the peak photoluminescence emission intensity (in counts s^{-1} W^{-1}) as a function of time. Typical photoluminescence excitation powers were 70 mW.

Temperature dependent measurements

Figure 6.42 shows the photoluminescence emission spectra of single crystal YBCO measured as a function of increasing temperature between 127 K and 224 K. Measurements were made after a 30 minute period which commenced after the sample had been repositioned to correct for movement of the sample due to thermal contraction of the sample holder. The inset graph shows the normalised emission spectra.
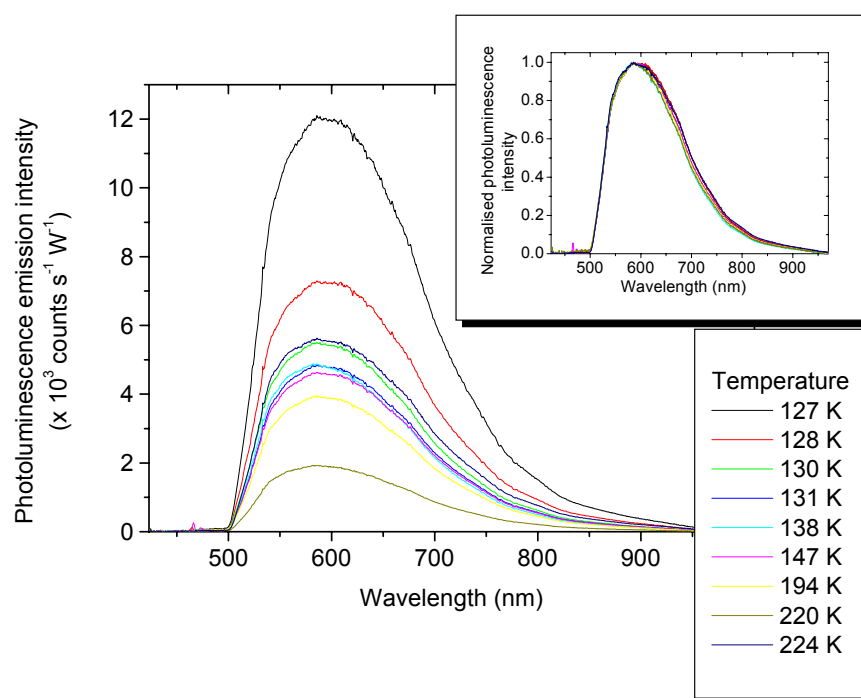
Figure 6.42. Photoluminescence emission spectra of single crystal YBCO measured as a function of temperature. Spectra were collected for increasing temperatures between 127 K and 224 K. The inset graph shows the normalised spectra. All spectra were measured after a 30 minute period which began once the sample had been repositioned to correct for thermal contraction. Typical photoluminescence excitation powers were 70 mW.

Figure 6.43 presents the peak photoluminescence emission intensity as a function of temperature for single crystal YBCO. The data is normalised to 1 at 124 K in Figure 6.44. Data has been collected for increasing, decreasing and a random order of temperatures over a three month period. The sharp increase in peak photoluminescence emission intensity below 130 K was only observed in the increasing temperature run and could not be reproduced in the random order or decreasing temperature measurement runs.

The data shown in Figure 6.43 and Figure 6.44 were collected over a three month period. This was due to technical complications with the laser which required the

equipment on the optical bench to be dismantled and reassembled after the decreasing temperature measurement but before the increasing and random order measurements. The change in intensity is due to a realignment of the system and re-optimisation of the excitation and emission optical pathways. To remove uncertainties created by the changes in the peak photoluminescence emission intensity due to optical alignment, all analysis is carried out using normalised intensities.
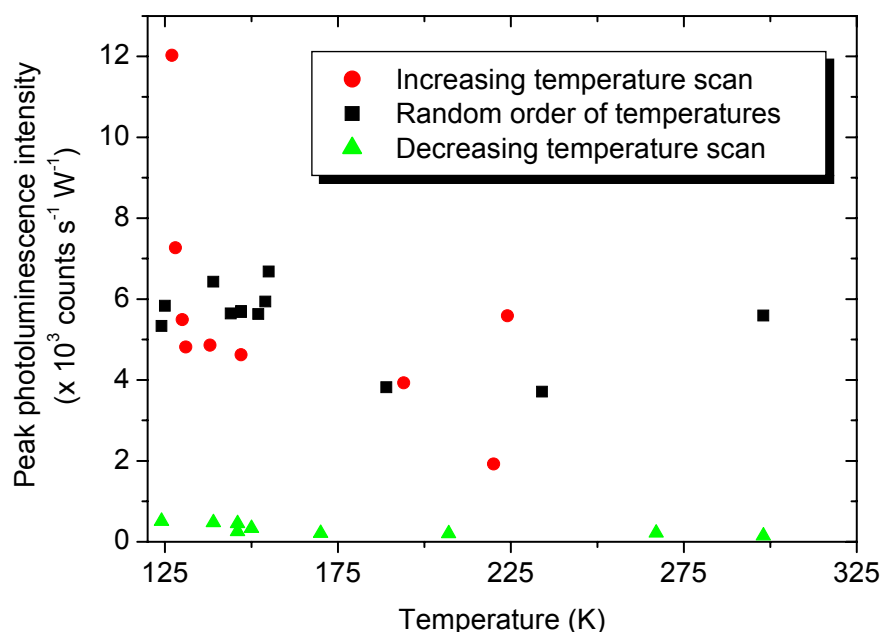
Figure 6.43. Peak photoluminescence emission intensity as a function of temperature for single crystal YBCO. The measurements were made over a three month period for increasing temperatures (red), a random order of temperatures (black) and decreasing temperatures (green). Typical photoluminescence excitation powers were 70 mW.
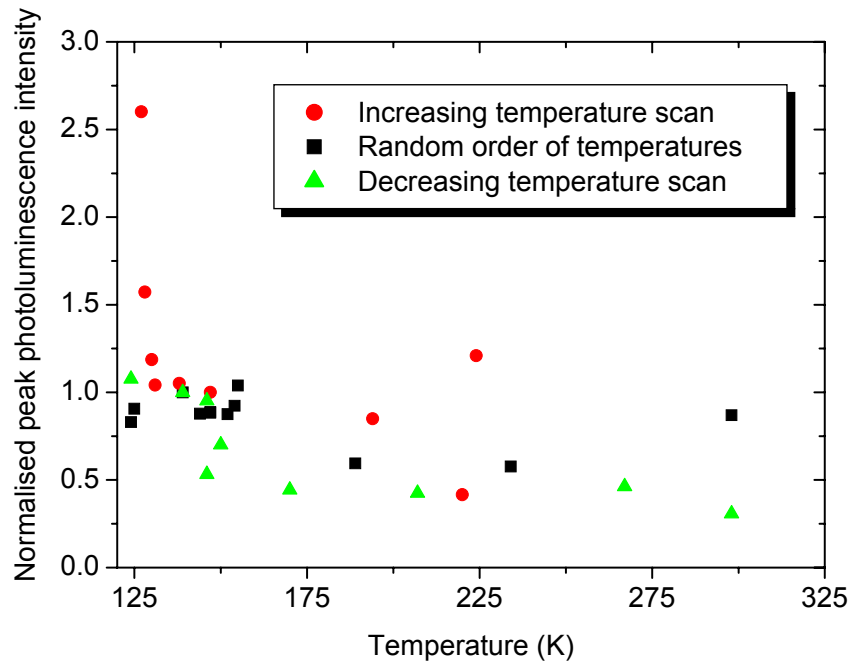
Figure 6.44. The normalised peak photoluminescence emission intensity of single crystal YBCO measured as a function of temperature and normalised to 1 at 147 K. The measurements were made over a three month period for increasing temperatures (red), a random order of temperatures (black) and decreasing temperatures (green). Typical photoluminescence excitation powers were 70 mW.

Figure 6.45 shows the FWHM as a function of temperature for single crystal YBCO measured as a function of increasing, decreasing and a random order of temperatures. No clear trend is observable across all three sets of data, however, a decrease in FWHM of approximately 30 nm is present in the increasing and random order temperature data below 200 K.
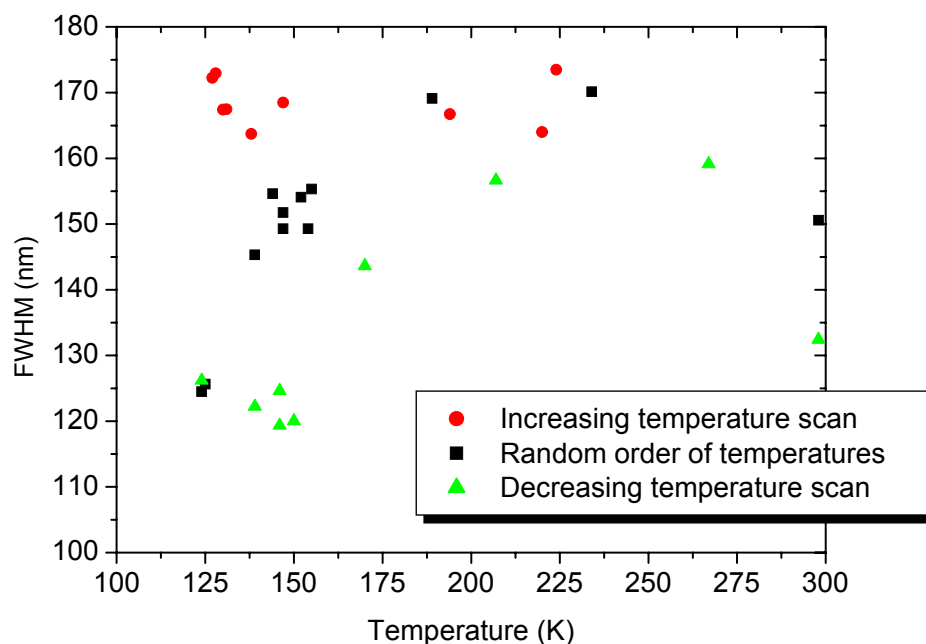
Figure 6.45. Variation in full width half maximum (FWHM) of the photoluminescence emission spectra measured as a function of temperature for single crystal YBCO. The measurements were made over a three month period for increasing temperatures (red), a random order of temperatures (black) and decreasing temperatures (green). Typical photoluminescence excitation powers were 70 mW.

6.6.3. Thin film YBCO

Excitation power dependence

The excitation power dependence of the photoluminescence emission from thin film YBCO is shown in Figure 6.46. Laser excitation power was increased from 71 mW to 120 mW and the power measured using a Melles Griot handheld laser power meter positioned between the final focussing lens and the sample. The inset graph shows the relationship between peak photoluminescence emission intensity and excitation power.
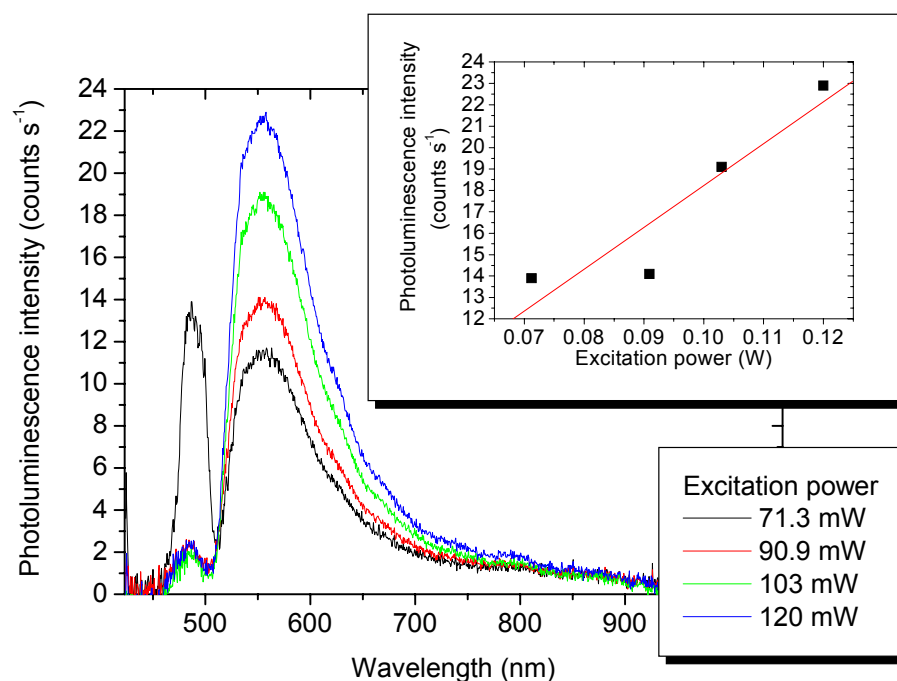
Figure 6.46 Photoluminescence emission spectra of the YBCO thin film measured for increasing excitation powers at 304 K. The inset graph shows the peak photoluminescence emission intensity as a function of excitation power. Laser power was manually increased from 71.3 to 120 mW.

Comparison between thin film and bulk sample photoluminescence emission spectra

Figure 6.47 presents a comparison of the photoluminescence emission spectra from thin film YBCO and single crystal YBCO. The spectra display the same peak wavelengths and FWHM but the single crystal emits a peak photoluminescence emission intensity approximately 19 times greater than the peak emission intensity from the thin film. The thin film has a 10 times higher intensity at 800 nm compared to the single crystal sample. Measurements on an STO substrate with no YBCO thin film present and on the back of the thin film sample substrate with the YBCO film present, produced
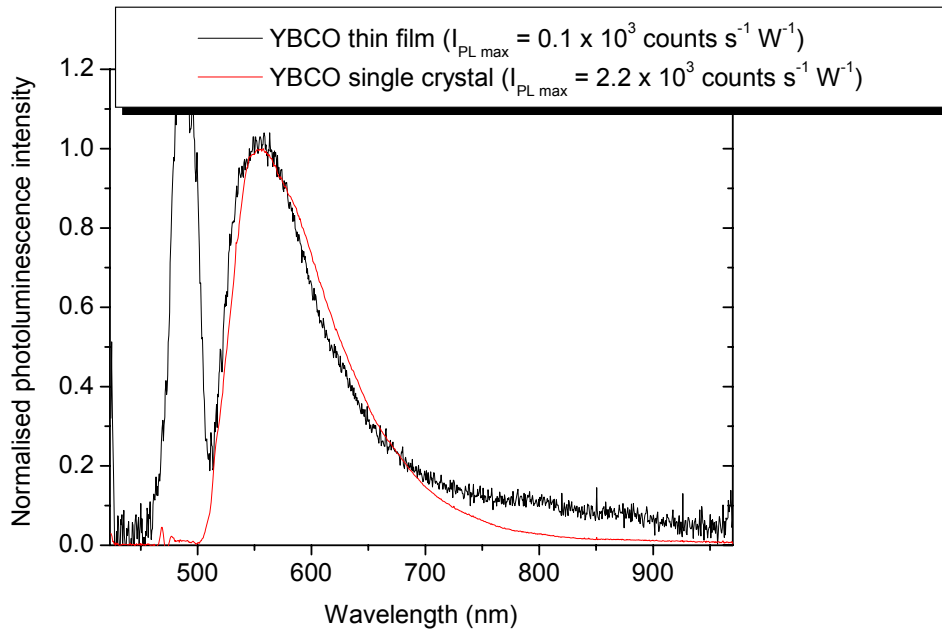
Figure 6.47 Comparison of the normalised photoluminescence emission spectra of the YBCO thin film and YBCO single crystal at 304 K. The peak photoluminescence emission intensity for each spectrum is given in the legend. Typical photoluminescence emission powers were 70 mW for the thin film and 53 mW for the single crystal sample.

emission peaks in this region due to the STO substrate and the mounting adhesive on the back of the substrate from the deposition process.

6.6.4. High temperature superconductors – Analysis and discussion

Photoluminescence emission measurements of YBCO in the literature show a wide variation in the observed spectra. The differences have been attributed to a strong dependence upon defect concentration, oxygen content, surface contamination, sample fabrication and excitation energy [13, 14, 19]. Photoluminescence emission peaks have been observed from 433 nm to 660 nm for excitation energies in the UV and visible regions. Photoluminescence emission at wavelengths between 530 nm and 580 nm has

been reported to be due to transitions between holes in the $3d^{10}$ to $3d^9$ oxygen derived valence bands and oxygen depleted regions [13, 19]. To our knowledge, no measurements are reported in the literature on the measurement of DyBCO.

Room temperature data for the high temperature cuprate superconductors

Spatial mapping of both the single crystal DyBCO and YBCO samples showed a variation in the photoluminescence emission spectra from across the sample surface (Figure 6.33, Figure 6.39). The peak photoluminescence emission wavelength was measured to be at 555 nm (2.2 eV) for the YBCO (single crystal and thin film) samples and 580 nm (2.1 eV) for the single crystal DyBCO sample. Close to the edge of the sample, photoluminescence from Apiezon N grease was observed in the DyBCO spectra.

An interesting observation was that pits in the sample surface often displayed a bright yellow/orange (570 – 590 nm) luminescence emission visible under close examination to the naked eye. CuO_2 has been reported to have a band gap at 570 nm (2.17 eV) which may explain the occasional bright points of yellow/orange luminescence [125]. The bright spots in pits on the cuprate samples were the only locations where luminescence was visible by eye unless the sample was contaminated by N grease when a light green/white luminescence was visible across a wide area on the sample surface.

Variations in peak photoluminescence emission intensity and FWHM for both the YBCO and DyBCO samples were most likely due to the luminescence produced on the uneven edges of the pits on the sample surface. In these locations the angle between the sample surface and detection optics would change leading to detection of the luminescence at a different wavelength. The peak at 800 nm in the 5mm position of the spatial mapping measurement of the DyBCO sample is due to light from the laser

directly reflecting into the collection optics leading to luminescence of the optical components (Figure 6.33).

A linear dependence of photoluminescence emission intensity with excitation power was observed for both single crystal DyBCO and YBCO (Figure 6.33, Figure 6.40) and a roughly linear dependence for the YBCO thin film (Figure 6.46).

Temperature dependent measurements for the high temperature cuprate superconductors

A 30 nm increase in FWHM with temperature was observed for two out of the three data sets measured for single crystal YBCO between 124 K and 304 K (Figure 6.45). The trend is consistent with the measurements of Garcia, who observed an increase in FWHM of approximately 30 nm between 65 K and 300 K [13]. Also consistent with the work of Garcia was the observed increase in peak photoluminescence emission intensity as a function of decreasing temperature. An increase in photoluminescence emission intensity of approximately a factor of 7 is shown in Figure 2.16 between 300 K and 125 K from the work of Garcia, which is much larger than the factor of two increase measured in this study (Figure 6.43, Figure 6.44). The sharp increase in luminescence intensity below 125 K will be discussed in section 6.7. An increase in photoluminescence emission intensity is consistent with the expectation that as temperature decreases there is a reduction in lattice vibrations and non radiative recombination processes thus reducing the processes competing with radiative recombination and increasing the probability of photoluminescence emission [188]. No change in the peak photoluminescence emission wavelength was observed as a function of temperature for single crystal YBCO.

The FWHM and peak photoluminescence emission wavelength of single crystal DyBCO showed no dependence upon temperature, remaining constant within the distribution of the data between 124 K and 300 K (Figure 6.38). Peak photoluminescence

intensity of the single crystal DyBCO sample also showed no apparent dependence upon temperature (Figure 6.36, Figure 6.37).

The peak photoluminescence intensity of the single crystal DyBCO sample measured at 124 K showed an increase in intensity of about a factor of three over the 9 days of measurements (Figure 6.36). The formation of an oxide layer on the sample surface (as was the case with the copper sample) was unlikely to have led to the increase in the intensity since the sample surface was already oxidised. The increase was also not correlated to a systematic change in spectral shape as was observed during the oxidation of the copper sample. The consistency of the spectral shape also makes the increase unlikely to be due to the destruction and restructuring of oxygen at the sample surface under laser excitation, as the spectral shape would have been expected to change with sample composition. Measurements of the sample surface structure and compositional analysis should be carried out between each set of photoluminescence emission spectra measurements in order to reach a conclusion as to the origin of the increase in photoluminescence emission intensity.

Reliability of data

The change in peak photoluminescence emission intensity of the DyBCO single crystal sample as a function of time rather than temperature (Figure 6.36) means that no conclusions can be drawn from this data as there is an unknown factor affecting the data, hence making the data unreliable.

The spectra measured for YBCO show a reproducible spectral shape across the sample surface (Figure 6.39) as well as the single crystal and thin film spectra comparing extremely well (Figure 6.47). Changes as a function of temperature show a reproducible trend across all measurements (Figure 6.44) with the spectral shape remaining consistent

throughout (Figure 6.42). For these reasons, it is concluded that the YBCO data is reliable and is not affected by the problems observed for the DyBCO sample.

Calculated spectra

Figure 6.48 and Figure 6.49 show the measured and calculated photoluminescence emission spectra for DyBCO and YBCO, respectively. The calculated spectra poorly model the measured spectra for both samples, with no peaks present in the spectrum calculated for YBCO.

Figure 6.48 Comparison of the normalised room temperature photoluminescence emission spectra of DyBCO and the photoluminescence emission spectrum calculated using equation (2.37). The calculated spectrum used data for the refractive index and extinction coefficient measured using the J.A Woollam elipsometer and density of states calculated by Dr Stewart Clark.

The mechanism of photoluminescence emission in the high temperature cuprates is described in the literature as originating from a variety of sources, including transitions within the Cu-O chains, transitions between holes in the oxygen derived $3d^{10}$ and $3d^9$ valence bands and photoexcitation in the CuO_2 plane [14, 15, 19, 20]. All of these processes are very different to the mechanism describing photoluminescence emission in gold and copper, which is what equation (2.37) was designed to model. Therefore, it is to be expected that equation (2.37) would not be suitable for modelling the photoluminescence emission from the high temperature cuprate superconductors.
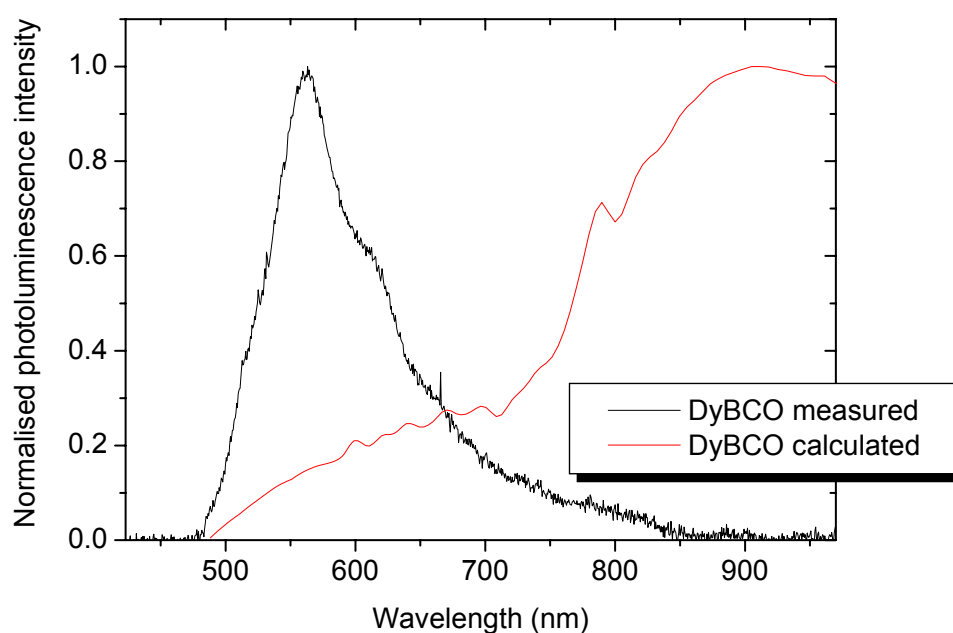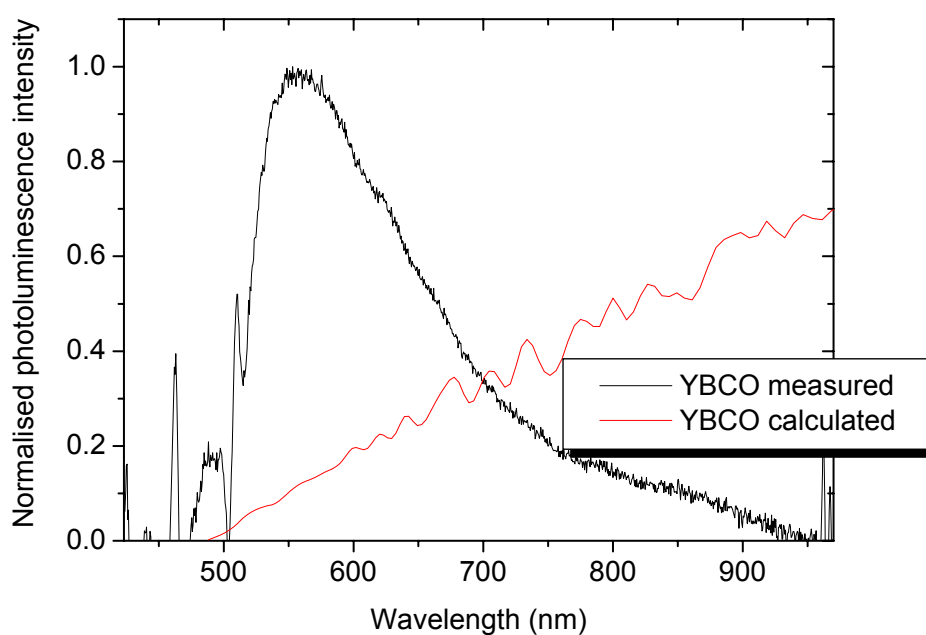

Figure 6.49 Comparison of the normalised room temperature photoluminescence emission spectra of YBCO and the photoluminescence emission spectrum calculated using equation (2.37). The calculated spectrum used data for the refractive index and extinction coefficient measured using the J.A Woollam elipsometer and density of states calculated by Dr Stewart Clark.

6.7. General discussion

There is little information in the published literature on the photoluminescence emission measurements from metals and superconductors. Measurements on the samples presented in this chapter have shown unusual behaviour in both materials which have not previously studied and those for which data has already been presented in the literature. In the following section the new observations will be compared with the processes already reported in the literature in an attempt to explain the observed features.

Oscillations in emission intensity over a period of hours

Peak photoluminescence emission intensity was observed to decrease over a period of hours in the niobium, $SnMo_6S_8$ and YBCO samples. The decreases were of the order of 22 % for the 99.99 % purity single crystal niobium sample (13 hour period, Figure 6.6), 7 % for polycrystalline $SnMo_6S_8$ (1 hour period, Figure 6.22) and 41 % for single crystal YBCO (10 hour period, Figure 6.41). The spectral shape did not change over the period of the measurements with the only change being the intensity of the spectra.

The variation in photoluminescence emission intensity over the measurement period for the three samples was different to that observed for gold and copper (Chapter 5), where the intensity oscillated during the same time period and showed a steeper initial decrease in the intensity over the first $30 - 60$ minutes. In the three superconductive samples measured here, a continuous decrease with no oscillations was observed over the 10 hour period for niobium and single crystal YBCO and 90 minute period for $SnMo_6S_8$. Data has not been collected for the variation in photoluminescence emission over a period of hours for polycrystalline $PbMo_6S_8$ or single crystal DyBCO.

No satisfactory explanation for the phenomenon has been found with no precedent evident in the literature. The only process reported to show a decreasing photoluminescence intensity over a period of hours under continuous excitation is not directly comparable to the samples in this study. A slow exponentially decreasing photoluminescence emission intensity has been observed in the literature from oxygen deficient YBCO over the course of an hour [20, 126]. The mechanism behind the time dependent emission was attributed to persistent photoconductivity (PPC) as discussed in Chapter 2 [20, 126, 127]. However, the process of PPC is reported to only occur in oxygen deficient YBCO and not for optimally doped samples (as were studied here), due to the requirement for oxygen vacancy trapping sites. The decrease in photoluminescence intensity observed during PPC (~ 6 %) is also much smaller than the decrease observed in niobium and YBCO. The work by Federici into PPC was also measured under much higher excitation powers (4 W all lines from an Ar+ laser) than our measurements (70 mW at 488 nm from an Ar+ laser).

Therefore, at present, no explanation can be given for the variation in photoluminescence emission over a period of hours and a systematic study should be conducted to give a clearer indication of the reproducibility, temperature dependence and physical processes involved.

Low temperature increase in photoluminescence emission intensity

A sharp rise in photoluminescence intensity was observed at low temperatures from the niobium, $PbMo_6S_8$ (Figure 6.17, Figure 6.18), $SnMo_6S_8$ (Figure 6.25, Figure 6.26) and one measurement of the single crystal YBCO sample (Figure 6.43, Figure 6.44) but was not observed for gold, copper or DyBCO. The onset temperature for the increase was approximately 90 K for niobium, 73 K for $PbMo_6S_8$ and $SnMo_6S_8$ and 131

K for YBCO. The shape of the photoluminescence emission spectra did not change upon entering the region of rapid increase for niobium (Figure 6.9), $PbMo_6S_8$ (Figure 6.16) and YBCO (Figure 6.42). Repeated measurements showed the increase to be independent of the order of the measurements on an individual sample.

Data for the $SnMo_6S_8$ sample will not be considered further in this discussion as photoluminescence emission peaks from impurities on the sample surface have been shown to display different temperature dependences to that of the main spectral peak making conclusions drawn using this sample unreliable.

The rapid increase in photoluminescence emission intensity at low temperatures is not thought to be related to a feature of the experimental hardware since the observation of an increase in photoluminescence emission intensity was independent of the order that measurements were made on the different samples. The samples were often remounted between measurements and the cryostat opened to atmosphere and re-evacuated. It therefore seems unlikely that an increase would not be observed for the measurements of copper, gold and DyBCO if the effect were related to the experimental hardware. Condensation of gases on to the surface of the samples would also be expected for all samples and should not occur selectively.

A sharp increase in photoluminescence emission intensity was observed by Tominaga in Nb_3Sn below 18 K [16]. In their work, the increase in luminescence intensity was attributed to an increase in the probability of relaxation of electrons and holes from the excited states to emitting states below the superconducting critical temperature. However, no explanation was given for the processes which led to the rate change. The increase in intensity did not occur close to T_C for any of our samples and so the change cannot be attributed to the onset of superconductivity in our measurements which leads us to question the reliability of the interpretation in the study by Tominaga.

At present, the origin of the rapid increase in photoluminescence emission intensity at low temperatures remains unknown and requires further investigation to determine the underlying processes producing this effect.

6.8. Conclusions

This chapter has presented a systematic study of the photoluminescence emission spectra of polycrystalline $PbMo_6S_8$ and single crystal YBCO as a function of temperature. The data are determined to be reliable through measurements as a function of position across the sample surface and excitation power dependence. For single crystal YBCO, a comparison has been made a high quality thin film and has shown extremely good agreement between the photoluminescence emission spectra of the two samples. A reproducible increase in peak photoluminescence emission intensity by a factor of 1.5 was observed as a function of temperature between 304 K and 80 K for $PbMo_6S_8$ and a factor of two increase between 296 K and 131 K for YBCO. FWHM showed a 20 nm decrease for $PbMo_6S_8$ and a 30 nm decrease for YBCO with peak photoluminescence emission wavelength remaining constant as a function of temperature for both samples.

Photoluminescence emission spectra for 99.99 % purity single crystal niobium were determined to be from an oxide on the sample surface and not from the bulk sample as no spectrum could be measured from a polished sample. Measurements of the Chevrel phase superconductor, $SnMo_6S_8$, were also considered to be unreliable as the spectra contained peaks attributable to impurities on the sample surface which displayed emission with a different temperature dependence to the main photoluminescence emission peak. Measurements on the doped Chevrel phase superconductors, $Sn_{1-x}Eu_xMo_6S_8$ x = 0.35 and $Pb_{1-x}Gd_xMo_6S_8$ x = 0.3 were not possible as reproducible results

could not be achieved due to damage occurring to the samples under laser illumination. Finally, an increase in the peak photoluminescence intensity of the high temperature superconductor DyBCO over the period of the variable temperature measurements meant that the data could not be reliably interpreted as an additional change was occurring to the sample which was not related to its temperature dependence.

A variation in photoluminescence emission intensity over a period of hours was observed from the niobium, $SnMo_6S_8$ and YBCO samples and as yet, no explanation has been found for the origin of this feature. A comparison has been made with experimental data in the literature. However, photoinduced conductivity (PPC) is the only precedent for a decrease in photoluminescence emission over a period of hours under continuous excitation and the process is only able to take place in non-optimally doped YBCO and not in the samples measured in this study. A theory has also not yet been found to explain the rapid increase in photoluminescence intensity at low temperatures observed in niobium, $PbMo_6S_8$, and YBCO.

Chapter 7. Conclusions and future work

This chapter considers possible future investigations for the measurement of low yield photoluminescence emission including design modifications to the instrumentation for measurements below the superconducting critical temperature.

In chapter 5 data were presented for the photoluminescence emission spectra of gold and copper measured using the high sensitivity instrument developed as part of this project. The spectra compared well to data in the literature and have been accurately modelled using the theory presented by Apell [64]. The first measurements of the photoluminescence emission of gold and copper as a function of temperature have been presented and show a reproducible increase in peak photoluminescence emission intensity by approximately a factor of two for gold and a factor of five for copper between 300 K and 80 K. FWHM and peak photoluminescence emission wavelength showed no change as a function of temperature. An oxide on the surface of the copper sample was observable as second peak in the copper photoluminescence emission spectrum which increased in intensity over a period of days. Further work is required to identify whether the copper spectrum is dominated by the emission from the oxide, however, the ability of the theoretical model to accurately reproduce spectra for both polished gold and copper is evidence against the domination of the oxide.

In chapter 6 we presented data for the photoluminescence emission spectra of polycrystalline $PbMo_6S_8$ and single crystal YBCO as a function of temperature. To our knowledge this the first time that this data has been presented for $PbMo_6S_8$. The data are considered to be reliable due to the homogeneity in spectral shape measured across the

sample surfaces and the reproducibility of measurements made as a function of temperature. A comparison between the photoluminescence emission spectra of single crystal and thin film YBCO showed extremely good agreement with the only marked difference between the two spectra being a higher peak photoluminescence emission intensity from the single crystal sample.

A reproducible increase in peak photoluminescence emission intensity by a factor of 1.5 was measured for polycrystalline $PbMo_6S_8$ and a factor of two for single crystal YBCO between 304 K and 80 K and 296 K and 131 K, respectively. FWHM decreased by 20 nm for $PbMo_6S_8$ and 30 nm for YBCO over the same temperature range with the peak photoluminescence emission wavelength remaining constant for both samples.

Photoluminescence emission spectra were also measured as a function of temperature for 99.99 % purity single crystal niobium, polycrystalline Chevrel phase $SnMo_6S_8$ and a single crystal DyBCO sample. However, data from these samples was considered to be unreliable due to a variety of factors and, as such, could not be included in a discussion of the photoluminescence emission from metals and superconductors. The emission spectrum from the niobium sample is thought to originate from an oxide layer on the sample surface since emission was only measurable from an unpolished sample cut using a diamond saw and not after the sample was polished. Peaks in the photoluminescence emission spectrum of $SnMo_6S_8$ have been attributed to impurities on the sample surface due to their change in relative intensity to the main peak depending upon the position of the measurement on the sample surface and their temperature dependence which was independent of the main photoluminescence emission peak. An increase in the peak photoluminescence emission intensity from the single crystal DyBCO sample was observed over the measurement period which could not be explained. As such, the data could not be reliably interpreted as an additional change was

occurring to the sample which was not related to its temperature dependence. Measurements as a function of temperature could not be made on the doped Chevrel phase superconductors $Sn_{1-x}Eu_xMo_6S_8$ x = 0.35 and $Pb_{1-x}Gd_xMo_6S_8$ x = 0.3 as damage occurred to the samples under laser illumination.

Modelling of the photoluminescence emission spectra of the superconducting samples was unsuccessful using the equation which successfully calculated the emission spectra of gold and copper. The calculated spectra were unable to produce any of the features observed in the measured spectra. Explanations for the poor agreement between the calculated and measured spectra include; the emission being from an oxide on the niobium sample and not from pure niobium for which the spectrum was calculated, the lack of inclusion of the density of states above the Fermi level in the calculation for the Chevrel phase materials and modelling of the wrong processes for the generation of photoluminescence emission from the high temperature cuprate materials.

A variation in photoluminescence emission intensity over a period of 12 hours has been observed for a range of samples and shows an oscillation with a period ~ 400 minutes for gold and copper and a continuous decrease in intensity with no oscillation for niobium, $SnMo_6S_8$ and YBCO. A rapid increase in peak photoluminescence emission intensity with no change of spectral shape is observed at low temperatures in niobium, $PbMo_6S_8$ and YBCO but is not present in measurements of gold, copper or DyBCO. At present, the physical processes underlying both of these features remain unexplained and require further investigation. No precedent is available in the literature to explain either phenomenon. A comprehensive study is required to identify whether the time dependence is characteristic of all metallic and superconducting samples.

The design, construction, calibration and operation of an instrument for the measurement of low yield photoluminescence emission as a function of temperature has

been a important component of this project. Key features of the instrument included a sample holder designed to maximise thermal conduction from the cold head of the cryostat to the sample which also included silicon wafers acting as an optical shield between the sample holder and the excitation source. Photoluminescence emission from components within the instrument such as glass filters, lenses, anodised sample holders and adhesives luminesced with up to 10^5 times greater intensity than the emission from the samples themselves. Extreme care and attention to detail was employed throughout the project to select high quality optical components and to construct sample holders which reduced background emission intensities to at least two orders of magnitude below the emission intensity of the metals.

Sample holder mounting techniques and thermometry have also been investigated in detail in this thesis. Our work has shown that the standard setup of most optical cryostats frequently does not achieve the temperatures stated on instrument dials unless radiation shielding, joints between the sample holder and the cold head, vacuum pressures and adhesives are all optimised and maintained correctly. Incorrect mounting of a single component such as the radiation shield around the sample was observed to increase the sample base temperature by 36 K.

Heating of the sample by laser illumination was the limiting factor in the sample base temperature during variable temperature measurements. To improve the base temperature, lower excitation powers are required, decreasing the intensity of the emission from the sample. Lower emission intensities will require longer measurement exposure times and hence will require a detector with a lower dark current to maintain or improve upon the existing signal to noise ratio. The use of an adhesive with a higher thermal conductivity, such as pressed indium, would also aid in achieving lower sample temperatures.

Two interesting avenues for future work have become apparent based on the conclusions of this work. The first is the measurement of photoluminescence emission below the superconducting transition temperature. The few studies of photoluminescence from superconductors as a function of temperature in the literature draw contradictory conclusions as to whether any changes are observed at T_C. A systematic study of both high and low temperature superconductors is required to identify if the observations of the different studies are due to the superconducting properties of the samples.

Before measurements below 70 K can be made, the apparatus must be developed to improve the base temperature of the samples under laser illumination. The use of pressed indium joints and lower laser excitation powers will help to achieve this and a careful calibration of sample temperature should then be carried out as a function of laser power. The geometry and preparation of samples should also be considered for a new study with the optimum materials being polished single crystals and thin films with surface areas greater than 10 mm x 10 mm. The larger samples will remove the requirement for a silicon shield behind the samples.

The second area where further investigation is warranted is the variation of photoluminescence emission over a period of hours. A systematic approach is needed to measure a range of samples (both superconductors and non-superconductors), mounted using different techniques at several temperatures (above and below T_C) with each measurement repeated multiple times. This will help to identify the processes producing photoluminescence emission across a range of samples.

Finally, it is our hope that future work using the instrument designs and discussions presented in this thesis will not simply be limited to the measurement of metals and superconductors but will be used across a wide range of disciplines including

work on doped semiconductors, tagging of biological molecules and in vivo medical diagnostics.

Appendix: Publications, talks and posters

Publications

Armstrong, H., D.P. Halliday, and D.P. Hampshire

Photoluminescence of gold, copper and niobium as a function of temperature

Journal of Luminescence, 2009. **129**(12): p. 1610-1614.

Talks

1. International Conference on Luminescence and Optical Spectroscopy of Condensed Matter (ICL'08), 9 July 2008, Lyon, France

Posters

1. IoP Superconductivity Group AGM, June 2006, London, UK

2. Applied Superconductivity Conference, ASC'06, August 2006, Seattle, USA

3. European Conference on Applied Superconductivity, EUCAS'07, September 2007, Brussels, Belgium

References

1. Needham, J., *Digression on Luminescence*, in *Science and Civilisation in China*. 1962, Cambridge University Press: Cambridge. p. 71-78.

2. Licetus, F., *Litheosphorus, sive de Lapide Bononiensi lucem in se conceptam ab ambiente ciaro moc in tenebris mire conservante liber*. 1604: Utini.

3. Dean, P.J., *Photo-Luminescence as a Diagnostic of Semiconductors*. Progress in Crystal Growth and Characterization of Materials, 1982. **5**(1-2): p. 89-174.

4. Lightowlers, E., *Photoluminescence Characterisation*, in *Growth and Characterisation of Semiconductors*, R. Stradling, Klipstein, P., Editor. 1990, Adam Hilger: Bristol. p. 135-163.

5. Perkowitz, S., *Optical characterization of semiconductors : infrared, raman, and photoluminescence spectroscopy*. 1993, Academic Press: London. p. 3-6.

6. So, M.K., et al., *Self-illuminating quantum dot conjugates for in vivo imaging.* Nature Biotechnology, 2006. **24**(3): p. 339-343.

7. Rothberg, L., *Photophysics of conjugated polymers*, in *Semiconducting polymers: Chemistry, Physics and Engineering*, G. Hadziioannou, G. Malliaras, Editor. 2007, Wiley-VCH Verlag GmbH & Co. KGaA: Weinheim. p. 179-204.

8. Antonietta Loi, M., E. Da Como, M. Muccini, *Morphology-correlated photophysics in organic semiconductor thin films by confocal laser microscopy and spectroscopy*, in *Photophysics of molecular materials*, G. Lanzani, Editor. 2006, Wiley-VCH Verlag GmbH & Co. KGaA: Weinheim. p. 153-181.

9.   Mooradian, A., *Photoluminescence of Metals.* Physical Review Letters, 1969. **22**(5): p. 185-&.

10.   Boyd, G.T., Z.H. Yu, and Y.R. Shen, *Photoinduced luminescence from the noble metals and its enhancement on roughened surfaces.* Physical Review B, 1986. **33**(12): p. 7923 LP - 7936.

11.   Whittle, D.J., *Single and multiphoton excitation of secondary light emission by the noble metals*, in *Physics*. 1982, University of Pennsylvania. p. 163.

12.   Bardeen, J., L.N. Cooper, and J.R. Schrieffer, *Theory of Superconductivity.* Physical Review, 1957. **108**(5): p. 1175-1204.

13.   Garcia, J.A., A. Remon, and J. Piqueras, *2.3 Ev Photoluminescence in Yba2cu3o7-X Ceramics.* Physics of the Solid State, 1994. **144**(1): p. 217-221.

14.   Eremenko, V.V., T.V. Sukhareva, and V.N. Samovarov, *Luminescence spectra and crystal structure of high-temperature superconductors.* Physics of the Solid State, 2000. **42**(5): p. 816-823.

15.   Sukhareva, T.V. and V.V. Eremenko, *Luminescence spectra and crystal structure of high-temperature superconductors.* Physics of the Solid State, 1997. **39**(10): p. 1548-1555.

16.   Tominaga, E., et al., *Multiphoton-induced luminescence from superconducting Nb3Sn.* PROGRESS IN CRYSTAL GROWTH AND CHARACTERIZATION OF MATERIALS, 1996. **33**(1-3): p. 73-79.

17.   Fraas, L.M., P.F. Williams, and S.P.S. Porto, *Photoluminescence Studies of Superconducting Nb$_3$Sn.* Solid State Communications, 1970. **8**(24): p. 2113-&.

18.   Rafailov, P.M., M. Dworzak, and C. Thomsen, *Luminescence and Raman spectroscopy on MgB2.* Solid State Communications, 2002. **122**(7-8): p. 455-458.

19. Pawar, S.H. and B.M. Todkar, *Luminescence in High-Tc Superconductors.* Indian Journal of Pure and Applied Physics, 1992. **30**(10-11): p. 562-576.

20. Federici, J.F., et al., *Defect mechanism of photoinduced superconductivity in YBa$_2$Cu$_3$O$_{6+x}$.* Physical Review B, 1995. **52**(21): p. 15592-15597.

21. Fox, M., *Optical Properties of Solids*, in *Oxford Master Series in Condensed Matter Physics*. 2001, Oxford University Press: Oxford.

22. Fox, M., *Optical Properties of Solids*, in *Oxford Master Series in Condensed Matter Physics*. 2001, Oxford University Press: Oxford. p. 3.

23. Fox, M., *Optical Properties of Solids*, in *Oxford Master Series in Condensed Matter Physics*. 2001, Oxford University Press: Oxford. p. 6.

24. Sokolov, A.V., *Optical properties of Metals*, P.O.S. Heavens, Editor. 1967, Blackie and Son Limited: Glasgow. p. 11.

25. Sokolov, A.V., *Optical properties of Metals*, P.O.S. Heavens, Editor. 1967, Blackie and Son Limited: Glasgow. p. 10.

26. Fox, M., *Optical Properties of Solids*, in *Oxford Master Series in Condensed Matter Physics*. 2001, Oxford University Press: Oxford. p. 5.

27. Pankove, J.I., *Optical Processes in Semiconductors*. 1971, Dover Publications Inc.: New York. p. 87.

28. Fox, M., *Optical Properties of Solids*, in *Oxford Master Series in Condensed Matter Physics*. 2001, Oxford University Press: Oxford. p. 259.

29. Sokolov, A.V., *Optical properties of Metals*, P.O.S. Heavens, Editor. 1967, Blackie and Son Limited: Glasgow. p. 4.

30. Pankove, J.I., *Optical Processes in Semiconductors*. 1971, Dover Publications Inc.: New York. p. 88.

31. Sokolov, A.V., *Optical properties of Metals*, P.O.S. Heavens, Editor. 1967, Blackie and Son Limited: Glasgow. p. 12.

32. Fox, M., *Optical Properties of Solids*, in *Oxford Master Series in Condensed Matter Physics*. 2001, Oxford University Press: Oxford. p. 261.

33. Sokolov, A.V., *Optical properties of Metals*, P.O.S. Heavens, Editor. 1967, Blackie and Son Limited: Glasgow. p. 16.

34. Sokolov, A.V., *Optical properties of Metals*, P.O.S. Heavens, Editor. 1967, Blackie and Son Limited: Glasgow. p. 15.

35. Sokolov, A.V., *Optical properties of Metals*, P.O.S. Heavens, Editor. 1967, Blackie and Son Limited: Glasgow. p. 14.

36. Fox, M., *Optical Properties of Solids*, in *Oxford Master Series in Condensed Matter Physics*. 2001, Oxford University Press: Oxford. p. 262.

37. Pankove, J.I., *Optical Processes in Semiconductors*. 1971, Dover Publications Inc.: New York. p. 90.

38. Fox, M., *Optical Properties of Solids*, in *Oxford Master Series in Condensed Matter Physics*. 2001, Oxford University Press: Oxford. p. 143 - 144.

39. Fox, M., *Optical Properties of Solids*, in *Oxford Master Series in Condensed Matter Physics*. 2001, Oxford University Press: Oxford. p. 144.

40. Jackson, J.D., *Classical Electrodynamics*. 1999, John Wiley and Sons: New York. p. 248.

41. Sokolov, A.V., *Optical properties of Metals*, P.O.S. Heavens, Editor. 1967, Blackie and Son Limited: Glasgow. p. 75.

42. Abeles, F., *Optical properties of metals*, in *Optical properties of solids*, A. F., Editor. 1972, North-Holland Publishing Company: Amsterdam. p. 103.

43. Sokolov, A.V., *Optical properties of Metals*, ed. P.O.S. Heavens. 1967, Glasgow: Blackie and Son Limited. 472.

44. Abeles, F., *Optical properties of metals*, in *Optical properties of solids*, A. F., Editor. 1972, North-Holland Publishing Company: Amsterdam. p. 93 - 162.

45. Pankove, J.I., *Optical Processes in Semiconductors*. 1971, Dover Publications Inc.: New York. p. 34-42.

46. Whittle, D.J., *Single and multiphoton excitation of secondary light emission by the noble metals*, in *Dissertation in Physics*. 1982, University of Pennsylvania. p. 22.

47. Dragoman, D.D.a.M., *Optical Characterization of Solids*. 2002, New York: Springer-Verlag. 451.

48. Dragoman, D.D.a.M., *Optical Characterization of Solids*. 2002, Springer-Verlag: New York. p. 56-62.

49. Singleton, J., *Band Theory and Electronic Properties of Solids*, in *Oxford Master Series in Condensed Matter Physics*. 2001, Oxford University Press: New York. p. 49-52.

50. Fox, M., *Optical Properties of Solids*, in *Oxford Master Series in Condensed Matter Physics*. 2001, Oxford University Press: Oxford. p. 54-60.

51. Abeles, F., *Optical properties of semiconductors*, in *Optical properties of solids*, A. F., Editor. 1972, North-Holland Publishing Company: Amsterdam. p. 43-54.

52. Fox, M., *Optical Properties of Solids*, in *Oxford Master Series in Condensed Matter Physics*. 2001, Oxford University Press: Oxford. p. 271-279.

53. Fox, M., *Optical Properties of Solids*, in *Oxford Master Series in Condensed Matter Physics*. 2001, Oxford University Press: Oxford. p. 269-270.

54. Harrison, W.A., *Parallel-Band Effects in Interband Optical Absorption.* Physical Review, 1966. **147**(2): p. 467 LP - 469.

55. Pankove, J.I., *Optical Processes in Semiconductors*. 1971, Dover Publications Inc.: New York. p. 161.

56. Fox, M., *Optical Properties of Solids*, in *Oxford Master Series in Condensed Matter Physics*. 2001, Oxford University Press: Oxford. p. 98.

57. Pankove, J.I., *Optical Processes in Semiconductors*. 1971, Dover Publications Inc.: New York. p. 107.

58. Woan, G., *The Cambridge Handbook of Physics Formulas*. 2003, CUP: Cambridge. p. 102.

59. Fox, M., *Optical Properties of Solids*, in *Oxford Master Series in Condensed Matter Physics*. 2001, Oxford University Press: Oxford. p. 151-154.

60. Singleton, J., *Band Theory and Electronic Properties of Solids*, in *Oxford Master Series in Condensed Matter Physics*. 2001, Oxford University Press: New York. p. 172-174.

61. Abeles, F., *Optical properties of metals*, in *Optical properties of solids*, A. F., Editor. 1972, North-Holland Publishing Company: Amsterdam. p. 123-142.

62. Lasser, R., N.V. Smith, and R.L. Benbow, *Empirical Band Calculations of the Optical-Properties of D-Band Metals .1. Cu, Ag, and Au.* Physical Review B, 1981. **24**(4): p. 1895-1909.

63. Cooper, B.R., H. Ehrenreich, and H.R. Philipp, *Optical Properties of Noble Metals. II.* Physical Review, 1965. **138**(2A): p. A494 LP - A507.

64. Apell, P., R. Monreal, and S. Lundqvist, *Photoluminescence of Noble-Metals.* Physica Scripta, 1988. **38**(2): p. 174-179.

65.   Whittle, D.J., *Single and multiphoton excitation of secondary light emission by the noble metals*, in *Dissertation in Physics*. 1982, University of Pennsylvania. p. 82 - 90.

66.   Whittle, D.J., *Single and multiphoton excitation of secondary light emission by the noble metals*, in *Dissertation in Physics*. 1982, University of Pennsylvania. p. 92 - 111.

67.   Whittle, D.J., *Single and multiphoton excitation of secondary light emission by the noble metals*, in *Dissertation in Physics*. 1982, University of Pennsylvania. p. 103-104.

68.   Vengurlekar, A. and T. Ishihara, *Photoluminescence in Au film: Enhanced emission for a corrugated film.* Journal of Luminescence, 2007. **122**: p. 796-799.

69.   Kittel, C., *Introduction to solid state physics*. seventh ed. 1996: John Wiley & Sons. p 271-279.

70.   Fox, M., *Optical Properties of Solids*, in *Oxford Master Series in Condensed Matter Physics*. 2001, Oxford University Press: Oxford. p. 160-162.

71.   Pitarke, J.M., et al., *Theory of surface plasmons and surface-plasmon polaritons.* Reports on Progress in Physics, 2007(1): p. 1.

72.   Abeles, F., *Optical properties of metals*, in *Optical properties of solids*, A. F., Editor. 1972, North-Holland Publishing Company: Amsterdam. p. 156-158.

73.   Melnyk, A.R. and M.J. Harrison, *Theory of Optical Excitation of Plasmons in Metals.* Physical Review B, 1970. **2**(4): p. 835 LP - 850.

74.   Boyd, G.T., et al., *Local-field enhancement on rough surfaces of metals, semimetals, and semiconductors with the use of optical second-harmonic generation.* Physical Review B, 1984. **30**(2): p. 519 LP - 526.

75. Pradhan, A.K., et al., *Surface Plasmon Excitation via Au Nanoparticles in CdSe Semiconductor.* Mesoscopic, Nanoscopic, and Macroscopic Materials, 2008. **1063**: p. 18-25.

76. Rivas, J.G., G. Vecchi, and V. Giannini, *Surface plasmon polariton-mediated enhancement of the emission of dye molecules on metallic gratings.* New Journal of Physics, 2008. **10**.

77. Moskovits, M., *Surface-Enhanced Spectroscopy.* Reviews of Modern Physics, 1985. **57**(3): p. 783-826.

78. Hecht, E., *Optics*, in *Optics*. 1998, Addison Wesley Longman, Inc.: New York. p. 331-337.

79. Johnson, P.B. and R.W. Christy, *Optical constants of copper and nickel as a function of temperature.* Physical Review B, 1975. **11**(4): p. 1315 LP - 1323.

80. Pells, G.P. and M. Shiga, *Optical Properties of Copper and Gold as a Function of Temperature.* Journal of Physics Part C Solid State Physics, 1969. **2**(10): p. 1835-&.

81. Rhodin, T.N., *Low Temperature Oxidation of Copper .1. Physical Mechanism.* Journal Am Chem Soc, 1950. **72**(11): p. 5102-5106.

82. Boggio, J.E., *Room-Temperature Oxidation of Cu(111) - Pressure Effects.* Journal of Chemical Physics, 1979. **70**(11): p. 5054-5058.

83. Davis, R.J., *All that glitters is not Au-0.* Science, 2003. **301**(5635): p. 926-927.

84. Hammer, B. and J.K. Norskov, *Why Gold Is the Noblest of All the Metals.* Nature, 1995. **376**(6537): p. 238-240.

85. Onnes, H.K., *Further Experiments with Liquid Helium. G On the Electrical Resistance of Pure Metals, etc VI. On the Sudden Change in the Rate at which the*

Resistance of Mercury Disappears. Communications from the Physical Laboratory of the University of Leiden, 1911. **124C**: p. 21-26.

86. Kamihara, Y., et al., *Iron-based layered superconductor: LaOFeP.* Journal of the American Chemical Society, 2006. **128**(31): p. 10012-10013.

87. Tilley, D.R. and J. Tilley, *Superfluidity and Superconductivity*, in *Superfluidity and Superconductivity*. 1990, IOP publishing Ltd.: Bristol. p. 13.

88. Struzhkin, V.V., et al., *Superconductivity at 10 - 17 K in compressed sulphur.* Nature, 1997. **390**: p. 382-384.

89. Tilley, D.R. and J. Tilley, *Superfluidity and Superconductivity*, in *Superfluidity and Superconductivity*. 1990, IOP publishing Ltd.: Bristol. p. 126.

90. Tilley, D.R. and J. Tilley, *Superfluidity and Superconductivity*, in *Superfluidity and Superconductivity*. 1990, IOP publishing Ltd.: Bristol. p. 133.

91. Gor'kov, L.P., *Microscopic derivation of the Ginzburg-Landau equations in the theory of superconductors.* Soviet Physics JETP, 1959. **9**(6): p. 1364-1367.

92. Tilley, D.R. and J. Tilley, *Superfluidity and Superconductivity*. 3rd ed. 1990, Bristol: IOP publishing Ltd.

93. Tinkham, M., *Introduction to Superconductivity*. 2nd ed. 1996, Singapore: McGraw-Hill Book Co. 110-147.

94. Abrikosov, A.A., *The Magnetic Properties of Superconducting Alloys.* Journal of Physics and Chemistry of Solids, 1957. **2**: p. 199-208.

95. Kleiner, W.H., L.M. Roth, and S.H. Autler, *Bulk Solution of Ginzburg-Landau Equations for Type II Superconductors: Upper critical field region.* Physical Review, 1964. **133**(5A): p. A1226-A1227.

96. Romaniello, P., et al., *Optical properties of bcc transition metals in the range 0-40 eV.* Physical Review B, 2006. **73**(7).

97.   Jani, A.R., N.E. Brener, and J. Callaway, *Band-Structure and Related Properties of Bcc Niobium.* Physical Review B, 1988. **38**(14): p. 9425-9433.

98.   Poole, C.P., H.A. Farach, and R.J. Creswick, *Superconductivity.* Second Edition ed. 2007, Oxford, UK: Elsevier Ltd. p 116.

99.   Fumagalli, P. and J. Schoenes, *Magneto-optical Kerr-effect study of the high-field superconductors $Eu_{1-x}Pb_xMo_6S_8$ and $Eu_{1-x}Sn_xMo_6S_{8-y}Se_y$.* Physical Review B, 1991. **44**(5): p. 2246-2262.

100.   Fischer, Ø. and M.B. Maple, *Superconductivity in Ternary Compounds Vol I - Structural, Electronic and Lattice Properties*, in *Superconductivity in Ternary Compounds Vol I - Structural, Electronic and Lattice Properties*, M.B. Maple and Ø. Fischer, Editors. 1982, Springer-Verlag: Berlin. p. 2 - 9.

101.   Mattheis, L.F. and C.Y. Fong, *Cluster model for the electronic structure of the Chevrel-phase comnpound $PbMo_6S_8$.* Physical Review B, 1977. **15**(4): p. 1760-1768.

102.   Kobayashi, K., et al., *Electronic structure of the Chevrel-phase compounds SnxMo6Se7.5: Photoemission spectroscopy and band-structure calculations.* Physical Review B, 2001. **63**(19): p. 195109.

103.   Shen, Z.X., et al., *Photoemission-Studies of High-T-C Superconductors - the Superconducting Gap.* Science, 1995. **267**(5196): p. 343-350.

104.   Harshman, D.R. and A.P. Mills Jr, *Concerning the nature of high-Tc superconductivity: Survey of experimental properties and implications for interlayer coupling.* Physical Review B, 1992. **45**(18): p. 10684-10712.

105.   Ruvalds, J., *Theoretical prospects for high-temperature superconductors.* Superconductor Science & Technology, 1996. **9**(11): p. 905-926.

106. Bonn, D.A., *Are high-temperature superconductors exotic?* Nature Physics, 2006. **2**(3): p. 159-168.

107. Tanaka, S., *High-temperature superconductivity.* Japanese Journal of Applied Physics, 2006. **45**(12): p. 9011-9024.

108. Sachdev, S., *Colloquium: Order and quantum phase transitions in the cuprate superconductors.* Reviews of Modern Physics, 2003. **75**(3): p. 913-932.

109. Basov, D.N. and T. Timusk, *Electrodynamics of high-T-c superconductors.* Reviews of Modern Physics, 2005. **77**(2): p. 721-779.

110. Sokolov, A.V., *Optical properties of Metals*, P.O.S. Heavens, Editor. 1967, Blackie and Son Limited: Glasgow. p. 67.

111. Sokolov, A.V., *Optical properties of Metals*, P.O.S. Heavens, Editor. 1967, Blackie and Son Limited: Glasgow. p. 72.

112. Lenham, A.P., *Absorption of Low-Energy Photons in Transition Metals.* Journal of the Optical Society of America, 1967. **57**(4): p. 473-&.

113. Elazrak, A., et al., *Infrared Properties of Yba2cu3o7 and Bi2sr2can-1cuno2n+4 Thin-Films.* Physical Review B, 1994. **49**(14): p. 9846-9856.

114. Bozovic, I., et al., *Optical Measurements on Oriented Thin Yba2cu3o7-Delta Films - Lack of Evidence for Excitonic Superconductivity.* Physical Review Letters, 1987. **59**(19): p. 2219-2221.

115. White, G.K. and S.B. Woods, *Electrical and Thermal Resistivity of the Transition Elements at Low Temperatures.* 1959. **251**(995): p. 273-302.

116. Phillips, J.C., *Physics of Complex Metals - Temperature-Dependent Resistivities in Ionic Superconductors and Stable Quasi-Crystals.* 1992. **46**(13): p. 8542-8558.

117. Balakirev, F.F., et al., *Signature of optimal doping in Hall-effect measurements on a high-temperature superconductor.* Nature, 2003. **424**(6951): p. 912-915.

118. Lee, J.Y., et al., *Penetration Depth in Oxygen Depleted Ybco Thin-Films.* Synthetic Metals, 1995. **71**(1-3): p. 1605-1606.

119. Uemura, Y.J., et al., *Basic Simularities among Cuprate, Bismuthate, Organic, Chevrel-Phase, and Heavy-Fermion Superconductors shown by Penetration-Depth Measurements.* Physical Review Letters, 1991. **66**(20): p. 2665-2668.

120. Schneider, T. and H. Keller, *Extreme Type II superconductors: universal properties and trends.* Int Journal Mod Phys, 1993. **8**: p. 487-528.

121. Uemura, Y.J., et al., *Systematic Variation of Magnetic-Field Penetration Depth in High-Tc Superconductors Studied by Muon-Spin Relaxation.* Physical Review B, 1988. **38**(1): p. 909-912.

122. Tilley, D.R. and J. Tilley, *Superfluidity and Superconductivity*, in *Superfluidity and Superconductivity*. 1990, IOP publishing Ltd.: Bristol. p. 67 - 68.

123. Damascelli, A., Z. Hussain, and Z.X. Shen, *Angle-resolved photoemission studies of the cuprate superconductors.* Reviews of Modern Physics, 2003. **75**(2): p. 473-541.

124. Devereaux, T.P., et al., *Electronic Raman-Scattering in High-T(C) Superconductors - a Probe of Dx2-Y2 Pairing.* Physical Review Letters, 1994. **72**(3): p. 396-399.

125. Reimann, K. and K. Syassen, *Raman-Scattering and Photoluminescence in Cu2o under Hydrostatic-Pressure.* Physical Review B, 1989. **39**(15): p. 11113-11119.

126. Federici, J.F. and D.M. Bubb, *The role of defects in persistent photoconductivity in YBa2Cu3O6+x.* Journal of Superconductivity, 2001. **14**(2): p. 331-340.

127. Gilabert, A., et al., *Photodoping effects in high critical temperature superconducting films and Josephson junctions.* Journal of Superconductivity, 2000. **13**(1): p. 1-20.

128. Nakazawa, E., *Fundamentals of luminescence, Transient characteristics of luminescence*, in *Phosphor Handbook*, W. Yen, Shinonoya, S., Yamamoto, H., Editor. 2007, CRC Press: Boca Raton. p. 83-90.

129. Tanimizu, S., Tamatani, M., Kano, T., Morita, M., Shionoya, S., Yokogawa, T., Kukimoto, H., Hatakoshi, G., Iga, K., Nakamura, S.,, *Fundamentals of luminescence, Transient characteristics of luminescence*, in *Phosphor Handbook*, W. Yen, Shinonoya, S., Yamamoto, H., Editor. 2007, CRC Press: Boca Raton. p. 155-322.

130. Perkowitz, S., *Optical characterization of semiconductors : infrared, raman, and photoluminescence spectroscopy*. 1993, Academic Press: London. p. 50-54.

131. Melles-Griot, *Material Properties*. 2008. p. Catalogue article.

132. Schott, *Optical Glass - Description of properties 2007*. 2007.

133. Newport, *Optical Materials*. 2008. p. Catalogue article.

134. Saint-Gobain, *Spectrosil*. 2008.

135. Crystran, *Crystran website Materials Data*. 2008.

136. Crystran, *The Design of Pressure Windows*. 2005, CRYSTRAN LTD.

137. Hungerford, G. and D.J.S. Birch, *Single-photon timing detectors for fluorescence lifetime spectroscopy*. Measurement Science and Technology, 1996. **7**(2): p. 121-135.

138. Princeton-Instruments, *OMA V*, in *Princeton Instruments Sales Brochure*. 2010.

139. Hamamatsu, *Photomultiplier tubes R 928*, in *Hamamatsu Sales Brochure*. 2010.

140. Hamamatsu, *Photomultiplier tube handbook*. Third Edition ed. 2010: Hamamatsu.

141. Horiba-Jobin-Yvon, *Symphony 1024 x 128 Cryogenic Back Illuminated CCD Detector*, in *Horiba-Jobin-Yvon Sales Brochure*. 2010.

142. Horiba-Jobin-Yvon, *Symphony 1024 x 256 Cryogenic Open Electrode CCD Detector*, in *Horiba-Jobin-Yvon Sales Brochure*. 2010.

143. Ekin, J.W., *Experimental Techniques for Low-Temperature Measurements*. 2007, Oxford University Press: New York. p. 26-28.

144. Jobin Yvon Inc, *Fluorolog -3 Operation Manual*, in *Fluorolog -3 Operation Manual*. 2002, Jobin Yvon: Edison. p. 2-7.

145. Jobin Yvon Inc, *Fluorolog -3 Operation Manual*, in *Fluorolog -3 Operation Manual*. 2002, Jobin Yvon: Edison. p. 4-9.

146. J.A. Woollam, C., *Guide to using WVASE32*, in *Guide to using WVASE32*, J.A. Woollam: Lincoln, NE, USA. p. 24-28.

147. Archer, R.J., *Determination of Properties of Films on Silicon by Method of Ellipsometry.* Journal of the Optical Society of America, 1962. **52**(9): p. 970-&.

148. J.A. Woollam, C., *Guide to using WVASE32*, in *Guide to using WVASE32*, J.A. Woollam: Lincoln, NE, USA. p. 219,-220, 229, 555.

149. Fox, M., *Optical Properties of Solids*, in *Oxford Master Series in Condensed Matter Physics*. 2001, Oxford University Press: Oxford. p. 7.

150. Weber, M.J., *Handbook of Optical Materials*, in *Handbook of Optical Materials*. 2003, CRC Press: New York. p. 317 - 329.

151. Quantum Design, *PPMS Hardware Manual*, in *PPMS Hardware Manual*. 2004, Quantum Design: San Diego. p. 2-4.

152. Quantum Design, *PPMS Heat Capacity Option User's manual*, in *PPMS Hardware and Options Manual*. 2004, Quantum Design: San Diego. p. 1-2.

153. Quantum Design, *PPMS Heat Capacity Option User's manual*, in *PPMS Hardware and Options Manual*. 2004, Quantum Design: San Diego. p. 1-3.

154. Leigh, N.R., *Specific heat measurements on Chevrel phase materials exhibiting coexistence of superconductivity and magnetism*, in *Specific heat measurements on Chevrel phase materials exhibiting coexistence of superconductivity and magnetism*. 2001, University of Durham: Durham. p. 140.

155. Quantum Design, *PPMS ACMS User's manual*, in *PPMS Hardware and Options Manual*. 2004, Quantum Design: San Diego. p. 1-3.

156. Olympus_America_Inc., http://www.olympusamerica.com/seg_section/uis2/seg_uis2_uplsapo_4x.asp, 2009.

157. Semrock, http://www.semrock.com/TechnicalInformation/TN_Filter_spectra_at_nonnormal_angles_of_incidence, 2009.

158. Erdogan, T., *Thin-film filters for Raman Spectroscopy.* Spectroscopy, 2004. **December 2004**: p. 113-116.

159. Standish, B., *High performance with fluorescence optical filters.* Bio Optics World, 2008. **Sept/Oct 2008**: p. 35-37.

160. Bentham-Instruments-Limited, *Multiple Grating Monochromators and Spectrographs*, Bentham Instruments Limited: Manual.

161. Cryomech, *Operation and Service Manual for Model ST405 Cryostat*, in *Operation and Service Manual for Model ST405 Cryostat*, Cryomech: Syracuse. p. 13.

162. Ekin, J.W., *Experimental Techniques for Low-Temperature Measurements*. 2007, Oxford University Press: New York. p. 58.

163. Apiezon-Products, *Apiezon cryogenic N grease technical data sheet*. 2005, www.apiezon.com.

164. Maycock, P.D., *Thermal conductivity of silicon, germanium, III-V compounds and III-V alloys.* Solid-State Electronics, 1967. **10**(3): p. 161-168.

165. Rosenberg, H.M., *The Thermal Conductivity of Germanium and Silicon at Low Temperatures.* Proceedings of the Physical Society. Section A, 1954. **67**(9): p. 837-840.

166. Ekin, J.W., *Experimental Techniques for Low-Temperature Measurements*. 2007, Oxford University Press: New York. p. 579.

167. Berman, R. and D.K.C. Macdonald, *The Thermal and Electrical Conductivity of Copper at Low Temperatures.* Proceedings of the Royal Society of London Series a-Mathematical and Physical Sciences, 1952. **211**(1104): p. 122-128.

168. Wasim, S.M. and N.H. Zebouni, *Thermal Conductivity of Superconducting Niobium.* Physical Review, 1969. **187**(2): p. 539-&.

169. Ekin, J.W., *Experimental Techniques for Low-Temperature Measurements*. 2007, Oxford University Press: New York. p. 547.

170. Clark, S.J., et al., *First principles methods using CASTEP.* Zeitschrift für kristallographie, 2005. **220**(5-6): p. 567-570.

171. Smith, N.V., et al., *Photoemission Spectra and Band Structures of D-Band Metals .4. X-Ray Photoemission Spectra and Densities of States in Rh, Pd, Ag, Ir, Pt and Au.* Physical Review B, 1974. **10**(8): p. 3197-3206.

172. Heimann, P., H. Neddermeyer, and H.F. Roloff, *Photoemission from (110) Faces of Noble Metals: Observation of One-Dimensional Density of States.* Physical Review Letters, 1976. **37**(12): p. 775 - 778.

173. Kupratakuln.S, *Relativistic Electron Band Structure of Gold.* Journal of Physics C - Solid State Physics, 1970. **3**(2): p. S109-&.

174. Ramchandani, M.g., *Energy Band Structure of Gold.* Journal of Physics C - Solid State Physics, 1970. **3**(1): p. S1-&.

175. Christensen, N. and B.O. Seraphin, *Relativistic Band Calculation and Optical Properties of Gold.* Physical Review B, 1971. **4**(10): p. 3321-&.

176. Macdonald, A.H., et al., *Non-Muffin-Tin and Relativistic Interaction Effects on the Electronic-Structure of Noble-Metals.* Physical Review B, 1982. **25**(2): p. 713-725.

177. Weinberger, P., *Electronic-Structure of Au and Pt and of the Dns1 Impurities in These Metals.* Journal of Physics F - Metal Physics, 1982. **12**(10): p. 2171-2184.

178. Berglund, C.N.S., W. E., *Photoemission Studies of Copper and Silver: Experiment.* Physical Review, 1964. **136**(4A).

179. Jepsen, O., D. Glotzel, and A.R. Mackintosh, *Potentials, Band Structures, and Fermi Surfaces in the Noble-Metals.* Physical Review B, 1981. **23**(6): p. 2684-2696.

180. Leigh, N.R., *Specific heat measurements on Chevrel phase materials exhibiting coexistence of superconductivity and magnetism*, in *Department of Physics*. 2001, University of Durham: Durham. p. 157 - 158.

181. Leigh, N.R. and D.P. Hampshire, *Deriving the Ginzburg-Landau parameter from heat capacity data on magnetic superconductors with Schottky anomalies.* Physical Review B, 2003. **68**: p. 174508.

182. The HTC Centre for Single Crystals, *Private Communications*. 2005: Birmingham University.

183. Wimbush, S., Driscoll, J., *Private Communications*. 2007: Cambridge University.

184.   Boyer, L.L., D.A. Papaconstantopoulos, and B.M. Klein, *Effect of Self-Consistency and Exchange on Electronic-Structure of Transition-Metals, V, Nb, and Ta.* Physical Review B, 1977. **15**(8): p. 3685-3693.

185.   Turzhevsky, S.A., et al., *Electronic structure and crystal chemistry of niobium oxide phases.* Physical Review B, 1994. **50**(5): p. 3200 LP - 3208.

186.   Jehng, J.M. and I.E. Wachs, *Structural chemistry and Raman spectra of niobium oxides.* Chemistry of Materials, 1991. **3**(1): p. 100-107.

187.   Jehng, J.-M. and I.E. Wachs, *Niobium oxide solution chemistry.* Journal of Raman Spectroscopy, 1991. **22**(2): p. 83-89.

188.   Sokolov, A.V., *Optical properties of Metals*, P.O.S. Heavens, Editor. 1967, Blackie and Son Limited: Glasgow. p. 27 - 28.